Dissertation
submitted to the
Combined Faculties for the Natural Sciences and for Mathematics
of the Ruperto-Carola University of Heidelberg, Germany
for the degree of
Doctor of Natural Sciences

put forward by
Dipl.-Phys. Holger Sihler
born in Ebersberg, Oberbayern

Oral examination: 18.6.2012

Halogen Activation in the Polar Troposphere

Referees: Prof. Dr. Ulrich Platt
PD Dr. Christoph S. Garbe

Zusammenfassung

Die vorliegende Arbeit beschäftigt sich mit dem Phänomen der Halogenaktivierung und der damit einhergehenden Zerstörung von bodennahem Ozon in der polaren Troposphäre. Mit aufsteigender Sonne im Frühjahr werden reaktive Halogenverbindungen aus Seesalz freigesetzt und tragen zu der katalytischen Zerstörung von Ozon mit weitreichenden Konsequenzen für die Chemie der arktischen und antarktischen Atmosphäre bei. Unter anderem entstehen dabei Brom-Monoxid (BrO) Radikale, welche mittels differentieller optischer Absorptionsspektroskopie (DOAS) nachgewiesen werden können. In Rahmen dieser Doktorarbeit werden LP-DOAS und MAX-DOAS Messungen, welche in Barrow, Alaska durchgeführt wurden, und Satellitendaten von GOME-2 verglichen und zu einer dreidimensionalen Beschreibung der BrO Verteilung kombiniert. Eine wesentliche Verbesserung der Korrelation zwischen Boden- und Satellitenmessungen wurde durch die Entwicklung eines neuen Algorithmus zum Nachweis von troposphärischem BrO in Satellitenmessungen, der den störenden Einfluss stratosphärischer Inhomogenitäten im Vergleich zu früheren Methoden wesentlich verringert, erreicht. Die nun verfügbaren, korrigierten Satellitenmessungen der Jahre 2007 bis 2010 bilden die Grundlage für weitere systematische Untersuchungen der BrO Verteilung in der arktischen Troposphäre, die sich auf die von Meereis und Schnee bedeckten Flächen konzentriert. Neben primären Freisetzungsmechanismen aus dem Meereis, die zu Beginn des Frühjahres bei tiefen Temperaturen offenbar effizienter sind, spielen auch meteorologische Mischungsprozesse eine wesentliche Rolle. Die zeitlichen und räumlichen Muster der BrO Verteilung lassen sich so mit der Chemie im Übergangsbereich zwischen halogenreicher, ozonarmer und ozonreicher Luft erklären, wie sie zum Beispiel entlang von Fronten auftreten kann. Darüber hinaus folgt daraus, dass die Ozonkonzentration im Frühjahr über weiten Teilen der arktischen Meereisoberfäche wesentlich geringer sein muss als in der freien Troposphäre.

Abstract

This thesis investigates the phenomenon of halogen activation and the resulting near-surface ozone depletion frequently observed in the polar troposphere. During polar sunrise, reactive halogen species released from sea salt are responsible for the catalytic destruction of ozone affecting the atmospheric chemistry of both the Arctic and the Antarctic. In particular, bromine monoxide (BrO) radicals are formed in this process which can be detected by differential optical absorption spectroscopy (DOAS). In this thesis, ground-based LP-DOAS and MAX-DOAS measurements conducted at Barrow, Alaska, and GOME-2 satellite data are compared and used to assess the three-dimensional distribution of BrO. The correlation between ground-based and satellite measurements is significantly improved by the development of a new satellite retrieval algorithm for tropospheric BrO. Compared to previous methods, this algorithm significantly reduces interferences originating from stratospheric inhomogeneities. The subsequent systematic distribution studies in the Arctic, where tropospheric BrO is mostly located over the sea-ice and snow, are based on the retrieved satellite measurements available for the years 2007 to 2010. In addition to primary release mechanisms, whose efficiency apparently increases at lower temperatures during early spring, meteorological processes also play a significant role. The temporal and spatial BrO pattern can be explained by the chemistry in the transition zone between halogen-rich, ozone-poor and ozone-rich air as, for instance, along fronts. It can be furthermore concluded that near-surface ozone concentrations above vast areas of the Arctic sea-ice must be significantly lower than in the free troposphere.

Contents

II. Methods and Instruments

III. Results and Discussion

parts of the work have already been published in:

Sihler, H., Platt, U., Beirle, S., Marbach, T., Kühl, S., Dörner, S., Verschaeve, J., Frieß, U., Pöhler, D., Vogel, L., Sander, R., & Wagner, T. 2012. Tropospheric BrO column densities in the Arctic from satellite: Retrieval and comparison to ground-based measurements. accepted for publication in *Atmos. Meas. Tech. Disc.*

Frieß, U., Sihler, H., Sander, R., Pöhler, D., Yilmaz, S., & Platt, U. 2011. The vertical distribution of BrO and aerosols in the Arctic: Measurements by active and passive differential optical absorption sprectroscopy. *J. Geophys. Res.*, **116**, D00R04.

Heue, K.-P., Brenninkmeijer, C. A. M., Baker, A. K., Rauthe-Schöch, A., Walter, D., Wagner, T., Hörmann, C., Sihler, H., Dix, B., Frieß, U., Platt, U., Martinsson, B. G., van Velthoven, P. F. J., Zahn, A., & Ebinghaus, R. 2011. SO_2 and BrO observation in the plume of the Eyjafjallajökull volcano 2010: CARIBIC and GOME-2 retrievals. *Atm. Chem. Phys.*, **11**(6), 2973–2989.

Liao, J., Sihler, H., Huey, L., Neuman, J., Tanner, D., Friess, U., Platt, U., Flocke, F. M., Orlando, J. J., Shepson, P. B., Beine, H. J., Weinheimer, A. J., Sjostedt, S. J., Nowak, J. B., Knapp, D. J., andW. Zheng, R. M. Staebler, Sander, R., Hall, S. R., & Ullmann, K. 2011. A comparison of Arctic BrO measurements by chemical ionization mass spectrometry and long path-differential optical absorption spectroscopy. *J. Geophys. Res.*, **116**, D00R02.

Morin, S., Erbland, J. H., Savarino, J., Domine, F., Bock, J., Friess, U., Jacobi, H.-W., Sihler, H., & Martins, J. M. F. 2012. An isotopic view on the connection between photolytic emissions of NO_x from the Arctic snowpack and its oxidation by reactive halogens. *J. Geophys. Res.*, **117**, D00R08.

Prados-Roman, C., Butz, A., Deutschmann, T., Dorf, M., Kritten, L., Minikin, A., Platt, U., Schlager, H., Sihler, H., Theys, N., Van Roozendael, M., Wagner, T., & Pfeilsticker, K. 2011. Airborne DOAS limb measurements of tropospheric trace gas profiles: case studies on the profile retrieval of O_4 and BrO. *Atmos. Meas. Tech.*, **4**(6), 1241–1260.

yet unpublished contributions have been made to:

Helmig, D., Boylan, P., Johnson, B., Oltmans, S., Fairall, C., Staebler, R., Weinheimer, A., Orlando, J., Knapp, D. J., Montzka, D. D., Flocke, F., Frieß, U., Sihler, H., & Shepson, P. B. 2012. Ozone Dynamics and Snow-Atmosphere Exchanges During Ozone Depletion Events at Barrow, AK. submitted to *J. Geophys. Res.*

Hörmann, C., Sihler, H., Bobrowski, N., Platt, U., & Wagner, T. 2012. Systematic investigation of bromine monoxide in volcanic plumes from space by using the GOME-2 instrument. in prep.

Part I.

Motivation and Scientific Background

1. Introduction

In addition to its main constituents, nitrogen and oxygen, the atmosphere contains a large variety of trace gases whose presence is crucial to sustain life on Earth. Ozone, for instance, which is mostly located in the stratosphere at an altitude between 20 and 25 km, absorbs most short-wave radiation from the Sun and thus protects living organisms from potentially fatal genetic damage (Hartley, 1880). The production of ozone in the stratosphere is mainly controlled by the photo-dissociation of oxygen molecules due to the absorption of high-energy photons (Chapman, 1930). The average concentration of ozone in the atmosphere is comparatively low. If compressed to the atmospheric conditions at sea-level, the concentrated total ozone column would be less than 5 mm thick.

About 10 % of the total ozone column is located in the troposphere residing between the surface and the stratosphere. In the troposphere, ozone is a source of the hydroxyl (OH) radical, which is the most important oxidizing agent responsible for the self-cleaning capacity of the atmosphere. The oxidation of atmospheric constituents by OH results in the removal of both natural and anthropogenic pollutants. At high concentrations, however, tropospheric ozone may also become harmful to microorganisms and plants, and affects the respiratory system of humans and animals. Natural tropospheric sources of ozone are mainly entrainment from the stratosphere, the photo-dissociation of oxygen by the remaining short-wave radiation, and thunderstorms. Poisonous tropospheric ozone concentrations occur in polluted areas where increased levels of nitrogen oxides in the presence of volatile organic compounds (VOCs) lead to a net production of ozone.

An important ozone sink is presented by another family of trace gases, the halogen compounds. Halogen compounds are approximately three orders of magnitude less abundant than ozone but have a substantial impact on its concentration in both the stratosphere and troposphere through catalytic destruction cycles. Stratospheric sources of reactive halogens are biogenic halocarbons (such as bromomethane and bromoform), which have a long tropospheric life-time but decay much faster in the stratosphere due to the higher amount of short-wave radiation. By far the largest ozone destruction potential is represented by anthropogenic emissions of chlorofluorocarbons (CFCs) leading to the formation of the ozone hole over Antarctica (Molina & Rowland, 1974; Farman *et al.*, 1985). This discovery led to a worldwide CFC ban whose success is already visible in experiments monitoring the total ozone column over Antarctica. In recent years, however, the depth of the ozone hole over the northern hemisphere is continuously increasing due to a steady cooling of the wintertime stratosphere. Lower temperatures in the stratosphere stimulate the formation of polar stratospheric clouds (PSCs). PSCs provide surfaces on which halogen compounds can be recycled via heterogeneous reactions leading to an increased ozone destruction

capacity (Solomon *et al.*, 1986).

Since the early 1980s, measurements in the Arctic troposphere revealed a frequent, almost complete removal of near-surface ozone during spring (e. g. Oltmans, 1981; Bottenheim *et al.*, 1986). These events, which were later also detected in the Antarctic troposphere, are called ozone depletion events (ODEs) (Oltmans *et al.*, 1989; Kreher *et al.*, 1996). Halogen compounds (mostly inorganic bromine radicals) were found to be responsible for the sudden ozone loss in the troposphere by Barrie *et al.* (1988) shortly after the discovery of ODEs. In the following years, many projects were dedicated to studying the natural sources of the bromine radicals, the impact on the ozone distribution, and potential release mechanisms. The result is an extensive list of publications which is reviewed in the next chapter with a focus on environmental factors influencing tropospheric halogen activation. Nevertheless, many questions still remain unanswered, for instance: what are the sources of reactive halogens, what triggers their release, and what is the impact on the global tropospheric ozone budget?

Another important phenomenon interconnected to tropospheric halogen activation is the frequently observed depletion of atmospheric mercury (Schroeder *et al.*, 2003; Steffen *et al.*, 2008). At least half of the atmospheric mercury originates from human activity such as coal and fossil fuel combustion whereas the type and magnitude of natural sources are still under debate. However, halogen radicals are now believed to be involved in the formation of mercury containing particles which may precipitate and contaminate the snow, soil and ocean. Mercury, being a heavy metal, may have adverse effects on the unique polar ecosystems and it potentially accumulates in the food chain.

The Arctic is amongst the regions most affected by climate change. Surface warming affects the distribution of sea-ice and the first summer with a complete lack of sea-ice at the North Pole is expected to occur during the next few years. The area covered by sea-ice not melting during summer, the so-called multi-year sea-ice, as well as the average sea-ice thickness are decreasing (e. g. Kwok *et al.*, 2009). These changes, happening on relatively short time-scales, are affecting the environment of the indigenous inhabitants of the Arctic who need to adapt to these changes. However, the climate in lower latitudes may also be affected by a warming Arctic as the sea-ice plays an important role in the North Atlantic deep-water formation and the subsequent thermohaline circulation furnishing Europe with a relatively mild climate owing to the Gulf Stream.

The phenomenon of halogen activation in the Arctic is likely affected by a changing climate as well. First-year sea-ice – sea-ice less than one year old – is believed to play an important role in the release of reactive halogen compounds into the atmosphere (Wagner *et al.*, 2001). The decay of multi-year sea-ice is partially compensated by an increasing area covered by first-year sea-ice possibly leading to an increased frequency of halogen activation (Hollwedel, 2005). This effect may partially be counterbalanced by the temperature dependence of the halogen release process. The frequency of elevated halogen levels is suspected to be inversely correlated to the surface temperature. As a side effect, both factors, first-year sea-ice area and surface temperature, may become important when analysing the composition of ice cores. Ice cores are a valuable record of the past climate. Processes changing the occurrence of halogen activation

which in turn alter the atmospheric composition as well as the precipitation of its constituents therefore influence the composition of ice cores. The concentration of mercury in ice cores, for instance, was found to be highly variable in the past (Vandal *et al.*, 1993).

This thesis investigates the phenomenon of polar tropospheric bromine activation by means of satellite measurements which are able to provide a global picture. The primary aspect of this work was the development of a new satellite retrieval algorithm in order to assess the tropospheric contribution of bromine radicals to the total column. The satellite measurements are amended with ground-based measurements that were also conducted as part of this thesis. The combination of both provides a comprehensive picture of the distribution of bromine compounds in the polar troposphere. Furthermore, several existing hypotheses about various environmental factors influencing the production of inorganic bromine species are tested by comparing satellite measurements to meteorological data. The presented study includes a careful discussion of meteorological parameters potentially controlling the satellite observations given here.

The presented work is divided into four parts. In the first part, the scientific background where underlying chemical reactions are formulated along with a review of environmental factors influencing halogen chemistry as well as a review of past studies using satellite data (Chapters 2 and 3). The next part presents the methods and instruments applied in this thesis with an emphasis on the development of the new satellite retrieval algorithm (Chapters 4 through 7). The results and discussion part presents the ground-based measurements at Barrow, Alaska (Chapter 8), the synthesis of satellite and ground-based data (Chapter 9), the distribution of bromine radicals in both hemispheres (Chapter 10), and the relationship between bromine activation as measured from satellites and different environmental parameters (Chapter 11). Finally, the conclusions and an outlook is formulated (Chapters 12 and 13).

2. The chemistry and physics of tropospheric ozone depletion events

In the troposphere, typical ozone (O_3) levels range from 20–30 nmol mol^{-1} in the southern hemisphere to 30–40 nmol mol^{-1} in the northern hemisphere. Exceptions are only areas with extremely low levels of nitrogen oxide (NO_x, x=1,2) and areas with very high NO_x levels. The Arctic, however, belongs to neither of these areas and it was therefore surprising to discover periods where O_3 concentrations dropped below the detection limit during Arctic springtime. Shortly after the discovery that ozone (O_3) is frequently depleted in the polar boundary layer (not to be confused with ozone depletion in the stratosphere) during spring (Oltmans, 1981; Oltmans & Komhyr, 1986; Bottenheim *et al.*, 1986), filter pack measurements of atmospheric compounds in the Arctic by Barrie *et al.* (1988) revealed a strong anti-correlation between atmospheric bromine compounds and O_3 (Figure 2.1).

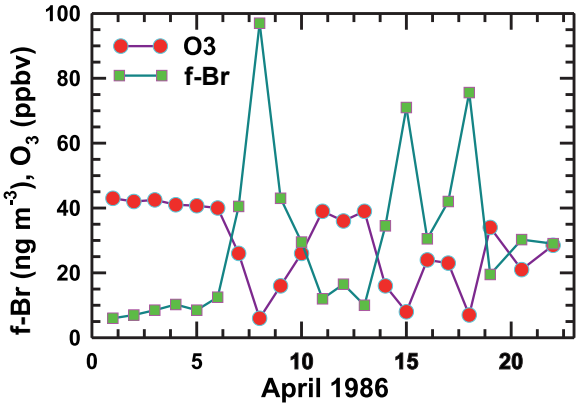

Figure 2.1.: *A comparison of daily mean ground level O_3 (red circles) and filterable Br (green squares) concentrations at Alert, Canada, in April 1986, illustrating the strong inverse correlation between the two parameters. Adapted from Barrie* et al. *(1988).*

Since then, numerous field-campaigns, theoretical studies, and laboratory studies were conducted leading to a number of published hypotheses trying to explain the origin of this presumably natural phenomenon. Furthermore, satellite measurements of the bromine monoxide radical (BrO) revealed that actually both, the entire Arctic (Figure 2.2) and Antarctic (Figure 2.3) are affected by bromine activation processes during spring (Barrie *et al.*, 1988; Kreher *et al.*, 1996). Simpson *et al.* (2007b) reviews the role of halogens during episodes where O_3 levels drop from background levels above 30 nmol mol^{-1} to below 10 nmol mol^{-1} called "ozone depletion events" (ODEs)

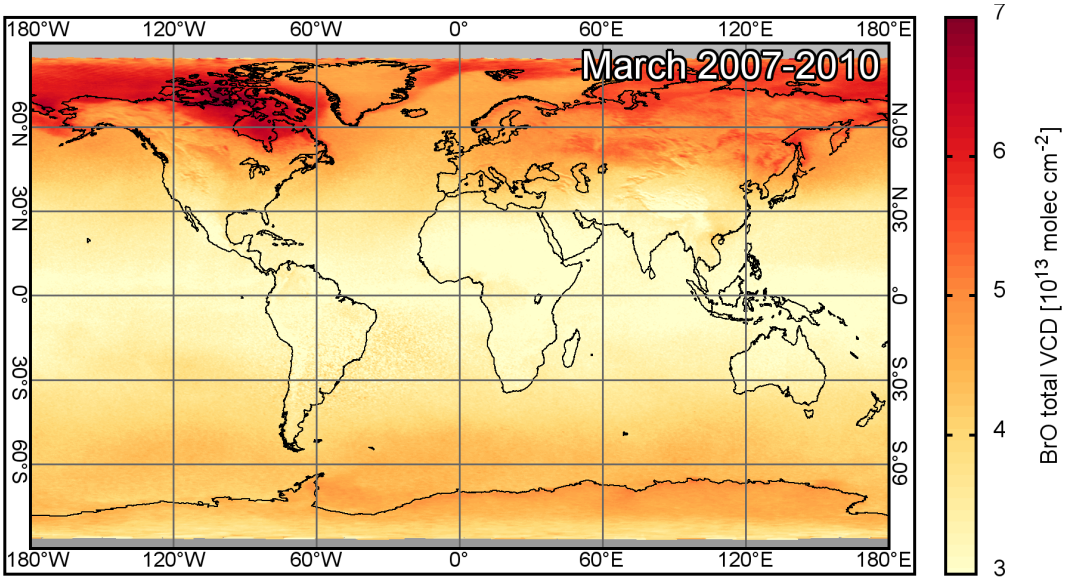

Figure 2.2.: *Vertical column density of BrO measured by the GOME-2 instrument. This map shows average BrO total column densities measured during March in the years 2007 through 2010 by the GOME-2 instrument. Large areas at the northern high-latitudes exhibit significantly enhanced BrO columns.*

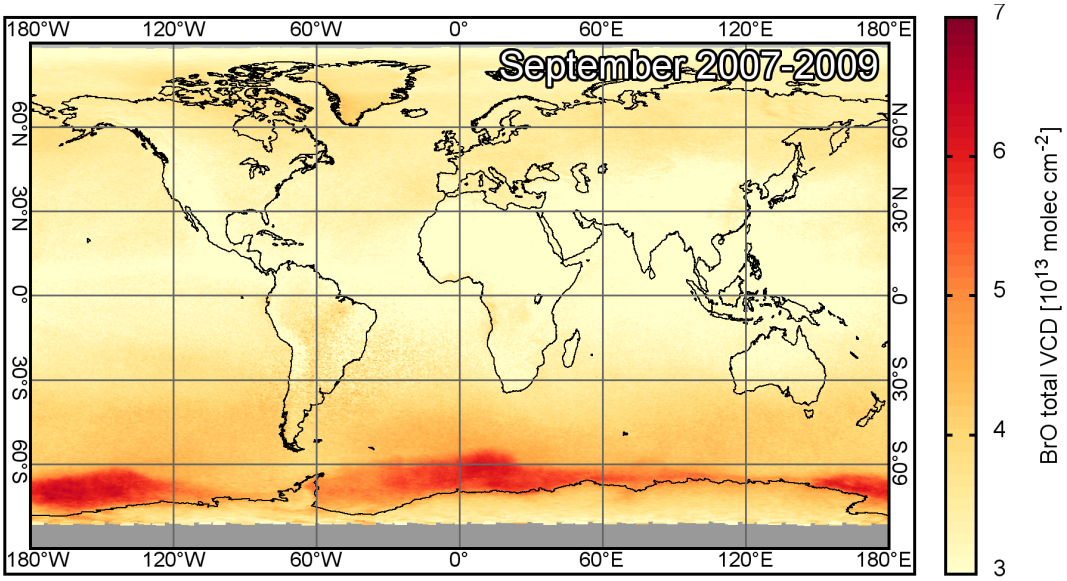

Figure 2.3.: *Same as Figure 2.2 but for September 2007 to 2009 showing significantly elevated BrO columns around Antarctica.*

according to Oltmans *et al.* (1989). Some years later, ODEs were detected in the Antarctic troposphere as well (Kreher *et al.*, 1996).

This chapter provides an introduction to the main mechanisms of ozone destruction by bromine compounds. For a review of the influences by chlorine and iodine chemistry it is kindly referred to Hönninger (2002) and Simpson *et al.* (2007b). The basic chemistry is firstly described in Section 2.1 followed by a description of boundary-layer physics, which has a strong influence on the chemistry at the surface (Section 2.2). Section 2.3 highlights the role of sea-ice as the most important halogen source and Section 2.4 reviews the existing hypotheses explaining ODEs connected to halogen activation. At the end of the chapter, results of a simple model illustrate the basic interconnection between chemistry and meteorology (Section 2.5).

2.1. Ozone destruction in the springtime polar boundary-layer

Atmospheric bromine radicals are known to play the key role in ozone destruction in the polar boundary layer (e. g. Barrie *et al.*, 1988; Hausmann & Platt, 1994). After the presence of bromine monoxide (BrO) radicals during polar ODEs became evident (Hausmann & Platt, 1994; Tuckermann *et al.*, 1997), BrO was found to be most important bromine species in ozone destruction. While the release mechanism of bromine is still not fully understood (see Section 2.4), it was already possible to identify the main reaction pathways of bromine compounds catalysing ozone destruction.

Firstly, bromine atoms are produced from the photolysis of molecular bromine (Br_2)

$$Br_2 + O_2 + h\nu \longrightarrow 2\,Br + O_2 \tag{R1}$$

during daylight. Consecutively, Br may react with O_3 to form BrO, which is converted back into Br in an auto-catalytic ozone destruction cycle (Barrie *et al.*, 1988; Hausmann & Platt, 1994):

$$2 \times (Br + O_3 \longrightarrow BrO + O_2) \tag{R2}$$
$$BrO + BrO \longrightarrow 2\,Br + O_2 \tag{R3}$$
$$\text{net:} \quad 2\,O_3 \longrightarrow 3\,O_2$$

Reactions R2 and R3 lead to set of differential equations for the concentrations of O_3, BrO and Br denoted by $[\cdot]$

$$\frac{d[O_3]}{dt} = -k_{R2}[O_3][Br] \tag{2.1}$$
$$\frac{d[BrO]}{dt} = -\frac{d[Br]}{dt} = k_{R2}[O_3][Br] - 2k_{R3}[BrO]^2 \tag{2.2}$$

where k_{R2} and k_{R3} are the rate constants of reaction R2 and the BrO-BrO self-reaction R3, respectively. At the end of this chapter, this set of differential equations is integrated in a basic 1D model (Section 2.5).

Both rate constants k_{R2} and k_{R3} are of the same order of magnitude (Atkinson *et al.*, 2007). Therefore, the rate of O_3 destruction is limited by the BrO-BrO self-reaction during the beginning of the ozone destruction when O_3 concentrations are high. Then, the set of equations 2.1 and 2.2 can be simplified to

$$\frac{\mathrm{d}[O_3]}{\mathrm{d}t} = -2k_{R3}[BrO]^2. \tag{2.3}$$

Thus, it is possible to estimate the timescale of ozone destruction. According to (2.3), the destruction rate of O_3 at a given BrO concentration of $[BrO] = 1\times10^9\,\mathrm{molec\,cm^{-3}}$ (corresponding to a mixing ration of $40\,\mathrm{pmol\,mol^{-1}}$ for $\rho_{air} = 2.5\times10^{12}\,\mathrm{cm^{-3}}$) can be estimated to

$$\frac{\mathrm{d}[O_3]}{\mathrm{d}t} = -4.4\times10^6\,\frac{\mathrm{molec}}{\mathrm{cm^3\,s}} \tag{2.4}$$

resulting in a O_3 destruction of $0.6\,\mathrm{nmol\,mol^{-1}}$ per hour or $15\,\mathrm{nmol\,mol^{-1}}$ per day resulting in complete destruction of 30–40 $\mathrm{nmol\,mol^{-1}}$ O_3 in somewhat more than 2 days. (Platt & Hönninger, 2003; Lehrer *et al.*, 2004; Atkinson *et al.*, 2007).

However, until now we assumed that reactive bromine (Br and BrO) destroys ozone without being removed from the atmosphere itself. There are two main processes that may reduce the amount of reactive bromine:

1. BrO may react with the hydroperoxyl radical (HO_2) forming hypobromous acid (HOBr)
$$BrO + HO_2 \longrightarrow HOBr + O_2 \tag{R4}$$
2. Br may react with hydrocarbons (formaldehyde (HCHO), higher aldehydes, HO_2, olefins, alkenes) yielding hydrogen bromide (HBr) or, in case of a reaction with olefins, yet unknown products. Both hydrogenated products, HOBr and HBr, may either photolyse producing reactive bromine again or, more likely, are deposited on aerosols or at the surface.

As a result, the life-time of BrO in the absence of BrO sources is approximately 100 s (Lehrer *et al.*, 2004).

Therefore, in order to explain the observed sustained destruction of ozone, a mechanisms is required that produces gaseous reactive bromine from bromine dissolved in aerosol particles or at the sea-ice surface. The "bromine explosion" reaction sequence provides an auto-catalytic mechanism which potentially amplifies the amount of gaseous bromine through heterogeneous reactions (Fan & Jacob, 1992; McConnell *et al.*, 1992; Platt & Lehrer, 1996; Wennberg, 1999). The bromine explosion reaction sequence is

$$HOBr + Br^-_{(aq)} + H^+_{(aq)} \longrightarrow H_2O + Br_2 \tag{R5}$$
$$Br_2 + O_2 + h\nu \longrightarrow 2\,Br + O_2 \tag{R1}$$
$$Br + O_3 \longrightarrow BrO + O_2 \tag{R2}$$
$$BrO + HO_2 \longrightarrow HOBr + O_2 \tag{R4}$$

$$\text{net:}\quad Br^-_{(aq)} + H^+_{(aq)} + HO_2 + O_3 + h\nu \longrightarrow Br + H_2O + 2\,O_2$$

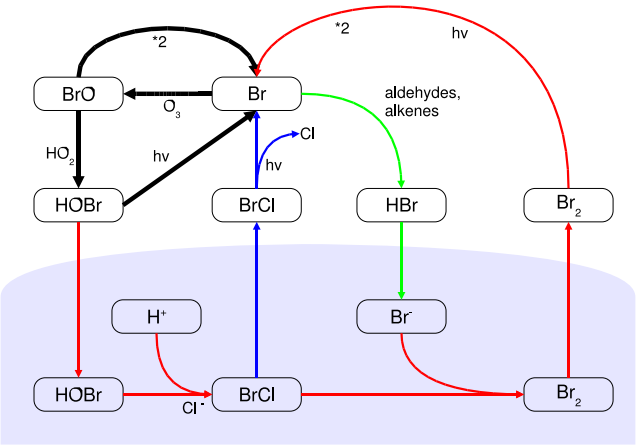

Figure 2.4.: *A simplified set of bromine explosion reactions. The blue area at the bottom is meant to represent the condensed phase (liquid brine or ice surface). Adapted from Simpson* et al. *(2007b).*

Reaction R5 produces one Br_2 molecule, which rapidly photolyses into two Br atoms (R1), from a single HOBr and leading to an exponential growth of the available reactive bromine to destroy ozone (Figure 2.4). In reality, however, also intermediate reactions involving chlorine (Cl) and possibly iodine (I) occur. These inter-halogen reactions may on the one hand reduce the effective yield of the bromine explosion to values below one and lead to a reduced growth rate, but on the other hand also increase the liberation of reactive bromine via heterogeneous reactions. It needs to be furthermore noted that Br and Cl atoms may also react with HO_2 or HCHO forming HBr and HCl, respectively. These reactions, which reduce the amount of reactive halogens, are much more likely for Cl than Br. However, the role of iodine in this context is still unknown.

The efficiency of the bromine explosion, however, depends on several factors which are still not fully understood or quantified, yet. One of the most important factors influencing the kinetics of the bromine explosion is the kind of surface on which the HOBr uptake (R5) occurs (aerosols and/or sea-ice of different types). Furthermore, the release of Br_2 is limited by the transport to the surface and the HOBr and HBr uptake efficiency which is still unknown. Reaction R5 consumes acidity in the form of protons H^+ which may not be provided by the alkaline ocean water. (As discussed below, the carbonate buffer of sea water is probably removed during the freezing process enabling the remaining brine solution to be acidified more easily.) Hence, (R5) is suspected to occur on aerosols providing the necessary acidity (e. .g Sander *et al.*, 2006). Another question is the availability of HO_2 which is typically low in polar regions. Once consumed, the production of HO_2 is limited by the amount of atmospheric water content which is positively correlated to the air temperature and therefore low in polar regions. Finally, light is required in order to photolyse Br_2 and other meteorological conditions like turbulent mixing and air temperature may alter the efficiency of the bromine explosion sequence. Obviously, the meteorology perturbs

the described chemistry because atmospheric transport changes the chemical composition in the time-scale of days in which ODEs occur (e. g. Hausmann & Platt, 1994). Therefore, an introduction into polar meteorology is given in the next paragraph before returning to a review of recent hypothesis trying to explain the properties of bromine activation in Section 2.4.

2.2. Meteorology of the polar atmosphere

The phenomenon of polar ozone depletion events is strongly dependent on the physics of the boundary layer as well as synoptic weather systems because the chemical and meteorological processes occur on a similar timescale. Meteorological processes within the boundary layer include turbulent exchange and horizontal transport, which are both thoroughly discussed in the scope of boundary-layer atmospheric chemistry in Anderson & Neff (2008). For a description of synoptic weather systems (e. g. Bjerknes, 1919) and the cyclogenesis at polar fronts it referred to the introductory meteorological literature.

Compared to regions at lower latitudes, the meteorology of polar regions is characterized by extreme seasonal changes in solar influx. As a consequence, the surface cools in winter in the absence of sun through radiative cooling. This leads to the production of sea-ice which still covers almost the entire Arctic Ocean and the waters adjacent to Antarctica in polar spring. Additionally, water precipitates as snow. Hence, the surface albedo at high latitudes is much enhanced when compared to lower latitudes. The spectral albedo in the UV/vis range may reach values of up to 0.98 depending on the type and age of snow (Grenfell *et al.*, 1994). This is a unique feature which will be utilized in Chapter 6 when the sensitivity of optical remote sensing instruments towards the surface is quantified.

Another consequence of the effective radiative cooling is the development of the *Arctic Dome* (Klonecki *et al.*, 2003; Stohl, 2006). The lower part of the Arctic troposphere, the Arctic dome, is isolated from the rest of the atmosphere due to its low potential temperatures (Sodemann *et al.*, 2011). Warmer air transported into the Arctic from lower latitudes may therefore not penetrate surface near layers because it is lifted into higher layers (up to 5–6 km near the North Pole) through buoyancy due to its higher potential temperature (for definition see Equation (2.5) below). Hence, the residence time within the Arctic dome is comparatively long and strong gradients towards air from lower latitudes may develop (Sodemann *et al.*, 2011).

The mean seasonal development of Arctic surface temperatures is shown in Figure 2.5. The Arctic Dome can be identified in the temperature maps for January and April (upper panels). The area between and including the Canadian Archipelago and Siberia feature the lowest mean surface air temperatures. In this area, the temperatures are below -30 °C and -20 °C in January and April, respectively.

2.2.1. The polar boundary layer

Following Stull (1988), the boundary layer may be defined as the "[..] part of the troposphere that is directly influenced by the presence of the Earth's surface, and

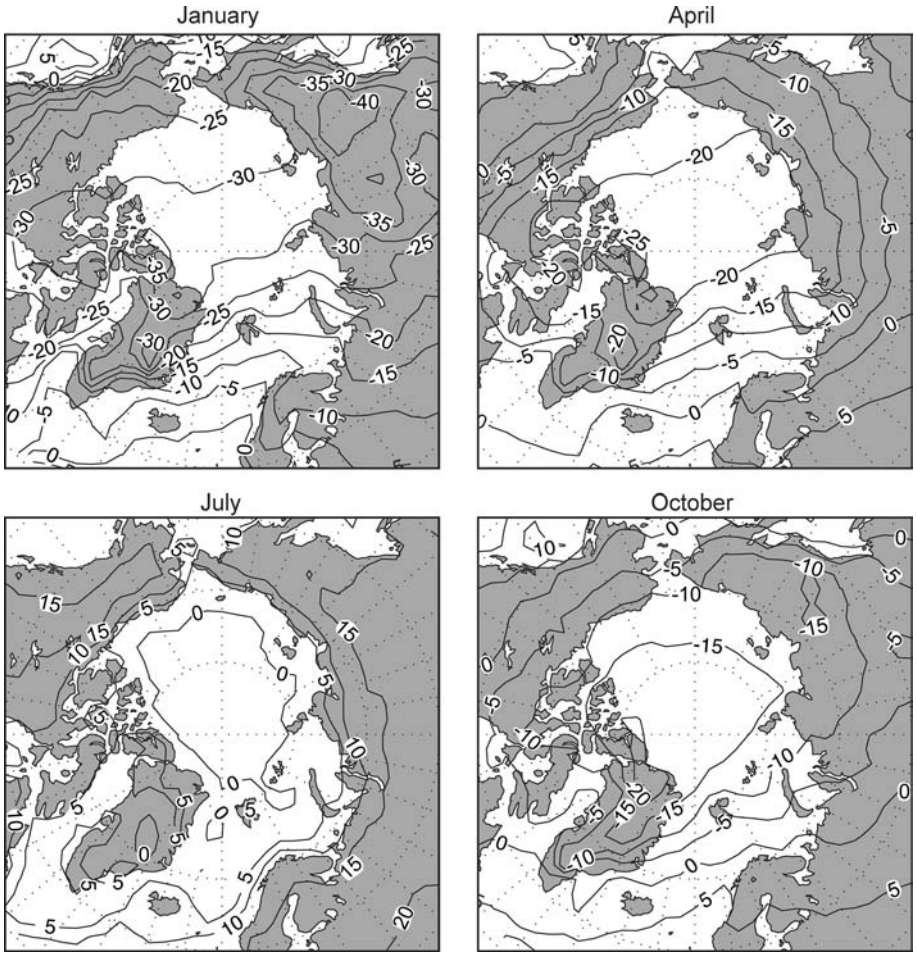

Figure 2.5.: *Mean surface air temperature (°C) for January, April, July and October. Adapted and updated from Rigor* et al. *(2000) by Serreze & Barry (2005).*

responds to surface forcings with a timescale of about an hour or less." In this context, surface forcings include not only transfer processes of heat, momentum, and moisture but also trace-gas emissions. Above the boundary layer, the atmospheric flow follows the geostrophic wind-pattern (Figure 2.6).

In polar regions, the boundary layer is often defined by a strong temperature inversion that separates the boundary (or mixed) layer from the free troposphere. The temperature inversion results from efficient radiative cooling of the surface air above snow or ice due to a high long-wave emissivity above 0.9 in connection with a high short-wave albedo and the absence of insulation. This typically leads to a stratified boundary layer whose height can be altered by surface wind shear and turbulence. Depending on the wind speed, vertical mixing by turbulent diffusion can be highly efficient within the boundary layer (Anderson & Neff, 2008). Within the boundary layer, however, turbulence is often suppressed by buoyancy and the surface layer affected by turbulence is topped by a layer of strong temperature inversion thus defining

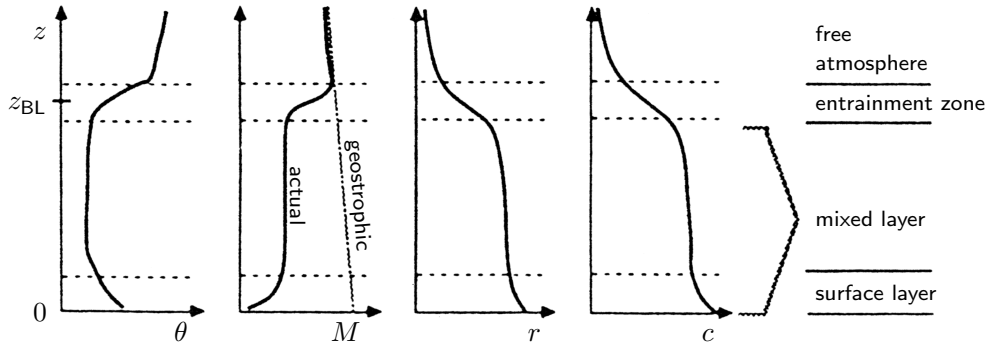

Figure 2.6.: *Typical daytime profiles of the potential temperature θ (defined in equation 2.5), wind speed M (where $M^2 = v_x^2 + v_y^2$), water vapour mixing ratio r, and pollutant concentration c. Adapted from Stull (1988).*

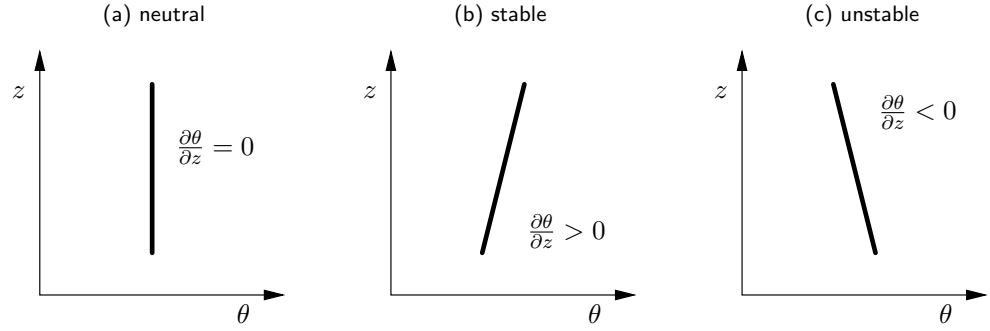

Figure 2.7.: *The stability of the vertical stratification depends on the potential temperature gradient.*

the boundary layer height.

2.2.2. Vertical stratification

The stability of a stratified atmosphere is commonly studied on observations of the potential temperature. The potential temperature θ is defined as the temperature of an air-parcel adiabatically brought to sea level

$$\theta = T \left(\frac{p_0}{p} \right)^{\frac{R}{c_p}} \tag{2.5}$$

where T is the absolute temperature, p the pressure, p_0 the sea level pressure (usually defined as p_0=1000 hPa), R the specific gas constant, and c_p the specific heat at constant pressure. Three conditions of the vertical stratification can be distinguished based on the vertical potential temperature gradient $\partial\theta/\partial z$: neutral, stable and unstable (Figure 2.7).

When neutrally stratified, a lifted air-parcel has the same temperature (and density) as its new surrounding and therefore its buoyant force is zero. The air-parcel is

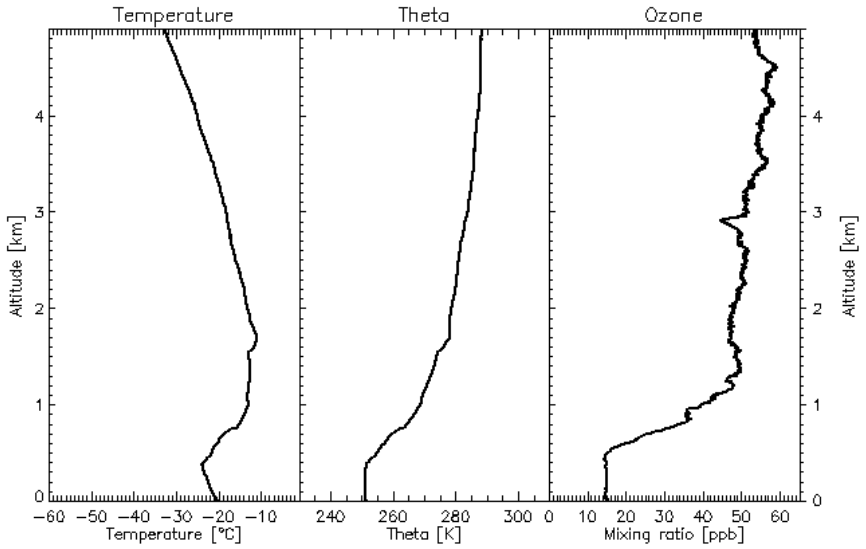

Figure 2.8.: *Temperature (left), potential temperature (center), and ozone mixing ratio (right) measured by an ozone sonde launched at Barrow 12 April 2009 13:31:13 AST.*

not further accelerated. In the case of stable stratification, a lifted air-parcel has a lower temperature than the surrounding air. Its density is higher and it is accelerated downward again. In analogy, if lowering the same air-parcel it would rise again as its density is smaller than the density of the surrounding air. This is contrary to the case of an unstable stratification in which a once lifted or lowered air-parcel will continue is movement until it is surrounded again by air with the same potential temperature or it touches the ground.

As an example, the vertical profiles of the temperature and potential temperature measured by an ozone sonde launched at Barrow, Alaska are shown in Figure 2.8. Starting at an altitude z=0 m, the temperature decreases first until z=500 m and then starts to increase. The potential temperature, on the other hand, is constant within the first 500 m ($\partial\theta/\partial z$=0) before it increases. Hence, it is concluded that the lowermost 500 m contain a neutrally stratified mixed layer. Additionally to the temperature profiles, Figure 2.8 shows the vertical profile of O_3. The mixing ratio of O_3 is constant in the lowest 500 m indicating a partial ozone depletion event.

Above the mixed layer follows the intermediate entrainment zone (Figure 2.6). The entrainment zone is characterized by a relatively strong potential temperature gradient between 500 m and 1200 m leading to a stable stratification. The entrainment zone acts as a lid between the free atmosphere and the mixed layer at the surface. Both the upward diffusion of momentum in the form of turbulence and the downward diffusion of ozone are limited.

The diffusive flux j_z can be calculated applying *Fick*'s first law

$$j_z = -K_z \frac{\partial c}{\partial z} \tag{2.6}$$

where K_z is the vertical (turbulent) diffusion coefficient (since $K_z \gg D$ where D

is the molecular diffusion coefficient, $K_z + D \approx K_z$) and c is the concentration of a substance, e. g. ozone. If we now assume a constant flux of O_3 through the entrainment zone where the concentration gradient is large, we can conclude that K_z is one to several orders of magnitude smaller than in the mixed layer.

2.2.3. Boundary layer height and Richardson number

It has been shown in the previous section that the estimation of the boundary layer height h_{BL} can be ambiguous and may depend on the observed properties. On the one hand, the stratification due to temperature inversion usually damps turbulence and leads to a smaller h_{BL}. On the other hand, wind shear produces turbulence modifying the stratification and leading to a dynamical stability and increased h_{BL}. One possibility to measure the dynamical stability is provided by the *Richardson* Number. The Richardson Number Ri is calculated from the ratio of the potential temperature gradient and the horizontal gradient of the wind speed. It can be defined as

$$\mathrm{Ri} = \frac{g(\partial\theta/\partial z)}{T(\partial v_x/\partial z)^2(\partial v_y/\partial z)^2} \tag{2.7}$$

where g is the gravity of Earth, v_x and v_y denote the wind speed in longitudinal and meridional direction, respectively. Small Ri denote cases where wind shear is high and buoyancy is unimportant, while large Ri denote cases where the stratification is dominant and the wind shear becomes negligible.

There are a number of different ways of calculating Ri in the literature. In this work, however, when calculating the boundary layer height from wind-fields provided by the European Centre for Medium-Range Weather Forecasts, it is referred to (ECMWF, 2004). In the ECMWF data, for instance, the boundary layer height h_{BL} is defined as the lowermost height at which Ri equals a critical Richardson Number $\mathrm{Ri_c}$=0.25.

2.2.4. Potential temperature and tropopause height

The stratosphere is the atmospheric layer above the troposphere (Figure 2.9), whereas the tropopause is the interface between stratosphere and troposphere. The height of the tropopause needs to be determined, in order to determine the thickness of the stratosphere, which is an important parameter in the determination of the tropospheric BrO column (Chapter 6). There are several proxies which are used to identify stratospheric air: chemicals such as O_3 and CO, the minimum temperature (i. e. to find the inflection point of the potential temperature gradient), or the potential vorticity. In polar regions, the potential vorticity is usually used to calculate the tropopause height from weather simulations data.

The potential vorticity is a meteorological property which is conserved under barotropic conditions. It is defined as

$$\mathrm{PV} = \frac{\mathrm{rot}_z\vec{v} + f}{\rho} \cdot \frac{\partial\theta}{\partial z} \tag{2.8}$$

where $\vec{v}$ is the velocity field of the atmosphere, f is the Coriolis parameter, and ρ is the density of air. Stratospheric air is stratified, meaning that $\partial\theta/\partial z$ is large, which

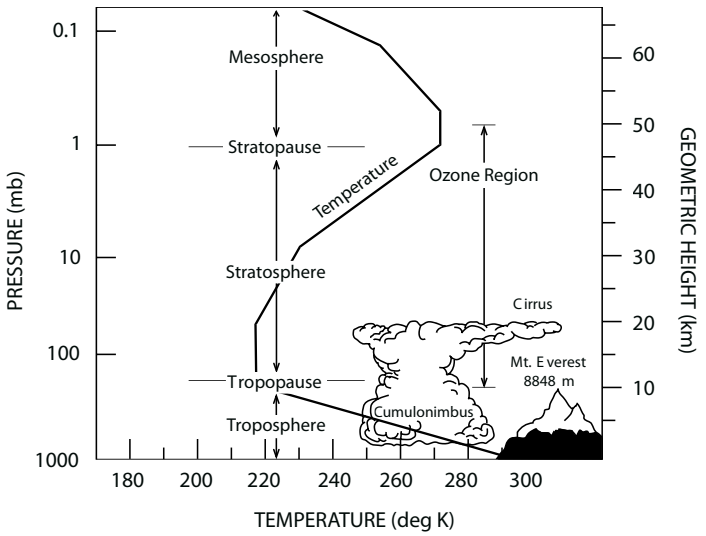

Figure 2.9.: *Schematic representation of the thermal structure of the atmosphere with its different layers. Adapted from Brasseur & Solomon (2005).*

allows the vorticity $\mathrm{rot}_z \vec{v}$ to accumulate. Furthermore, the lower density and larger potential temperature gradient compared to tropospheric air result in a relatively large PV.

PV is usually measured in potential vorticity units (PVUs). One PVU is defined as

$$1\,\mathrm{PVU} = 10^{-6} \frac{\mathrm{K\,m^2}}{\mathrm{s\,kg}} \tag{2.9}$$

In this thesis, the dynamic definition of the tropopause height is employed. When analysing wind fields provided by a weather model, the highest model layer fulfilling $\mathrm{PV} \leq 2\,\mathrm{PVU}$ is interpreted as the tropopause height (cf. Section 7.3).

2.3. Sea ice as the source of reactive halogen species

As discussed in Section 2.1, the bromine explosion process requires surfaces with a high salinity and high acidity (low pH). The major source for bromine is most likely sea salt (Simpson *et al.*, 2007b). In polar regions, there are two fundamental sources of sea salt relevant for atmospheric chemistry: marine sea salt aerosols and the ice covered ocean surface. However, both the concentration of aerosols as well as their specific bromine content are not sufficient to provide enough bromine to explain the observed concentrations in the gas-phase. The ice surface is therefore the most probable primary source for atmospheric bromine (Lehrer, 1999).

Sea ice formation begins at temperatures below -1.7°C. During the freezing process a highly saline brine layer forms on top of the newly build fresh ice. At -10°C, for example, the salinity of brine can be four times as high as of salt-water (Richardson, 1976). During the freezing process, the chemical composition of the brine layer changes

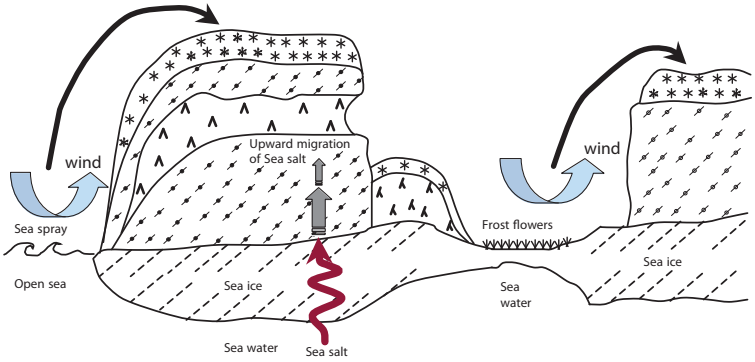

Figure 2.10.: *Illustration of the three processes suspected of supplying sea salt ions to marine snow: wind-transport of sea spray, upward migration from sea ice and wind-blown frost flowers. Adapted from Dominé* et al. *(2004).*

as certain salts precipitate when reaching their specific solubility (Koop *et al.*, 2000; Sander *et al.*, 2006; Morin *et al.*, 2008). However, the brine surface may be covered by frost-flowers, which provide a larger surface area and a salt ion reservoir, or buried under a wind-blown snow pack soon after the formation on the sea-ice (Martin *et al.*, 1996; Rankin, 2002; Kaleschke *et al.*, 2004). The largest fraction of the polar sea-ice is covered by snow leading to the question which surface type is the most effective to supply bromine ions to the surface. In this context, snow photochemistry is suspected to play also an important role for atmospheric chemistry (Grannas *et al.*, 2007). If halogens are activated in the snow pack, a process transporting salt to the snow is required. Figure 2.10 illustrates the possible processes suspected to supply salt ions to the surface snow (Dominé *et al.*, 2004).

Another important prerequisite for the bromine explosion is acidity below pH 6.5 (Lehrer, 1999; Frieß, 2001). Sea-water, however, is alkaline (pH=8). Therefore, whatever surface supplies the bromine explosion with additional bromine needs to be acidified. The carbonate buffering the pH of sea water precipitates during the formation of the brine layer (Sander *et al.*, 2006). Initially alkaline aerosols can then be acidified by scavenging gaseous acids, e. g. H_2SO_4 from the oxidation of SO_2. SO_2 may originate from both natural sources, such as volcanoes and dimethyl sulfide (DMS, emitted by phytoplankton), as well as anthropogenic emissions.

As an illustration, the amount of bromide in 1 cm^3 in sea water is related to typical atmospheric concentrations in the column above it. Sea water on top the sea-ice may be the result of either the freezing process (described above) or a spill-over of salt-water at an ice-floe crack (see Figure 2.11a). The concentration of bromide ions in sea water is approx. 67 mg kg^{-1} (Drever, 1982), and the corresponding amount of Br^- ions in 1 cm^3 of sea water is about 5×10^{17}. In other words, the sea salt from a layer of sea ice with 1 cm thickness contains 5000 times more bromide than observed in a particularly strong enhancement of the tropospheric column of 1×10^{14} molec cm^{-2} as measured from satellite and from the ground. The remaining question is, how bromine is released into the gas-phase and what the prerequisites for these processes are.

(a) *ice-crack spill-over*

(b) *fresh frost-flower*

Figure 2.11.: *Salt-water provides a huge source for halogens. (a) Frequently sea-ice movement shoves ice floes on top of each other leading to salt-water spills. Recent snow-scooter tracks illustrate that these spills and their freeze-over can occur within one day. (b) Provided air temperatures are low, frost-flowers form on the brine-layer on top of frozen sea-water.*

2.4. Impact of different environmental factors on halogen activation

There is already a significant number of publications reporting the observation of ozone depletion events (ODEs) and the corresponding bromine chemistry in the polar troposphere. Several hypotheses and models trying to explain these observations have already been published and Simpson *et al.* (2007b) provides a good review. Here, however, existing publications are classified with respect to the environmental parameter the observations were found to correlate with. This compilation includes field observations as well as theoretical hypotheses and model simulations.

2.4.1. Temperature

The most discussed parameter of ODEs and bromine activation is probably the air-temperature. Several processes suspected to play an important role are temperature dependent. On the one hand, the air temperature alters the meteorology of the boundary layer, but on the other hand, the temperature may also change the involved release and recycling mechanisms for halogens. Therefore, the interpretation of the results can be ambiguous.

Impact of temperature on meteorological and surface conditions

- Tarasick & Bottenheim (2002) concluded from their systematic study of historical ozonesonde profiles that the process leading to an ODE may be favoured by greater atmospheric stability caused by low surface temperatures. Furthermore

it was found from a comparison of all Arctic stations included in the study, that surface temperatures below -20°C seem to be a prerequisite for ODEs.

- Tarasick & Bottenheim (2002) also note that the growth of frost flowers is faster at low temperatures (Martin *et al.*, 1996). Frost flowers are a potential source of halogen atoms as well as sea salt aerosols.

- Regionally averaged satellite measurements showed an anti-correlation with surface temperature over regions regularly affected by high BrO column densities (Zeng *et al.*, 2003, 2006).

- From the O_3 measurements conducted aboard the TARA vessel, Bottenheim *et al.* (2009) concluded that temperature was well above -20°C during most ODEs. This conclusion opposes some of the conclusion drawn by Tarasick & Bottenheim (2002).

Impact of temperature on the activation mechanism

- Additionally to the meteorological effects of low temperatures, Tarasick & Bottenheim (2002) also note that low temperatures increase the concentration of halogen ions in the quasi brine layer as described by Koop *et al.* (2000). The concentration of Br^- increases at temperatures below -21°C due to the precipitation of $NaCl{\cdot}2\,H_2O$.

- From equilibrium calculations with atmospheric CO_2, Sander *et al.* (2006) conclude that most of the carbonate has precipitated below -8°C. Carbonate precipitation reduces the buffer capacity of the brine enabling aerosols formed from the brine to be acidified more easily. However, Morin *et al.* (2008) argue that ikaite would precipitate earlier than calcite and therefore leaving the buffer capacity unchanged.

- Sander *et al.* (2006) also found from their model study, that the temperature dependent fractionation of

$$BrCl + Br^- \rightleftharpoons Br_2Cl^- \tag{R6}$$

in the heterogeneous phase is important. At low temperatures, the equilibrium is shifted towards Br_2Cl^- resulting in a higher amplification ratio of the bromine explosion mechanism due to an increase of the Br_2/BrCl ratio emitted to the gas-phase.

- Generally, as pointed out by Morin *et al.* (2008), the precipitation of different salts is highly temperature dependent, and these processes are still not fully understood.

- Pöhler *et al.* (2010b) observed maximum bromine levels to be negatively correlated to air temperature. As the contact to the sea-ice surface of activated airmasses was only shortly before the measurement, the conditions under which

the emission of reactive halogen species occur were suspected to depend on the temperature.

2.4.2. Wind speed

Another important meteorological parameter is wind speed. Together with the potential temperature gradient, it is an important factor when determining the stability of the boundary layer (Section 2.2). Additionally, ODEs measured at the surface are usually terminated by the break-up of the inversion leading to a recovery to background O_3 levels from aloft.

- Morin *et al.* (2005) argued that a stratified boundary layer probably leads to maximum tropospheric BrO in the transition layer (see Figure 2.6).
- Increased wind-speed could possibly lead to an increased diffusion of gaseous Br_2 produced by snow photochemistry in the interstitial air from the snow-pack into the atmosphere (wind-pumping) (Morin *et al.*, 2008).
- In the parametrisation of their blowing snow model, Yang *et al.* (2008) presume that there is no sea salt aerosol production from blowing snow at wind speeds of about $7\,m\,s^{-1}$ or less.
- From a study on a bromine activation event linked to a strong low pressure system in Antarctica, Jones *et al.* (2009) observed that depleted boundary layer ozone coincided with high wind speeds and saline blowing snow. Furthermore, Jones *et al.* (2009) identify from model calculations that there are possibly two conditions under which ODEs are observed: one at low wind and stable stratification of the boundary layer and one at high wind speeds linked to the presence of blowing snow.

2.4.3. Surface pressure

The surface pressure is an indicator for meso-scale weather systems. Furthermore, surface wind speed is obviously a function of the pressure gradient.

Jacobi *et al.* (2010) compared O_3 mixing ratios measured over the ice on-board TARA, Polarstern, and Narwhal vessels and conclude that low O_3 is probably the normal state of the Arctic boundary-layer. Concentrations of O_3 returned to background levels through northward passage of lows. While ignoring the relative pressure offset of several events, a negative correlation between O_3 mixing ratio and atmospheric pressure has been found for all observed O_3 concentration gradients. Generally, the correlation to pressure was found to be stronger than to temperature.

Therefore, Jacobi *et al.* (2010) warns to interpret the correlation between temperature and O_3 as a causal relationship as the temperature threshold changes between the events. The authors furthermore doubt that O_3 destruction is as fast as the observed strong O_3 gradients might suggest because changes in O_3 may as well be due to a change of air-mass.

2.4.4. Tropopause height

Concerns raised by Salawitch *et al.* (2010) that total column measurements of BrO are strongly correlated to the total O_3 is mostly connected to the fact that a lower troposphere increases the stratospheric partial column of both O_3 and BrO (cf. Section 6). Furthermore, low tropopause heights were observed in areas affected by increased tropospheric columns by (Begoin *et al.*, 2010). In the same time, however, there were also regions with low tropopause height without significant tropospheric enhancement leading to the conclusion, that a low tropopause is probably a by-product of meteorological conditions, i. e. low pressure systems, also leading to BrO enhancement in the troposphere (Begoin *et al.*, 2010; Theys *et al.*, 2011).

2.4.5. Presence of aerosols

Aerosols are supposed to play an important role in the recycling mechanism of bromine compounds because they provide a surface for heterogeneous reactions.

- Enhanced multiple scattering occurring on aerosol particles during episodes of elevated BrO concentrations indicated that heterogeneous chemistry (recycling of bromine) on airborne particle play an important role (Frieß *et al.*, 2004, 2011).
- Similarly, Begoin *et al.* (2010) concluded from a comparison of satellite measurements and simulated trajectories that effective recycling in aerosols are potentially necessary to explain long-range transport of BrO in elevated layers.

Surface type or region

The type of surface – e. g. pure ice, frost-flowers, or snow pack – determines the kind of release process leading to halogen activation into the atmosphere (cd. Figure 2.10). Especially the role of first-year sea-ice compared to multi-year sea-ice (ice that did not melt during the previous summer) is stressed.

- The surface of multi-year sea-ice is known to have a much lower salinity than the surface of fresh first-year sea-ice. This agrees with the observation by Wagner *et al.* (2001) who did not measure any significant amounts of BrO from space after the melting of all first-year sea-ice in June.
- Wagner *et al.* (2007) almost continuously observed enhanced BrO concentrations over the Antarctic sea-ice by ship-borne measurements. Frequently, the BrO enhancements were probably located in elevated layers at the upper edge of the boundary layer. Only low BrO concentrations were found outside the first-year sea-ice belt.
- Apparently, satellite measurements of BrO correlate to the distribution of surfaces potentially covered by frost-flowers (Kaleschke *et al.*, 2004). Such regions are characterized by new openings of the sea-ice and very low temperatures (Sander *et al.*, 2006). However, Simpson *et al.* (2007a) performed backward trajectory calculations and could not find a significant correlation between contact

time with potential frost-flowers and BrO abundances at Barrow. A positive correlation with first-year sea-ice contact time was found using the same data (Simpson *et al.*, 2007a).

- Yang *et al.* (2008) argues that small snow particles enriched in salts from the ice underneath can easily become airborne during blowing snow events, and thus can act as a source of halogens.

- Yet, at least two different source regions have been identified in the Arctic.
  - From the extensive trajectory study conducted by Bottenheim & Chan (2006), the authors conclude that the region between Franz Josef Land and Severnaya Zemlya is a common origin for ozone depleted air arriving at Alert, Greenland and Ny Ålesund, Svalbard.
  - From O_3 measurements aboard TARA, backward trajectory calculations suggest the Siberian coast, where open leads and polynyas develop during Spring, to be a further potential source region for ozone depleted air (Bottenheim *et al.*, 2009).

2.4.6. Summary of environmental parameters influencing reactive Br

From these studies it can be concluded, that halogen activation and ODEs probably correlate negatively with temperature (except the TARA observations) and positively with wind-speed. Furthermore, synoptic effects and distinct source regions defined by surface type and temperatures may be important.

2.5. Model study on horizontal diffusion and ozone destruction

This section illustrates some consequences of the catalytic O_3 destruction scheme formed by the two reactions (R2) and (R3) on page 9. A computational model including the basic chemical reactions leading to halogen induced ozone depletion and horizontal diffusion has been implemented in order to study the interconnected processes quantitatively. It is noted that more elaborate models also implement many further reactions and recycling mechanisms which are neglected here (e. g. Hausmann & Platt, 1994; Lehrer *et al.*, 2004; Piot, 2007; Piot & von Glasow, 2008; Toyota *et al.*, 2011).

The general idea of this model is to study the chemistry of two initially separated air-masses with different trace-gas concentrations under diffusion. The included chemistry is the most simplified ozone destruction scheme which has already been discussed and developed further by Hausmann & Platt (1994). The scheme presented here includes neither source nor sinks for bromine species. Furthermore, the branching of the BrO destruction into either 2Br or Br_2 as well as BrO photolysis are neglected because the photolysis of Br_2 is comparatively fast during daytime and BrO loss through photolysis only becomes dominant at rather low BrO concentrations, respectively.

	run A		run B		
	$x < 0$	$x > 0$	$x < 0$	$x > 0$	
[O_3]	40	20	0.1	40	nmol mol^{-1}
[BrO]	0.5	40	0	0	pmol mol^{-1}
[Br]	0	0	40	0.5	pmol mol^{-1}

Table 2.1.: *Initial concentration values of O_3, BrO and Br for two different model runs denoted A and, B. Each pair of concentrations corresponds to two differently conditioned air-masses located at positive and negative x.*

It has already been mentioned that the chemistry of ODEs is linked to meteorology and that strong temporal gradients of O_3 were observed near the surface. This is puzzling as horizontal diffusion should in principle decrease these gradients. The development of the chemistry is studied to two sets of initial values applied on two initially divided model air-masses interconnected by diffusion.

2.5.1. Model description

The model is implemented by a horizontal succession of 200 interconnected boxes of 1 km width each including three chemical species to be integrated in time. The three species are O_3, BrO, and Br which are interconnected by the set of differential equations (2.1) and (2.2) on page 9. Horizontal diffusion is achieved by assuming turbulent diffusion

$$\frac{\mathrm{d}c}{\mathrm{d}t} = -K_x \frac{\mathrm{d}^2 c}{\mathrm{d}x^2} \tag{2.10}$$

where c is the concentration and K_x is the diffusion coefficient constant in horizontal x-direction. The actual value for the horizontal diffusion coefficient K_x=10^8 cm^2 s^{-1} is an approximation for horizontal diffusion on a regional scale up to 100 km (Hidalgo & Crutzen, 1977; Roedel, 2000). The flux at the boundaries is set to zero.

The ambient temperature is set to T = 253 K (-20°C) and the pressure is set to p = 1013.25 Pa. The rate coefficients for this temperature are calculated to k_{R2} = 7.2×10^{-13} cm^3 molec^{-1} s^{-1} and k_{R3} = 2.7×10^{-12} cm^3 molec^{-1} s^{-1}, respectively (NIST, 2000; Atkinson *et al.*, 2007). The integration time-step is 1 s and the total runtime of the model is 12 h.

2.5.2. Model results

In order to study the interconnection between chemistry and meteorology, two model runs with different sets of initial values are defined. The initial concentration values are compiled in Table 2.1. The initial values represent two separated air-masses (x either positive or negative) which are differently conditioned.

In run A, O_3 is already partially destroyed and BrO concentrations are high in the right air-mass while the left air-mass contains background O_3 and no bromine. In run

B, the left air-mass is high in bromine atoms and low in O_3 while the right air-mass is conditioned vice versa.

Run A - Activated air-mass diffuses into air with background O_3

The initial values and the results of model run A are depicted in Figure 2.12. High BrO concentrations diffuse into the left air-mass where O_3 concentrations are higher than on the partially depleted right side. In the right air-mass, 10 nmol mol^{-1} of ozone are auto-catalytically destroyed in 12 h leading to the production of minor bromine atoms concentrations.

The diffusion of O_3-rich air from left to right does not compensate for the O_3 destruction from 40 pmol mol^{-1} BrO. Hence, the O_3 gradient between both air-masses is enhanced compared to pure diffusion as denoted by the dashed line.

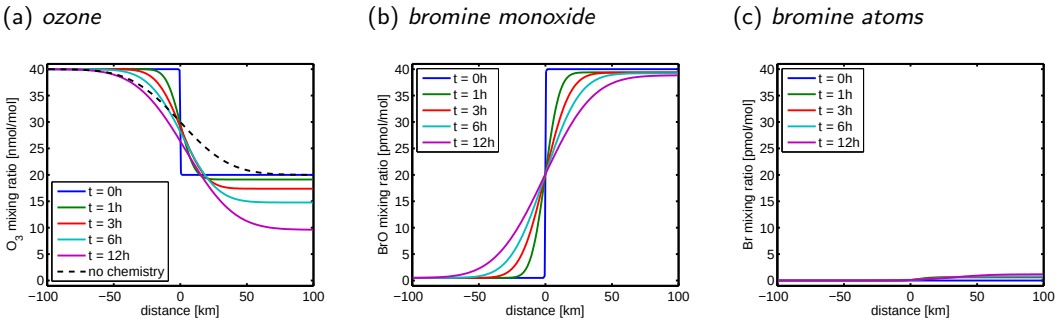

Figure 2.12.: *Results of model run A, where both O_3 and BrO diffuse from right to left while some O_3 is auto-catalytically destroyed.*

Run B - Bromine enriched air diffuses into air with background O_3

The initial values and the results of model run B are depicted in Figure 2.13. After starting the model, significant BrO concentrations are produced in the transition zone where O_3 rich air and bromine rich air overlap. The increase in BrO during the first hour of the model run can be explained by the destruction of the residual 0.1 nmol mol^{-1} of O_3 initially present on the left side. As time develops, more and more bromine diffuses into the O_3 rich air broadening the BrO peak in the middle. In the same time, the O_3 flux does not suffice to replace already destructed O_3, again leading to an increased O_3 gradient when compared to the chemically unperturbed diffusion of O_3.

Discussion and outlook of model exercise

Even though the presented model is an extremely simplified representation of the real process, it is still capable to illustrate the chemistry and relate the O_3 destruction rate to regional diffusion processes. One may furthermore imagine the modelled

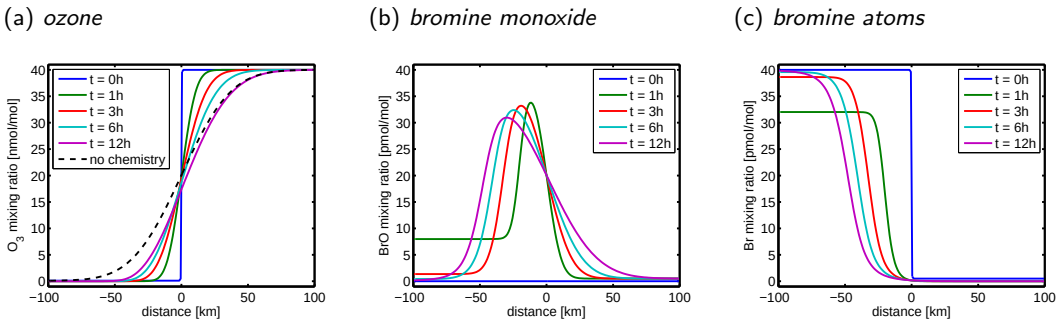

Figure 2.13.: *Results of model run B, where O_3 diffuses from right to left and BrO vice versa. (a) Note that destruction chemistry increases the O_3 concentrations gradient with respect to chemically unperturbed case. (b) The BrO profile is characterized by relatively high values in the transition zone.*

horizontal bulk being transported horizontally (in x-direction) and estimate the time-dependence of the concentrations an observer at the ground would measure as the modelled air-mass passes. E. g. at a wind-speed of $10\,\mathrm{m\,s^{-1}}$ the 100 km of diffusion length after 12 h would take approx 3 h to pass. For the observer standing still (Euler picture) this would appear as a complete O_3 destruction within 3 h. This estimate is related to ground-based measurements of O_3 and BrO (Chapter 8) as well as satellite measurements of BrO (Chapter 11). Furthermore, the model calculations illustrate that a direct anti-correlation between O_3 and BrO cannot always be expected.

3. Satellite measurements of bromine monoxide

In principle, satellite instruments measure total column densities including contributions from both the stratosphere and troposphere. When the first satellite instrument was designed which was also capable to detect BrO, elevated levels of reactive bromine were only suspected in the stratosphere. However, satellite images were soon successfully searched also for tropospheric BrO enhancements after elevated levels of bromine were detected in the polar troposphere (Chapter 2). Several approaches for the separation of the total BrO column density may be into stratospheric and tropospheric contribution had therefore to be developed since the first observations of tropospheric BrO enhancements. In this thesis, a new algorithm to solve this task is developed (Chapter 6) based on the experience from some previously published approaches presented below.

This chapter provides two short reviews presenting the available satellite instruments capable to detect BrO (Section 3.1) as well as a summary of published satellite observations of BrO (Section 3.2). Furthermore, the different approaches to separate the tropospheric and the stratospheric column are discussed (Section 3.3). Two studies comparing satellite measurements of BrO with model results are presented in Section 3.4.

3.1. Available satellite instruments capable to detect BrO

The first observation of atmospheric BrO from space was enabled by the Global Ozone Monitoring Experiment (GOME) instrument aboard the ERS-2 satellite launched on 21st April 1995. The second spectroscopic satellite instrument capable to detect tropospheric BrO was launched on 1st March 2002: the SCanning Imaging Absorption spectroMeter for Atmospheric CHartographY (SCIAMACHY) on-board the Envisat satellite. This instrument provided a much higher spatial resolution than GOME.

Another instrument capable to detect atmospheric BrO is the Ozone Monitoring Experiment (OMI) on-board the Aura satellite launched on 15th July 2004. OMI features a yet unmatched horizontal resolution and an extremely wide swath, so that the spatial overlap in polar regions allows to study bromine events at a high temporal resolution (Figure 3.1).

The most recent instrument in orbit is the second Global Ozone Monitoring Experiment (GOME-2) instrument on-board the MetOp-A satellite launched on 19th October 2006. The satellite retrieval for tropospheric BrO column densities presented in this thesis is applied on GOME-2 data (cf. Section 5.2), but is, in principal, also applicable to the satellite sensors mentioned above. The instrumental design of GOME-2

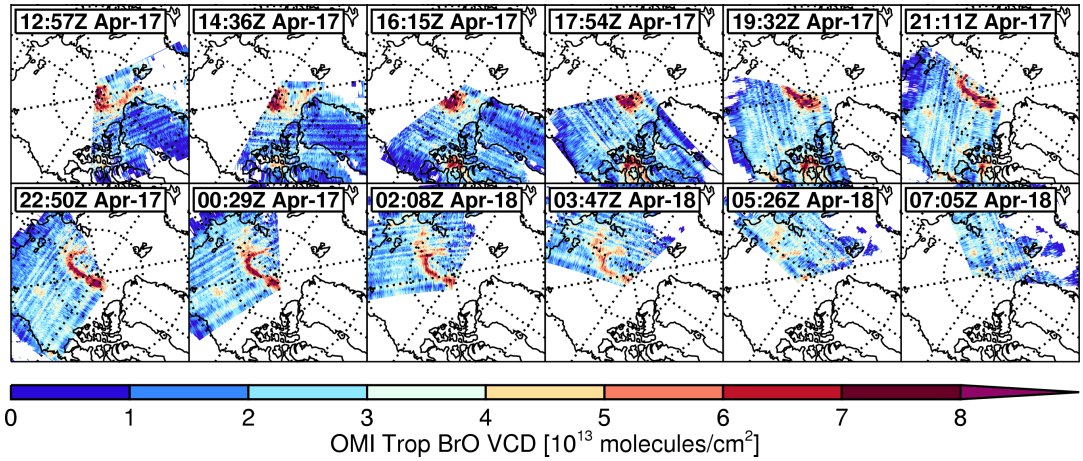

Figure 3.1.: *OMI tropospheric BrO VCD for different orbits in April 2008. Adapted from (Choi* et al.*, 2011).*

is similar to the GOME instrument but features a four times higher spatial resolution (almost reaching the resolution SCIAMACHY) and a much wider swath. This enables also GOME-2 to probe the same air-mass several times a day in polar latitudes (Begoin *et al.*, 2010; Theys *et al.*, 2011; Choi *et al.*, 2011).

3.2. Observations of stratospheric and tropospheric BrO from space

Three years after the launch of the GOME instrument, the first observation of tropospheric enhancements in polar regions was published by three independent groups (Wagner & Platt, 1998; Richter *et al.*, 1998; Chance, 1998). Areas covering several million km^2 of enhanced BrO columns were detected. These "BrO clouds" appeared within less than a day implying local production of BrO. In the same year, also Hegels *et al.* (1998) reported the global distribution of BrO as detected by GOME without stressing the impact on tropospheric chemistry.

After its first detection, the horizontal and temporal distribution of elevated BrO columns were discussed (e. g. Wagner *et al.*, 2001; Richter *et al.*, 2002; Zeng *et al.*, 2003; Hollwedel *et al.*, 2004; Hollwedel, 2005). These studies revealed that the troposphere over both the Arctic and the Antarctic are frequently affected by bromine activation during spring. The frequency of elevated BrO columns was found significantly enhanced over regions covered by first-year sea-ice. These observations led to the assumption, that freshly frozen sea-ice is an important prerequisite for tropospheric bromine activation. Furthermore, enhance BrO columns were also detected over parts of the frozen Caspian Sea whose salinity is still one third of the worlds oceans (Wagner *et al.*, 2001).

Taking benefit from the higher spatial resolution provided by SCIAMACHY, the quality of comparisons between the spatial patterns of enhanced BrO and ground-

based measurements of O_3 was much improved (e. g. Jacobi *et al.*, 2006). Another advantage of a higher spatial resolution is the possibility to detect smaller plumes because their signal is less diluted when larger areas are averaged.

After ground-based measurements have provided evidence for bromine emissions from volcanoes (Bobrowski *et al.*, 2003), Afe *et al.* (2004) conducted a first systematic search for volcanic BrO in satellite measurements but did not find any enhanced BrO signal in the plumes investigated. Five years later, however, volcanic BrO was observed for the first time from space using the GOME-2 instrument. Theys *et al.* (2009a) detected BrO in the plume of Kasatochi volcano on the Aleutian Islands and successfully compared the satellite measurements with a particle dispersion model illustrating the atmospheric circulation pattern. Furthermore, Heue *et al.* (2011) presented BrO measurements in the plume of Eyjafjallajökull volcano comparing airborne MAX-DOAS by the CARIBIC project and satellite measurements. This comparison was performed using GOME-2 BrO data obtained in this work. The same data is utilized in a systematic study of the BrO abundance in all volcanic plumes detected by GOME-2 measurements prepared by Hörmann *et al.* (2012).

3.3. Previously applied column separation approaches

As outlined above, satellite measurements of BrO integrate the concentration in the total column including stratospheric as well as possible tropospheric abundances. Depending mostly on the tropopause height, the magnitude of the stratospheric partial column may become comparable to that of a tropospheric event. When the tropopause lowers, the stratospheric air is adiabatically compressed and hence the stratospheric column of BrO increases additionally to an increase of the overall thickness of the stratosphere (Wagner, 1999). Spatial structures mimicking tropospheric bromine events may appear in maps of the total BrO column. The observed stratospheric partial column depends in particular on the meteorology, stratospheric chemistry, measurement geometry, and the sensitivity to various altitudes given by atmospheric radiative transfer. These factors need to be kept in mind when discussing satellite measurements of tropospheric BrO enhancements.

Figure 3.2 illustrates two stratospheric profiles of BrO, O_3 and NO_2 at two different longitudes as simulated by EMAC model for the 21st April 2007 (Jöckel *et al.*, 2010). This model does not contain the halogen chemistry in the polar troposphere. When comparing Figures 3.2a and 3.2b, it is possible to observe that the tropopause height, which is governed by meteorological parameters, has a strong influence on the vertical extent of the stratospheric species. The lower edge of BrO and O_3 change in a similar way which makes it possible to trace stratospheric air-masses from observations of O_3. Furthermore, the fractionation of bromine species in the stratosphere (mostly into BrO and $BrONO_2$ as depicted in Figure 6.12 on page 79) is determined by the NO_2 concentrations. The column densities of both O_3 and NO_2 can be measured from space and hence both parameters can be used to monitor variations in the stratospheric BrO column density.

The possibility to distinguish stratospheric and tropospheric air by observing the

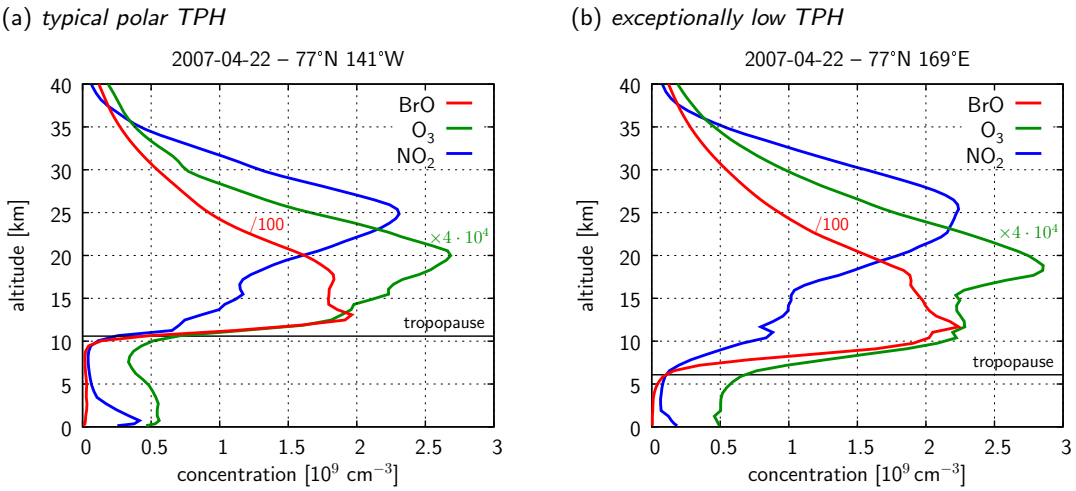

Figure 3.2.: *Simulated vertical profiles of BrO, O_3 and NO_2 characterized by different tropopause heights (TPHs): (a) a typical TPH of 12 km and (b) a relatively low TPH of 7 km. Note that both profiles are simulated for the same day, solar zenith angle, and latitude. The lower edge of the profiles follow the tropopause height calculated from the temperature profile. EMAC simulation M2E24 (exp05) provided by courtesy of P. Jöckel (Jöckel* et al.*, 2010).*

O_3 column was already utilized by Wagner & Platt (1998) who observed a strongly increased BrO column while the column of O_3 and NO_2 remained almost unchanged (Figure 3.3). This observation led to the conclusion, that the enhancement must be located in the troposphere. Additionally, it was found that neither the O_2 nor the $(O_2)_2$ column density changed drastically during the observed BrO event. Both species are sensitivity indicators for the troposphere and hence the possibility, that the observation was actually due to variations of the sensitivity, was ruled out.

Since then, different groups have developed several approaches to separate possible tropospheric events from stratospheric disturbances. These approaches are summarized in the flowing.

3.3.1. Reference sector approach

The reference sector approach is based on the assumption that the stratospheric BrO columns mainly depend on latitude and much less on longitude (Richter & Wagner, 2011). This approach was already applied by Richter *et al.* (1998) as illustrated in 3.4. Presumably, averaged columns measured at a certain latitude were subsequently subtracted from measurements at different longitudes, but at the same latitude. The reference sector approach was also applied by (Hollwedel, 2005) who also discussed the possibility to use nadir measurements at large SZA and therefore very high sensitivity to stratospheric BrO (cf. Section 6.3.1) in order to extrapolate the stratospheric column at lower SZA.

It is noted that there is some scientific dispute whether the contribution of the

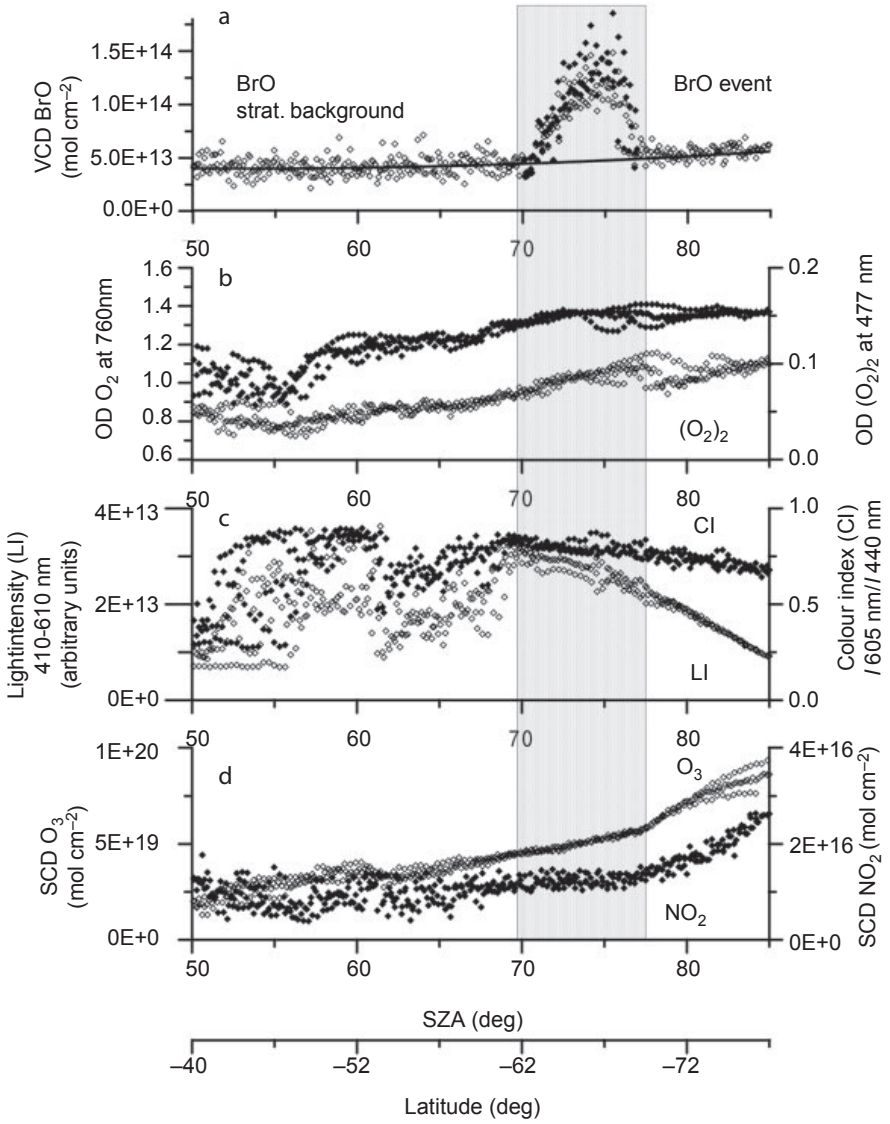

Figure 3.3.: *Latitudinal variation of the column densities of atmospheric trace gases, the average light intensity and a colour index for part of an orbit on 15 September 1996 as a function of the solar zenith angle and corresponding (approximate) latitude. (a) Open diamonds, BrO VCD calculated using the stratospheric AMF; filled diamonds, the enhancement expressed as tropospheric BrO VCD (calculated using tropospheric AMFs). (b) Open diamonds, absorption of $(O_2)_2$ (right axis); filled diamonds, absorption of O_2 (left axis). (c) Open diamonds, measured average intensity (410–610 nm, left axis); filled diamonds, colour index (intensity ratio at the wavelengths 605 and 440 nm, right axis). (d) Open diamonds, SCD of O3 (left axis); filled diamonds, SCD of NO2 (right axis). Adapted from (Wagner & Platt, 1998).*

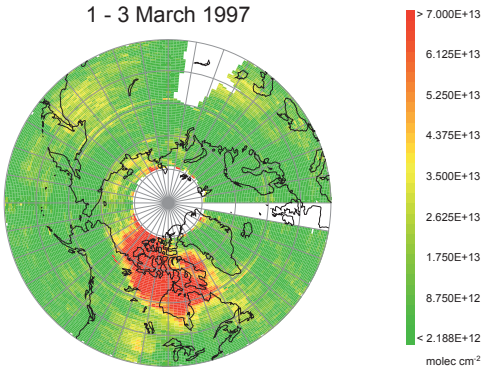

Figure 3.4.: *Selected three day composite of tropospheric BrO from GOME. The values given are excess tropospheric vertical columns derived from the measurements as discussed in the text. The sector used as the stratospheric BrO reference has been left blank. Adapted from (Richter* et al.*, 1998).*

stratospheric BrO to the total BrO column was potentially underestimated in the early studies using satellite data (Salawitch *et al.*, 2010). In this context, different estimates of the contribution of very short-lived (vsl) substances to the stratospheric BrO concentration may have led to confusing discrepancies (cf. Dorf *et al.*, 2006). The influence of a longitudinal dependence of the tropopause height (and hence the stratospheric partial column) on the interpretation of the tropospheric is also discussed in this thesis in Section 10.2). However, as was pointed out by e. g. Begoin *et al.* (2010) and Theys *et al.* (2011), stratospheric disturbances are more probably creating more broadband distortions from which tropospheric events may be distinguished as they appear on much smaller spatial scales. Furthermore, small scale variations of the tropopause height did not coincide with the structure of BrO enhancements which were evaluated by Begoin *et al.* (2010).

3.3.2. Distributed reference area approach

This approach is based on the assumption that the stratospheric column is mainly a function of latitude. The measurements are divided into half-degree latitude bands and it is furthermore assumed that the stratospheric column corresponds to the 10th percentile column in each band (Zeng *et al.*, 2003, 2006). As a result, the reference measurements in every latitude interval are located at different longitudes.

3.3.3. Stratospheric chemistry model

In recent years, global 3D chemical transportation model (CTM) simulations have gained in accuracy to model the concentration of many absorbers. Using the CTM output, the stratospheric BrO column can directly be subtracted from the total column. This approach has been applied by at least two groups: Toyota *et al.* (2011) used total columns measured by GOME (Richter *et al.*, 2002) and subtracted stratospheric columns simulated by the SLIMCAT model (Chipperfield, 1999; Chipperfield *et al.*,

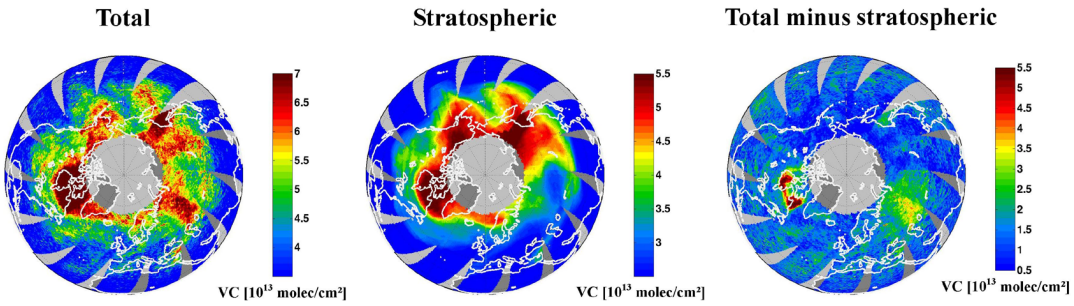

Figure 3.5.: *GOME-2 total BrO columns (left), stratospheric BrO columns calculated from the BASCOE climatology at GOME-2 overpass (center) and the difference between the total and stratospheric BrO columns (right). Total BrO columns are estimated using stratospheric air mass factors. The results are presented for 25 February 2008. Adapted from (Theys* et al.*, 2011).*

2005) as depicted in Figure 3.7a. Salawitch *et al.* (2010), on the contrary, used BrO measurements by OMI and applied their own model calculations of the stratospheric column.

However, chemistry models are potentially biased because the bromine budget and the chemical mechanisms may be incomplete and necessary parametrisations may result in systematic errors. Model results also depend on the choice of initial values and boundary conditions which are usually difficult to define.

3.3.4. Stratospheric climatology approach

A more elaborate approach has been proposed by Theys *et al.* (2009b). Model results from a 3D-CTM optimized for stratospheric bromine chemistry are parametrised using a dynamical (O_3) and chemical (NO_2) indicator. These parameters are stored in a climatology of monthly and latitudinal means. The stratospheric partial column is finally calculated from the time and location of the measurement, column measurements of both O_3 and NO_2, and tropopause height values provided by an assimilated meteorological model (Figure 3.5). This climatological approach has already been applied in a number of publications (Theys *et al.*, 2011; Begoin *et al.*, 2010; Choi *et al.*, 2011).

3.4. Selected published comparison to model results

Several publications in the past compared satellite BrO measurements to different models describing stratospheric chemistry designed to address some of the scientific questions presented in Section 2.4 (Begoin *et al.*, 2010; Salawitch *et al.*, 2010; Theys *et al.*, 2011; Toyota *et al.*, 2011, are the most recent publications). Here, two selected examples of remarkable agreement between model study and satellite observation are adapted from the original publications.

3.4.1. Comparison to FLEXPART forward dispersion model

In the case study published by Begoin *et al.* (2010), GOME-2 measurements of BrO are compared to results from the atmospheric dispersion model FLEXPART (Stohl *et al.*, 1998). A distinct event of a particular strong BrO enhancement observed on 26th March 2007 is used to initialize the distribution of a chemically inert tracer substance. The model subsequently simulates the dispersion of initial distribution by atmospheric transport processes. Additionally, the dependence on different initialization heights was studied.

Astonishingly, the transport pattern of BrO in connection with a distinct low pressure system (which was accompanied by relatively low tropopause heights) showed the highest correlation with the transport pattern of a "BrO plume" initialized in an elevated layer around 2 km altitude. Due to the relatively short life-time of BrO, it was concluded that there must exist a highly efficient recycling mechanism for reactive bromine taking place either on transported aerosols or on a preconditioned surface exposed to the transported air-mass.

Figure 3.6 shows the distribution as measured by GOME-2 and simulated by FLEXPART after two days, on 28th March 2008, assuming an initialization height between 1 and 3 km. Despite some minor deviations, this figure suggests that the BrO observed by GOME-2 at least behaves as if it was transported in an elevated layer between 1 and 3 km altitude.

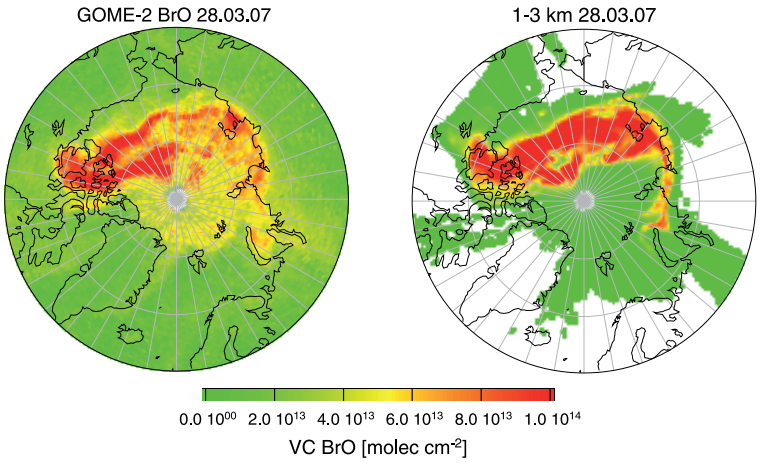

Figure 3.6.: *(left) stratospheric corrected GOME-2 measurement data using boundary layer AMF (400 m); (right) daily averaged FLEXPART model result adjusted to GOME-2 measurement data. Adapted from (Begoin* et al.*, 2010).*

3.4.2. Comparison to tropospheric chemistry model

The knowledge of the processes leading to polar bromine activation (bromine explosion) are still not entirely understood. The influence of various parameters leading to enhanced BrO levels can be studied using 3D tropospheric chemistry models. How-

ever, the number of 3D model studies is still sparse due to the complexity of the phenomenon.

Toyota *et al.* (2011) presented a study in which the snowpack on sea-ice is assumed as the only source of reactive halogen species. Tropospheric BrO columns calculated from model results for April 2001 (Figure 3.7b) were compared to satellite columns measured by GOME. (Figure 3.7a). The authors conclude that reactive bromine is probably released from the snow on the sea-ice during Arctic spring is mainly controlled by meteorological factors. Furthermore, the appearance of "BrO clouds" seem to be less controlled by the availability of bromine species but rather ozone-rich air masses transported horizontally and vertically to the surface enriched with bromine. The simulations suggested, that a large fraction of the O_3 at the sea-ice surface is depleted (Figure 3.7c).

3.5. Conclusion of published satellite measurements

The first satellite measurements of tropospheric BrO in polar regions were published soon after GOME, the first satellite-borne spectroscopic instrument capable to detect BrO, was in orbit. Since then, different methods to correct the BrO column measurements for stratospheric contributions were implemented and several papers of the BrO observations and the possible implications could be published based on the GOME data. The frequency of published research utilizing BrO data from satellites increased again significantly with the launch of GOME-2 providing a highly improved resolution and coverage applying an already established technique.

Detailed knowledge about the underlying chemistry and improved computing capacity furthermore permitted the development of sophisticated stratospheric chemistry models. The output of these models has been applied to separate the tropospheric and stratospheric partial columns which allowed for a more detailed comparison to complementary data-sources and model data alike.

In this thesis, however, a self-contained satellite retrieval for tropospheric BrO has been developed which is presented in Chapter 6. In contrast to other published retrievals, this retrieval is independent from external model input which makes it especially suitable for comparison with other data sources because it minimizes systematic errors originating from potentially incomplete chemistry models. The comparison between satellite measurements and meteorological model data presented in this chapter already revealed a striking correlation based on case studies. In Chapter 11, the tropospheric BrO VCDs derived in this work are systematically compared to different meteorological parameters instead which allows a general conclusion on the meteorology of bromine activation in the Arctic.

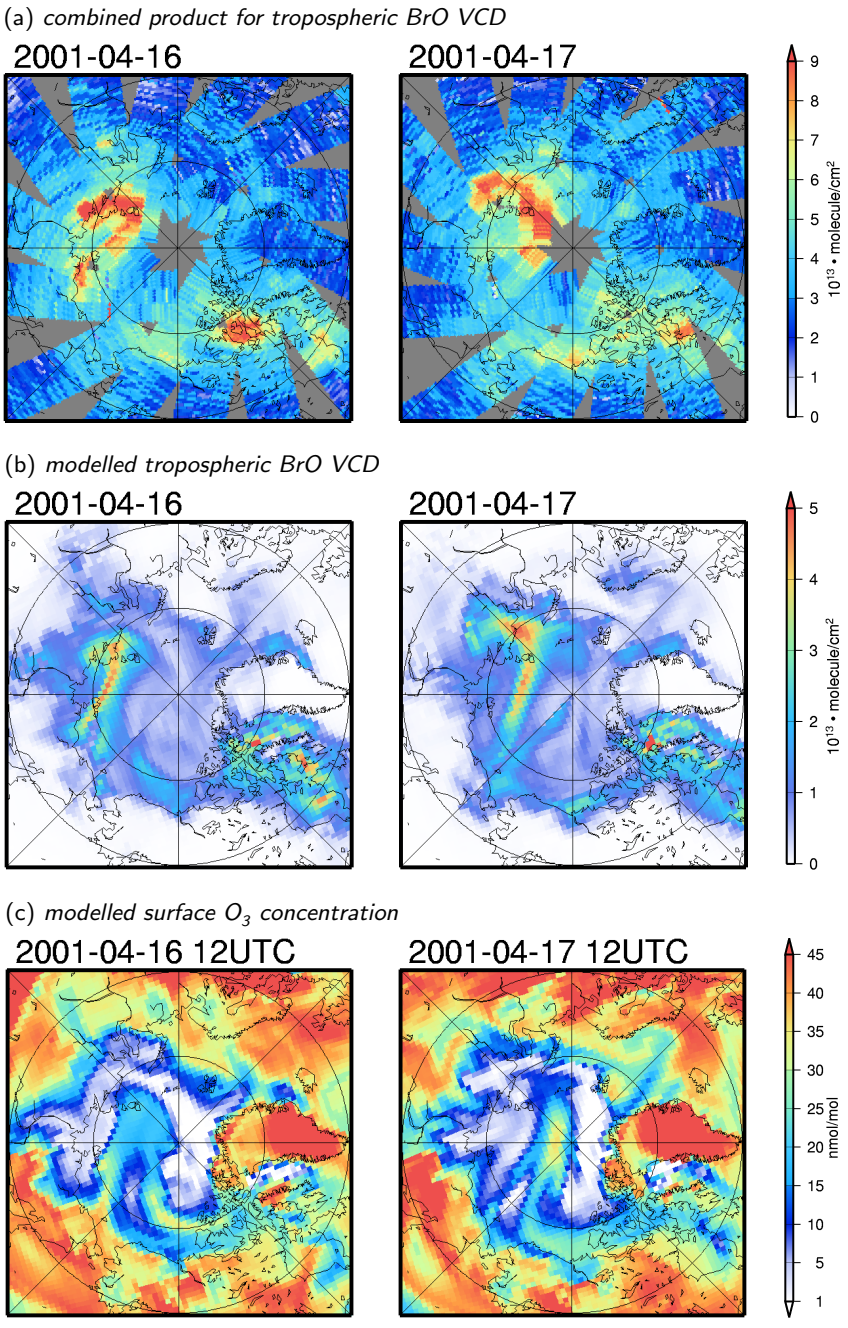

Figure 3.7.: *Adapted comparison of a 3-D model study conducted by Toyota* et al. *(2011) to a combined product for tropospheric BrO VCDs (see text): (a) GOME-SLIMCAT tropospheric BrO VCDs (in molecule cm^{-2}) for 16 and 17 April 2001; (b) modelled BrO VCDs (in molecule cm^{-2}); (c) surface ozone mixing ratios (in nmol mol^{-1}).*

Part II.

Methods and Instruments

4. Differential optical absorption spectroscopy

Differential Optical Absorption Spectroscopy (DOAS) is a method to remotely sense the abundance of a variety of trace gases in the atmosphere. It was first introduced by Perner *et al.* (1976) and Platt *et al.* (1979). Since then, the DOAS technique has been constantly improved and enhanced over the years (e.g., Stutz & Platt, 1996; Platt *et al.*, 2009). It is based on analysing the spectral composition of light that has been partly absorbed during its path through the atmosphere. Hence, the atmospheric chemistry may be studied without changing its nature, for example by titration on inlet-surfaces, or the exposure to strong radiation. The satellite and ground-based measurements central to this thesis utilize DOAS for the spectral evaluation. This chapter therefore introduces the principles and symbols of DOAS while (Platt & Stutz, 2008) provides a detailed description of the underlying concepts and principles. Richter & Wagner (2011) also provides a valuable introduction focusing on the application of DOAS to satellite measurements.

4.1. Absorption spectroscopy

Absorption spectroscopy is based on the principle that molecules may enter excited states when irradiated by electromagnetic radiation. Absorption occurs when electronic, vibrational and rotational states are excited. As the energy levels of these states depend on the molecular structure, every molecule absorbs light at distinct wavelengths. The absorption process in general is described by the Lambert-Beer law. At a given wavelength λ, the Lambert-Beer law

$$\mathrm{d}I(\lambda) = -I(\lambda)\,\sigma(\lambda)\,\rho(s)\,\mathrm{d}s \tag{4.1}$$

relates the decrease of the intensity $-\mathrm{d}I$ along a sufficiently small path element $\mathrm{d}s$ to the intensity I, the absorption cross-section σ and the number density ρ of the absorber.

Equation (4.1) may be partially integrated to calculate the intensity of the radiation after having travelled a path of length L through the atmosphere

$$I(\lambda, L) = I_0(\lambda) \exp\left[-\sigma(\lambda) \int_0^L \rho(s)\,\mathrm{d}s\right] \tag{4.2}$$

in case of a known initial intensity I_0. If we assume ρ not to change along the path, the right-hand side may also be integrated

$$I(\lambda) = I_0(\lambda) \exp[-\sigma(\lambda)\rho L]. \tag{4.3}$$

Introducing of the optical density τ

$$\tau(\lambda) = \ln \frac{I_0(\lambda)}{I(\lambda)} \tag{4.4}$$

the number density – or concentration – of the absorber is given by

$$\rho = \sigma(\lambda)\, L\, \tau(\lambda). \tag{4.5}$$

4.2. Atmospheric absorption spectroscopy

In the atmosphere there is usually more than one type of absorbing molecule present. The exponent in (4.2) becomes

$$\sigma(\lambda)\rho(s) \longrightarrow \sum_i \sigma_i(\lambda)\rho_i(s). \tag{4.6}$$

with the molecular absorption cross-sections σ_i of all species i involved and their respective number densities ρ_i.

Furthermore, radiation is scattered out of or into the light path by the following two processes: *Rayleigh scattering* describes the dipole scattering of light by molecules and particles much smaller than λ. By approximation, the Rayleigh scattering cross-section σ_R is proportional to λ^{-4} (Rayleigh, 1899). The Rayleigh scattering coefficient ϵ_R yields

$$\epsilon_R(\lambda, s) = \sigma_R(\lambda)\, \rho_R(s) \tag{4.7}$$

with the number density of Rayleigh scatterers ρ_R. *Mie scattering* occurs when light is scattered by particles like aerosol particles and cloud droplets with a spatial dimension r in the order of *lambda* and above. The Mie scattering cross-section σ_M is less wavelength dependent than σ_R and depends on the size and shape of the particle (Mie, 1908). The Mie scattering coefficient ϵ_M is defined as

$$\epsilon_M(\lambda, s) = \sigma_M(\lambda)\, \rho_M(s) \tag{4.8}$$

where ρ_M is the number density of Mie scatterers in the atmosphere. Therefore, the exponent in (4.2) needs to be expanded

$$I(\lambda, L) = I_0(\lambda) \exp\left[- \int_0^L \left(\epsilon_R(\lambda, s) + \epsilon_M(\lambda, s) + \sum_i \sigma_i(\lambda)\rho_i(s) \right) \mathrm{d}s \right] \tag{4.9}$$

to account for the multitude of absorbers and the described scattering processes.

Unfortunately, this form of the Lambert-Beer law cannot be directly applied to trace gas measurements in the atmosphere for several reasons:

- It is nearly impossible to distinguish between the contributions of the different scattering processes in the atmosphere and broad-band absorption of continuum bands of the absorbers. Furthermore, different absorbers may not be distinguished.

- The initial intensity I_0 may often not be not determined accurately enough, for instance when (scattered) sun-light is used.
- Atmospheric turbulence and the spectral response of the instrument change the shape and amplitude of I. Both may be time-dependent and are generally under-determined.
- Light from sources other than the initial light source may interfere with the initial spectrum $I_0(\lambda)$. This is particularly problematic when an artificial light-source is applied and sun-light is scattered into the measurement light-path.

DOAS provides a technique avoiding these difficulties of spectroscopy in the atmosphere.

DOAS takes advantage of the fact that aerosol extinction processes, the effect of turbulence, and many trace gas absorptions show very broad or even smooth spectral characteristics. Certain trace gases, however, exhibit narrow-band absorption structures. The basic principle of DOAS is thus to separate broad- and narrow-band spectral structures in an absorption spectrum in order to isolate these narrow trace gas absorptions (Platt & Stutz, 2008). Figure 4.1 illustrates the separation of the absorption cross-sections σ_i introduced in Equation (4.6)

$$\sigma_i(\lambda) = \sigma_{i,0}(\lambda) + \sigma_i'(\lambda) \tag{4.10}$$

into broad-band and narrow-band contributions $\sigma_{i,0}$ and σ_i', respectively. Correspondingly, the initial intensity I_0 is separated

$$I_0(\lambda) = I_0'(\lambda) + D'(\lambda) \tag{4.11}$$

into a broad-band intensity I_0' and a narrow-band intensity variation D'. The definition of *broad-band* and *narrow-band* mostly depends on the wavelength region evaluated and the width of characteristic absorption features of σ_i.

The sum of the molecular absorption in Equation (4.6) now becomes

$$\sum_i \sigma_i(\lambda)\rho_i(s) \longrightarrow \sum_i \sigma_{i,0}(\lambda)\rho_i(s) + \sum_i \sigma_i'(\lambda)\rho_i(s) \tag{4.12}$$

and Equation (4.9) can be split into narrow-band and broad-band part

$$I(\lambda, L) = I_0(\lambda)\, \exp\left[-\int_0^L \sum_i \sigma_i'(\lambda)\rho_i(s)\,\mathrm{d}s\right] B(\lambda) \tag{4.13}$$

with

$$B(\lambda) = \exp\left[-\int_0^L \left(\epsilon_R(\lambda, s) + \epsilon_M(\lambda, s) + \sum_i \sigma_{i,0}(\lambda)\rho_i(s)\right)\mathrm{d}s\right] \tag{4.14}$$

summarizing all broad-band contributions.

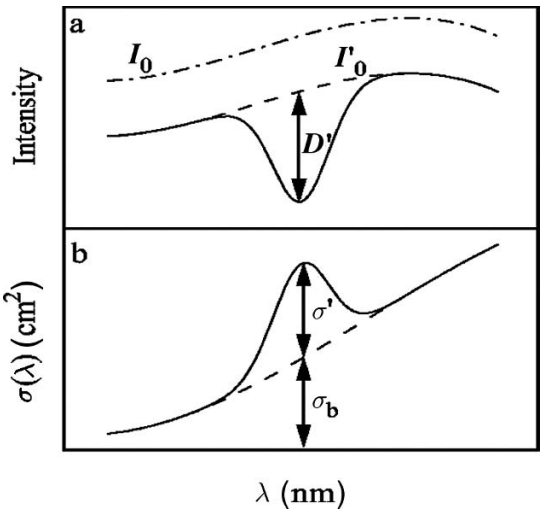

Figure 4.1.: *Principle of DOAS: I_0 and σ are separated by an adequate filtering procedure into a narrow-band (D', and σ') and broad-band part (I'_0 and σ_b). Figure and caption adapted from (Platt & Stutz, 2008).*

In practice, (4.13) is often rewritten in optical density space using Eq. (4.4)

$$\tau = \int_0^L \sum_i \sigma'_i(\lambda)\rho_i(s)\,\mathrm{d}s + \mathcal{P}_r(\lambda) \tag{4.15}$$

where the broad-band contributions B are represented by a polynomial $\mathcal{P}_r$ of the order r. In analogy to Eq. (4.4), the first term in Eq. (4.15) is regularly called the differential optical density τ'

$$\tau'(\lambda) = \ln \frac{I'_0(\lambda)}{D'(\lambda)}. \tag{4.16}$$

4.3. Long-path differential optical absorption spectroscopy

Long-path differential optical absorption spectroscopy (LP-DOAS) instruments are the first implementation of the DOAS technique (Perner *et al.*, 1976). Its light-source is artificial and therefore LP-DOAS is classified as *active* DOAS. The light propagates along a well-known path through the atmosphere and is reflected by a retro-reflector installed several hundreds of meters from the sending/receiving-telescope. The spectroscopic detection is achieved by a spectrometer as illustrated in Fig. 4.2, which shows a modern setup of an LP-DOAS instrument (Platt & Stutz, 2008; Sihler, 2007; Merten *et al.*, 2011).

Xenon-arc lamps are the most common light source (Platt & Stutz, 2008). Whenever a high stability or a low power consumption are needed, however, tungsten lamps or light-emitting diodes (LEDs) may be advantageous (Lotter, 2006; Kern *et al.*, 2006; Sihler, 2007; Sihler *et al.*, 2009). In general, any artificial light source may be applied in LP-DOAS as long as its emission spectrum is sufficiently broad.

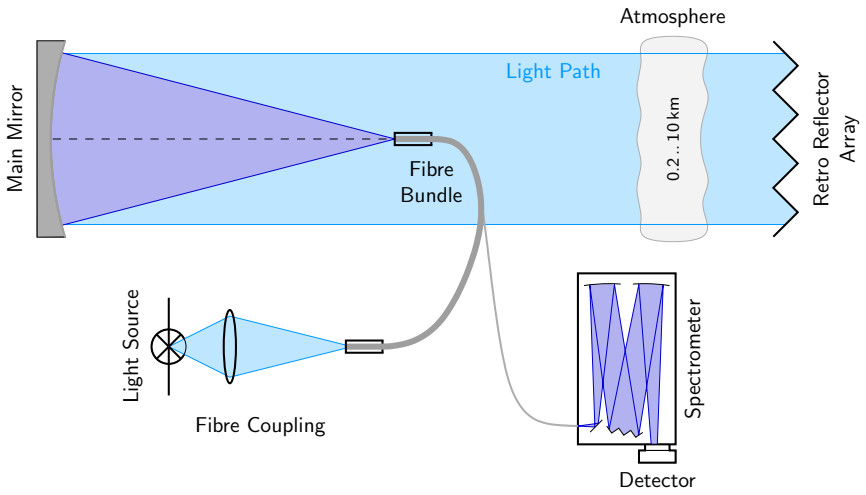

Figure 4.2.: *Setup of a Long-Path DOAS instrument with light source, fibre bundle, telescope, retro-reflector array, and spectrometer with detector. The length of the light path usually ranges between 200 m and 10 km one-way. Adapted from (Sihler, 2007).*

LP-DOAS instruments can only measure concentrations of trace-gases integrated (or averaged) along the light-path as a consequence of the stationary setup. Hence, the spatial dependence of ρ vanishes and Eq. (4.15) can rewritten

$$\tau = L \sum_i \sigma'_i(\lambda)\bar{\rho}_i + \mathcal{P}_r(\lambda) \tag{4.17}$$

with the spatially averaged number density $\bar{\rho}_i$.

In practice, when evaluating Eq. (4.17) in order to calculate $\bar{\rho}_i$ from measured values of differential absorption cross-sections σ'_i, light-path length L, and optical density τ, a combination of the Levenberg-Marquart Method and a standard non-linear least-squares fit is applied (Bevington, 1969; Press *et al.*, 1992; Kraus, 2006; Sihler, 2007). With a reference to the existing literature (e. g. Kraus, 2006; Platt & Stutz, 2008), the spectral processing and its mathematical description will not be detailed here.

4.4. Passive differential optical absorption spectroscopy

In contrast to the active LP-DOAS approach, DOAS is also performed in a passive sense using natural light sources (*passive* DOAS). Historically, zenith-scattered light DOAS (ZSL-DOAS) was the first ground-based passive DOAS implementation using scattered sun-light (Noxon, 1975; Noxon *et al.*, 1978; Solomon *et al.*, 1987a,b, 1989; Schiller *et al.*, 1990; Aliwell *et al.*, 2002; Platt & Stutz, 2008, and references therein). A technique that uses scattered sun-light measured at elevation angles other than the zenith is multi-axis DOAS (MAX-DOAS) (e.g. Hönninger *et al.*, 2004; Bruns *et al.*, 2004).

Ground-based MAX-DOAS is an established technique to determine the concentration of trace-gases in the troposphere (Hönninger & Platt, 2002). However, the

effective path of photons sampled for one measurement of I is determined by a multitude of different photon paths and is generally not exactly known. Therefore, only a slant column density (SCD) S_i

$$S_i = \int \rho_i(s)\,\mathrm{d}s \tag{4.18}$$

of trace gas species i is obtained from passive DOAS measurements. Hence, (4.15) can be rewritten for the case of passive DOAS measurements in analogy to (4.17)

$$\tau = \sum_i \sigma_i'(\lambda) S_i + \mathcal{P}_r(\lambda). \tag{4.19}$$

In analogy to active DOAS, also (4.19) is solved using the Levenberg-Marquart Method.

4.4.1. Differential optical absorption spectroscopy from satellites

Spectra measured by satellite-borne spectrometers can also be evaluated with the DOAS technique. The spectral composition of sunlight, scattered by the Earth's atmosphere and reflected by the Earth's surface, is analysed to obtain the global distribution of various trace gases. One important difference between satellite measurements and ground-based measurements is the ability to obtain the initial intensity spectrum I_0 without any atmospheric absorption.

4.4.2. The satellite nadir geometry

The satellite measurements that are evaluated in this work have been obtained from a nadir-looking satellite instrument described in Section 5.2. The nadir (direction) points from the satellite to the Earth's center of gravity. The nadir is approximately perpendicular to the Earth's surface at the sub-satellite point Σ, which is the intersection of the surface with the straight line between satellite and the Earth's center of gravity. The viewing direction of the satellite is not stationary but periodically panning at around the nadir and perpendicular to the flight direction in order to capture a larger fraction of the Earth's surface. The captured surface fraction is called the *swath* of the instrument.

Three angles define the viewing geometry of the satellite instrument with respect to the Sun.

- The line of sight angle (LOS) ψ is the angle between the viewing direction and the nadir.
- The solar zenith angle (SZA) ϑ is the angle between the instruments nadir and the direction of the Sun.
- The solar relative azimuth angle (SRAA) β is the angle between the instruments viewing direction and the Sun in the plane parallel to the surface.

These definitions are illustrated in Figure 4.3 in case of a simplified plane-parallel coordinate system .

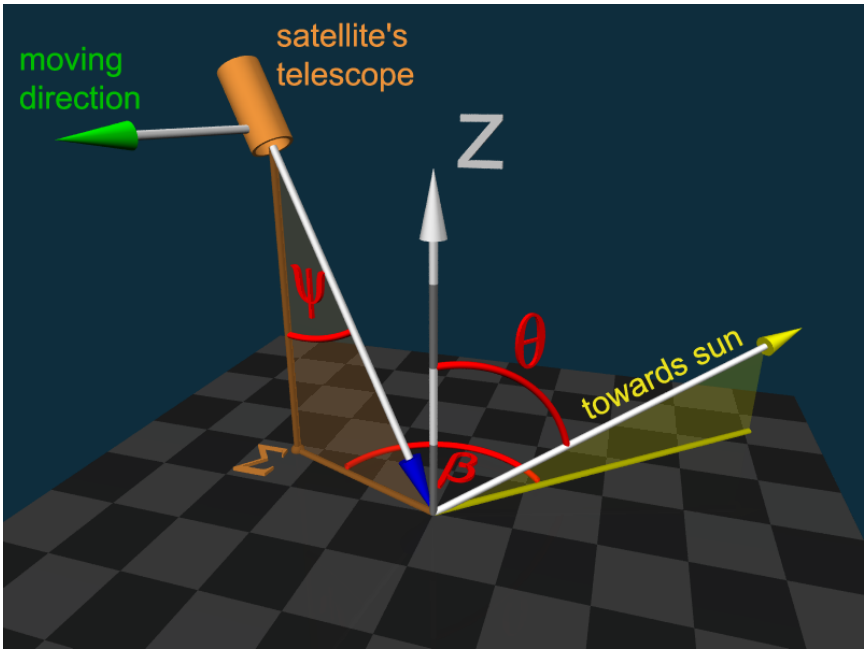

Figure 4.3.: *Angle definition of the satellite nadir geometry in the plane-parallel coordinate system: line of sight (LOS) angle ψ, solar zenith angle (SZA) θ, and solar relative azimuth angle (SRAA) β (see text). The satellite's telescope (orange cylinder) above the sub-satellite point Σ points at the surface (blue arrow). The position of the Sun (yellow arrow) and the moving direction of the satellite (green arrow) are indicated.*

4.5. Atmospheric radiative transfer and the air mass factor

So far, as described in Section 4.4, DOAS provides a method to derive SCDs from measured spectra, but a comparison between two SCDs is not straightforward if the viewing geometry or the atmospheric distribution of scatterers and hence the average light path of the sampled photons changes. This section describes how measured SCDs are converted into vertical column densities (VCDs) using results from atmospheric radiative transfer (RT) modelling techniques. With the presented formulation it is possible to decouple the spectroscopic retrieval of trace gas SCDs using DOAS from the transformation into a vertically integrated property.

The VCD V_i of species i is defined as the integral from the surface to the top of atmosphere (TOA) Θ

$$V_i = \int_0^\Theta \rho_i(z)\,\mathrm{d}z. \tag{4.20}$$

In order to calculate the V from the measured S, the air mass factor (AMF) A

$$A = \frac{S}{V}, \tag{4.21}$$

needs to be calculated. The AMF is a measure for the measurement sensitivity. It generally depends on the angles ϑ, ψ and β and the optical properties of the probed

atmosphere. Unfortunately, the knowledge about the optical properties is often sparse and approximations are needed.

As a first approximation, the geometrical AMF

$$A_{\mathrm{g}} = \frac{1}{\cos\psi} + \frac{1}{\cos\vartheta} \tag{4.22}$$

may be applied for cloud-free scenes and relatively small SZA $\vartheta < 80°$ when the light is almost exclusively reflected by the surface (Richter & Wagner, 2011). This approximation is particularly useful when analysing stratospheric compounds because the majority of scattering occurs in the troposphere underneath and the stratospheric light-path remains almost geometric (compare to Sections 6.3.1 and 6.4).

For more complex situations the deviations from the geometric approach become significant and a more general approach is required. As a solution, the AMF is calculated using numerical RT simulations. The central task of RT algorithms is to model the radiances I and I_0 at the detector with and without the trace gas, respectively. Then, the SCD may be expressed as a function of the modelled τ and the absorbing cross-section σ using (4.9), (4.4) and (4.18)

$$S = \frac{1}{\sigma} \ln \frac{I}{I_0}. \tag{4.23}$$

The AMF may then be calculated via

$$A = \frac{\ln I - \ln I_0}{\sigma V} \tag{4.24}$$

using the definition of the AMF (4.21).

4.5.1. Measurement sensitivity in 1D

A height-resolved AMF, the Box-AMF, defines the vertical dependence of the measurement sensitivity of a specific atmospheric layer j. The Box-AMF $\hat{A}_j$ can be expressed as

$$\hat{A}_j = \frac{S_j}{V_j} \tag{4.25}$$

with the partial slant and vertical column densities S_j and V_j, respectively (Richter & Wagner, 2011). $\hat{A}_j$ can be derived by averaging simulated geometrical path lengths through layer j weighted by their modelled intensity.

From Eq. 4.25 follows that

$$A = \frac{S}{V} = \frac{\sum_j S_j}{V} = \sum_j \hat{A}_j \frac{V_j}{V}. \tag{4.26}$$

Hence, the total AMF A may be now calculated from simulated $\hat{A}_j$ simply weighted by the relative trace gas concentration profile V_j/V. A detailed study on the sensitivity of satellite-borne DOAS measurements depending on the trace gas profile is presented in Section 6.3.

4.5.2. Measurement sensitivity in 3D

It is possible to generalize the introduced Box-AMF concept into 3 dimensions. Equation (4.26) can be rewritten

$$S = \sum_{j,m,n} \hat{A}_{j,m,n}\, V_{j,m,n} = \sum_{j,m,n} \hat{A}_{j,m,n}\, h_j\, \rho_{j,m,n} \tag{4.27}$$

using collocated data of simulated 3D-Box-AMFs $\hat{A}_{j,m,n}$ and given 3D-VCDs $V_{j,m,n}$ or 3D-number densities $\rho_{j,m,n}$, respectively. The height of layer j is denoted by h_j.

Figure 4.4 is a visualization of the spatially resolved sensitivity of a satellite instrument with nadir viewing direction simulated using the McArtim RT-model published by Deutschmann *et al.* (2011). In the presented cloud-free case over a bright surface with an albedo of 0.85, vertical section of the geometric light-path is easily recognizable by its large contribution. However, there is an additional sensitivity to gas in the path from the surface towards the sun and an overall blue "glow" indicating that absorption from a much larger volume contributes to the measurement.

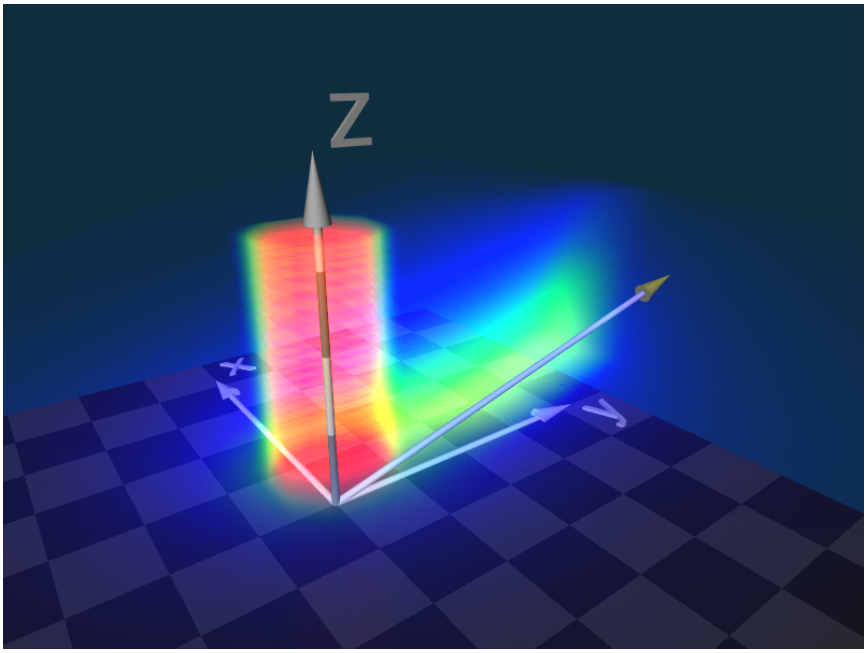

Figure 4.4.: *A visualization of the spatially resolved sensitivity of the satellite nadir geometry at an SZA of 75°. The normalized sensitivity, which increases from transparent-blue, green and yellow to red, is principally located within the field-of-view of the satellite (red cylinder in the center). However, the sensitivity along the geometric path to the Sun (white arrow with yellow tip) is blurred at its edges leading to somewhat smaller values. This image has been calculated from output of the McArtim software (Deutschmann* et al.*, 2011) using a ground-albedo of 0.85; the edge length of the checkerboard-squares is 10 km.*

4.6. DOAS measurements in this thesis

DOAS is a commonly used method to quantify the abundances of trace gases in the atmosphere. In this thesis, DOAS was applied the spectral evaluation of both ground-based and satellite measurements. Ground-based measurements using an active LP-DOAS instrument were conducted at Barrow, Alaska (see Section 5.1 and Chapter 8), and satellite measurements using the GOME-2 instrument (see Section 5.2, Chapters 10 and 11). Furthermore, MAX-DOAS measurements were also conducted at Barrow which were subsequently evaluated by Dr. Udo Frieß and published in Frieß *et al.* (2011).

The main scope of the DOAS measurements presented here was to measure the abundance of BrO radicals (cf. Section 2.1) in the polar troposphere. The comparison of both ground-based and satellite measurements are presented in Chapter 9 and reveal a striking correlation taking the vertical distribution of BrO into account. The result is a combined picture merging the accuracy of ground-based measurements with the beneficial spatial coverage of satellite sensors.

Furthermore, the result of radiative transfer calculations are used in order to quantify the sensitivity of satellite measurements to near-surface absorbers (Section 6.5) using DOAS measurements of the $(O_2)_2$ collision complex. The necessary radiative calculations, however, use the one dimensional approximation whereas the 3D-Box-AMF formulation given here is included for completeness.

5. Instruments

This chapter describes the instruments and measurement techniques applied in this work. It is focused on spectroscopic instruments whose data is analyzed using the DOAS technique described in the previous chapter (Chapter 4). Mainly two different DOAS instruments were applied: (1) ground-based active DOAS measurements were performed at Barrow in spring 2009, and (2) satellite data acquired by the GOME-2 instrument has been analyzed for tropospheric BrO column densities. The instruments deployed at Barrow are described in Section 5.1 and the GOME-2 satellite instrument is described in Section 5.2. Furthermore, data from other satellite instruments are compared to GOME-2 measurements in Chapter 11. These satellite instruments are described in Section 5.3.[1]

5.1. Instrumentation at Barrow 2009

In spring 2009, ground-based measurements were performed in the scope of the internationally coordinated Ocean – Atmosphere – Sea Ice – Snowpack (OASIS) project at Barrow, Alaska. A major focus of the OASIS campaign was to study halogen chemistry and its impact on the Arctic environment. The Institute of Environmental Physics, Heidelberg contributed to this project by providing LP-DOAS and MAX-DOAS measurements of a variety of atmospheric trace-gases focusing on BrO. The LP-DOAS measurements are an essential part of the presented work and the instrument as well as the measurement layout are described in Sections 5.1.1 and 5.1.2, respectively. Furthermore, complementary measurements performed at Barrow are shortly described in Section 5.1.3. Figure 5.1 shows a map of the different measurement locations.

5.1.1. LP-DOAS instrument

This section describes the LP-DOAS measurements as well as the measurement procedures as performed between 13 March and 16 April 2009 at Barrow, Alaska, USA. The LP-DOAS instrument used in this work was previously deployed aboard the Amundsen RV in Spring 2008 and is described in Pöhler *et al.* (2010b) and Liao *et al.* (2011). The data evaluation and the results of the measurements are presented in Chapter 8.

Figure 4.2 on page 43 shows a sketch of an LP-DOAS instrument and its components (Section 4.3). At Barrow, the LP-DOAS instrument was divided into an outside and inside part. On the one hand, the active components (computer, spectrograph, controller, etc.) of the LP-DOAS instrument at Barrow were located inside the

[1] Parts of this chapter are already published in Liao *et al.* (2011) and Frieß *et al.* (2011).

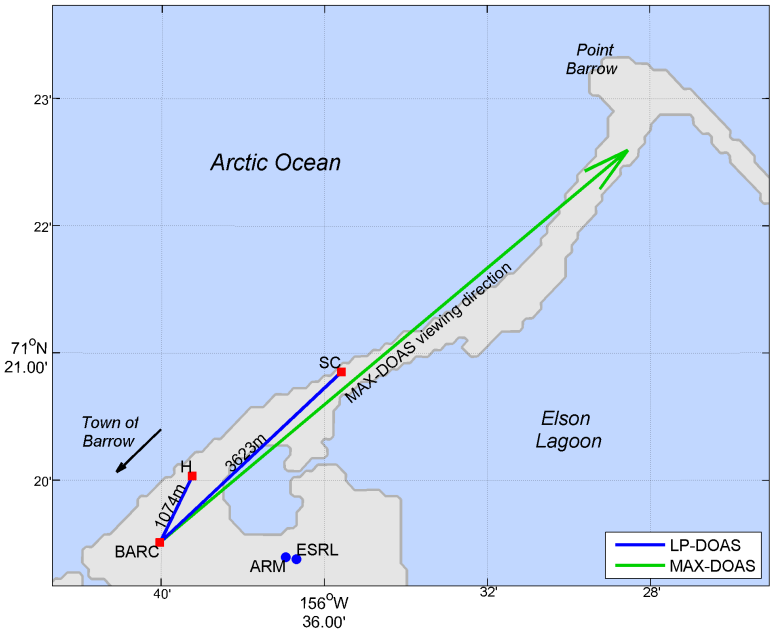

Figure 5.1.: *Map of the measurement locations at Barrow. The DOAS instruments were operated at the BARC Building. The blue lines indicate the light paths of the LP-DOAS, with H (hangar) and SC (summer camp) showing the locations of the LP-DOAS retro-reflector arrays. The green line indicates the viewing direction of the MAX-DOAS. Also shown are the locations of the ARM and ESRL sites where complementary measurements were performed. Adapted from Frieß* et al. *(2011).*

Barrow Arctic Research Center (BARC) building (Figure 5.1). On the other hand, the passive components (telescope and two retro-reflectors) were located outside in the comparatively harsh Arctic environment. The outside components are described below in Section 5.1.2.

The active part of the LP-DOAS instrument consisted of the following components (cf. Figure 4.2). Radiation from a broadband light source (Xenon arc-lamp, usually Osram XBO 75; Osram XBO 500 between March 19 and 30) was coupled into a single 600 µm mode-mixing quartz fibre using a fused silica lens. The exit end of the single fibre was connected to six transmitting 200 µm fibres at one arm of a Y-bundle (total length 10 m). At the bottom of the Y, which was placed close to the focal point of a telescope mirror (30 cm diameter, 1.5 m focal length), these six fibres surrounded a single 200 µm receiving fibre. The pointing of the telescope could be adjusted by stepper-motors. The receiving fibre, the other arm of the Y, led to an Acton 300i spectrometer equipped with a CCD camera (Spec-10:2KBUV) manufactured by Roper Scientific. For stray-light reduction, a BG24A-filter or a UH-5 filter (both manufactured by Schott, 2 mm thickness) was placed behind the entrance slit of the spectrometer.

The light path through the atmosphere could be blocked using an aluminium diffuser plate placed at about 1 mm distance in front of the single end of the Y-bundle.

This "shortcut" configuration was applied after each measurement and was used to record the light source reference spectrum I_0. In addition, a "background spectrum" for each spectrum was obtained with the artificial light-source blocked. This was necessary to eliminate a possible signal offset due to scattered sunlight entering the telescope. The offset, as well as the dark-current signal of the CCD-electronics, were also accounted for in the evaluation procedure.

Varying spectral structures originated from fluctuations of the light source and of ambient illumination (scattered sun light), which was an issue during the day due to reflecting surfaces close to the retro-reflector arrays. In order to minimize these effects atmospheric absorption spectra I and reference spectra I_0, as well as their respective background signal, were recorded in quick succession. The light path had to be manually adjusted depending on meteorological conditions. During periods of poor visibility due to fog, clouds, mirages, or blowing snow, a shorter light path pointing at the Hangar retro-reflector was chosen.

5.1.2. LP-DOAS measurement layout

The setup of the LP-DOAS and complementary instruments is shown in Figure 5.1. The main research site included two trailers and the Barrow Arctic Research Center (BARC) building.

The LP-DOAS telescope was located at the north-east side of the BARC building (71° 19' 31" N, 156° 40' 02" W). It was connected to the inside instrumental parts by the fibre Y-bundle and the electrical connections controlling the stepper-motors. During the second half of the campaign, the LP-DOAS telescope was protected by a plywood shelter in order to reduce wind stress (Figure 5.2a).

Two retro-reflectors (Summercamp and Hangar) were installed at a distance of 3623 m and 1074 m from the telescope and provided a light path of 7246 m and 2148 m, respectively (blue line in Figure 5.1). The Summercamp retro-reflector (24 retro-cubes) was mounted on the south west wall of a Inupiat summer housing located at 71° 20' 51" N, 156° 35' 35" W (Figure 5.2d). The Hangar retro-reflector (7 retro-cubes, Figure 5.2c) was mounted on a lamp post located at 71° 20' 02" N, 156° 39' 14" W close to an army hangar visible in Figure 5.2b, respectively. The height above the surface of both LP-DOAS light-paths was approx. 2 m and varied little with horizontal position.

5.1.3. Complementary measurements

At Barrow, instruments of a unique multitude were deployed due to the broad focus of the OASIS project. However, only those measurements used in this work are described.

MAX-DOAS

The second instrument deployed by the Institute of Environmental Physics was a MAX-DOAS instrument (Section 4.4) also described in Wagner *et al.* (2007); Frieß *et al.* (2011). For the details of the spectral evaluation it is referred to Frieß *et al.* (2011).

(a) *outside DOAS instrumentation*

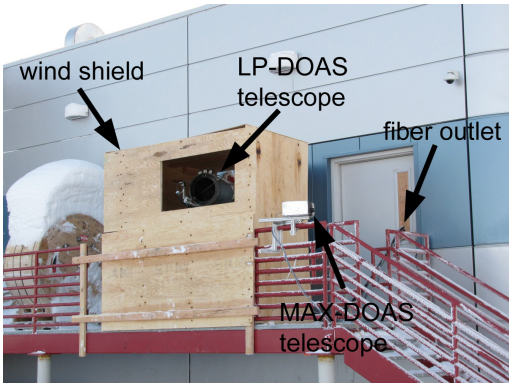

(b) *viewing of the LP-DOAS*

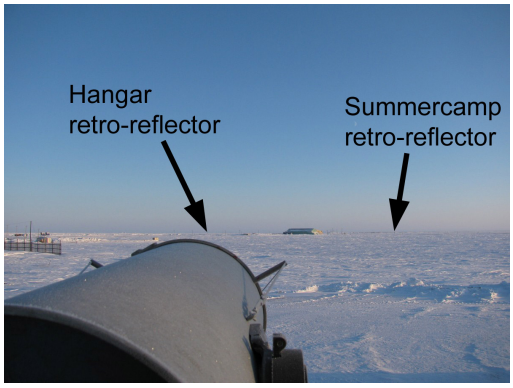

(c) *Hangar retro-reflector*

(d) *Summercamp retro-reflector*

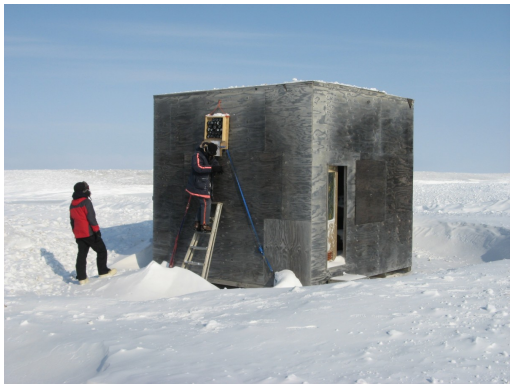

Figure 5.2.: *Images of the outside parts of both DOAS systems deployed by the Institute of Environmental Physics, Heidelberg during the OASIS Barrow campaign in spring 2009.*

The telescope unit of the MAX-DOAS instrument collects scattered sunlight at a fixed azimuth angle of 60° (green arrow in Figure 5.1) and different elevation angles using a quartz glass prism. Measurements were taken sequentially at elevation angles of 90° (zenith), 20°, 10°, 5°, 2°and 1°. During twilight (SZA>87.5°), measurements were performed at 90° and 2° elevation only. The light was focused on a quartz fibre bundle (14 × 200 mm) using a quartz lens of 100 mm focal length. This optical setup resulted in a field of view of 0.95°.

The fibre bundle conducts the light to a spectrograph/detector unit, consisting of an Acton 300i spectrometer and a back-illuminated Andor CCD with 2048 × 512 pixels. Spectra are recorded at wavelengths between 330 and 398 nm with a spectral resolution of 0.56 nm full-width half-maximum (FWHM). During the day, spectra are recorded with a total integration time of 60 seconds. To increase the signal-to-noise ratio during twilight, the integration time is increased to up to 200 seconds at 95° SZA.

The differential SCDs of O_4 and BrO derived from MAX-DOAS measurements at different elevation angles were processed as described by Frieß *et al.* (2011). Using the

optimal estimation method, the O_4 SCDs are first used to retrieve a vertical aerosol extinction profile. The aerosol information is then used in connection with the BrO SCDs in order to retrieve vertical profiles of BrO concentrations. The vertical profiles are discretised in steps of 100 m. It is therefore possible to compare the concentration within the lowest 100 m derived from MAX-DOAS measurements to the concentrations measured by LP-DOAS (see Section 8.5). Furthermore, the integrated VCDs retrieved for the altitude range between 0 and 2 km are compared to tropospheric VCDs from GOME-2 in Chapter 9.

Chemical ionization mass spectrometer

Chemical ionization mass spectroscopy (CIMS) is a further technique capable to measure BrO concentrations in air. It is an *in-situ* technique meaning that it is not a remote sensing technique averaging over a larger air volume but rather sampling the air at one certain location. The detection of halogen compositions by CIMS has only been recently realized and the LP-DOAS measurements performed at Barrow were the first the CIMS could be successfully compared with (Finley & Saltzman, 2008; Kercher *et al.*, 2009; Neuman *et al.*, 2010; Liao *et al.*, 2011).

Compared to the DOAS technique, which relies on appropriate optical absorption features with a sufficiently large differential optical density, the CIMS may measure a larger variety of halogen compounds such as Br_2 and $ClNO_2$ which cannot be detected by DOAS at typical atmospheric abundances (Platt & Stutz, 2008). However, an important disadvantage of the CIMS technique is that chemically unstable radicals (such as HOBr and BrO) partially convert into other more stable compounds at the inlet walls. Unlike DOAS, CIMS measurements need to be carefully calibrated in order to estimate realistic concentrations.

The CIMS instrument was located in one of the two trailers about 200 meters to the south-east of the LP-DOAS telescope. For a detailed description of the CIMS setup at Barrow it is kindly referred to Liao *et al.* (2011).

Meteorological, O_3, NO_2, and NO measurements

Temperature and pressure data from two sources are considered. On the one hand, meteorological measurements were performed by the collaborators from Environment Canada within the OASIS project. These were located at about 200 m distance from the LP-DOAS telescope close to the two trailers. On the other hand, data provided by the Barrow Atmospheric Baseline Observatory of the NOAA Earth System Research Laboratory (ESRL) and the Barrow facility of the U.S. Department of Energy's Atmospheric Radiation Measurement (ARM) program was utilized. Both ESRL and ARM sites are located approximately 2 km east of the DOAS measurement site (Figure 5.1).

In-situ surface ozone was monitored by a continuously operating TEI (Thermoenvironmental Corp.) Model 49C UV absorption analyzer at the ESRL from an inlet at 12 m above the ground. Furthermore O_3, NO_2, and NO mixing ratios were measured every 1 s using an NCAR-built chemiluminescence instrument. Regular (daily) release ozone sondes were launched from the ESRL. Finally, incoming and upwelling

short-wave and long-wave radiation components were quantified with a radiometer mounted 2 m above ground on a boom facing south (Helmig *et al.*, 2012). Radiometer measurements were taken in order to calculate the photolysis rate of Br_2.

5.2. Global ozone monitoring experiment 2 – GOME-2

The GOME-2 instrument (second Global Ozone Monitoring Experiment) is a nadir scanning spectrometer aboard the MetOp-A satellite (e. g. Callies *et al.*, 2000; Munro *et al.*, 2006). MetOp-A is the first of a series of three polar-orbiting satellites of identical design crossing the Equator at 09:30 local time. Its platform carries a set of instruments primarily used for operational meteorology. Most of the work presented in this thesis is based on data acquired by the Global Ozone Monitoring Experiment 2 (GOME-2) instrument.

5.2.1. Description of the GOME-2 instrument

The instrument is scanning in a whisk-broom scheme (scan direction perpendicular to flight direction) with a swath-width of 1920 km, as depicted in Figure 5.3, which allows an almost global coverage each day. Polar regions, however, are sampled several times a day. One *scan* is defined as the time interval needed for one complete sweep of the scan mirror from East to West and back.

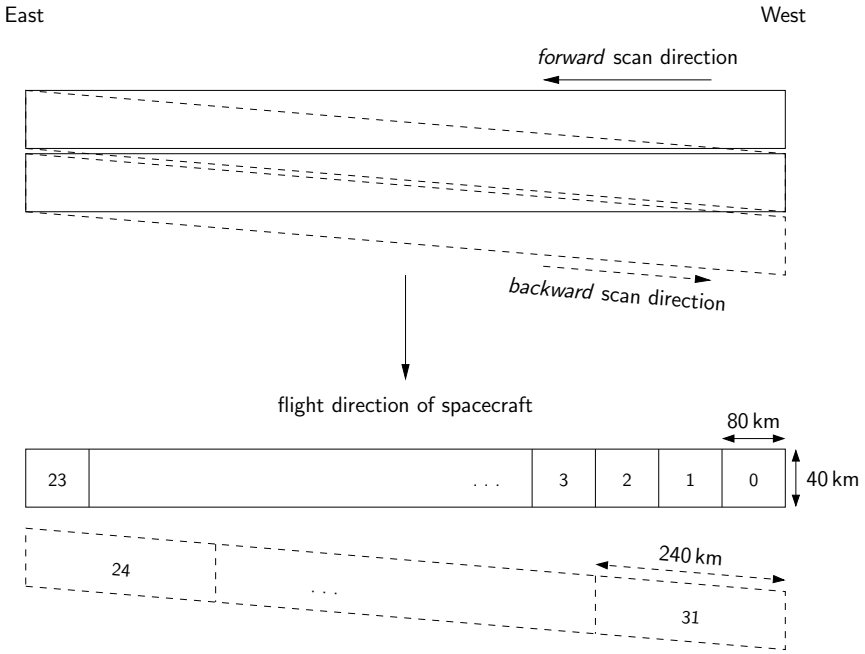

Figure 5.3.: *Default scan pattern of the GOME-2 instrument. The angular velocity of the scan mirror is three times slower during the forward scan (solid line) than in the backward scan (dashed line) resulting in different sizes of the respective ground-pixels (not to scale). Figure adapted from (EUMETSAT, 2011).*

As default for GOME-2, one scan takes 6 s consisting of a 4.5 s *forward* scan and 1.5 s *backward* scan at threefold speed (EUMETSAT, 2011). At an integration time of 187.5 ms per spectrum, the default sequence results in 24 and 8 measurements, also called *satellite pixels*, during the forward and backward scan, respectively. The corresponding widths of the ground-pixels are ∼80 km and ∼240 km. The minimum height of one GOME-2 pixel is approx. ∼40 km (sub-satellite) which increases towards the edges of the swath due to an increased distance to the surface at a constant opening angle of the instrument's aperture.

The GOME-2 spectrometer has four main channels operating in the UV/Vis spectral range between 240 and 790 nm (Figure 5.4). The spectral sampling of the main channels lays between 0.12 and 0.21 nm while the spectral resolution differs between to 0.26 and 0.51 nm FWHM. The reduced spectral resolution of GOME-2 is an improvement to the first GOME instrument. The GOME instrument featured a higher optical resolution producing malicious structures in the DOAS retrieval known as *undersampling* (Chance *et al.*, 2005).

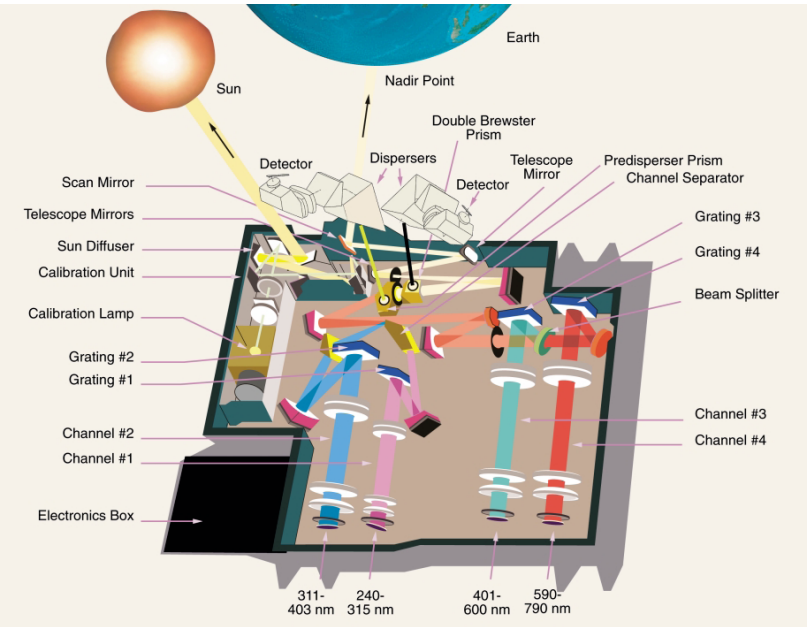

Figure 5.4.: *The optical layout of the GOME-2 instrument. Adapted from Callies* et al. *(2000).*

5.2.2. Rendering of maps from GOME-2 output

One of the advantages of satellite measurements is the possibility to map the column density of a certain trace gas, or any other scalar property, at global scale. However, the orientation and resolution of provided satellite data depends on the specification of the instrument as well as the orientation and orbit of the satellite. Hence, satellite image data, as for example obtained by the Advanced Very High Resolution

Radiometer (AVHRR) instrument, is typically inclined and distorted with respect to the Earth's coordinates. The transformation of satellite image-data into conformal coordinates is called *image registration*. Registered images are easier to be interpreted than the respective raw satellite data.

The GOME-2 instrument, however, does not provide image data in the first place, but spectra obtained over a certain fraction of the Earth's surface – i. e. one satellite pixel. Therefore, data based on the resolution of GOME-2 needs to be *rendered*, also denoted as *gridding*, to two-dimensional map-coordinates in order to be properly displayed. This section describes the algorithm applied to render this kind of satellite data.

Global cylindrical projection

The vertices of the satellite ground-pixel, which are given in geographical latitude φ and geographical longitude λ, need to be transformed into two dimensional, orthogonal coordinates (x, y) first. The *equidistant cylindrical* projection is very common to plot maps of the whole globe due to its simplicity:

$$x = \lambda \qquad \text{and} \qquad y = \varphi. \tag{5.1}$$

Both parallels and meridians are equidistant and parallel. This projection, however, is neither equal-area nor conformal (Pawlowicz, 2005). It is therefore not suitable to map the poles where the errors of the area are largest. Also, the distortions within augmented maps of regions at higher latitudes are disturbing.

Azimuthal equal-area projection

The *azimuthal equal-area* projection, sometimes also called *Lambert azimuthal equal-area*, provides a solution. The transformation equations are

$$x = k' \cos\varphi \sin(\lambda - \lambda_0) \tag{5.2}$$

$$y = k' \left[\cos\varphi_1 \sin\varphi - \sin\varphi_1 \cos\varphi \cos(\lambda - \lambda_0)\right] \tag{5.3}$$

with

$$k' = \sqrt{\frac{2}{1 + \sin\varphi_1 \sin\varphi + \cos\varphi_1 \cos\varphi \cos(\lambda - \lambda_0)}} \tag{5.4}$$

where φ_1 and λ_0 denote the standard parallel and the central longitude, respectively (Weisstein, 2000). This projection preserves the area of each satellite pixel and hence the relative information content all over the map. Even though this projections is not conformal, distortions of smaller regions are significantly reduced compared to the equidistant cylindrical projection.

Most maps in this thesis are centred around the North Pole with the Greenwich meridian pointing at the bottom. The parameters φ_1 and λ_0 in this special case are

90°N and 0°E, respectively. Equations (5.2) through (5.4) then simplify to

$$x = k' \cos\varphi \sin(\lambda) \tag{5.5}$$

$$y = -k' \sin\varphi_1 \cos\varphi \cos(\lambda) \tag{5.6}$$

$$k' = \sqrt{2/(1+\sin\varphi)}. \tag{5.7}$$

Spatial averaging of satellite-pixels

The outlines of the satellite pixels provided for any measurement (one spectrum) overlap for manifold reasons.

1. The outlines of pixels within one scan, as provided with the GOME-2 data, overlap.
2. Forward and backward scans overlap (Figure 5.4).
3. When averaging over a period longer than one orbit (101 min) one may encounter overlapping pixel. This is especially true at high latitudes where there are several overpasses each day.

Spatially averaging is therefore needed in order to map GOME-2 data. Here, the principle of averaging rastered pixels is presented.

Firstly, the outlines of all satellite pixels are projected into the maps (x, y)-coordinate system (see above). The two dimensional coordinate system is discretised on $m \times n$ nodes indexed (i, j). In order to be able to calculate a weighted mean later, the two intermediate $m \times n$-matrices $\mathbf{M}$ and $\widehat{\mathbf{M}}$ are defined to store the sum of elements and the sum of statistical weights, respectively.

For each measurement k, there is one scalar V_k to be averaged over the area defined by the four vertices A, B, C and D (Figure 5.5). For any satellite pixel k, the implemented algorithm provides a two dimensional discretised weight $\mathbf{P}_k = (p_{ij}(k))$. $\mathbf{M}$ and $\widehat{\mathbf{M}}$ can then be calculated by

$$\mathbf{M} = \sum_k \frac{\mathbf{P}_k V_k}{\hat{p}(k)} \tag{5.8}$$

$$\widehat{\mathbf{M}} = \sum_k \frac{\mathbf{P}_k}{\hat{p}(k)} \tag{5.9}$$

using the sum of all elements $p_{ij}(k)$

$$\hat{p}(k) = \sum_{i,j} p_{ij}(k) \tag{5.10}$$

in order to normalize the weight of each pixel in spite of its shape.

The matrix $\mathbf{N}$ representing the spatially weighted map is finally given by

$$\mathbf{N} = \frac{\mathbf{M}}{\widehat{\mathbf{M}}}. \tag{5.11}$$

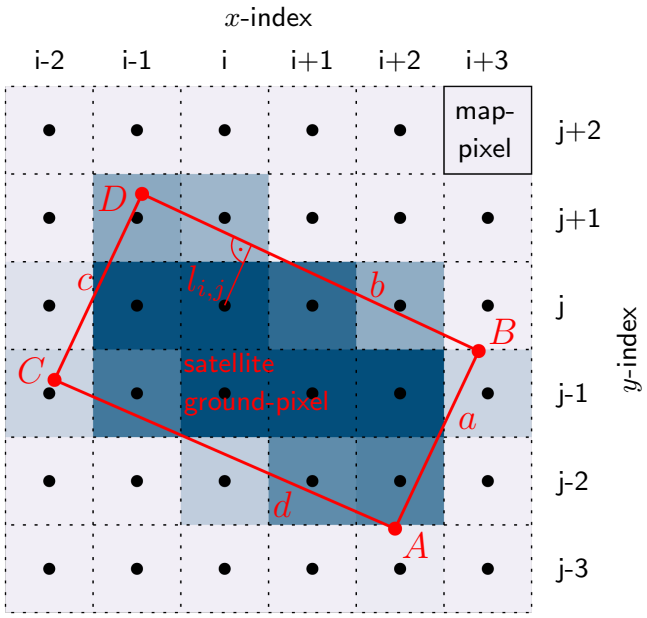

Figure 5.5.: *Rasterization of the statistical weight $p(k)$ (shades of blue) of one quadrangular satellite ground-pixel.*

5.2.3. Interpolation of external data to GOME-2 resolution

Data from sources other than GOME-2 are generally not provided in the resolution of GOME-2. Therefore, in order to merge external data with the BrO-VCDs derived in this work, spatial interpolation is required. The choice of the interpolation algorithm, however, depends on the temporal and spatial resolution of the external data source.

High spatial resolution, low temporal resolution

Data with a spatial resolution higher than the resolution of GOME-2 are, for example, topographic data and satellite imaging data like sea-ice concentration maps. For this type of data-set an algorithm has been implemented, which is similar to the spatial averaging of satellite maps described in the previous section.

Again, a two dimensional discrete weight $\mathbf{P}_k$ is calculated for each satellite pixel k, using the $m \times n$-resolution of the data matrix $\mathbf{R} = (r_{ij})$ to be interpolated. The interpolated value of $\mathbf{R}$ corresponding to the GOME-2 pixel k, r_k, is then given by

$$r_k = \sum_{i,j} \frac{p_{ij}(k)\, r_{ij}}{\hat{p}(k)}. \tag{5.12}$$

Poor spatial resolution

In the case of data with a spatial resolution lower than of GOME-2, like results from meteorological model simulations, it is sufficient to use *bilinear* interpolation. In this case, the GOME-2 pixel is represented by its center coordinates.

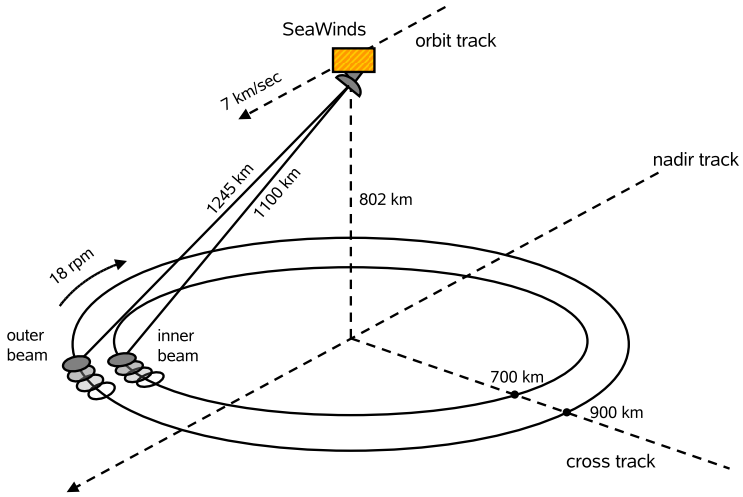

Figure 5.6.: *Measurement geometry of SeaWinds on QuickSCAT. Adapted from (Swan, 2011) based on (Spencer* et al.*, 2000).*

Meteorological data as provided by ECMWF is available at time steps of 6 h (section 7.3). In this case, it is possible to use *trilinear* interpolation to compute the corresponding value of a certain parameter using the time t_k at which the GOME-2 measurement k took place as a third parameter.

5.3. Additional satellite instruments

In addition to the GOME-2 instrument described in the previous section, data from further satellite instruments is utilized in this work. This section presents the details of the QuickSCAT instrument used to classify the sea-ice concentration into first-year and multi-year sea-ice (Section 5.3.1). Furthermore, the CALIPSO instrument providing information about the vertical distribution of aerosols and clouds is described (Section 5.3.2).

5.3.1. SeaWinds instrument on QuikSCAT

The QuikSCAT (Quik SCATterometer) satellite was launched by the NASA on 19 June 1999. Its scientific payload is the SeaWinds instrument mainly developed to measure the wind speed and direction over oceans (Graf *et al.*, 1998). The SeaWinds instrument transmits and receives microwave radiation at 13.4 GHz by means of a rotating parabolic dish antenna (Figure 5.6). The instrument rotates at a constant 18 revolutions per minute sending out two differently polarized beams at two different off-nadir angles. The outer beam is vertically polarized, resulting in a broader swath width of 1800 km, whereas the inner beam is horizontally polarized with a smaller swath width of 1400 km.

	CALIOP/CALIPSO	GOME-2/MetOp-A
footprint	70 m diameter	$80 \times 40\,\mathrm{km}^2$
swath-width	–	1920 km
equator crossing	13:30 LT	9:30 LT
flight altitude	705 km	817 km
orbital period	99 min	101 min
inclination	98.2°	98.7°

Table 5.1.: *Differences between the CALIOP and GOME-2 satellite instruments on CALIPSO and MetOp-A, respectively.*

The measurements of the microwave backscatter cross-section collected by SeaWinds may also be utilized to measure the distribution of sea-ice and the classification into first-year and multi-year sea-ice (Howell *et al.*, 2006, 2008; Kwok, 2004; Kwok *et al.*, 2006; Simpson *et al.*, 2007a; Walker *et al.*, 2006). Multi-year sea-ice exhibits a larger backscatter coefficient due to its larger grain size when compared to the younger first-year sea-ice. Gridded maps of the microwave backscatter coefficient were obtained from CERSAT (`http://cersat.ifremer.fr/`) at a resolution of $12.5\,\mathrm{km} \times 12.5\,\mathrm{km}$ and are compared to tropospheric BrO columns in Section 11.4.

5.3.2. CALIPSO optical cloud properties

Another interesting satellite instrument whose measurements are utilized in this thesis is the Cloud-Aerosol Lidar with Orthogonal Polarization (CALIOP) instrument carried by the Cloud-Aerosol Lidar and Infrared Pathfinder Satellite Observations (CALIPSO) satellite (NASA, 2006; Winker *et al.*, 2007). CALIOP is an active instrument measuring the time-resolved backscatter signal of a pulsed laser beam from which, among other parameters, the height and optical density of clouds may be derived independently from the surface albedo. Hence, CALIOP provides a sensitivity towards the vertical distribution of aerosols and clouds unique for satellite instruments. The trade-off, however, is a comparatively narrow foot-print of only 70 m corresponding to the width of the transmitted laser beam.

In this work, CALIPSO measurements are utilized at two occasions. Firstly, both the cloud optical density and layer top altitude retrieved from CALIPSO are used to validate the selectivity and to test the response of the surface sensitivity filter algorithm towards clouds over bright surfaces (Section 6.5.3). Secondly, cloud and aerosol optical densities measured over land and ocean are compared to the occurrences of significantly elevated BrO VCDs in the troposphere (Section 11.6).

The specification of the satellites MetOp-A and CALIPSO and the measuring principle of the respective GOME-2 and CALIOP instruments differ fundamentally (see Table 5.1). The most dominant difference is the footprint of each instrument. CALIOP samples a single 70 m wide cross-section of the atmosphere while GOME-2 averages over $3200\,\mathrm{km}^2$. CALIOP thus only probes 0.2% of the atmospheric volume within one GOME-2 pixel at most. A one-to-one comparison of GOME-2 and CALIOP measure-

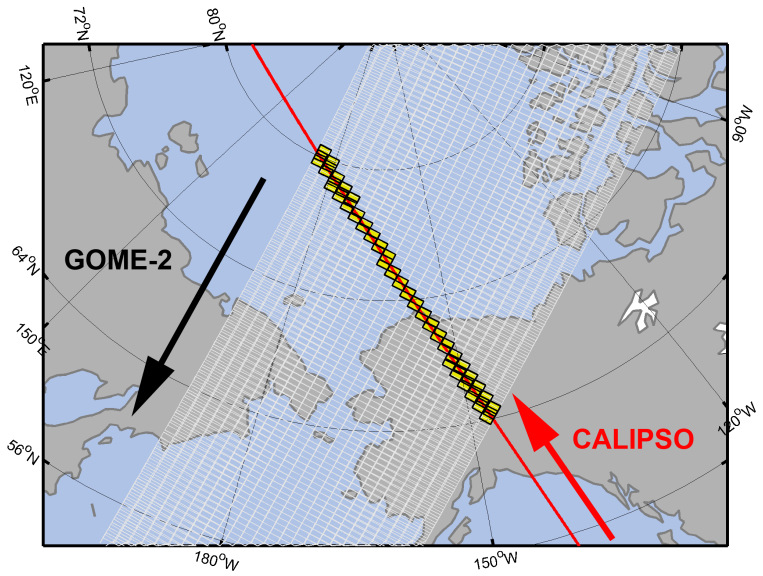

Figure 5.7.: *Overlapping swath of CALIPSO and GOME-2 measurements are indicted by the GOME-2 pixels highlighted in yellow for one orbit overpassing the Bering Strait on 1 April 2007.*

ments is therefore problematic but it is still possible to compare averages assuming the cloud properties CALIOP measures are to some extent representative for the whole GOME-2 pixel. Furthermore, CALIPSO flies on another orbit than MetOp-A. CALIPSO crosses the equator around 13:30 local time (LT) in ascending node while MetOp-A has an equator crossing time of 09:30 LT in descending node. In polar regions, however, the orbits of both satellites partly overlap (Figure 5.7). The time-difference between a CALIPSO and a MetOp-A overpass varies periodically and there are chances for almost simultaneous measurements.

6. Satellite retrieval for tropospheric BrO

The development of a new algorithm to retrieve tropospheric BrO column densities from GOME-2 measurements is one of the main achievements of this thesis. Unlike most previously published algorithms (cf. Chapter 3), it only uses GOME-2 measurements without external information from models or climatologies. This makes it particularly useful for statistical analyses as presented in Chapter 11 because it avoids systematic biases possibly induced from external data sources. The retrieved tropospheric BrO columns are compared to ground-based measurements in Chapter 9.[1]

This chapter begins with the motivation for the development of a new retrieval algorithm and a description of the main concept (Section 6.1). After that, the slant column densities (SCDs) of various trace-gases are retrieved from GOME-2 radiance measurements (Section 6.2) followed by a study on the sensitivity to stratospheric and tropospheric trace-gas species estimating possible error sources of the retrieval (Section 6.3). A combination of the retrieved SCDs is then utilized to separate tropospheric and stratospheric BrO SCDs (Section 6.4) and to assess the sensitivity to near-surface BrO concentrations (Section 6.5). The chapter closes with a discussion of the algorithm and sample results (Section 6.6).

6.1. Motivation and algorithm description

When analysing an existing satellite data set on BrO column densities for tropospheric BrO enhancements, one of the largest uncertainties comes from the variability of the stratospheric BrO column (Wagner & Platt, 1998; Wagner, 1999; Theys *et al.*, 2009b; Salawitch *et al.*, 2010; Choi *et al.*, 2011) which needs to be assessed in order to study BrO in the troposphere. When the tropopause lowers, the stratospheric air is adiabatically compressed and, hence, the stratospheric column of BrO increases additionally to an increase of the overall thickness of the stratosphere. Spatial structures mimicking tropospheric bromine events may thus appear in maps of the total BrO column. The challenge is to separate possible tropospheric events from stratospheric disturbances.

Several retrievals of tropospheric BrO columns use the output of stratospheric chemistry models for stratospheric BrO correction as summarized in Section 3.3 above (Theys *et al.*, 2009b; Begoin *et al.*, 2010; Salawitch *et al.*, 2010; Theys *et al.*, 2011; Toyota *et al.*, 2011; Choi *et al.*, 2011). These algorithms are either using simulated stratospheric columns of BrO directly or derive a parametrization of the stratospheric BrO column based on model results first and then apply a climatology from which

[1] Parts of this chapter have been accepted for publication in Sihler *et al.* (2012).

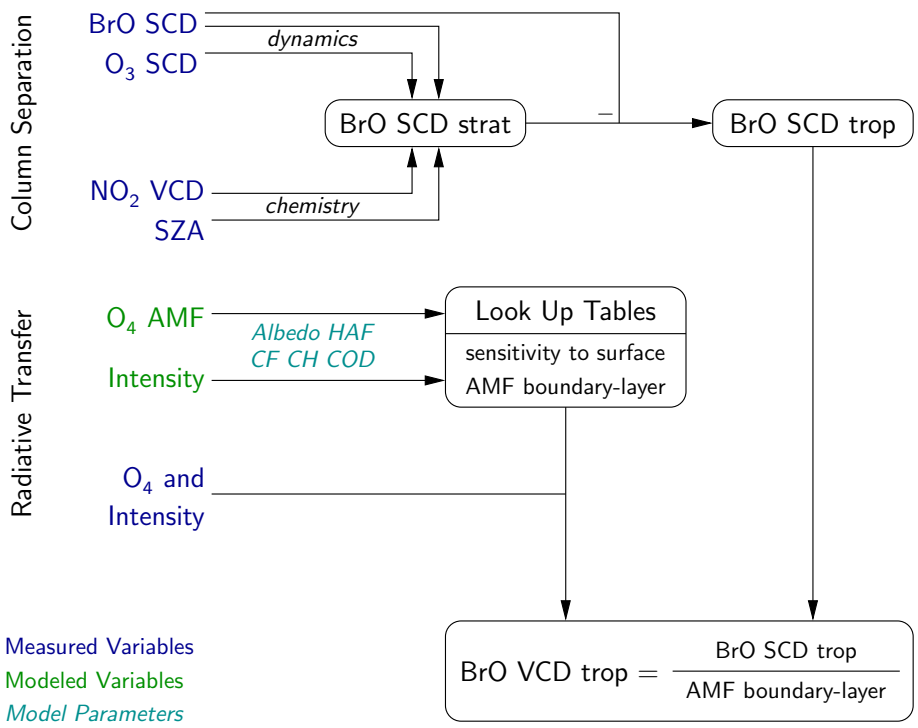

Figure 6.1.: *Retrieval scheme for tropospheric BrO VCDs in polar regions. The column separation algorithm utilizes the SCDs of O_3 and NO_2 as proxies for dynamics and chemistry, respectively, in order to calculate a residual tropospheric BrO VCD. Radiative transfer calculations are used to quantify the sensitivity towards BrO located close to the surface based on O_4 AMFs and intensity measurements. The radiative transfer parametrization for discrete observation geometries is stored in look up tables used to calculate the parametrization for any given observation geometry.*

the stratospheric BrO column is calculated using measured O_3 and NO_2 column data. However, chemistry models are potentially biased because the chemical mechanisms may be incomplete, and necessary parametrizations may result in systematic errors. Model results also depend on the choice of initial values which are usually difficult to obtain.

The retrieval proposed in this thesis overcomes these drawbacks by retrieving the parameters to estimate the stratospheric BrO column using only the measurements themselves. In the first stage of the retrieval, simultaneously retrieved O_3 and NO_2 column densities are used to account for dynamic and chemical effects, respectively (Figure 6.1). The algorithm contains the following four steps: First, the column measurements of BrO and O_3 are binned according to the respective NO_2 column, the solar zenith angle (SZA), and the line of sight (LOS) angle. In a second step, the measurements without a significantly enhanced BrO/O_3 column ratio are considered to calculate the mean stratospheric BrO/O_3 column ratio within each bin. Then, the stratospheric BrO column for each pixel is calculated using the measured O_3 and

NO_2 column densities, the SZA, and the LOS angle. Finally, the difference between measured total and calculated stratospheric column yields a residual BrO column.

During the second stage of the retrieval, an algorithm estimating the sensitivity of the satellite measurement towards BrO located in the boundary layer (BL) is developed (Figure 6.1). Hence, it is possible to study surface processes involved in bromine activation on a per-pixel basis. Parameters affecting this sensitivity are the surface albedo as well as the thickness and height of overlying clouds. In polar regions, the detection of clouds from satellites is particularly difficult for instruments measuring in the UV and visible spectral range due to ambiguities between cloud particles and the ice- or snow-covered underlying surface. Various studies to measure optical properties of clouds over ice in polar regions from space (e. g. Vasilkov *et al.*, 2010; O'Byrne *et al.*, 2010; Munneke & Reijmer, 2011) are based on data from a multitude of sensors and satellites. The ice-mode of FRESCO+ (Wang *et al.*, 2008) derives the surface height of an Lambertian reflector with monthly averaged climatological albedo value using O_2 absorption measurements. In this work, a slightly different approach is chosen: Individual reflectances are combined with the corresponding differential absorption of the $(O_2)_2$ collision complex (denoted O_4 in this work) in order to assure the sensitivity above a given threshold. The scale height of O_4 is approx. 4 km (Greenblatt *et al.*, 1990; Acarreta *et al.*, 2004) thus providing a better sensitivity to near-surface concentrations compared to O_2.

6.2. Calibration and evaluation of GOME-2 spectra

First of all, UV/vis spectra recorded by GOME-2 (Section 5.2) are evaluated using the DOAS technique (Chapter 4). This section presents the details of the spectral evaluation which is preceded by the spectral calibration of Band 2B of the GOME-2 instrument.

The spectral calibration determines the dispersion relation of the instrument. It assigns a wavelength to each spectral channel and furthermore determines the wavelength dependence of the instrument slit function. Both parameters are needed in order to calculate absorption cross-sections from high-resolution absorption cross-sections provided in the literature. The calibration is computed from a solar irradiance spectrum recorded on 15 August 2008 using the Kurucz solar flux atlas and a single O_3 reference cross-section (273 K) using the Windoas software (courtesy of M. van Roozendael and C. Fayt from IASB/BIRA) (Kurucz *et al.*, 1984; Gür *et al.*, 2005).

After obtaining the instrument calibration, the DOAS method (cf. Chapter 4) is applied in three different wavelength ranges to derive SCDs of BrO, O_3, O_4 and NO_2 from calibrated GOME-2 spectra. Table 6.1 summarizes the parameters and molecular absorption cross-sections applied in the DOAS evaluation.

For the retrieval of BrO SCDs, several modifications compared to previously published retrievals are applied to the settings of the DOAS fit. The wavelength range between 336 and 360 nm combines the standard wavelength ranges used for GOME (Wagner & Platt, 1998; Aliwell *et al.*, 2002) and SCIAMACHY (Afe *et al.*, 2004;

retrieved SCD	BrO and O_3	O_4	NO_2
GOME-2 band	2B	2B	4
channel	301–503	459–759	185–288
wavelength [nm]	336–360	355–390	431–453
O_3 (243 K)	Gür *et al.* (2005)	∗	–
O_3 (223 K)	Gür *et al.* (2005)	–	–
O_3 (221 K)	–	–	Burrows *et al.* (1998)
BrO (228 K)	Wilmouth *et al.* (1999)	–	–
O_4	Greenblatt *et al.* (1990)	∗	∗
NO_2 (220 K)	Vandaele *et al.* (1998)	∗	∗
OClO (293 K)	Bogumil *et al.* (2003)	–	–
SO_2 (273 K)	Bogumil *et al.* (2003)	–	–
H_2O (300 K)	–	–	Rothman *et al.* (1992)
CHOCHO	–	–	Volkamer *et al.* (2005)
Ring$\times\lambda^4$	yes	yes	no
Ring (norm)	yes	yes	yes
reciprocal	yes	yes	no
polynomial	4th order	3rd order	4th order

Table 6.1.: *Compilation of fit ranges, reference cross-sections and parameters of the three DOAS evaluations of calibrated radiance spectra measured by GOME-2. The slant column densities (SCDs) of BrO, O_3, O_4 and NO_2 are retrieved. The asterisk (∗) denotes that the reference in the column to the left is applied. The synthetic Ring spectra account for (wavelength-dependent) inelastic Raman scattering and the reciprocal intensity spectrum accounts for instrumental stray-light (see text). The fit-polynomial models broadband absorption.*

De Smedt *et al.*, 2004) and encompasses four absorption bands of the BrO molecule. Furthermore, formaldehyde (HCHO) was excluded from the spectral evaluation in order to reduce the noise level of the BrO retrieval. This approach is appropriate when only polar regions are taken into account where HCHO abundances are generally low. In addition to molecular absorption cross-sections, two spectra are included in the evaluation procedure to account for the wavelength dependent Ring effect (Grainger & Ring, 1962) following the suggestions of Wagner *et al.* (2009); both are calculated and normalized using the DOASIS software version 3.2 (Kraus, 2004). Furthermore, a reciprocal intensity spectrum is included in the fit in order to account for possible stray light within the instrument. A fourth-order polynomial is finally included to account for broad-band effects like surface reflection as well as Mie and Rayleigh scattering. Figure 6.2 shows a typical fit result obtained by DOASIS, which furnishes us with total SCDs of BrO S. As an example, total VCDs of BrO and O_3 measured on 25 March 2009 over the Arctic are plotted in Figures 6.4a and 6.4b, respectively.

Owing to the strong differential structure of ozone, the SCD of O_3 may also be derived from the same DOAS evaluation as BrO at much higher signal-to-noise ratio.

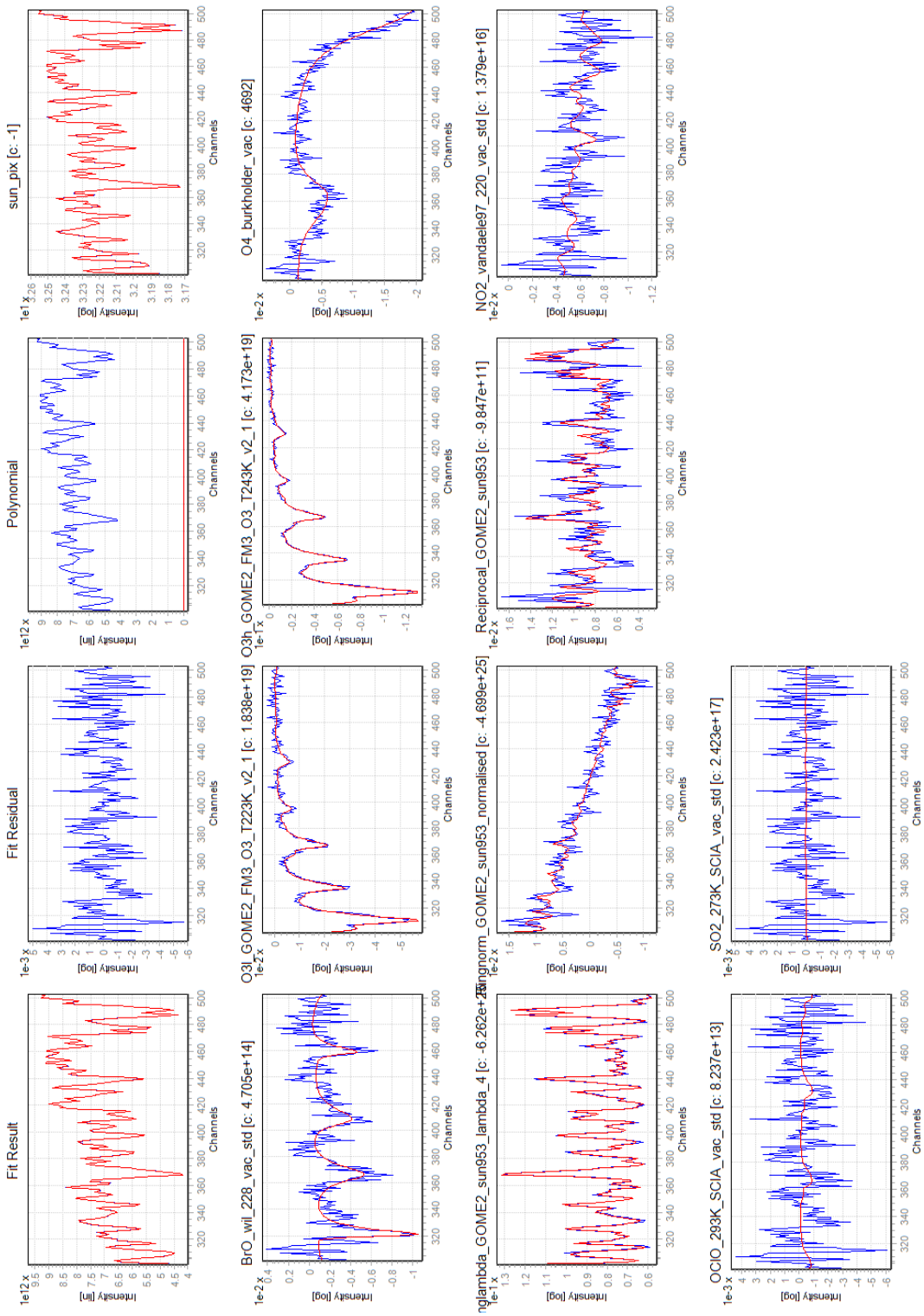

Figure 6.2.: *DOAS fit example of earth radiance spectrum recorded at 12:39:01 UTC on April 12, 2009. BrO and O_3 SCDs are evaluated in the wavelength range between 336 and 360 nm. The mean location of this measurement is 84°N and 5.8°E. The SZA and LOS angles are ϑ=75° and ψ=27°, respectively.*

The O_3-SCD is calculated as the sum of the fit results of both O_3 references corresponding to different temperatures. This approach of a retrieval for O_3 potentially leads to SCDs with a systematic error which, however, cancels out later during the parametrization of the stratospheric BrO-column (Section 6.4). O_3-VCDs computed from O_3-SCDs and the geometric AMF A_g (see definition (4.22) on page 46) are shown in Figure 6.4b for 25 March 2009.

Using radiances in another wavelength interval, the SCD of O_4 is retrieved in the range between 355 and 390 nm using the setting compiled in Table 6.1. This spectral range includes two absorption bands of O_4 at 360 nm and 380 nm. It was found during the calibration process, that by shifting the convolved O_4 cross-section by 2.4 channels towards longer wavelengths a more stable O_4 retrieval was achieved. A typical fit result yielding an O_4 SCD of $5.7\times10^{46}\,\mathrm{molec^2\,cm^{-5}}$ is shown in Figure 6.3.

Finally, the SCD of NO_2 is retrieved from radiances measured in Band 4 of the GOME-2 instrument in the range between 431 nm and 453 nm. In contrast to the previous two settings, a single Ring spectrum (also calculated using the DOASIS software) was found to be sufficient due to a weaker Raman signal at longer wavelengths in connection with the rather narrow fit range.

6.3. Sensitivity to stratospheric and near-surface absorbers

This section discusses some particular aspects of the radiative transfer (RT) in the polar atmosphere. For any measurement technique using scattered solar light, the RT through the different layers of the atmosphere determines the sensitivity towards these layers, respectively. Satellite measurements used in this thesis cover a large variety of atmospheric conditions (surface albedo, clouds, aerosols) and viewing geometries due to the global coverage of the instrument. In general, the properties of the atmosphere and the surface are not accessible directly from the measurement alone. It is therefore important to study influences of the parameters in order to assess possible errors arising from the assumptions made in order to calculate the air-mass factor (Section 4.5). The box air-mass factor $\hat{A}$ contains the sensitivity contribution of discrete atmospheric layers. Using the knowledge about $\hat{A}$ and the profile of an absorber, it is possible to calculate the AMF of this absorber using equation (4.26) on page 46.

Polar regions offer a rather special RT due to the high surface albedo. The probability that a photon reaching the satellite penetrated near-surface layers is increased. Hence, satellite measurements in the UV spectral range have an increased sensitivity to near-surface absorption processes. This effects generally outweighs the effect of a large optical thickness due to Rayleigh scattering at comparatively large SZAs in polar regions (Wagner, 1999).

Throughout the thesis, the radiances and AMFs are calculated using the McArctim software package (Deutschmann *et al.*, 2011). McArtim is a Monte Carlo RT model developed by Tim Deutschmann at the Institute of Environmental Physics in Heidelberg. It supports raytracing in spherical coordinates and the possibility to model cloud and aerosol particle distributions. The simulations presented in this section were performed at a wavelength of 360 nm corresponding to the evaluation wavelength range

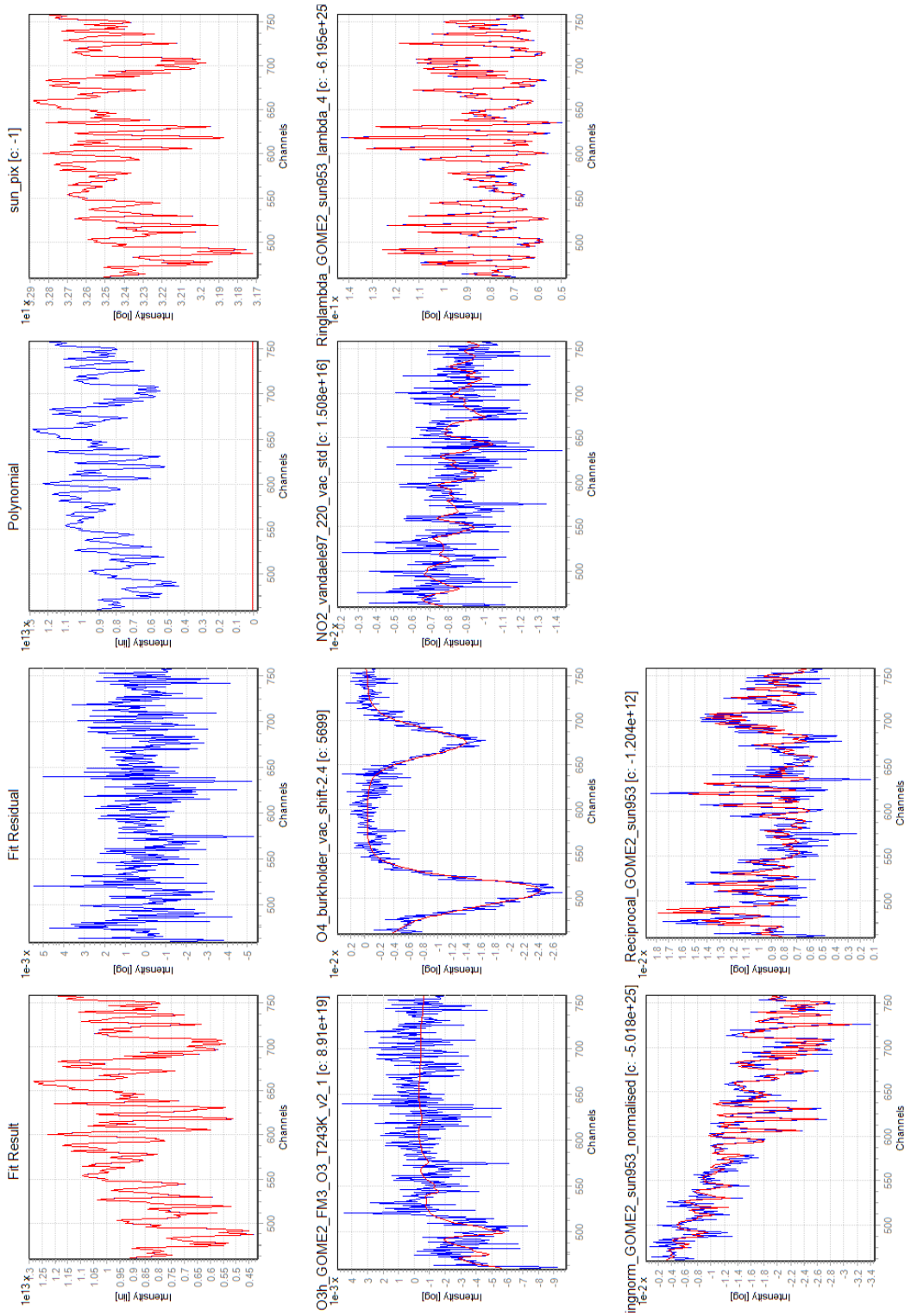

Figure 6.3.: *Same as Figure 6.2 but applying fit-settings for the retrieval of O_4 between 355 and 390 nm.*

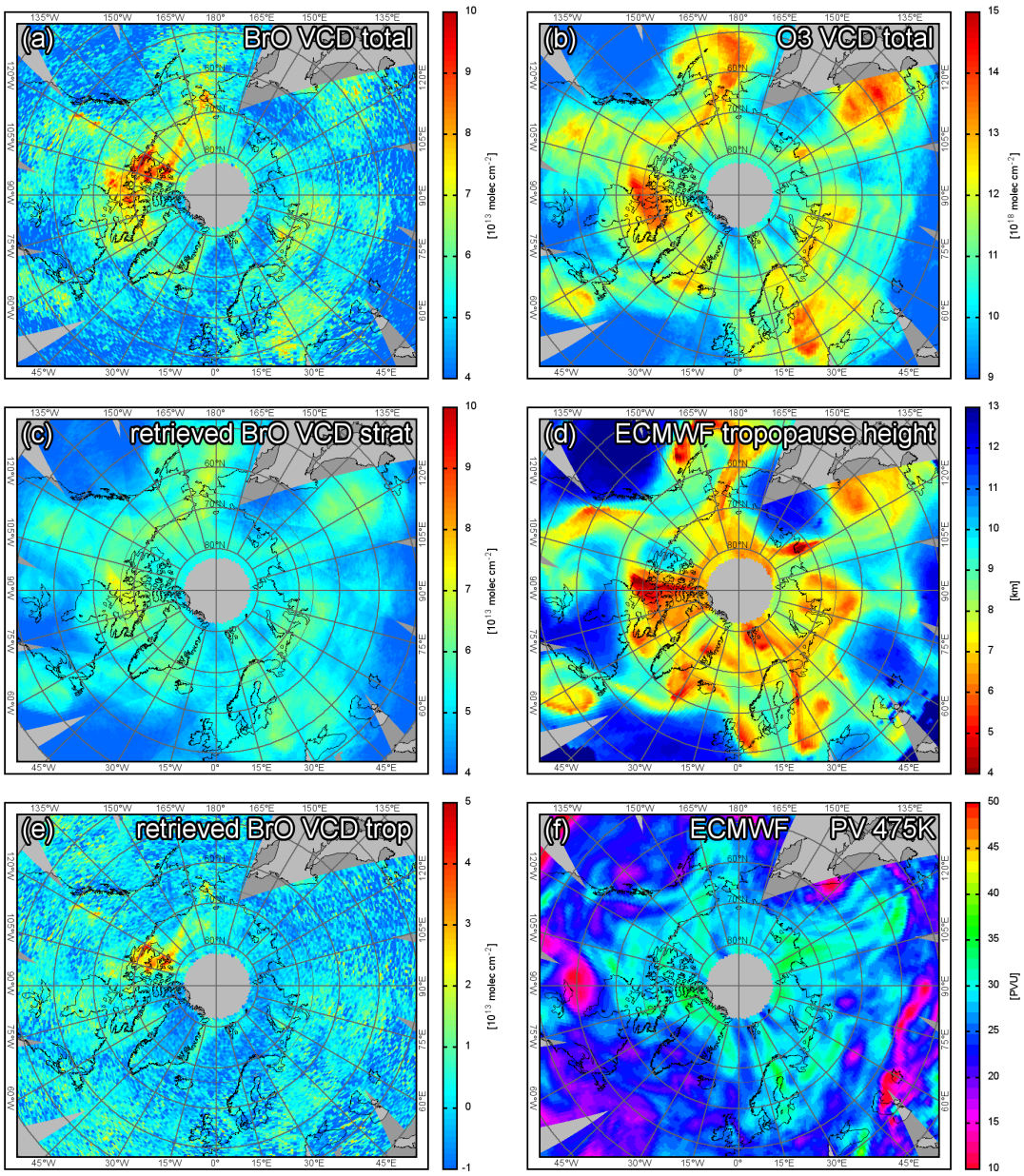

Figure 6.4.: *Illustration of the decomposition of the total BrO-VCD into stratospheric and tropospheric contribution for 25 March 2009. The top row shows VCDs of BrO (a) and O_3 (b) assuming a geometric AMF. Coinciding spatial structures of enhanced VCDs are visible e. g. over Eastern Europe and Northern Siberia, which are attributed to stratospheric dynamics and variations of the tropopause height (d). The BrO SCD_{strat} (c) is retrieved from measurements of BrO, O_3, and NO_2 alone. The BrO VCD_{trop} (e) is the difference between (a) and (c). The PV at the 475K isentrope (f) may be used to identify regions within the polar vortex (see Section 6.4.2). All VCDs are calculated using a geometric AMF, gray areas contain no data.*

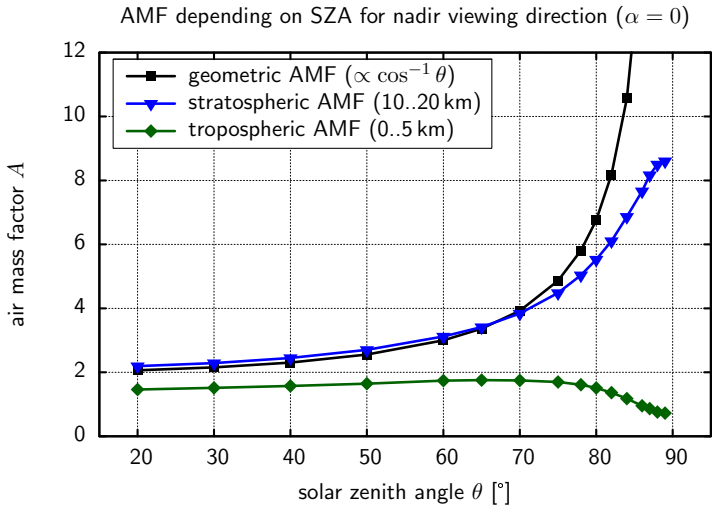

Figure 6.5.: *The dependence of different nadir air mass factors (AMFs) on the solar zenith angle (SZA) in the UV (λ =360 nm) calculated for a surface albedo of 0.1 and nadir geometry.*

of O_4 and BrO.

As an introduction, Figure 6.5 depicts the dependence of the AMF for different altitudes on the SZA for a surface albedo of 0.1. The geometric AMF is a fairly good approximation for the stratospheric AMF for SZAs smaller than 70°. The tropospheric AMF, assumed as a box profile between the surface and at 5 km altitude, depends less on the SZA than of the stratospheric AMF, assumed as a box profile between 10 and 20 km altitude. However, the tropospheric AMF decreases compared to the stratospheric AMF at SZAs larger than 75°. This drop of the relative sensitivity for near-surface layers also decreases the relative contribution of this layer to the measured slant column. Errors in the determination of the stratospheric partial column therefore induce a much higher relative error on the retrieved tropospheric partial column for high SZA.

The altitude dependence of $\hat{A}$ is illustrated in Figure 6.6 where twelve $\hat{A}$ for three different solar zenith angles and four different values for the surface albedo are shown. The sensitivity to absorbing trace-gases in high altitudes is obviously dominated by the SZA while the sensitivity to near-surface concentrations mainly depends on the surface albedo. It is furthermore noted, that the gradient of $\hat{A}$ at the surface is less depending on altitude over a bright surface than over a darker surface. $\hat{A}$ is almost constant at an SZA of 70° and a surface albedo of 0.9 . For these settings, the AMF is almost independent from the vertical distribution of the trace-gas.

RT specific to the new retrieval algorithm

Atmospheric BrO is located in both the stratosphere and troposphere Figure 3.2. The sensitivity towards stratospheric BrO is high for observations in polar regions. The

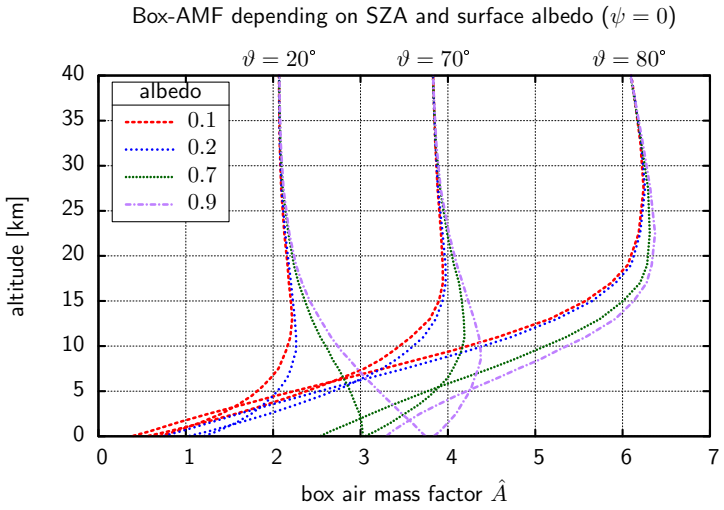

Figure 6.6.: *Altitude dependent box air-mass factor for three different solar zenith angles ϑ and four different surface albedo assuming a pure Rayleigh (clear-sky) atmosphere.*

retrieval presented in this chapter estimates the stratospheric BrO contribution in the SCD-space without applying a stratospheric AMF. The O_3 slant column density (SCD) is used in Section 6.4 as a proxy for stratospheric BrO without taking the different vertical profile into account. The error arising from this simplification is studied in Section 6.3.1.

The surface sensitivity algorithm presented in Section 6.5 utilizes absorption measurements of the O_2-O_2 collision dimer (abbreviated O_4). Different box-profiles are compared to the O_4 AMF in order to assess possible pitfalls when using this proxy (Section 6.3.2). Furthermore the effect of low clouds altering the sensitivity towards near-surface BrO is studied in Section 6.3.3. It is noted that the final implementation of the retrieval only includes measurements with an SZA below 80° while the presented calculations also include larger SZAs.

6.3.1. Sensitivity to stratospheric absorbers

A varying tropopause height influences the column density of stratospheric O_3 and BrO. The algorithm developed to separate stratospheric and tropospheric contributions of the measured BrO SCD utilizes the O_3 SCD as a tracer for stratospheric air. This approach requires that O_3 and stratospheric BrO have a similar AMF and, hence, a similar profile.

This sensitivity study applies profiles of O_3 and stratospheric BrO extracted from the output of 3D chemical transport simulations performed by Jöckel *et al.* (2010). The profiles for two different tropopause heights are depicted in Figure 3.2 on page 30. The profiles of O_3 and stratospheric BrO are used to calculate the AMF from modelled $\hat{A}$ depending on ϑ. The albedo is set to either 0.1 or 0.9.

The absolute AMFs as well as the BrO/O_3 AMF ratio are shown in Figure 6.7b. For

(a) *AMF depending on SZA (albedo 0.1)*

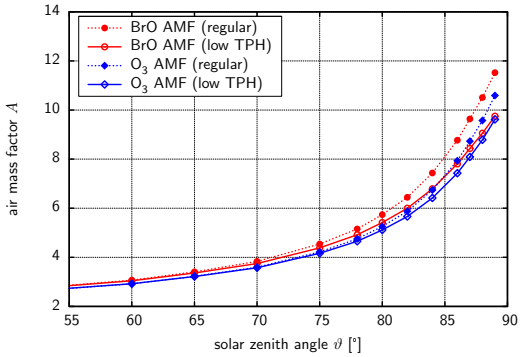

(b) *AMF ratio depending on SZA (albedo 0.1)*

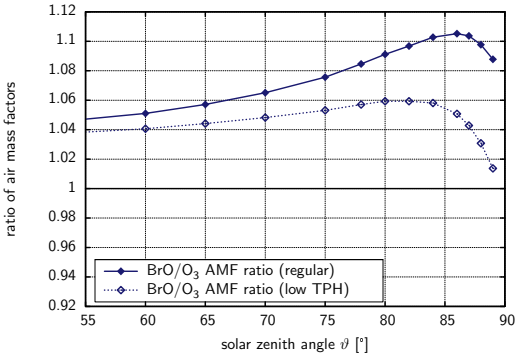

(c) *AMF depending on SZA (albedo 0.9)*

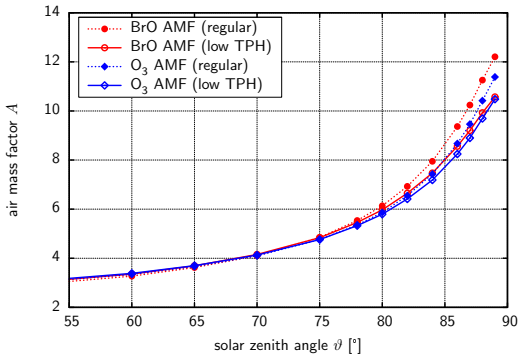

(d) *AMF ratio depending on SZA (albedo 0.9)*

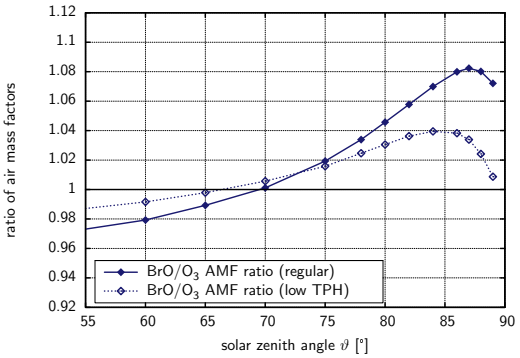

Figure 6.7.: *Stratospheric AMF for different absorber profiles depending on ϑ for two different albedo values and nadir geometry ψ=0. The BrO and O_3 profiles for the regular and low tropopause height (TPH) correspond to the profiles shown in Figure 3.2 on page 30.*

both albedos the different AMFs diverge with increasing ϑ. The difference between the BrO AMF and O_3 AMF reaches 10 % for a regular tropopause and over a dark surface, while reaching only about 5 % at ϑ=80° over a bright surface. These values decrease to 6 % and 4 %, respectively, for a lower tropopause.

As a result, the systematic error introduced by assuming the same AMF for both O_3 and BrO may reach 10 %. However, this value is an upper limit of the true error caused by this simplification. The separation algorithm described in Section 6.4 reduces these systematic errors to some extent. Measurements with different tropopause heights and surface albedos are averaged thus reducing the influence of a high tropopause. Furthermore, it is important to note that the difference between BrO and O_3 AMF decreases for a lower tropopause resulting in a smaller systematic error when the stratospheric contribution to the total BrO column is larger.

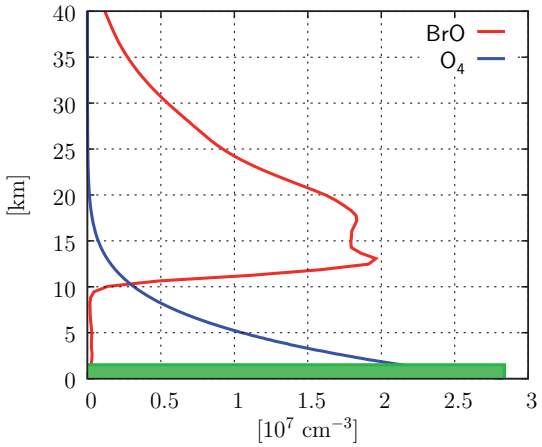

Figure 6.8.: *Concentration profile of stratospheric BrO as in Figure 3.2, relative profile of O_4. The green box corresponds to a mixing ratio of 1 pptv BrO within the lowest 1 km. However, maximum BrO concentrations (mixing ratios) can be up to 40 times lager.*

6.3.2. Sensitivity to near-surface absorbers

Ground-based measurements showed that most of the enhanced tropospheric BrO column is located within the boundary layer (BL) or at least near the surface. As described above, the sensitivity to near-surface absorbers is governed by the surface albedo. Fortunately, polar regions are covered by sea-ice and snow furnishing us with very bright surfaces with an albedo in the UV of up to 0.98 (Grenfell *et al.*, 1994). This allows us to gain a high sensitivity to BrO concentrations close to the surface. The determination of the albedo, however, is difficult because discrimination between a bright surface and thick clouds can be ambiguous.

In this work, radiance measurements in connection with absorption measurements of the $(O_2)_2$ oxygen collision complex are used to determine the sensitivity to near-surface layers (Wagner & Platt, 1998; Greenblatt *et al.*, 1990; Wagner *et al.*, 2002). The atmospheric concentration profile of $(O_2)_2$ is proportional to the square of the O_2 concentration exponentially decreasing with altitude. The profile of $(O_2)_2$ has a scale height of approx. 4 km (Figure 6.8) and depends only slightly on density changes due to pressure and temperature variations. In this thesis, $(O_2)_2$ is abbreviated with O_4 which must not be confused with the weakly bonded O_4 dimer which has negligible effects under the discussed atmospheric conditions (e.g. Yilmaz, 2012).

For the sensitivity filter algorithm presented in Section 6.5, a box-profile with a height of 500 m is assumed for the tropospheric BrO profile. This value represents a average value of previously observed scale heights compiled in Table 6.2.

Surface layer height

Differences over bright surfaces are much reduced compared to darker surfaces. For an albedo of 0.8 and ϑ=70°, the AMF difference between 0.1 and 5 km profile height is smaller than 10 % (Figure 6.9a) . The variations with ϑ are of the same order. It is

reference	height of surface layer	species	method
Anlauf *et al.* (1994)	50–400 m	O_3	ozonesonde
Solberg *et al.* (1966)	3000–4000 m	O_3	ozonesonde
Wessel *et al.* (1998)	500–1000 m	O_3	ozonesonde
Bottenheim *et al.* (2002)	100–1400 m	O_3	ozonesonde
Tarasick & Bottenheim (2002)	0–2000 m	O_3	ozonesonde
Hönninger & Platt (2002)	1000±500 m	BrO	MAX-DOAS
Hönninger *et al.* (2004)	∼1000 m	BrO	LP-/MAX-DOAS
Frieß *et al.* (2004)	1500 m	O_3	ozonesonde
Wagner *et al.* (2007)	≤1000 m	BrO	MAX-DOAS
Prados-Roman *et al.* (2010)	∼1000 m	BrO	AMAX-DOAS
Frieß *et al.* (2011)	∼500 m	BrO	MAX-DOAS
Seabrook *et al.* (2011)	200–600 m	O_3	O_3-DIAL

Table 6.2.: *Height of the chemically perturbed surface layer in polar spring from selected publications.*

noted, that 5 km is a rather pessimistic assumption compared to previously published scale heights (Table 6.2). A more realistic maximum layer height of 2 km leads to a relative error below 5 %.

Furthermore, the surface AMFs in Figure 6.9a decrease significantly between 70° and 80° with a minimum close to 90°. When compared to the stratospheric AMF for BrO in Figure 6.7, a threshold SZA of 80° for the retrieval of tropospheric BrO can be defined. Below this threshold, the stratospheric AMF is less than twice as high as the surface AMF. Above this threshold, the uncertainties of the stratospheric AMF are becoming large and the relative sensitivity for the troposphere decreases significantly.

The AMF for near-surface absorbers over a dark surface is always below 2 and depends only slightly on the SZA (Figure 6.9b). The AMF difference between different box profile heights exceed 50 %. These conditions need to be avoided in order to assure significant sensitivity.

Surface albedo

It is now clear that the surface AMF depends more strongly on the surface albedo than on the layer height. In Section 6.5, the O_4 AMF is used as a proxy for the surface AMF and it is therefore important to study the relationship between AMF O_4 and the surface AMF. Figure 6.10 displays the AMF for different surface heights and the O_4 AMF depending on the surface albedo for a constant ϑ=70°.

The AMF of O_4 is larger than for a box profile with a layer height of 5 km independent from the surface albedo. There is also a considerable spread among the AMF for different layer heights. However, all displayed AMFs converge towards 4.3 for an albedo close to 1. Differences between different layer heights decrease.

(a) *bright surface: albedo 0.8* (b) *dark surface: albedo 0.1*

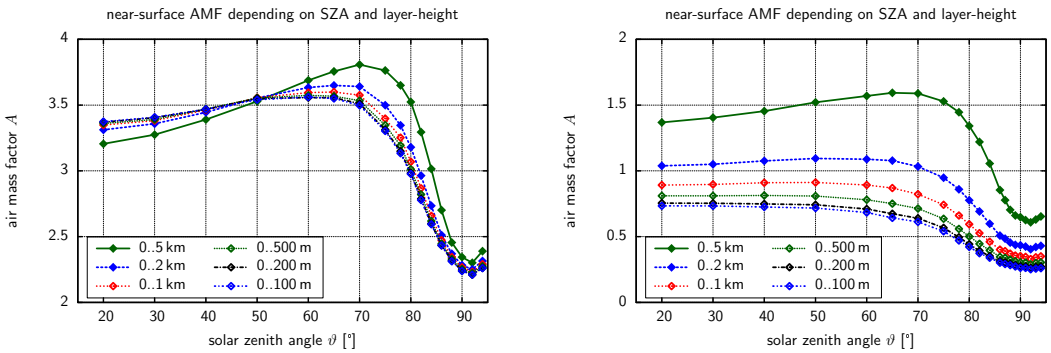

Figure 6.9.: *Near surface AMF depending on ϑ and the height of the box-profile for two different surface albedos: (a) albedo 0.8 and (b) albedo 0.1. Note the different ordinates.*

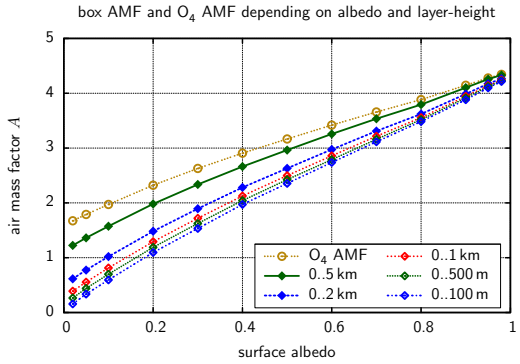

Figure 6.10.: *Surface AMF and O_4 AMF depending on the surface albedo at a constant SZA (ϑ=70°). There are no clouds/aerosols present (clear-sky).*

6.3.3. Influence of clouds and aerosols on the surface sensitivity

Until now, only clear-sky cases (i. e. without aerosols/cloud particles) were considered. The presence of clouds, however, severely alters the RT. For satellite measurements in the UV, clouds mostly perturb the sensitivity below and inside the cloud. Above the clouds, the sensitivity changes only slightly. The slight changes, however, will determine the accuracy of the sensitivity filter described in Section 6.5.

The introduction of clouds into the RT model increases the number of parameters which need to be determined: number of cloud/aerosol layers, cloud optical density, vertical cloud extent, horizontal cloud extend, single scattering albedo, and parametrization of scattering process. In this sensitivity study, however, only two parameter-combinations are selected for the sake of simplicity. Here, a single relatively low cloud layer between 1 and 2 km is considered. Low clouds are very difficult to detect from the O_4 absorption because most O_4 absorption takes place above the cloud.

(a) *OD 10, 1–2 km* (b) *OD 50, 1–2 km*

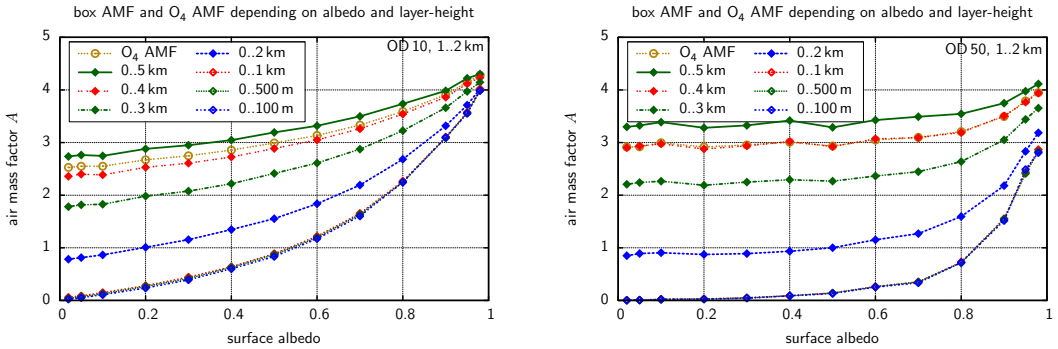

Figure 6.11.: *Surface AMF and O_4 AMF depending on the surface albedo. Same geometry and settings as Figure 6.10 but with clouds within a layer between 1 and 2 km altitude and an optical density (OD) of 10 and 50, respectively.*

Figure 6.11a shows the surface AMFs and the O_4 AMF calculated for a low cloud with an optical thickness of 10 and for different surface albedos. Compared to the clear-sky case, the variation between different layer heights are large. The box profiles below the cloud (100 m, 500 m, and 1 km box height) are almost identical. At an albedo of 0.8, the AMFs below the cloud are reduced by a factor of two. This AMF increase (or light path enhancement) below the cloud at larger albedos is caused by photons trapped between cloud and surface once they penetrated the cloud.

This effect is even more pronounced at an optically thicker cloud (OD=50, Figure 6.11b). Below an albedo of 0.6 all AMFs are almost constant. However, the O_4 AMF is still sensitive to the surface albedo above 0.6. Between an albedo of 0.6 and 0.9 the O_4 AMF increases by 15 % corresponding to an increase of the AMF below the cloud to 1.5. Hence, it is possible to derive an AMF for the lowest 100 m of 1.5 by assuring that the O_4 AMF is above 3.5 for this specific geometry. Certainly, this approach assumes the top of the clouds not to be lower than 2 km and the optical density of the cloud not to exceed 50.

In conclusion, thinner clouds are easier to detect above dark surfaces than thicker clouds. Furthermore, the surface AMFs and the O_4 AMF show a better correlation for higher clouds shielding a larger fraction of the O_4 column underneath.

6.4. Separation of tropospheric and stratospheric BrO slant-columns

This section describes how the measured total SCD of BrO is separated into background stratospheric and residual tropospheric slant column density S_{strat} and S_{trop}, respectively.

$$S = S_{\text{strat}} + S_{\text{trop}} \tag{6.1}$$

Furthermore, the standard deviation of the measurement σ_0 of BrO is estimated. This allows to evaluate the significance of a possible tropospheric signal. For the sake of clarity, SCDs S and VCDs V without subscripted chemical formula denote BrO column densities throughout this chapter.

6.4.1. Concept of the BrO column separation

The main task of the BrO column separation is to compute the SCD of BrO contained in the stratosphere, S_{strat}. O_3 is chosen as a tracer for the stratospheric partial column. The ratio z_0 of the stratospheric BrO SCD to the O_3 SCD, S_{strat,O_3} is defined as

$$z_0 := \frac{S_{\text{strat}}}{S_{\text{strat},O_3}} \tag{6.2}$$

Knowing z_0 and S_{strat,O_3} would allow us to compute the SCD of BrO directly:

$$S_{\text{strat}} = S_{\text{strat},O_3} \cdot z_0. \tag{6.3}$$

However, measurement data obtained by GOME-2 furnishes us only with a set of values of the ratio z between the total BrO-SCD S and of the total O_3-SCD S_{O_3} in the stratosphere and troposphere combined:

$$z := \frac{S}{S_{O_3}}. \tag{6.4}$$

Since almost the entire O_3 column is located in the stratosphere, z becomes

$$z := \frac{S}{S_{O_3}} = \frac{S_{\text{strat}} + S_{\text{trop}}}{S_{\text{strat},O_3}} =: z_0 + z', \tag{6.5}$$

where z' is defined as the ratio between S_{trop} and S_{strat,O_3}. In addition, measurement errors are included in z, which allows us to write

$$z = \bar{z}_0 + \zeta_{\sigma_0} + z', \tag{6.6}$$

where $\bar{z}_0$ is the mean of z_0 and ζ_{σ_0} is Gaussian distributed with zero mean and σ_0 standard deviation. The quantity z' can be interpreted as an error contribution due to elevated concentrations of BrO in the troposphere. The distribution of z' is unknown a priori. However, it leads to an overestimation of S_{strat}, if the simple mean $\bar{z}$ is used as an estimator for $\bar{z}_0$. The ratio z_0 in the stratosphere, (6.2), depends on different concentration profiles of BrO and O_3 and the corresponding stratospheric AMFs, but mainly on the stratospheric NO_2 chemistry.

The chemistry of the stratosphere leads to significant deviations between S_{strat} and S_{strat,O_3}. The partitioning of inorganic bromine species $Br_y = \{BrO + BrONO_2 + Br_2 + HOBr + HBr + \dots\}$ is not constant (Dorf *et al.*, 2006; Theys *et al.*, 2009b; Salawitch *et al.*, 2010). It turns out that the BrO/Br_y concentration ratio, which is typically of the order of 0.6 (see Figure 6.12), is primarily depending on the stratospheric NO_2

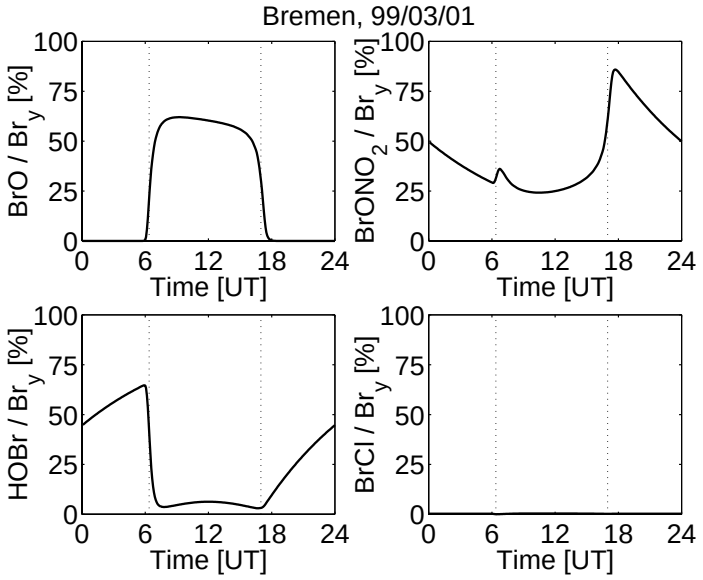

Figure 6.12.: *Diurnal cycle of the relative contribution of the most abundant bromine species BrO, $BrONO_2$, HBr, and BrCl in the lower stratosphere (480 K isentropic level, 58 hPa) as calculated by a photochemical model. This example for Bremen (53°N) for 1 March 1999 shows the typical bromine partitioning at midlatitudes. Adapted from Sinnhuber* et al. *(2002).*

concentration. This is due to the fact that NO_2 acts as a sink for stratospheric BrO producing bromine nitrate ($BrONO_2$)

$$BrO + NO_2 + M \longrightarrow BrONO_2 + M \tag{6.7}$$

which decreases the BrO concentration while leaving the concentration of Br_y unchanged. $BrONO_2$ is the second most abundant Br_y-species during daylight (e. g. Sinnhuber *et al.*, 2002; Atkinson *et al.*, 2007; Theys *et al.*, 2009b). The main loss mechanism of $BrONO_2$, however, its photolysis leading to a quasi stationary state between BrO and $BrONO_2$ depending on the NO_2 concentration and the actinic flux.

As a result, the ratio z_0 of BrO SCD to O_3 SCD in (6.2) decreases with increasing concentration of NO_2 also depending on the SZA ϑ determining the actinic flux. The concentration of NO_2 is not accessible from nadir measurements alone and therefore the NO_2 vertical column density V_N is used in the column separation process instead. Furthermore, our algorithm also accounts for a slight dependence of z_0 on the line-of-sight (LOS) angle ψ. The stratospheric BrO SCD S_{strat} is therefore mainly a function of ϑ, V_N, and ψ:

$$S_{strat}(\vartheta, V_N, \psi) = S_{strat,O_3} \cdot \bar{z}_0(\vartheta, V_N, \psi). \tag{6.8}$$

Although the stratospheric AMFs of BrO and O_3 are similar, (6.8) can, in addition, also compensate differences of both AMFs since $\bar{z}_0$ depends also on ϑ and ψ. Unfortunately, however, the assumptions made so far are not applicable to the chemistry

inside the polar vortex and during ozone-hole conditions. Extremely cold temperatures alter the chemistry of the stratosphere rendering reaction (6.7) insufficient to describe the chemistry affecting BrO. Moreover, there can be massive chemical loss of stratospheric O_3 thus S_{strat,O_3} can no longer be used to account for dynamical effects. Therefore, our algorithm in its present form is inapplicable for an estimation of the stratospheric BrO within the polar vortex occurring in springtime Antarctica in general and in some areas of the northern hemisphere during winters with low stratospheric temperatures as depicted in Figure 6.13.

Finally, in order to calculate S_{strat} as a function of ϑ, V_{N}, and ψ, $\bar{z}_0(\vartheta, V_{\mathrm{N}}, \psi)$ is computed from

$$z(\vartheta, V_{\mathrm{N}}, \psi) = \bar{z}_0(\vartheta, V_{\mathrm{N}}, \psi) + \zeta_{\sigma(\vartheta, V_{\mathrm{N}}, \psi)} + z'(\vartheta, V_{\mathrm{N}}, \psi). \tag{6.9}$$

The precise procedure how this is done is explained in the following subsection.

6.4.2. Implementation of the column separation algorithm

This section describes the implementation of the algorithm to calculate the tropospheric SCD of BrO. The algorithm is divided into four steps:

(I) normalization of the BrO SCDs,

(II) selection of reference measurements for one day and partitioning of reference measurements in the $(\vartheta, V_{\mathrm{N}})$-plane for five different ψ-ranges,

(III) calculation of a mean background stratospheric BrO/O_3-SCD ratio $\bar{z}_0$ in each partition after filtering significantly enhanced ratios, and

(IV) mapping of $\bar{z}_0(\vartheta, V_{\mathrm{N}}, \psi)$ on all observations and calculation of the stratospheric BrO SCD according to (6.8).

The statistical analysis to retrieve $\bar{z}_0$ requires a sufficiently large base population of measurements T_0. The analysis is performed separately for each day D. In order to increase the size of T_0 all measurements within a 7-day period $P = [D-3, D+3]$ are considered. This approach improves the statistical significance and reduces noise. It is similar to a running average filter and can be justified since the stratospheric chemistry usually only changes slightly within one week.

(I) Measured BrO SCDs are normalized to a VCD of $V_{\mathrm{norm}} = 3.5 \cdot 10^{13}\,\mathrm{molec\,cm^{-2}}$ within a reference sector over the Pacific Ocean as suggested by Richter *et al.* (2002). This normalization is performed for each pixel-number of one scan separately (GOME-2: 32 pixels per scan, pixel-numbers correspond to discrete LOS angles).The boundaries of the reference sector are ±10° latitude and 150° E to 100° W longitude. Pixels with a footprint significantly different from the nominal $\approx 80 \times 40\,\mathrm{km^2}$ (narrow-mode and backscan pixels) are excluded from counting as reference measurements. The normalized SCDs S are calculated by subtracting the median difference between SCDs in the reference sector and the normalized SCD $S_{\mathrm{norm}} = V_{\mathrm{norm}} \cdot A_{\mathrm{g}}$ from the measured SCDs.

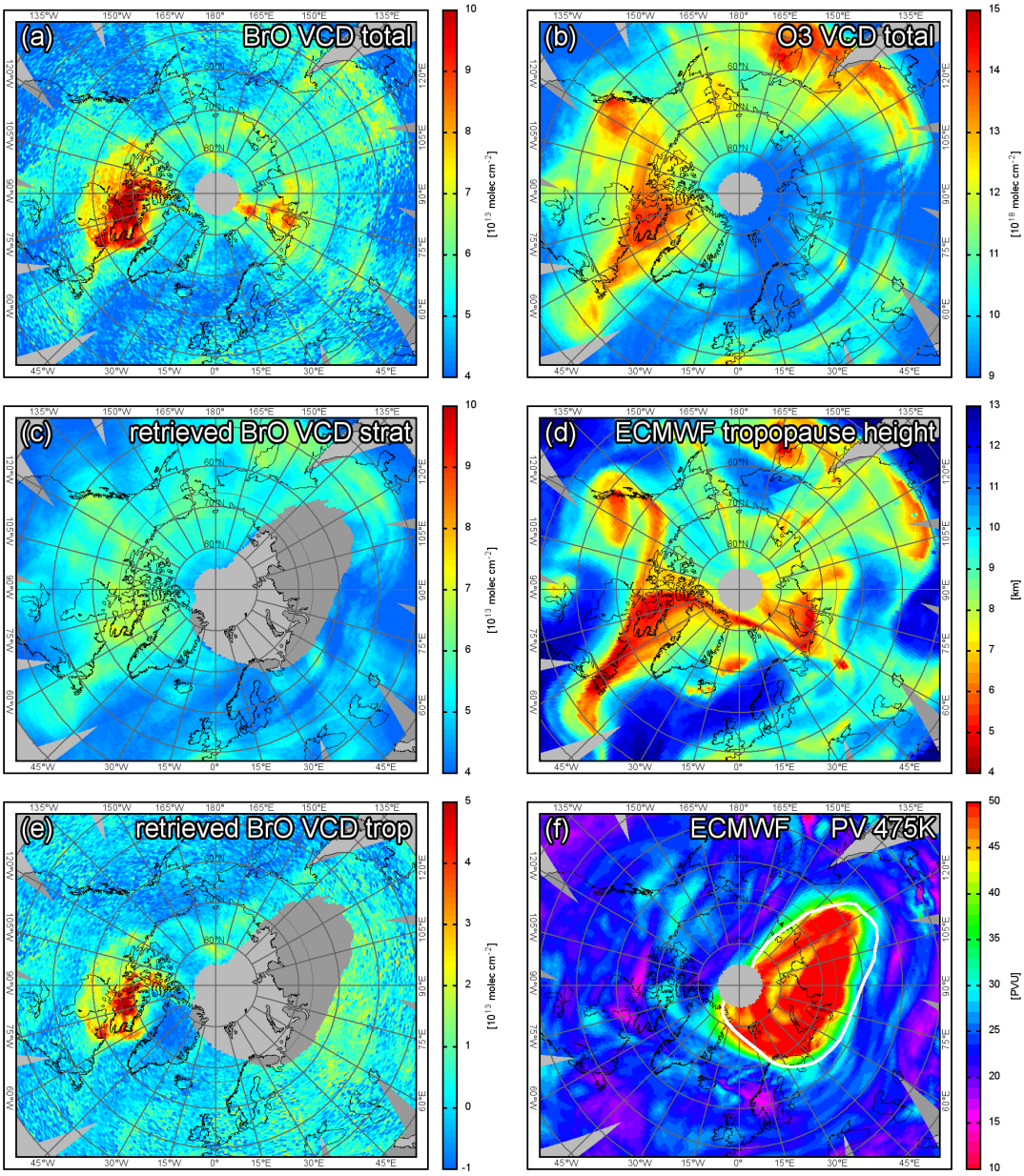

Figure 6.13.: *Same as in Figure 6.4, but for 1 April 2007. The white contour in (f) marks the 75 PVU-isoline at the 550 K isentrope. The decomposition into stratospheric and tropospheric column fails within the polar vortex, because there is no clear correlation between O_3-VCD and the tropopause height (d) any more*

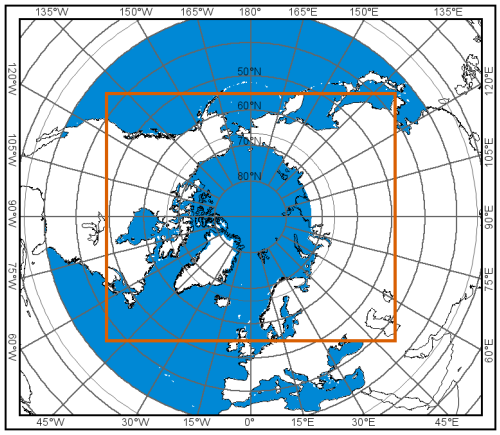

Figure 6.14.: *Map of the geographical area encompassing the reference measurements used to estimate the stratospheric BrO column highlighted in blue. The orange rectangle denotes the limits of the other maps in this chapter.*

(II) A subset $T \subset T_0$ of measurements is selected to avoid interferences with anthropogenic NO_2 emissions and to increase the accuracy of the stratospheric information in the nadir observations. T, from which the stratospheric correction is computed, contains only those observations with an SZA smaller than 80°, latitudes above 30° N, a fit-error for BrO smaller than $5 \cdot 10^{13}$ molec cm^{-2}, an O_4-SCD larger than $6.5 \cdot 10^{42}$ molec^2 cm^{-5}, a non-negative NO_2-VCD smaller than $8 \cdot 10^{15}$ molec cm^{-2} below 60° N. Narrow-mode and backscan pixels are excluded from T as well as potential measurements within the polar vortex, as for example depicted in Figure 6.13f. Areas inside the polar vortex are identified using information about the potential vorticity derived from meteorological model data (ECMWF operational analysis, regular 1°×1° grid with 91 hybrid pressure levels, 6 h time resolution, cf. Section 7.3). Columns exceeding a potential vorticity of 35 PVU at the 475 K isentrope surface or 75 PVU at 550 K are discarded from the further analysis. Furthermore, T does not contain any measurements with a ground elevation above 1000 m and no measurements over land masses at latitudes below 73° N. The latter selection rule accounts for areas with a strong anthropogenic NO_2 signal like Prudhoe Bay or Norilsk which would interfere with the algorithm. After applying these filters, the final subset T contains $N_\alpha \approx 10^5$ reference observations for each day from which the stratospheric BrO column is estimated. The geographical area encompassing T is illustrated in Figure 6.14.

(III) A mean stratospheric BrO/O_3 ratio $\bar{z}_0(\vartheta, V_N, \psi)$ is calculated from T. Obtaining an estimate of $\bar{z}_0$, (6.9), by measured values of $z_\alpha \in T$ with coordinates $(\vartheta_\alpha, V_{N\alpha}, \psi_\alpha)$, $\alpha = 1, \ldots, N_\alpha$, containing an arbitrary error with a Gaussian and a positive unknown contribution, requires a technique of approximating a function on an unstructured set of points where the data to be approximated contains uncertainties. Traditionally, least-squares approximations (Quarteroni *et al.*, 2002) are used to approximate scattered data. More elaborate methods use radial basis functions or Kriging (Press *et al.*, 2002) in order to treat scattered data. Common to these methods is that some knowledge about the distribution, such as the variance, is necessary

in order to compute an approximant. In addition, they are relatively costly, given that the number of measured values N_α is large ($\approx 10^5$), making it necessary to have an efficient method to process a large number of these data sets.

For the method proposed in the present discussion, the fact that the function $\bar{z}_0(\vartheta, V_\mathrm{N}, \psi)$ depends only slowly on ϑ, V_N, and ψ is utilized. In addition, trilinear interpolation is used in order to avoid spurious oscillations which can occur when using polynomials of higher degree. Since $\bar{z}_0$ depends only slowly on ϑ, V_N, and ψ, the points at which z is given are regrouped in subsets for which $\bar{z}_0$ is almost constant. For a domain $\Omega = [\vartheta_a, \vartheta_b] \times [V_{\mathrm{N}a}, V_{\mathrm{N}b}] \times [\psi_a, \psi_b]$, this boils down to finding a partition Ω_β, $\beta = 1, \ldots, N_\beta$ of Ω, such that Ω_β contains enough points to allow for statistics on z_α for which $(\vartheta_\alpha, V_{\mathrm{N}\alpha}, \psi_\alpha) \in \Omega_\beta$. On the other hand Ω_β should be small enough, such that $\bar{z}_0$ does not vary too much with respect to ϑ, V_N, and ψ in Ω_β. It is clear that such a partition is not unique and that the shape of the subsets Ω_β might influence the accuracy of the present method.

Computing of a 2D partition Ω

This section describes the partitioning of Ω, allowing a trilinear reconstruction of $\bar{z}_0(\vartheta, V_\mathrm{N}, \psi)$.

A partition Ω_β of $\Omega = [\vartheta_a, \vartheta_b] \times [V_{\mathrm{N}a}, V_{\mathrm{N}b}] \times [\psi_a, \psi_b]$ is computed as follows. First of all, all previously selected reference measurements T are divided in the ψ-direction into N_ψ bins defined by the limits ψ_k with $k = 1, \ldots, N_\psi - 1$ in order to separate the weak ψ-dependence from the following algorithm (Figure 6.15). In the ϑ and V_N-direction, however, a partitioning algorithm accounting for non-uniform distributions is required. Partitions all containing a similar number of observations is desirable in order to achieve a homogeneous statistics of the asymmetry filter applied on every partition separately.

The two dimensional partitioning algorithm applied on each ψ-bin is based on a partition of Ω which can be indexed by two indices i, j for the ϑ and V_N-direction, respectively:

$$\Omega_\beta = \Omega_{i,j}. \tag{6.10}$$

The necessary steps are explained by means of a concrete example.

In order to sample the $\bar{z}$-surface in the two dimensions of the $(\vartheta, V_\mathrm{N})$-plane, T is subdivided into N_ϑ times N_V partitions $\Omega_{i,j} \subset \Omega$ with $i = 1, \ldots, N_\vartheta$ and $j = 1, \ldots, N_V$, respectively. The partitioning is performed on the two-dimensional domain Ω

$$\Omega = [25°, 80°] \times [0, 8 \cdot 10^{15}\,\mathrm{molec\,cm^{-2}}] \tag{6.11}$$

encompassing the SZA interval between 25° and 80° and the NO_2-VCD interval between 0 and $8 \cdot 10^{15}\,\mathrm{molec\,cm^{-2}}$, respectively. The partitioning is first initialized and then iteratively optimized until each partition contains an almost equally large subset of T.

The partitioning of Ω is initialized in two steps. Figure 6.16 shows an example of this procedure performed on Ω for 25 March 2009. (1) T is divided into N_ϑ preliminary partitions along the ϑ-axis each containing an equal number of observations except

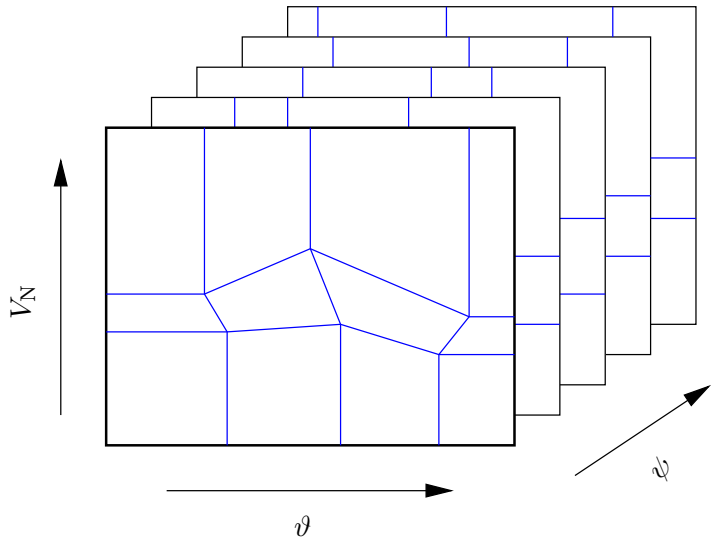

Figure 6.15.: *Partitioning Ω in three dimensions ϑ, V_N, and ψ. The partitions in the (ϑ,V_N)-plane (blue) are calculated for all five ψ subspaces separately.*

the last two columns ($i = N_\vartheta - 1, N_\vartheta$) whose size is weighted by two in order to allow for a higher density of bins at this edge of the domain (cf. Figure 6.17). The borders between the partitions are denoted h_i ($i = 1, \ldots, N_\vartheta - 1$) in Figure 6.16. (2) Subsequently, the preliminary partitioning nodes defining the boundaries of each partition in V_N-direction are calculated. For each $i = 1, \ldots, N_\vartheta - 1$, a set union T_i

$$T_i = \bigcup_{j=1}^{N_V} T_{i,j} \bigcup_{j=1}^{N_V} T_{i+1,j} \tag{6.12}$$

is constructed containing all observations in the column left and right of the respective h_i. Each T_i is then divided into N_V partitions in V_N-direction defining the (ϑ, V_N)-coordinates of the preliminary partitioning nodes. This time, however, the first and last partition (top and bottom row) contain only half as many observation compared to the six partitions in between. The modification to the basic scheme of partitions containing an equal number of measurements prevents the outer partitions from becoming too large on the cost of retrieval noise. Finally, this procedure leads to a total of $\vartheta \times N_V$ initial partitioning nodes defining the boundaries of the partitions as depicted in Figure 6.16.

After computing the initial coordinates of the partitioning nodes, the coordinates of the nodes are iteratively fine-tuned until all partitions contain an almost equal number of measurements. The fine-tuning is first performed for the node in the bottom left of Figure 6.16 and then consecutively followed by the nodes to the right and then line-by-line upward. The fine-tuning is implemented as follows: It is tested how the variance of the number of measurements in the adjacent partitions behaves when the position of the actual boundary slightly changes. The node is consecutively displaced horizontally by $\pm\Delta\vartheta$ and vertically by $\pm\Delta V_N$. If the variance at one of the four positions is smaller

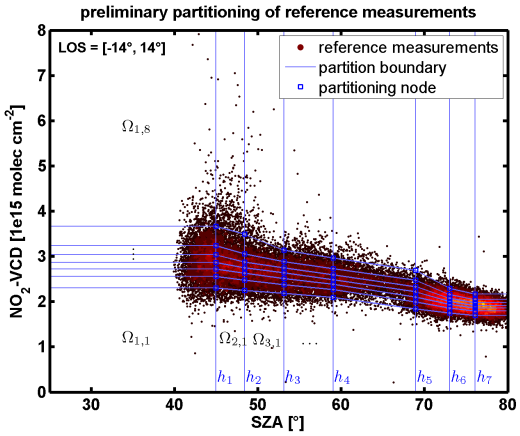

Figure 6.16.: *Preliminary partitioning ($N_\vartheta, N_V = 8$) of reference measurements (color-coded density) for the near-nadir direction ($|\psi| \leq 14°$) whose final partitioning is shown in Figure 6.18.*

than at the old position, the new position with the minimum variance is chosen as the new position and the procedure is repeated in the neighbourhood of the new position. The fine-tuning of each node is repeated up to five times before moving on to the next node. $\Delta\vartheta$ and ΔV_N depend on the minimum distance to neighbouring nodes in the respective direction and decrease in each iteration.

In order to finalize the partitioning algorithm, the number of measurements in all partitions is computed after all nodes have been fine-tuned separately. The fine-tuning algorithm is terminated when the number variation is less than 20 % (the first and last row of partitions $T_{i,j}$ for $i = V_\vartheta$ and $j = 1, V_N$ are treated differently as described above). Otherwise the fine-tuning is repeated for all nodes until the 20 %-criterion is reached. Usually, the algorithm converges after 5 repetitions or less. Figure 6.18 illustrates the final partitioning of Ω. Numerical inspection revealed that a value of $N_\vartheta = 5$ and $N_\vartheta = N_V = 8$ lead to sufficiently accurate results. The limits of the bins in ψ-direction are fixed to $\pm 14°$ and $\pm\ 34°$, respectively (Figure 6.15). Furthermore, the partitioning algorithm is benchmarked for different N_α in Section 6.4.3 below.

Asymmetry filter to separate the stratospheric mode

For each partition Ω_β, a filter algorithm is applied as presented in the following. The filter algorithm is based on the assumption that an ensemble of z, (6.9), is normally distributed around $\bar{z}_0$. Significant outliers, if any, are mostly due to enhancements of the tropospheric BrO column and to a lesser degree, due to a partially depleted O_3 column. Both effects lead to an increase of a particular z by z' in (6.9), which in turn leads to an increasing asymmetry of the otherwise symmetric normal distributed z (Figure 6.19). The asymmetry a_β of the distribution of $z = z(\Omega_\beta)$ in partition Ω_β is defined as

$$a_\beta(z) = \frac{\bar{z} - \tilde{z}}{\sigma}, \tag{6.13}$$

(a) *equally sized partitions* (b) *weighted partition size*

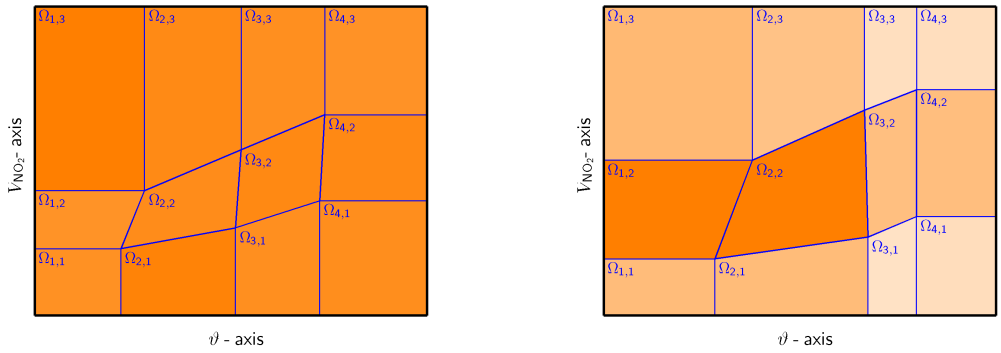

Figure 6.17.: *Illustration of two different schemes of partition sizing indicated by the color saturation: in (a) every partition contains an almost equal number of points whereas the partitioning in (b) required a varying number of points in each partition (N=1200, N_θ=4, N_V=3). The number of points in the top and bottom row as well as in the two most right columns contain half as many points. As a result, the partition in the right corners contain only one quarter of the points (indicated by light orange) than the partitions in the left center ($\Omega_{1,2}$ and $\Omega_{2,2}$, dark orange). The colouring and partition limits in (b) correspond to the numbers given in Figure 6.22d.*

where $\bar{z}$ denotes the mean, $\tilde{z}$ the median, σ the standard deviation of z. If a_β is larger than a threshold, i.e. the distribution is skewed towards higher BrO/O_3 SCD ratios, a subset of z accounting for the stratosphere needs to be calculated before $\bar{z}$ and σ can be used as estimators for $\bar{z}_0$ and the standard deviation σ_0 of z_0, respectively.

A filter algorithm is designed to find a subset of z with a symmetric distribution identified as the *stratospheric mode* (Figure 6.19). The asymmetry of the distribution of z is iteratively minimized by cropping values with an offset $\Delta z = |z - \bar{z}|$ larger than a given threshold δz. In step k of the iteration, the asymmetry a_k of the distribution of

$$z_k = \{z | -\delta z_k < z - \bar{z}_{k-1} < \delta z_k\} \tag{6.14}$$

is calculated with $\bar{z}_{k-1}$ denoting the mean of the distribution in the previous step. Starting with $\delta z_0 = \max(z) - \bar{z}$, the threshold δz_k is iteratively decreased until $a_k \leq 0.001$ or a maximum of $k = 20$ steps is reached (see green bars in Figure 6.19). The minimal asymmetry calculated from this algorithm is limited by numerical accuracy and the termination condition of 0.001 was found to provide still a reasonable small residual asymmetry of the output. The result is a filtered mean $\bar{z}_\beta = \bar{z}_k$. The standard deviation σ_β, however, is not calculated based on the cropped distribution of z_k. This approach would lead to an underestimation of the true standard deviation because the cropped distribution (green bars in Figure 6.19) has a larger kurtosis than the

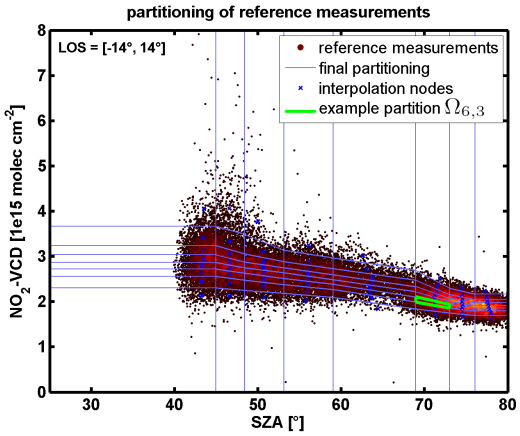

Figure 6.18.: *Partitioning of reference measurements (color-coded density) in the* $(\vartheta, V_{\mathrm{N}})$*-plane for the near-nadir direction* ($|\psi| \leq 14°$) *for 25 March 2009. Each partition contains an almost equal number of measurements from which BrO/O*$_3$ *SCD ratios are retrieved. The example partition* $\Omega_{6,3}$ *is depicted in Figure 6.19. The mean of measurements within each partition (blue crosses) are used as nodes for interpolating the results (Figure 6.20).*

normal distribution. Therefore, it is computed only using measurements with $z_m < \bar{z}_\beta$

$$\sigma_\beta = \sqrt{\frac{1}{n-1} \sum_m \left(z_m - \bar{z}_k\right)^2} \tag{6.15}$$

because this selection is assumed not to include any measurements with a significant tropospheric signal. See Section 6.4.3 below for a benchmark test applying the presented filter algorithm on simulated distributions for different N_β.

(IV) The above computed values $\bar{z}_\beta$ and σ_β are mapped to the center of gravity of the points $(\vartheta_\alpha, V_{\mathrm{N}\alpha}, \psi_\alpha)$ in Ω_β and used for trilinear interpolation, which furnishes us two functions $\bar{z}_0(\vartheta, V_{\mathrm{N}}, \psi)$ and $\sigma_0(\vartheta, V_{\mathrm{N}}, \psi)$. Now the SCD of BrO in the stratosphere S_{strat} and its standard deviation, σ_{strat} can be computed by:

$$S_{\mathrm{strat}} = S_{\mathrm{strat,O_3}} \cdot \bar{z}_0(\vartheta, V_{\mathrm{N}}, \psi), \tag{6.16}$$

$$\sigma_{\mathrm{strat}} = S_{\mathrm{strat,O_3}} \cdot \sigma_0(\vartheta, V_{\mathrm{N}}, \psi). \tag{6.17}$$

As an example, Figures 6.4e and 6.13e illustrate the resulting tropospheric BrO VCD for 25 March 2009 and 1 April 2008, respectively. It is interesting to note that, as depicted in Figure 6.20a, the retrieved $\mathrm{BrO/O_3}$ SCD ratio increases markedly from $< 4.8{\cdot}10^{-6}$ to $> 5.5{\cdot}10^{-6}$ for $\mathrm{NO_2}$-VCDs below $2{\cdot}10^{15}$ molec cm^{-2} at high solar zenith angles. This observation confirms the predictions of the simple model for stratospheric chemistry mentioned above. Normally, $\mathrm{NO_2}$ is a sink for stratospheric BrO leading to an anti-correlation between BrO and $\mathrm{NO_2}$. Therefore, the abundance of BrO is enhanced with respect to $\mathrm{O_3}$ at low $\mathrm{NO_2}$ concentrations.

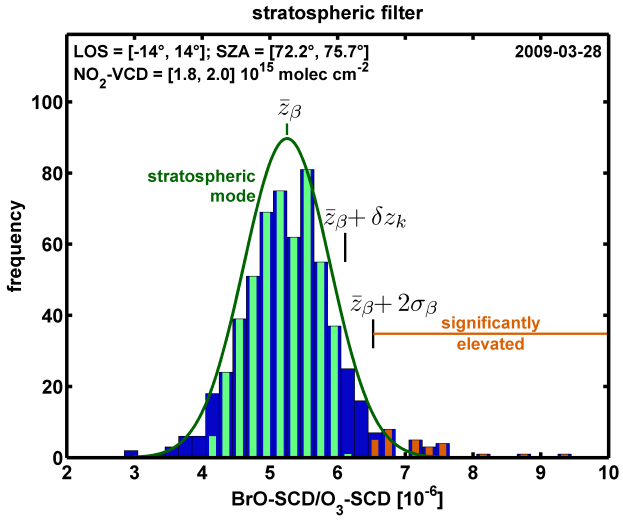

Figure 6.19.: *Example frequency distribution of measured BrO-SCD to O_3-SCD ratios (blue) from the example partition $\Omega_{6,3}$ in Figure 6.18. The algorithm retrieves the limits of a subdivision with minimal asymmetry (green) containing mostly measurements of the stratospheric background. Significantly enhanced measurements (high BrO, low O_3) appear in the right tail of the distribution (red). See text for details.*

6.4.3. Test of the applied algorithms using simulated data

In the previous section, two numerical algorithms were developed, i. e. the partition of data into equally sized 2D partitions and the asymmetry filter to identify the stratospheric mode. Both algorithms are pragmatically motivated and were assumed to converge a priori. In this section, both algorithms are benchmarked using simulated measurements in order to test their numerical stability. First, the partitioning algorithm is tested followed by a test of the asymmetry filter. In the end of this section, both algorithms are applied in combination to a more realistic setting in order to assess the possible numerical error sources.

Benchmark test of the 2D partitioning algorithm

In order to test the capability of the partitioning algorithm depending on the number of data points N, the domain Ω is populated with simulated measurements and consecutively partitioned. Figure 6.21 shows the resulting partition for four different N=24, 120, 1200, 1200 in 12 partitions (N_θ=4 and N_V=3) supposedly equal in size. As described above, the partitioning terminates as soon as the number variation between the bins is less than 20 %. If this criterion is not be achieved after 20 iterations, the algorithm terminates as well leading to a larger number variation.

The results in Figure 6.21 reveal that the partitioning did not fully met the convergence criterion for small $N \leq$120. For larger N, however, the algorithm generates partitions meeting the convergence criterion.

In a second test, the number of measurements are weighted depending on the

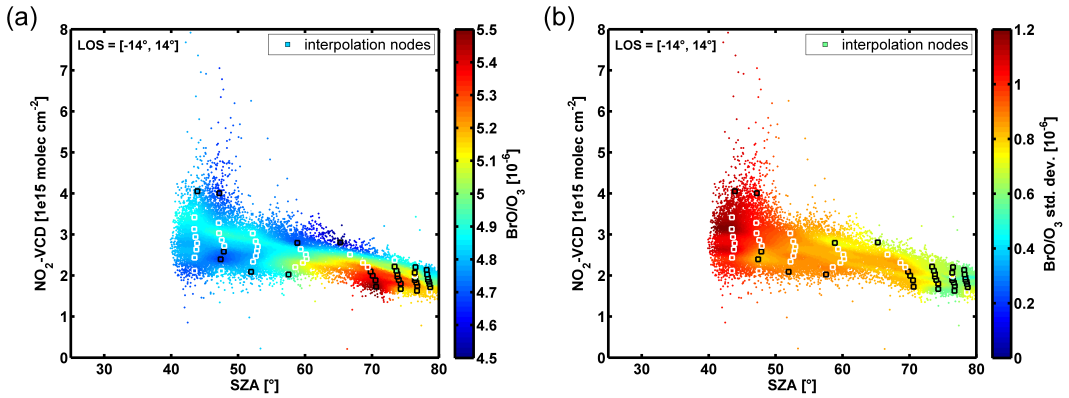

Figure 6.20.: *Interpolation (a) of the BrO/O_3 SCD ratio surface and (b) its standard deviation σ depending on SZA and NO_2-VCD. The nodes of the bilinear surface interpolation (squares) are the mean of the partitions displayed in Figure 6.18. The distributions of some partition with a negligible asymmetry are not filtered before the interpolation and indicated by white squares.*

partition. The partition sizes in the upper and lower row as well as both last columns for large θ are weighted twice (fourfold in the corners) as illustrated in Figure 6.17. This modified scheme allows a higher partition density towards the edges of Ω. The results from the second test are shown in Figure 6.22. The partitioning algorithm achieves a reasonable partition also using the scheme with modified partition weights. Hence, a successful implementation of the partitioning algorithm may be concluded. Furthermore, the algorithm is assumed to also converge when applied to real data where N is usually large.

Benchmark test of the asymmetry filter

In order analogy to the previous section, the asymmetry filter is tested using simulated data. The simulation are intended to test the asymmetry filter towards its performance under difficult situations. The algorithm is tested towards the number of measurements required to accurately determine the stratospheric contribution. It is furthermore tested whether the stratospheric mode may be retrieved even if most measurements are actually enhanced and most tropospheric enhancement is small.

The stratospheric mode is assumed Gaussian whereas the tropospheric contribution follows a log-normal distribution. The simulated data are assumed to contain at least a contribution from the stratospheric mode. Furthermore, log-normally distributed random numbers are added to a fraction $p_t < 1$ of all measurements accounting for possible tropospheric enhancements.

For a first test, only a small percentage of 30 % of the measurements is assumed to exhibit tropospheric enhancements. The results shown in Figure 6.23 exhibit, that the asymmetry filter is capable to retrieve the mean of the stratopheric mode (within statistical limits) even for a relatively small sample size of N=50.

In the second test case, the same sample size is generated differently. An increased

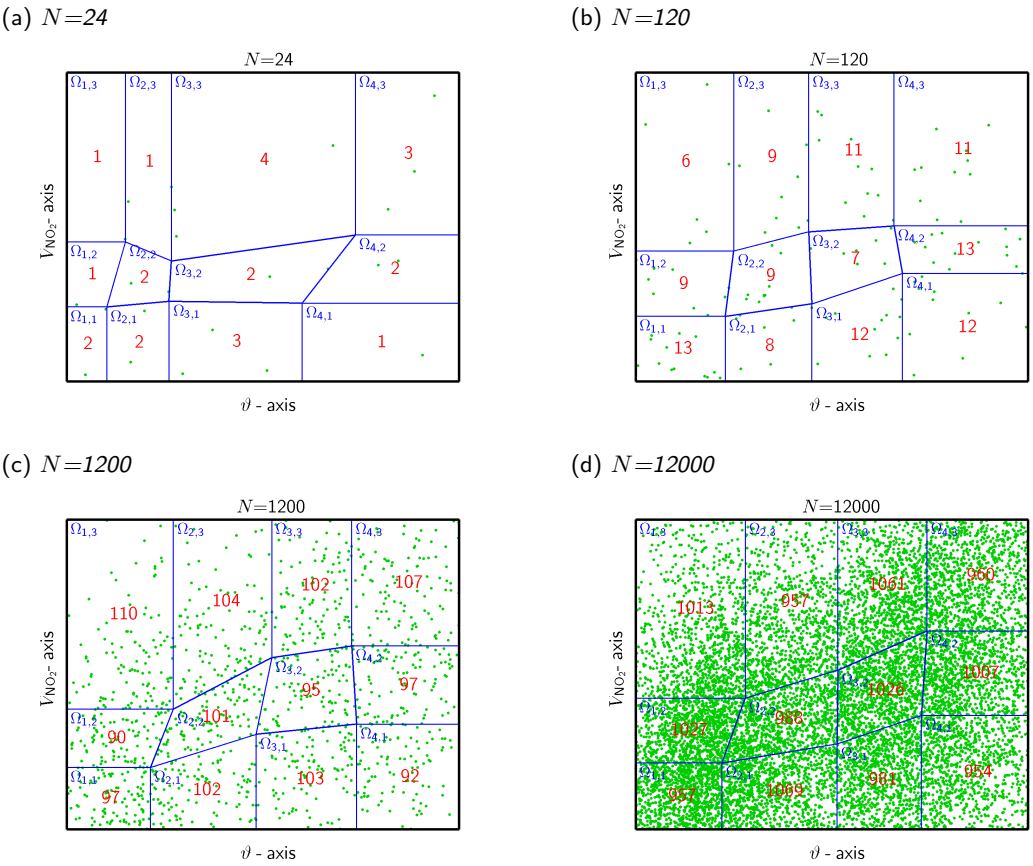

Figure 6.21.: *Partitioning of the domain Ω into 12 smaller sets $\Omega_{i,j}$ containing an almost equal number of points (see text). The number of points within each partition (i,j) are indicated in red.*

number of 60 % percent of the measurements is assumed to be enhanced due to tropospheric activity. Furthermore, as shown in Figure 6.24, the distribution of tropospheric measurements is located closer to the stratospheric mode. This time, the asymmetry filter fails to determine the stratospheric mode for a very small sample size (N=50). For a larger sample size (N=5000), however, the stratospheric mode is retrieved at high accuracy.

In a final test, the distribution of tropospheric enhancement is shifted towards very small values leading to a shifted maximum of the accumulated distribution of simulated measurements (Figure 6.25). Again, 60 % percent of measurements are assumed to be enhanced. The results reveal that the filter successfully retrieves the mean of the stratospheric mode also for small sample sizes. It is noted that the retrieved stratospheric mode is shifted right for N=50 due to interferences with the tropospheric measurements. However, the mean is shifted even for N=50000 measurements due to the strong overlap and the resulting ambiguity of both underlying modes.

In conclusion, the implemented asymmetry filter has proved to be capable to sepa-

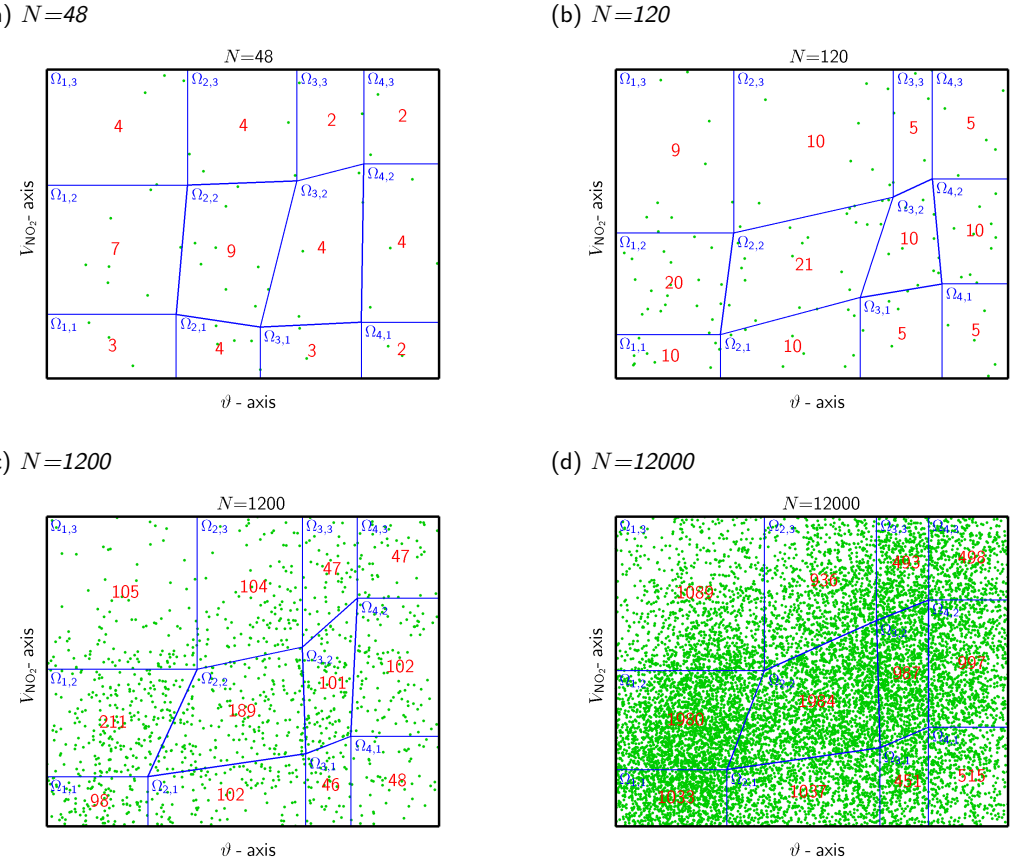

Figure 6.22.: *Same as Figure 6.21 but partitioned into differently sized partitions* $\Omega_{i,j}$ *(see text).*

rate the stratospheric mode even for small samples under these idealized conditions. Only very small sample sizes and many, hardly enhanced tropospheric columns are found to have a malicious effect on the separation algorithm.

Proof of concept of column separation algorithm using simulated measurements

As a last benchmark test in this section, the capability of the algorithm to retrieve the true $\bar{z}_0(\vartheta, V_N)$ is benchmarked using data simulating an asymmetric distribution in z.

As a matter of fact, the true $\bar{z}_0$ is not known for the satellite nadir geometry. Therefore, the whole numerical algorithm is benchmarked using simulated measurements instead. The simulations are based on mathematical distributions without any a priori chemistry or radiative transfer. The retrieved $\bar{z}_0$ may then be compared to the known model function z_m used as an input for the measurement simulation.

Within the domain defined in (6.11), the surface

$$z_m : z = a\hat{x}\cos\hat{y} + b \tag{6.18}$$

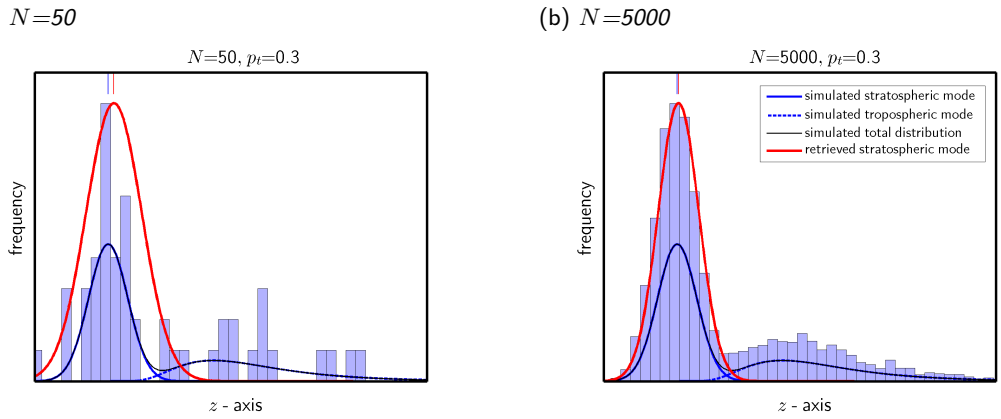

Figure 6.23.: *Asymmetry filter applied on simulated data of a symmetric stratospheric mode and a superimposed tropospheric enhancement applied to 30 % of simulated measurements. The mean of original retrieved stratospheric mode are indicated by the blue and red line at the top of the panels, respectively.*

is chosen with the normalized coordinates $\hat{x} = (\vartheta - 25°)/55°$ and $\hat{y} = V_\mathrm{N}/(8 \cdot 10^{15}\,\mathrm{molec\,cm^{-2}})$ to model the stratospheric response of $\mathrm{BrO/O_3}$-SCD ratio measurements (Figure 6.26a). The parameters in (6.18) are $a = 5 \cdot 10^{-7}$ and $b = 4.9 \cdot 10^{-6}$, respectively. Then, $2 \cdot 10^4$ measurements of $(\vartheta, V_\mathrm{N}, z)$-triplets are simulated to sample z_m using several random-number generators.

The $(\vartheta, V_\mathrm{N})$-plane is populated by two normal distributions as displayed in Figure 6.26b. Then, for each $(\hat{x}, \hat{y})$-pair, a normally distributed "tropospheric" value centred around 0 with a standard deviation $\sigma_{z,1} = 0.4 \cdot 10^{-7}$ is added to the respective value of z_m. Additionally, normally distributed values ($\sigma_{z,2} = 1.5 \cdot 10^{-6}$, offset $\Delta z_2 = 1.5 \cdot 10^{-6}$) are added to 15 % of the measurements to model events of enhanced $\mathrm{BrO/O_3}$-fractions. As an example, the resulting distribution of z of measurements falling within the interval centred at $\vartheta = 70.9°$ and $V_\mathrm{N} = 2.2 \cdot 10^{15}\,\mathrm{molec\,cm^{-2}}$ is shown in Figure 6.26d.

After the generation of measurements, the algorithm to derive $\mathrm{BrO/O_3}$-fractions is applied as described in Sect. 6.4. The results are compiled in Figure 6.26 with axes similar to Figures 6.18, 6.19, and 6.20. The difference between z_m and the retrieved surface $\bar{z}_0$ and the relative error σ_0 are illustrated in Figures 6.26e and 6.26f, respectively. Both plots show that the algorithm succeeds in reproducing the model function within the sampled area. Residual linear structures of the difference are caused by the bilinear interpolation between the nodes of retrieved surface. The relative error almost never (<1 %) exceeds 2 % and the relative mean error is 0.5 %.

In conclusion, the presented algorithm is capable to reproduce a given model surface for the stratospheric $\mathrm{BrO/O_3}$-SCD ratio within the sampled area. The described simulator was used to test different combinations of parameters for the algorithm (number of nodes, partitioning scheme, interpolation method, convergence thresholds). The final implementation of parameters was found to provide a reasonable trade-off between resolution and sampling error.

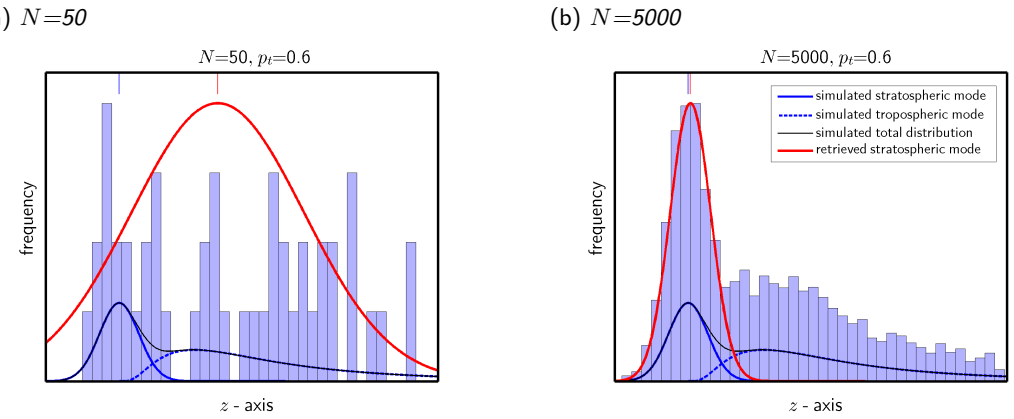

Figure 6.24.: *Same as Figure 6.23 but with 60 % of the measurements showing tropospheric enhancements. The asymmetry filter fails to retrieve the stratospheric contribution correctly if the number of measurements is very small (a).*

6.5. Surface sensitivity filter and air-mass factor

In order to finally retrieve the desired residual tropospheric VCD of BrO from the tropospheric SCD using

$$V_{\text{trop}} = \frac{S_{\text{trop}}}{A_{\text{trop}}} \tag{6.19}$$

the tropospheric air-mass factor A_{trop} needs to be calculated. This section describes how A_{trop} can be retrieved from radiance measurements and O_4 SCDs and that each measurement can be classified into *sensitive* to the boundary-layer (BL) and *possibly obscured*. The concentration of O_4 is proportional to the square of the O_2 concentration and therefore its scale height is approximately 4 km. Hence, its absorption is a good indicator for the photons having penetrated the lower part of the atmosphere (e. g. Wagner & Platt, 1998).

6.5.1. Concept of the boundary layer sensitivity filter

Ground-based measurements showed that most of the enhanced tropospheric BrO column is located within the BL and often close to the surface (e. g. Hönninger *et al.*, 2004; Wagner *et al.*, 2007; Pöhler *et al.*, 2010b; Prados-Roman *et al.*, 2010; Frieß *et al.*, 2011). It is therefore assumed, as an approximation, that the residual tropospheric column of BrO is entirely located between 0 and 500 m above the ground with a constant concentration (box profile). It is noted, that the exact value of the BrO mixed layer-height may differ in reality, but radiative transfer simulations showed its choice is not critical for the presented considerations. Therefore, instead of a real AMF_{trop}, the AMF for the lowest 500 m (AMF_{500}, denoted A_{500}) is retrieved and used in this work.

For nadir satellite observations, the sensitivity to the ground represented by AMF_{500} mostly depends on the surface albedo and whether clouds with a large cloud optical

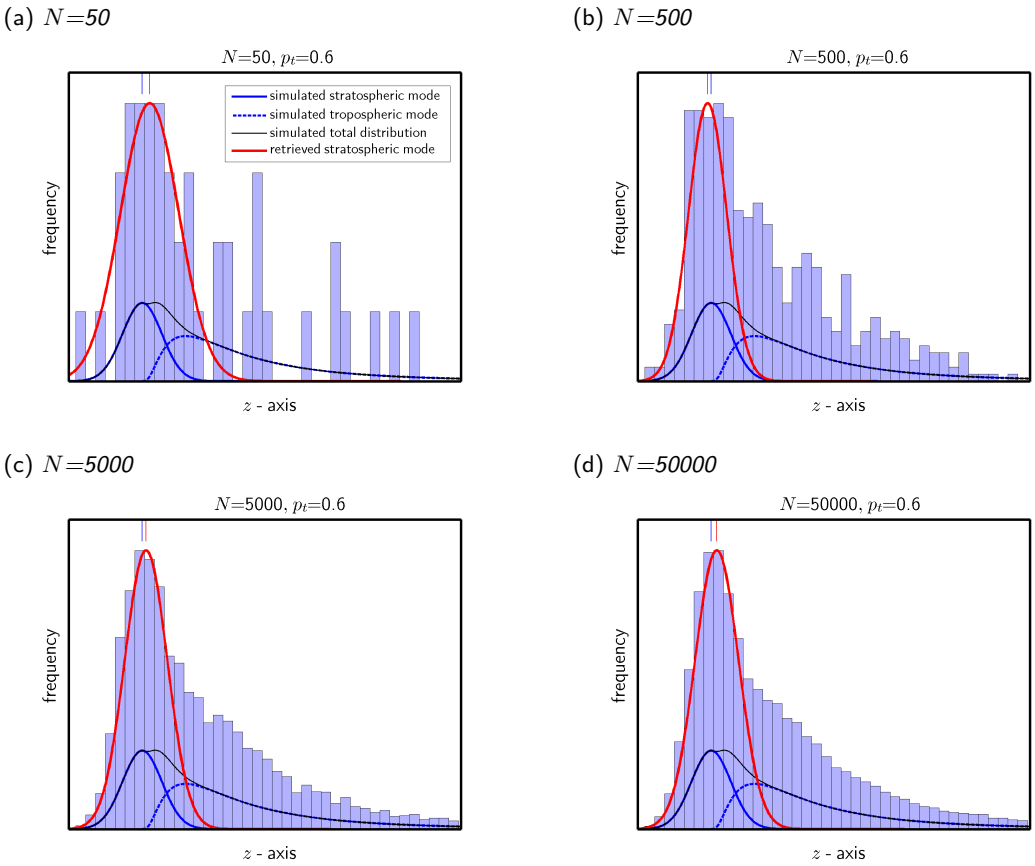

Figure 6.25.: *Same as Figure 6.24 but presuming only a slight enhancement due to tropospheric column contributions. The stratospheric mode is captured by the retrieval even if more than 60 % of the measurements feature only a small contribution from the troposphere.*

density (COD) are present. Under clear-sky conditions, the absorption signal from trace-gases located close to the ground is reduced over a dark surfaces due to little reflection by the ground compared to Rayleigh and Mie scattering in the atmosphere. But over bright surfaces, a substantial fraction of the observed photons penetrates near-surface layers. To a large extent, this is still true even for cloudy scenes. Thick clouds, however, effectively shield the absorption signal from these layers.

The distinction between sea-ice, snow, thick aerosol layers, water clouds and ice clouds by satellite remote sensing is not unambiguously possible (Vasilkov *et al.*, 2010) and therefore surface albedo and COD can not be readily derived from our measurements directly.

Instead, we chose an approach relying on proxies to parametrize AMF_{500}. The two proxies used in the proposed algorithm are the reflectance R and the O_4 AMF. R is

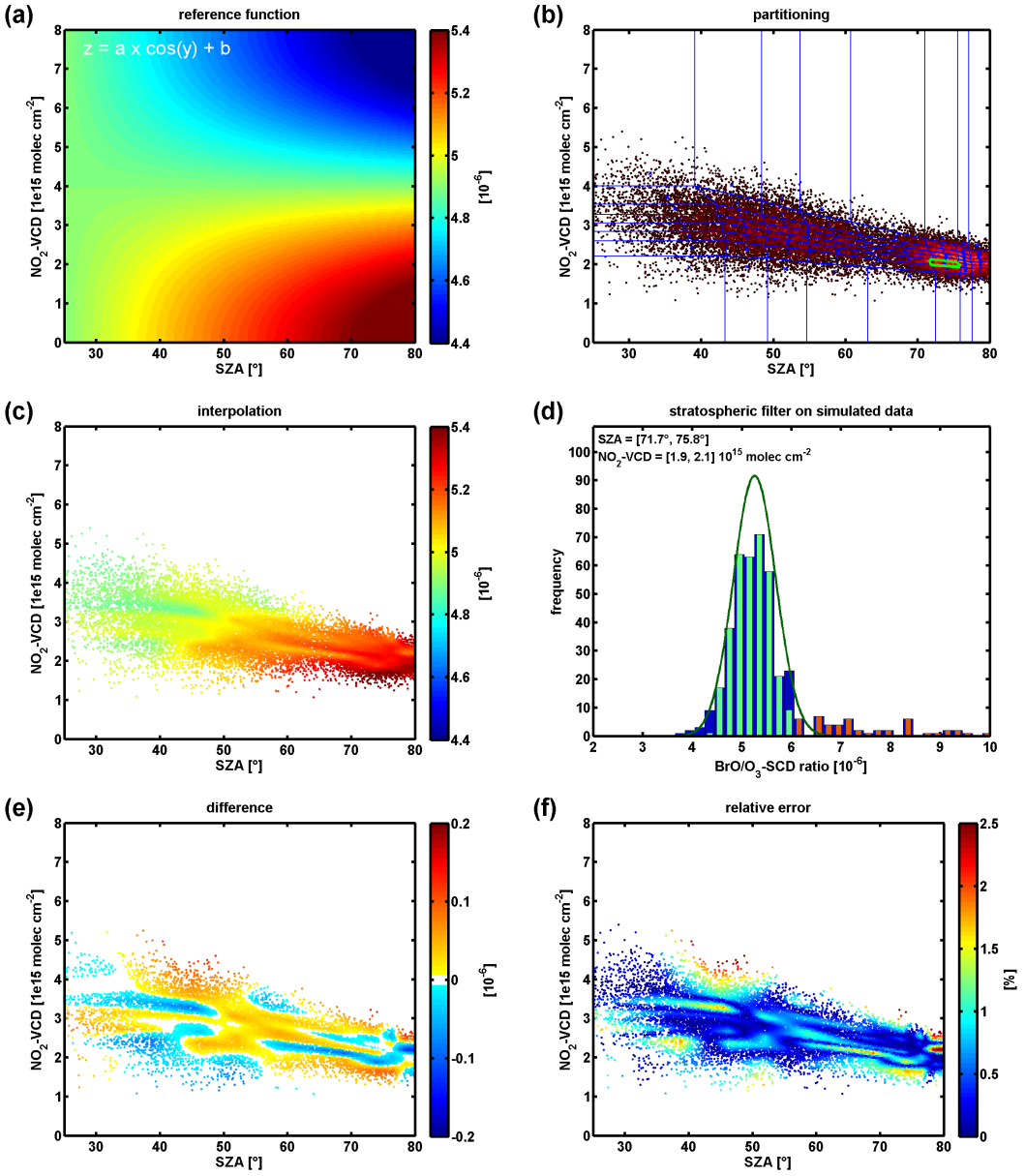

Figure 6.26.: *Benchmark test of the separation algorithm using simulated measurements modelling a (a) known surface. (b) Partitioning of measurements, (c) interpolated surface nodes, (d) application of asymmetry-filter. (e) The difference between true and retrieved surface function shows only small deviations. (f) The relative error almost never exceeds 2 %.*

calculated

$$R = \frac{L}{E} \tag{6.20}$$

where L and E are the Earth radiance and solar irradiance measured by GOME-2 at 372 nm, respectively. The wavelength of 372 nm for R was chosen in order to minimize interferences with trace-gases like O_4 absorbing in the same range. The O_4 AMF, A_O, is calculated from the measured O_4 SCD S_{O_4} using the O_4 VCD integrated from sea level to the top of the atmosphere $V_{O_4} = 1.33 \cdot 10^{43}\,\mathrm{molec^2\,cm^{-5}}$

$$A_O = \frac{S_{O_4}}{V_{O_4}} \cdot 0.8 \tag{6.21}$$

also applying an empirical correction factor of 0.8 which has already been suggested by Wagner *et al.* (2009b) and Clémer *et al.* (2010) and was confirmed by sensitivity studies conducted for this work. Figure 6.27b depicts A_O measured on 25 March 2009.

Results from a computational radiative transfer model are used to study the interrelation between modelled values for R, A_O and A_{500}. For this purpose, triples of (R, A_O, A_{500}) were modelled for a comprehensive set of surface albedos and aerosol/cloud scenarios. The main objective in the next step is to identify the range (or area in the (R, A_O)-plane) where an AMF_{500} exceeds a certain sensitivity threshold AMF_{500}^{min}. The range limits are geometrically approximated, parametrised, and saved in look-up-tables (LUTs) for discrete viewing geometries. When finally analysing the measurements, the LUT parameters are interpolated depending on the viewing geometry. Whether a measurement fulfils the AMF_{500}^{min}-criterion or not is then decided based on the measured R and A_O.

Finally, the AMF for the boundary layer A_{500}^{meas} is derived from the same modelled values depending on R and A_O. The parameters a_0, a_x and a_y of the surface

$$A_{500}^{meas}(R, A_O) = a_0 + a_x \cdot R + a_y \cdot A_O \tag{6.22}$$

are derived from a least-squares fit of a selection of modelled (R, A_O, A_{500})-triples with $AMF_{500} > AMF_{500}^{min}$. In analogy to the surface sensitivity algorithm, a_0, a_x and a_y are also stored in LUTs.

6.5.2. Implementation of the sensitivity filter and AMF calculation

This section describes the implementation of the surface sensitivity filter algorithm. For each set of viewing geometries, the algorithm consists of five steps:

(I) modeling of (R, A_O, A_{500})-triplets for a fixed set of aerosol scenarios and surface albedos,

(II) interpolation of additional (R, A_O, A_{500})-triplets accounting for partial cloud cover and different surface scenarios,

(III) parametrization of the range of the (R, A_O)-plane where AMF_{500} exceeds a given threshold AMF_{500}^{min},

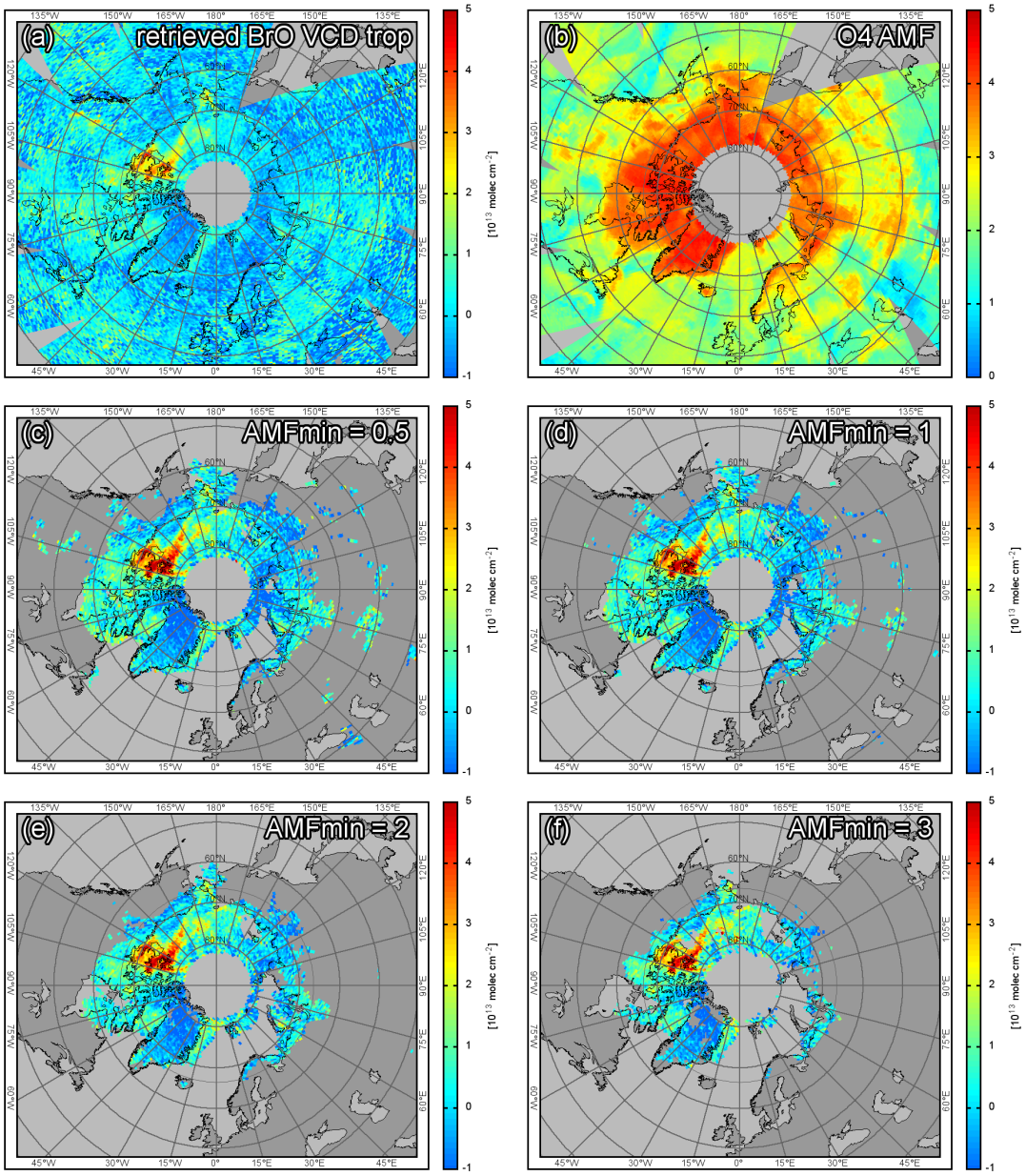

Figure 6.27.: *Illustration of the sensitivity filter and tropospheric AMF for 25 March 2009 (same as Figure 6.4). (a) The retrieved tropospheric BrO VCD (a) are filtered according to its minimum sensitivity to trace gas concentrations close to the surface using (b) measured AMFs of O_4. Panels (c) through (f) show tropospheric BrO VCDs for different sensitivity thresholds AMF_{500}^{min}=0.5, 1, 2, 3, respectively. Note that the sensitivity to the choice of AMF_{500}^{min} is low. (a) is calculated using A_g, (c)–(f) are calculated using A_{500}. Areas without any sensitive measurements are left gray.*

parameter	node
SZA [°]	28, 44, 56, 64, 66, 68, 72, 76, 80, 82, 84, 86
SRAA [°]	0, 20, 32, 36, 44, 48, 52, 56, 60, 64, 116, 120, 124, 128, 132, 136, 144, 148, 160, 180
LOS [°]	0 (nadir), 16, 32, 48
elev. [km]	0, 1, 2, 3, 4, 5, 6

Table 6.3.: *Summary of all modelled geometries for which the threshold parametrization is performed. The solar zenith angle (SZA), solar relative azimuth angle (SRAA) and line-of-sight angle (LOS) are defined in the satellite system, respectively.*

layer [km]	OD
0 – 1	1, 3, 10, 20, 50
1 – 2	1, 3, 10, 50
3 – 4	50
7 – 8	1, 3, 10, 50

Table 6.4.: *Modelled layers of scattering media (aerosols and/or clouds) defined by their lower and upper edge over ground and the optical density (OD).*

(IV) derivation the a-parameters in (6.22),

(V) allocation of derived parameters in look-up-tables. The LUTs are finally needed to interpolate the stored parameters for each GOME-2 pixel depending on its viewing geometry. The interpolated parameters are needed to decide whether a pixel is sensitive to the boundary layer and to calculate AMF_{500} using (6.22).

There are four parameters defining the satellite viewing geometry: the SZA ϑ, the solar relative azimuth angle (SRAA), the LOS angle ψ and the ground elevation. These parameters span the four dimensional LUTs whose discretisation nodes are summarized in Table 6.3. Each LUT has a total of 6720 entries corresponding to 6720 different viewing geometries.

(I) R, A_O and AMF_{500} are modelled for different surface albedos and aerosol scenarios using the McArtim software package (Deutschmann *et al.*, 2011). For each LUT entry, R, A_O, and A_{500} are calculated for the albedos 0.03, 0.09, 0.24, 0.39, 0.54, 0.66, 0.78, 0.90, 0.96 for a pure Rayleigh atmosphere (clear-sky) and the aerosol/cloud scenarios summarized in Table 6.4. For the calculation of AMF_{500}, a tropospheric box profile between 0 and 500 m is assumed.

(II) Further (R, A_O, A_{500})-triplets are interpolated from the Monte Carlo model results for two reasons: Firstly, interpolation increases the number of values populating the (R, A_O)-plane and hence increasing the accuracy of the subsequent parametrisation, and, secondly, through interpolation it may be accounted for real gradients of surface albedo and partial cloud cover. Large albedo gradients are typical for ice-edges over oceans or areas of fresh-fallen snow over land. Therefore, the surface albedo is

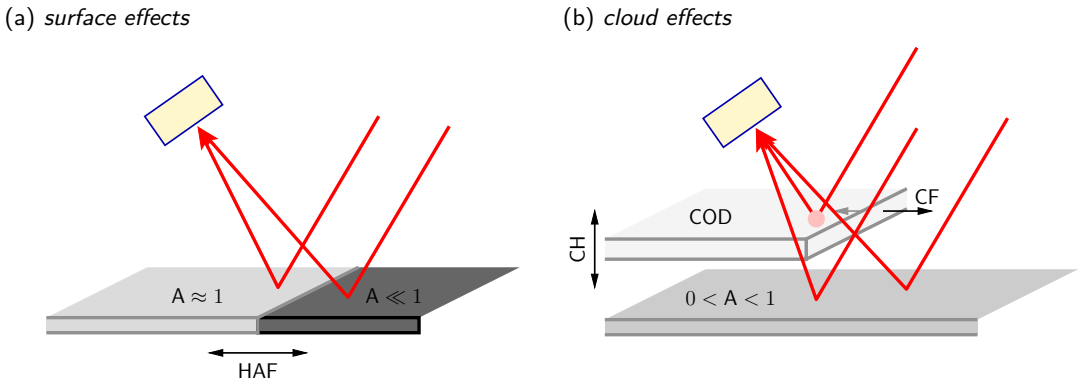

Figure 6.28.: *Illustration of (a) surface and (b) cloud parameters included in the radiative transfer calculations. The surface is characterized by the albedo (A) whereas a single cloud layer is characterized by cloud height (CH) and cloud optical density (COD). Additionally the high albedo fraction (HAF, η_s) and the cloud fraction (CF, η_c) are varied in order to interpolate more realistic and intermediate values to span the the (R, A_O)-plane.*

parametrised by two properties: the albedo at a wavelength of 372 nm and the high albedo fraction of the surface η_s (Figure 6.28a).

η_s is the geometric fraction of the ground pixel assumed to have a very high albedo R_{high} =0.96. The reflectance R defined by (6.20) then depends on η_s and the modelled reflectances R_{high} and R_{low} over surfaces with an albedo of 0.96 and below 0.96, respectively.

$$R(\eta_s) = (1 - \eta_s)R_{\text{low}} + \eta R_{\text{high}} \tag{6.23}$$

The number of photons crossing the boundary between both parts is assumed to be negligible (independent pixel approximation). Accordingly, the modelled AMF depends on η_s following

$$A(\eta_s) = \frac{(1 - \eta_s)R_{\text{low}}A_{\text{low}} + \eta_s R_{\text{high}}A_{\text{high}}}{(1 - \eta_s)R_{\text{low}} + \eta_s R_{\text{high}}} \tag{6.24}$$

where the modelled A_{low} and A_{high} are weighted by the modelled radiances (Martin *et al.*, 2002).

Furthermore, scattering media in the atmosphere, i. e. clouds and/or aerosol layers, are modelled as a single layer with a geometric thickness of 1 km containing particles with a single scattering albedo of 1.00 and a Henyey-Greenstein asymmetry parameter of $g = 0.85$ (King, 1987). The parametrization of scattering media in our model atmosphere has three dimensions: The cloud fraction η_c, the cloud height (CH) and the cloud optical density (COD). η_c is defined as the fraction of a scenery which is covered by clouds. In analogy to the definition of η_s, photons are assumed to travel either through cloud-free (cf) or cloud-covered (cc) sceneries (Figure 6.28b). The radiances and AMFs depending on the cloud-fraction may then be interpolated using

$$R(\eta_c) = (1 - \eta_c)R_{\text{cf}} + \eta_c R_{\text{cc}} \tag{6.25}$$

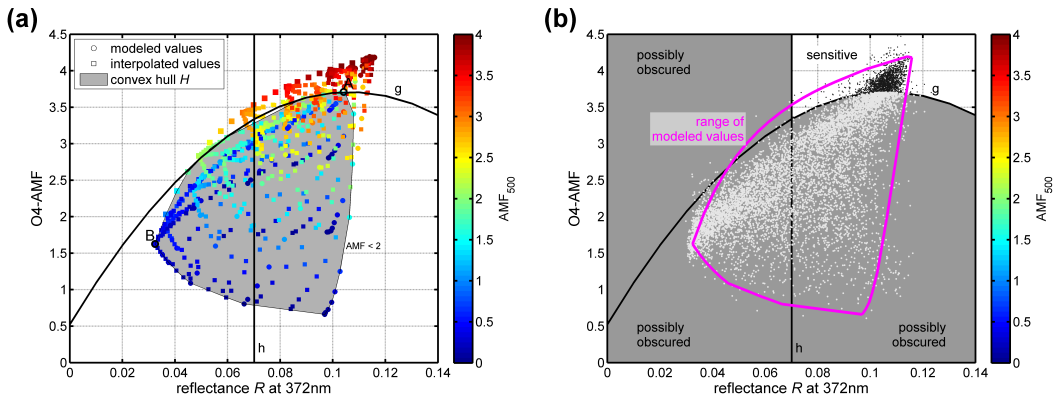

Figure 6.29.: *(a) Modelled and interpolated (R, A_{O}, A_{500})-triplets for a nadir geometry at SZA=66°. The convex hull H (shaded area) including all $AMF_{500} < 2 = AMF_{500}^{min}$ is parametrised in order to provide a threshold for the surface sensitivity filter. (b) Classification of all GOME-2 nadir observations of 2008 at the same SZA based on measured R and $A_{\mathrm{O}}$with a threshold of $AMF_{500}^{min} = 2$. The described filter distinguishes between measurements sensitive to the lowest 500 m of the atmosphere (black dots) and those that are possibly obscured by clouds and/or too low albedo (grey area, bright dots). The convex hull (magenta) of modelled values contains approx 94% of the measurements.*

and

$$A(\eta_c) = \frac{(1-\eta_c)R_{\mathrm{cf}}A_{\mathrm{cf}} + \eta_c R_{\mathrm{cc}}A_{\mathrm{cc}}}{(1-\eta_c)R_{\mathrm{cf}} + \eta_c R_{\mathrm{cc}}} \tag{6.26}$$

respectively.

Summing up the interpolation steps for the radiance and both AMFs for fractional η_s and COD: (1) η_c is varied from 0.2 to 0.8 for every constant albedo using (6.25) and (6.26), respectively. (2) For the clear-sky case, η_s ranges from 0.05 to 0.95 with steps of 0.05 using (6.23) (6.24), respectively. (3) With clouds, η_s and η_c were varied from 0 to 1 and from 0.2 to 1, respectively, both with steps of 0.2. This scheme results in 938 modelled and interpolated (R, A_{O}, A_{500})-triplets. As an example, all triplets are shown in Figure 6.29a for a nadir looking geometry and SZA=60°. R is plotted along the abscissa-axis and A_{O} is plotted along the ordinate-axis. AMF_{500} values are color-coded. The comparison between modelled and measured (R,A_{O})-pairs in Figure 6.29b shows that the range of modelled values (for a specific viewing geometry) includes almost all corresponding measurements. Obviously, the numerical radiative transfer model McArtim is capable to reproduce the range of real measurements for the considered cloud scenarios.

(III) The limits of range P in the (R, A_{O})-plane containing AMF_{500}-values smaller than $\mathrm{AMF}_{500}^{\mathrm{min}}$ is parameterised. P is the inverse of the range where an AMF_{500} exceeding $\mathrm{AMF}_{500}^{\mathrm{min}}$ can be assured. The limits of P are geometrically approximated in order to obtain a suitable parametrisation. Therefore, a convex hull H containing all AMF_{500} smaller than $\mathrm{AMF}_{500}^{\mathrm{min}}$ is constructed.

As depicted by the shaded area in Figure 6.29a, the characteristic shape of H enables us to approximate its upper edge with a parabola g

$$g(R) = g_0 + g_1 R + g_2 R^2. \tag{6.27}$$

Before g is approximated to the upper edge of H, the intensity threshold h is introduced. Using the reflectances of the upper right corner A and left corner B of H, R_A and R_B, respectively, h is given by the mean

$$h = (R_A + R_B)/2 \quad . \tag{6.28}$$

Finalizing the parametrisation of the edge, g is derived from a least-squares fit using the points of the upper edge of H with $R \geq h$.

(IV) A least-squares surface fit of all triples in the upper right section (greater than g, and h) is performed using the model function in (6.22).

(V) For a given $\mathrm{AMF}_{500}^{\mathrm{min}}$, h, g_0, g_1, g_2 and the surface fit parameters a_0, a_x and a_y are stored in seven separate LUTs, which are then used to interpolate the thresholds and $\mathrm{AMF}_{500}^{\mathrm{meas}}$ for any observation geometry for any measured R and A_{O}.

Finally, an observation is flagged as *sensitive* if A_{O} and R are larger than g and h, respectively, or otherwise as *possibly obscured*. If the measurement is sensitive, AMF_{500} is derived using interpolated values for a_0, a_x and a_y.

6.5.3. Validation of surface sensitivity filter

In the previous sections, a sensitivity filter assuring a given sensitivity to near-surface trace-gas concentrations was developed. Several parameters of the implementation were determined by numerical inspection. Due to the complexity, however, it is especially important to validate the presented algorithm in order to unravel potential flaws.

A validation requires independent measurements. Unfortunately, there is no independent satellite data to compare with the retrieved sensitivities and therefore other data sets need to be applied: (1) Results of the surface sensitivity filter are validated through a case study of imaging satellite data in the red and near infra-red spectral region and (2) compared to optical properties of clouds measured by the CALIOP instrument.

Comparison to AVHRR image data

As described in Section 6.5, the sensitivity of GOME-2 measurements to surface near trace-gas concentrations is difficult to quantify over sea-ice and snow covered land due to ambiguities in the optical properties of the surface (ice/snow) and clouds (water/ice). However, by comparing the results of the presented sensitivity algorithm to AVHRR reflectance measurements it is possible to test the general response of the algorithm towards the shielding effect of (A) thin clouds over a dark lead, (B) thick clouds over ice, and (C) over only partially snow-covered land (Figure 6.30a).

(a) *GOME-2 and AVHRR channel 1* (b) *GOME-2 and AVHRR channel 3a*

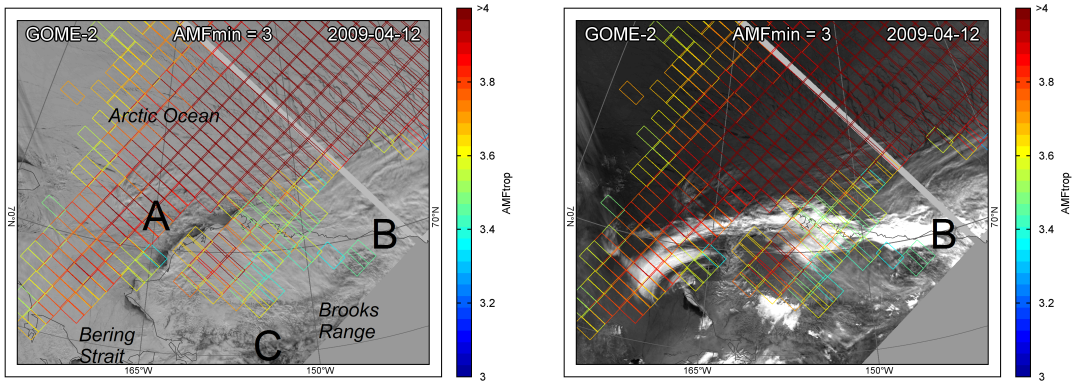

Figure 6.30.: *Overlay image of derived AMF_{500} (color-coded) and AVHRR reflectance measurements (monochrome background) over northern Alaska and the Arctic Ocean: (a) AVHRR channel 1 (630 nm), (b) AVHRR channel 3a (1.61 µm). Blue quadrangles indicate satellite pixels with an assured sensitivity to near-surface absorbers ($AMF_{500} \geq 3$). Pixels above leads at the north-west coast of Alaska (A), above clouds (B), and over the dark Brooks Range (C) are labelled possibly obscured ($AMF_{500} < 3$) and not plotted (see text).*

The AVHRR/3 instrument is also borne by the MetOp-A satellite and measures reflectances at five spectral bands between the visible red and the thermal infrared spectral range at a spatial resolution of 1.1 km. The black-and-white images in Figure 6.30 show AVHRR reflectance measurements at 630 nm (channel 1) and 1.6µm (channel 3a), respectively. Both images show the area around northern Alaska and the Arctic Ocean from 4 April 2009 at 22:43:42 UTC. The scenery in Figure 6.30a is dominated by large bright areas of sea-ice in the Bering Strait, the Arctic Ocean, as well as snow between the north coast of Alaska and the Brooks Range in the south. The color-coded outlines of individual satellite pixels represent pixels assured to be sensitive to the surface with $AMF_{500}^{min} = 3$.

While the center of the satellite swath features the highest AMF_{500} (dark red pixels in the upper part), the algorithm manages to detect regions with a reduced sensitivity to the surface. Clearly, the sensitivity to the surface is reduced over dark surfaces like (A) the Barrow lead at the north-west coast of Alaska and (C) over the darker slopes of the Brooks Range to the bottom of the figure. (B) The shielding effect of clouds is a little bit more subtle and best visible in the comparison with near-IR data (Figure 6.30b). In this spectral region, clouds and suspended particles generally reflect more incoming solar radiation than features on the ground including snow and ice because the particles are smaller (Palm *et al.*, 2011). Furthermore, the linear crack-like features in the sea-ice are almost completely blurred by clouds which can be identified by their shadows towards the north-west (Figure 6.30a).

CALIOP

In order to validate the selectivity and response of the presented sensitivity filter (Section 6.5) towards clouds over bright surfaces, filter results are compared to measurements of the Cloud-Aerosol Lidar with Orthogonal Polarization (CALIOP) instrument. The specification of CALIPSO satellite and the measuring principle of the CALIOP instrument is described in Section 5.3.2. The differences to the GOME-2 instrument on MetOp-A (Section 5.2) are compiled in Table 5.1 on page 60.

In this study, four years of provisional CALIPSO Lidar Level 2 5 km cloud layer data are compared to the classification of GOME-2 pixels regarding the sensitivity to the surface (Section 6.5). The comparison focuses on the ability of the algorithm to detect clouds over bright surfaces possibly reducing the sensitivity to trace-gases at the surface. Therefore, only pixels featuring a high sea-ice concentration of 95% are considered here. Sea-ice concentration maps derived from microwave-radar measurements were provided by the Integrated Climate Data Center (ICDC), see Kaleschke *et al.* (2001) and Spreen *et al.* (2008) for a detailed description of the product. Additionally, only measurements in the northern hemisphere below 83° N latitude are compared. The time-difference between both measurements is limited to 30 min and every GOME-2 pixel taken into account must contain at least 70 km of the CALIPSO ground-track. Finally, 17 000 collocated measurements meet these selection criteria in the months February to June of the years 2007 to 2010.

Depending on $\mathrm{AMF}_{500}^{\mathrm{min}}$ two properties of the CALIPSO data-set, the cloud optical density (COD) and layer top altitude (LTA) of the uppermost layer, are selected, averaged and classified following the sensitivity algorithm applied on the specific GOME-2 pixel they are collocated with. The resulting mean and median values are illustrated in Figure 6.31. Within the limitations of a comparison of different data-sets, it can be concluded that the algorithm is capable to identify the shielding effect of clouds over sea-ice. Both the mean and the median cloud optical density of the sensitive pixels are always lower than of those classified as possibly obscured. A higher threshold $\mathrm{AMF}_{500}^{\mathrm{min}}$ increases the sensitivity of the filter towards filtering also thinner clouds, and an increase of $\mathrm{AMF}_{500}^{\mathrm{min}}$ leads to a decrease of the mean cloud optical density.

However, the mean layer top altitude was expected not to play such an important role because AMF_{500} is almost constant for clouds higher than 500 m. This dependence on $\mathrm{AMF}_{500}^{\mathrm{min}}$ may be due to the utilization of O_4 as a tracer whose SCD depends on the cloud top altitude also above 500 m. It is furthermore possible that this behaviour is an artefact caused by the limited sensitivity of the CALIOP instrument for large optical densities. The CALIPSO data may contain some cross-correlation between COD and LTA because higher clouds are potentially thicker than can be resolved by CALIOP.

Discussion of reflectivity filter validation results

In this section, the results of the surface sensitivity filter algorithm were compared to two independent satellite data-sets. Firstly, a case-study using AVHRR image data

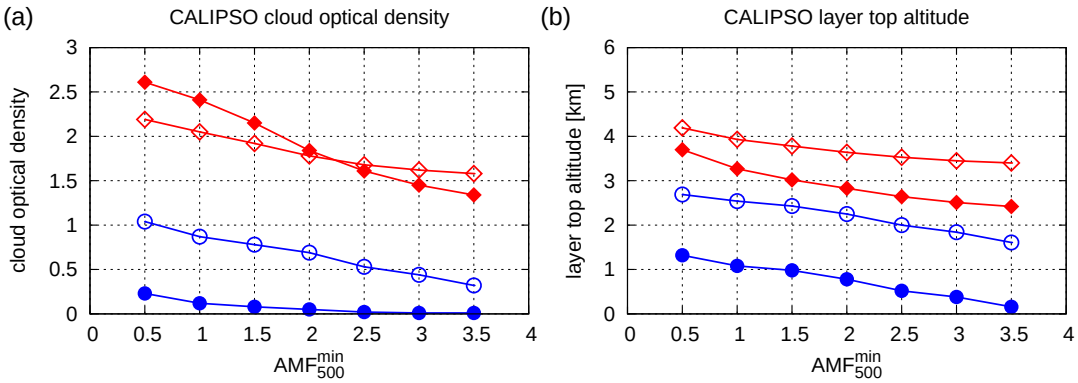

Figure 6.31.: *Mean and median (a) cloud optical density and (b) layer top altitude measured by CALIPSO depending on the sensitivity threshold AMF^{min}_{500} applied on collocated GOME-2 measurements. Collocated measurement are divided according to the retrieved surface sensitivity: AMF_{500}>AMF^{min}_{500} (sensitive to the surface; blue circles) and AMF_{500}<AMF^{min}_{500} (possibly obscured; red diamonds). Note that the difference between mean and median values indicates asymmetric distributions. Error bars are omitted for the sake of clarity.*

showed that the filter algorithm manages to identify areas where the sensitivity to the surface is potentially decreased. Secondly, GOME-2 measurements over sea-ice were compared with to CALIOP measurements providing information about the cloud cover.

From the comparison with CALIOP data it can be concluded that the filter algorithm is capable to detect clouds over sea-ice that are possibly reducing the sensitivity to near-surface absorbers. The filter threshold AMF^{min}_{500} showed to have an influence on the median of both COD and LTA (Figure 6.31).

6.6. Sample results and discussion of the retrieval algorithm

Finally, some sample results of the presented retrieval algorithm are discussed. The retrieved tropospheric BrO VCDs are furthermore applied in Chapters 9, 10, and 11 in order to further validate the retrieved VCDs, to study the vertical and horizontal distribution of BrO, and to study the processes involved in the release and production of BrO, respectively.

Tropospheric VCDs of BrO resulting from the column separation algorithm are displayed for 25 March 2009 in Figure 6.4e and for 1 April 2007 in Figure 6.13e. Both figures illustrate the capability of the algorithm to separate the residual tropospheric column from the measured total column and to reduce the correlation to the tropopause height on a large scale. Fine-structured areas of elevated BrO remain in the retrieved tropospheric columns. For 1 April 2007, the pixels in the east sector fall into areas where the O_3-VCDs are reduced due to ozone hole conditions. These are removed from the retrieval.

Figure 6.27 shows the tropospheric BrO columns for different choices of the AMF^{min}_{500}

threshold. The algorithm successfully removes measurements over areas outside the Arctic with a relatively low surface albedo. The comparison between Figures 6.27c through 6.27f shows that the maps depend only slightly on the choice of $\mathrm{AMF}_{500}^{\mathrm{min}}$.

It is important to note, that the presented algorithm – compared to previously published algorithms – depends neither on results from stratospheric chemistry models, gridded measurements from other satellite instruments nor surface albedo climatologies avoiding the disadvantages of using a potentially biased model description and possible short-term deviations from climatological values. Apart from the potential vorticity data provided by ECMWF to identify areas potentially disturbed by ozone hole chemistry, only data measured by the GOME-2 instrument is required.

Another distinct advantage of the column separation algorithm is, that measurement errors are derived based on observations and not based on the mathematical fit error of the SCD retrieval. As pointed out by Stutz & Platt (1996), the fit error may underestimate the true error in the presence of erroneous reference cross-section alignment and systematically structured residual spectra. However, these malicious influences are difficult to quantify. In this work, empirically derived measurement errors are derived in order to provide a realistic error estimation which also includes the error of the column separation. Hence, it is possible to decide whether a measured BrO column density significantly exceeds the stratospheric background in the SCD space. This can be particularly advantageous when calculating the correlation to independent data-sources by avoiding a systematic bias from potentially flawed assumptions of the vertical distribution and the state of the atmosphere which are necessary to solve the radiative transfer problem.

Several newly developed numerical algorithms are implemented in the retrieval. Both the partitioning as well as the asymmetry filter algorithm were tested on simulated measurements and proved to produce realistic results. Applied to simulated measurements, the combination of both components of the decomposition algorithm retrieved the correct values. This confirms the choice of parameters in the retrieval.

Furthermore, results of the surface sensitivity filter algorithm were compared to two independent satellite data-sets. Firstly, a case-study using AVHRR image data showed that the filter algorithm manages to identify areas where the sensitivity to the surface is potentially reduced. Secondly, GOME-2 measurements over sea-ice were compared to CALIOP measurements providing information about the cloud cover. From the comparison with CALIOP data it can be concluded that the filter algorithm is capable to detect clouds over sea-ice that are possibly reducing the sensitivity to near-surface absorbers. The filter threshold $\mathrm{AMF}_{500}^{\mathrm{min}}$ showed to have an influence on the median of both COD and LTA (Figure 6.31).

The final result of the presented algorithm are tropospheric VCDs of BrO with a quantified sensitivity to near-surface layers. These VCDs are the basis for several studies presented in the results part of this thesis. In Chapter 9, the tropospheric BrO VCDs are compared to ground-based measurements providing a consistent picture of the BrO distribution on different scales. Then, the average distribution of BrO in the Arctic is investigated in Chapter 10 before the BrO measurements are correlated to meteorological data in order to study the processes involved in bromine activation in Chapter 11.

It is finally noted that the results from this retrieval are submitted for publication to *Atmospheric Measurement Techniques* and were already contributing to two research articles by Prados-Roman *et al.* (2010) and Heue *et al.* (2011) both presenting airborne MAX-DOAS (AMAX-DOAS) measurements. Prados-Roman *et al.* (2010) presented measurements of BrO profiles obtained in the Arctic during the ASTAR campaign in spring 2007. Their results were compared to columns derived from the method by Theys *et al.* (2011) and the method presented here. All three data-sets were found to be consistent within the respective errors. Furthermore, the comparison of horizontal gradients measured by both GOME-2 and AMAX-DOAS revealed reasonable qualitative agreement between both techniques as presented in Figure 6.32 (Prados-Roman, 2010). In this comparison, however, also the influence of the limited horizontal resolution of GOME-2 becomes apparent. The AMAX-DOAS resolves the reduced BrO mixing ratio above an open lead. A feature which is not captured by GOME-2. Finally, in the paper by Heue *et al.* (2011), columns of SO_2 and BrO derived form GOME-2 measurements have been successfully compared to columns measured by the CARIBIC instrument analysing the plume of the Eyjafjallajökull volcano in May 2010. In the study by Heue *et al.* (2011), however, a different normalization procedure optimized for the detection of volcanic plumes on a regional scale was applied (Hörmann *et al.*, 2012).

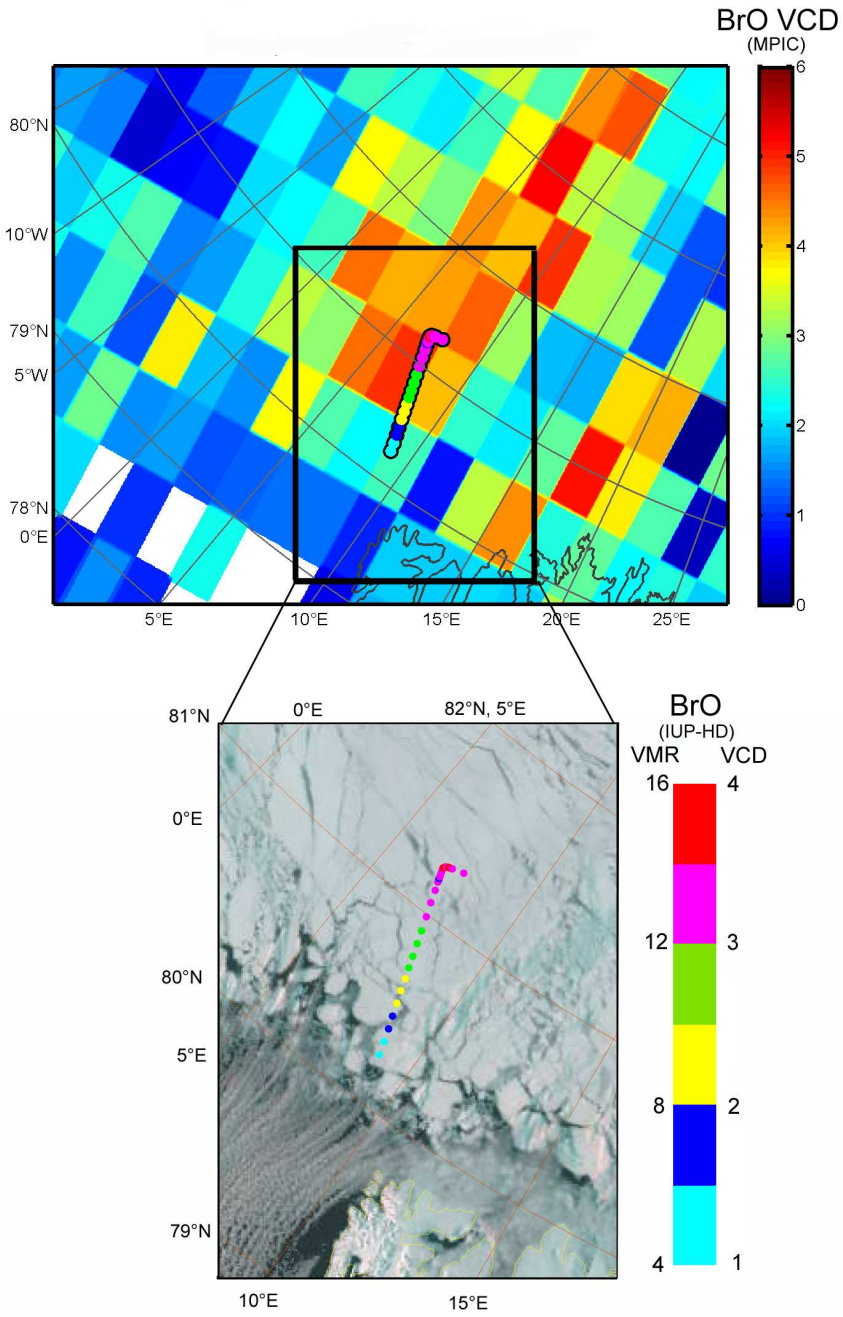

Figure 6.32.: *Boundary layer BrO vertical column density inferred from satellite (MPIC) and aircraft (IUP-HD) measurements (8 April 2007). (top) Satellite BrO boundary layer column density retrieved from this work. Additionally, the boundary layer BrO VCD retrieved from AMAX-DOAS measurements performed by Prados-Roman (2010) (with the corresponding color-code given in the bottom panel). (bottom) Boundary layer BrO, given in volume mixing ratio (vmr) in units of ppt and VCD (10^{13} molec cm^{-2}, assuming a 1 km well-mixed BL. The satellite image in the bottom shows the sea-ice extent of that day (courtesy of ESA). Adapted from Prados-Roman (2010).*

7. Additional data sources and methods

This chapter describes data sources and methods used in addition to the satellite measurements (Sections 5.2 and 5.3, Chapter 6) and the ground-based measurements at Barrow (Section 5.1 and Chapter 8).[1]

First, the setup of ground-based measurements of BrO aboard the Amundsen icebreaker are described in Section 7.1, followed by the scheme used to compute collocated measurements of GOME-2 and ground-based measurements in Section 7.2. After that, the meteorological fields from a meso-scale weather model are described in Section 7.3, which are also used for the calculation of backward trajectories presented in Section 7.4.

7.1. Ground-based measurements in the Amundsen Gulf

In the scope of the International Polar Year (IPY) 2007–2008, the Amundsen research vessel (RV), an icebreaker operated by the Canadian Coast Guard, participated in the Circumpolar Flaw Lead (CFL) system study (Barber *et al.*, 2010; Pöhler *et al.*, 2010b). One of many projects collaborating with the CFL project was the Ocean – Atmosphere – Sea Ice – Snowpack (OASIS) project which was responsible for studying the interactions between the domains defined in the project title. Within OASIS, measurements of the atmospheric chemistry were contributed, among others, by the Institute of Environmental Physics in Heidelberg. In spring 2008 and 2009, LP-DOAS as well as MAX-DOAS measurements were conducted from aboard the Amundsen RV in the Amundsen Gulf and respectively at Barrow, Alaska as part of this thesis (Pöhler *et al.*, 2010b; Liao *et al.*, 2011; Frieß *et al.*, 2011). This section presents the measurement setup aboard the Amundsen RV including LP-DOAS and MAX-DOAS measurements. In this thesis, the measurements of BrO in the Amundsen Gulf are used to compare tropospheric BrO VCDs retrieved from GOME-2 measurements (Chapter 6) to ground-based measurements in order to create a conclusive picture of the distribution of tropospheric BrO (Chapter 9). The results from Barrow, however, are presented in the next chapter (Chapter 8).

LP-DOAS measurements were conducted during March and April 2008 in the tropospheric boundary layer directly over the sea-ice of the Amundsen Gulf. Furthermore, a MAX-DOAS instrument was operated between 15 February and 20 October 2008. Both LP-DOAS and MAX-DOAS instruments were placed on top of the vessel at a height of about 19 m over the sea-ice as depicted in Figure 7.1 (Pöhler *et al.*, 2010b). The results from the LP-DOAS averaging the concentration between 1 and 19 m height above the sea-ice were thoroughly discussed by Pöhler *et al.* (2010b),

[1] Parts of this chapter have been accepted for publication in Sihler *et al.* (2012).

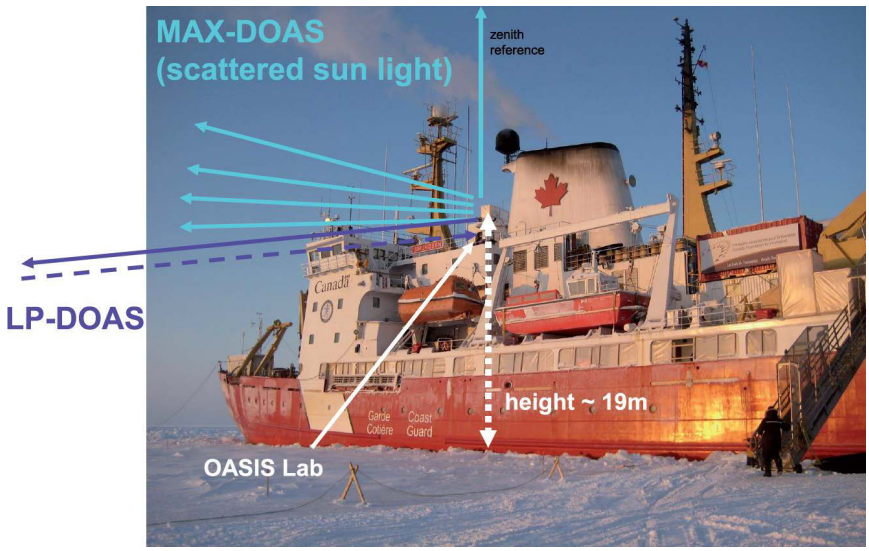

Figure 7.1.: *The DOAS instrument set aboard the Amundsen icebreaker in the Amundsen Bay in Spring 2008. Adapted from (Pöhler* et al.*, 2010a).*

whereas the MAX-DOAS measurements conducted by the same contributors are yet unpublished.

The MAX-DOAS recorded spectra at the elevation angles of -0.2°, 1.6°, 2.5°, 4.3°, 10.6° 18.7° and the zenith (90°). The differential optical density was calculated from the spectra at lower elevations divided by the closest zenith reference measurement resulting in a differential slant column density (dSCD). The retrieved BrO SCDs between 15 February and 25 April 2008 are shown in Figure 7.2. However, measurements after 18 April 2008 needed to be discarded as the simultaneously retrieved O_4 dSCDs at small elevation angles showed low values. This indicates that the opening angle of the MAX-DOAS telescope was comparatively large (∼4°). The large opening angle probably results from a misalignment of the optical components and leading to large uncertainties at very low elevation angles due to light reflected by the snow. As a result, the information content of the BrO concentration profile in the lowest part of the atmosphere is very low and had to be discarded as well. The attempt to use the MAX-DOAS data from the Amundsen for a similar profile retrieval as conducted by Frieß *et al.* (2011) did therefore not succeed and a simplified evaluation scheme for tropospheric BrO VCDs had to be chosen. In the end, BrO VCDs were calculated using the dSCD between 10.6° and 90° divided by the differential AMF assuming clear-sky conditions and a surface albedo of 0.99 (Grenfell *et al.*, 1994). The results from this calculation are shown in Figure 9.1 on page 132.

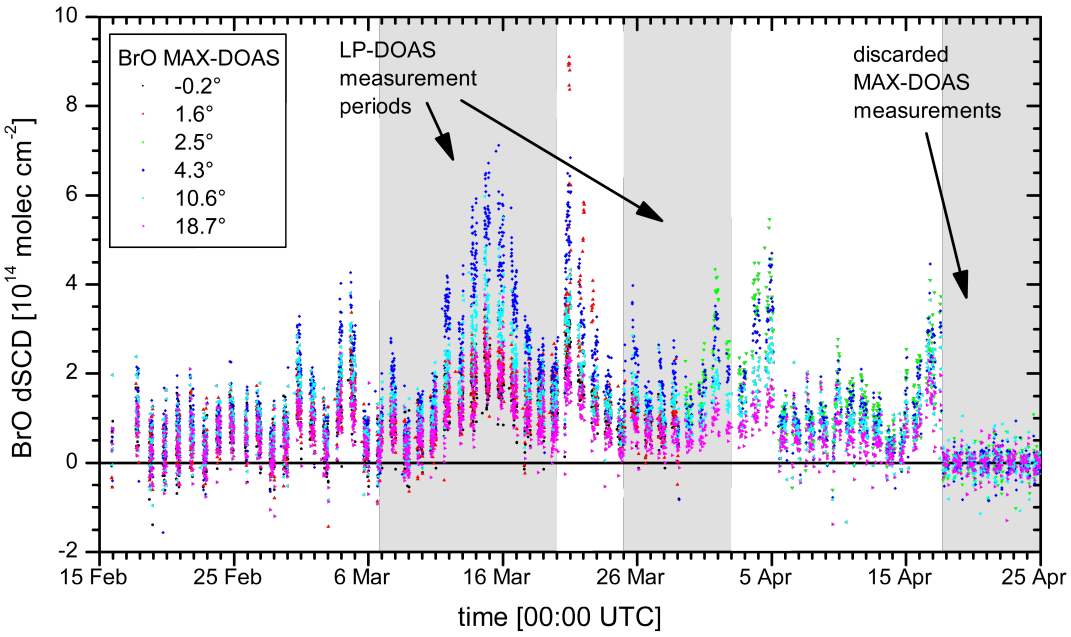

Figure 7.2.: *Differential BrO SCDs derived from MAX-DOAS measurements aboard the Amundsen icebreaker in the Amundsen Gulf south of Banks Island in 2008. The interval shaded in gray indicates the periods of LP-DOAS measurements (cf. Figure 9.2 on page 132). Courtesy of Denis Pöhler, IUP Heidelberg.*

7.2. Collocating satellite data and ground-based measurements

In this section, the method used to collocate satellite and ground-based measurements is described. This method is applied when comparing GOME-2 measurements of BrO to ground-based measurements of both LP-DOAS and MAX-DOAS in Chapter 9. One challenge of such comparisons is the rather coarse spatial resolution of GOME-2 ($80\times40\,\mathrm{km}^2$). As a result, one GOME-2 pixel encompasses an air column only partially probed by ground-based instruments several hours prior and after the GOME-2 overpass. The fraction of probed air depends on the wind-speed and altitude of the air-mass. The edge of a specific BrO enhancement detected by GOME-2 may have already been measured by the ground-based instruments or may reach it in the near future after the overpass. Hence, a scheme was developed to derive the time interval, in which the ground-based measurements need to be averaged. This scheme takes the surface wind speed and direction as well as the relative location of the ground-based measurement site relative to the satellite pixel into account (Figure 7.3). Averages of collocated subsets are calculated for each overpass of the satellite. It is noted that a polar orbiting satellite may pass the same site several times a day during daylight depending on latitude, season, and type of swath. The swath of GOME-2 covers the studied sites up to three times a day at an SZA below 80°.

The averaging scheme bases on the assumption that the variations of the BrO

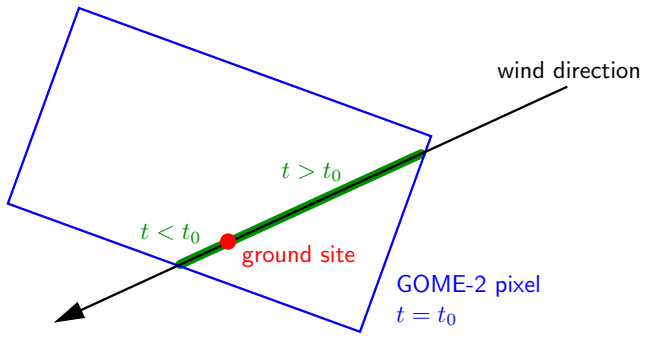

Figure 7.3.: *Collocation scheme for ground-based and GOME-2 measurements. The time interval in which on-site measurements are averaged (green) is calculated according to the GOME-2 pixel outlines (blue) and over-pass time t_0 as well as surface wind-speed and direction.*

concentration within a certain air-mass are small in time-interval used to average the ground-based measurements. This assumptions can be justified by the LP-DOAS measurements by Pöhler *et al.* (2010b) who observed an average diurnal BrO concentration profile which varied only slightly during the day when the photolysis rate of Br_2 was almost constant. GOME-2 overpasses are during the time of day, when variations of the BrO concentrations over the sea-ice were small compared to the measurement error of the satellite instrument.

First of all, only those satellite measurements are selected which are sensitive to the ground (Section 6.5) and whose pixel footprint includes the location of the ground-based measurement. In a second step and for each satellite pixel, the time-interval is calculated in which ground-based measurements are averaged. This calculation combines surface wind-speed and direction with the relative location of the measurement site within the GOME-2 pixel as depicted in Figure 7.3. If the measurement site is located close to the pixel edges, the averaging time-interval includes only those measurements corresponding to the air probed by both the satellite and ground-based instrumentation. This approach leads to a mean duration of approx. three hours which is limited to two hours prior and after the time of the satellite overpass. Additionally, daily means including the overpass averages of each day are computed.

7.3. Operational Meteorological fields from ECMWF

Meteorological data was obtained from the European Centre for Medium-Range Weather Forecasts (ECMWF). This data is used in manifold applications in this thesis. Principally, the Lagrangian trajectory calculations presented in the subsequent section (Section 7.4) require the ECMWF data as input. Furthermore, the potential vorticity at two different isentropic levels was utilized to identify satellite measurements within the polar vortex as presented in Section 6.4. In Section 11.1 and Chapter 11, the surface parameters from ECMWF are compared to tropospheric BrO VCD measurements by GOME-2 in order to identify possible correlations.

	parameter name	ECMWF name	unit	symbol
3D fields	temperature	T	K	T
	zonal wind	U	$\mathrm{m\,s^{-1}}$	
	meridional wind	V	$\mathrm{m\,s^{-1}}$	
	vertical velocity	OMEGA	$\mathrm{Pa\,s^{-1}}$	ω
	specific humidity	Q	$\mathrm{kg\,kg^{-1}}$	
2D fields	surface pressure	PS	hPa	p_{surf}
	sea level pressure	SLP	hPa	
	sea-ice coverage	SICE	%	
	land-sea mask	LSM	%	
	2 m temperature	T2M	K	$T_{2\mathrm{m}}$
	boundary layer height	BLH	m	
	surface geopotential height	Z	m	

Table 7.1.: *Meteorological parameters obtained from the European Centre for Medium-Range Weather Forecasts (ECMWF).*

Volumetric as well as surface ECMWF parameters were obtained via the Meteorological Archival and Retrieval System (MARS). The obtained parameters are compiled in Table 7.1. All meteorological parameters are taken from the ECMWF operational analysis sampled on a regular 1°×1° grid with 91 hybrid pressure levels and a time resolution of 6 h. The only exception is the diagnostic boundary-layer height which is was extracted from forecast calculation at 0 h and +6 h time-step based on the operational analysis at 00:00 and 12:00 UTC (ECMWF, 2004; Dörner, 2010). The geopotential height is the geopotential divided by the WMO defined gravity constant of $9.80665\,\mathrm{m\,s^{-2}}$ which is constant for all latitudes and all heights. The vertical resolution is finest in geometrical height in the planetary boundary layer and coarsest near the model top. The "σ-level" follow the Earth's surface in the lower-most troposphere, where the Earth's orography displays large variations. In the upper stratosphere and lower mesosphere they are surfaces of constant pressure with a smooth transition in between (ECMWF, 2004).

In order to calculate the height of a specific model level above sea-level, the pressure data needs to be calculated for all 91 model levels based on the a_i and b_i ($1 \leq i \leq 92$) parameters provided by ECMWF.

$$p_i = \frac{a_{i+1} + a_i}{2} + \frac{b_{i+1} + b_i}{2} \cdot p_{\mathrm{surf}} \qquad (1 \leq i \leq 91) \tag{7.1}$$

where p_i is the pressure at level i counting here from the surface upward. Subsequently, the height of z_i of model level i can then be calculated from the surface upwards via

the hydrostatic pressure of an ideal gas

$$z_1 = z_0 + \frac{p_{\text{surf}} - p_1}{g \cdot p_1} \cdot T_{2\text{m}} \cdot R_d \tag{7.2}$$

$$z_2 = z_1 + \frac{p_{\text{surf}} - p_2}{g \cdot p_1} \cdot T_1 \cdot R_d \tag{7.3}$$

$$z_i = z_{i-2} + \frac{p_{i-2} - p_i}{g \cdot p_{i-1}} \cdot T_{i-1} \cdot R_d \qquad (3 \leq i \leq 91) \tag{7.4}$$

where z_0 is the surface elevation and R_d=286.9 J kg^{-1} K^{-1} is the specific gas constant for dry air (Dörner, 2010).

Quality of ECMWF data with respect to the Arctic environment

The comparison of BrO VCDs to meteorological parameters in Section 11.5 extensively utilizes the surface parameters provided by ECMWF. However, the interior of the Arctic is void of frequent surface observations leading to larger uncertainties of the weather model calculations in this area compared to other regions (ECMWF, 2007). However, assimilated satellite observations (sea-ice cover, surface skin temperature) provide some information input.

Earlier studies conducted during the Surface Heat Budget of the Arctic Ocean (SHEBA) experiment 1997–1998 concluded that the near-surface temperature in the ECMWF model is often too high in winter, whereas the surface-wind speed was generally well predicted (e. g. Beesley *et al.*, 2000; Tjernström *et al.*, 2004). Apparently, the sea-ice model exhibited problems in parametrising the heat flux of the sea-ice as well as underestimating the surface albedo (Xie *et al.*, 2006).

Since the SHEBA project, however, several improvements have been applied to the ECMWF model. On the one hand, further satellite missions increased the available data basis. On the other hand, the number of model layer was increased to 91 in 2006 resulting in an improved representation of near-surface processes (e. g. Byrkjedal *et al.*, 2008). A study published ECMWF (2007) states that within the boundary layer and around the tropopause the errors reach 2 K. Furthermore, (Gayet *et al.*, 2009) concluded from a comparison to airborne measurements conducted during the Arctic Study of Tropospheric Aerosol, Clouds and Radiation (ASTAR) campaign that the boundary layer height variation along the flight track were reproduced by the ECMWF operational analyses.

It is hence concluded, that the errors of ECMWF surface data are small compared to the errors of the BrO retrieval presented in this work and that recent improvements to the ECMWF model parameters provide a resolution sufficient for the study conducted in Chapter 11.

7.4. Lagrangian trajectory modelling

Backward trajectories were calculated in order to study the history of an air-mass probed by GOME-2. In this thesis, Lagrangian backward trajectory calculations

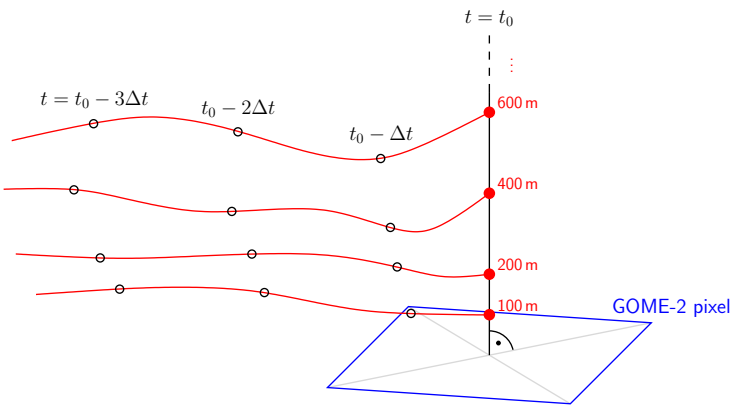

Figure 7.4.: *Definition of backward trajectory end-points: All trajectories end at defined altitudes above the center of one GOME-2 pixel at* $t{=}t_0$.

were performed using the LAGRangian ANalysis TOol (LAGRANTO) software (e. g. Wernli & Davies, 1997; Stohl *et al.*, 2001). LAGRANTO requires a time-series of 3-dimensional wind fields (described in the previous section) and offers the opportunity to record diagnostic variables along the trajectory.

In the study presented in Section 11.5.4, backward trajectories ending at ten different altitudes above the center of each GOME-2 pixel were calculated (Figure 7.4). The end heights were 100, 200, 400, 600, 800, 1000, 1500, 2000, 2500, and 3000 m, respectively. The pixels were binned into 12 min intervals according to their overpass time; the ensemble of trajectories ending within each bin were computed separately. The trajectory calculation was performed in two steps: First, the trajectories were calculated in time-steps of 12 min until the previous ECMWF time-step (00:00, 06:00, 12:00, or 18:00 UTC). Then, the simulation time-step is increased to 30 min with output every 60 min in order to reduce computing time and amount of data output. The length of the trajectories is set to 5 days. Figure 7.5 illustrates resulting backward trajectories corresponding to a single, highlighted GOME-2 pixel. The plot furthermore shows that different end heights result in a horizontal divergence of several thousand kilometres after only a few days.

The altitude above ground h of the trajectory at every time-step is calculated using the international barometric equation

$$h = \left(1 - \left(\frac{p}{p_0}\right)^{1/5.255}\right) \cdot \frac{T_0}{0.0065\,\mathrm{K\,m^{-1}}} \tag{7.5}$$

where p is the pressure, p_{surf} is the surface pressure, and $T_{2\mathrm{m}}$ is the surface air temperature (Stöcker, 2004). Furthermore, the land-sea mask, the sea-ice coverage, as well as boundary layer height were recorded in the LAGRANTO output. Using this information, it is possible to calculate whether the trajectory resided within or above the boundary layer above a certain surface (sea-ice, land, ocean). In this work, a trajectory within the boundary layer is assumed to have contact with near-surface air as the boundary layer is usually well-mixed. In previous studies using ground-based

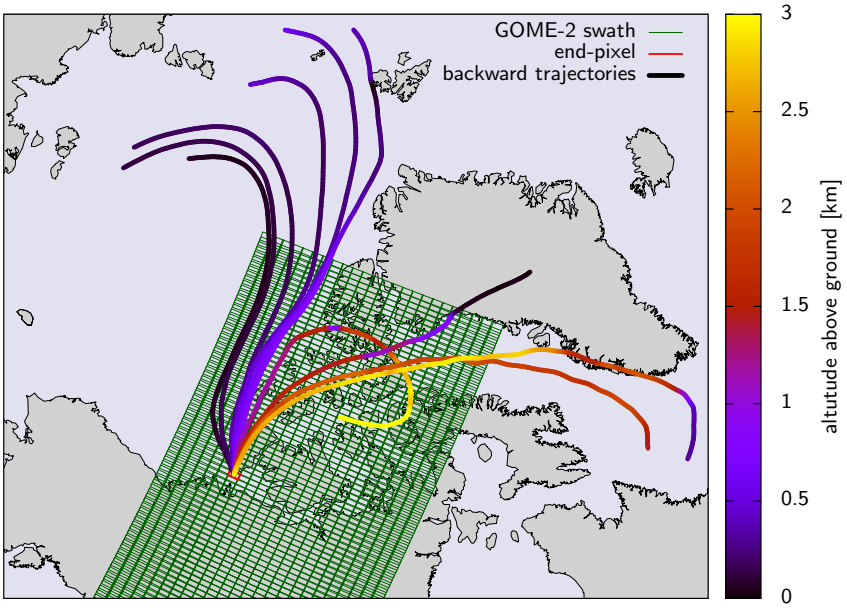

Figure 7.5.: *Backward trajectories (3.5 days) corresponding to a single GOME-2 but ending at 10 different altitudes between 100 m and 3 km. The highlighted pixel also covers the locations of the Amundsen ice-breaker on 13 March 2008.*

measurements, however, another criterion was applied to calculate the surface contact time (Frieß *et al.*, 2004; Simpson *et al.*, 2007a; Wagner *et al.*, 2007; Frieß *et al.*, 2011). In these studies, a fixed height threshold of 100 m above the surface was assumed to assure contact with the surface. Nevertheless, a sensitivity study conducted to find the best threshold level exhibited a significantly better correlation to tropospheric BrO VCDs for the residence times in the boundary layer than the surface contact time. Therefore, the boundary layer height criterion is applied in this work, whereas a more detailed study may be necessary to find a conclusive answer which threshold would generally result in the realistic correlations.

Part III.

Results and Discussion

8. The Barrow campaign, spring 2009

In this chapter, the results from LP-DOAS measurements at Barrow, Alaska, USA are presented. Measurements took place at the Barrow Arctic Research Center (BARC) between March 13 and April 16, 2009 (cf. Section 5.1) to investigate the abundance and distribution of halogen compounds and ozone. The spectral evaluation is presented in Section 8.1. The results are then compared to complementary in-situ measurement in Section 8.2. The correlation between BrO and O_3 mixing ratios at low O_3 concentrations are investigated in Section 8.3. Also, the horizontal variability of BrO at Barrow is investigated using two different LP-DOAS light-paths in Section 8.4. Finally, the BrO results from LP-DOAS are compared to BrO mixing ratios derived from MAX-DOAS measurements by Frieß *et al.* (2011) in Section 8.5. The correlation between both measurements is further discussed in Chapter 9, where results from Barrow are also compared to GOME-2 satellite measurements in order to investigate the vertical and horizontal distribution of BrO.[1]

The research activities during the OASIS campaign at Barrow were manifold (cf. Section 5.1) and allowed the comparison of the data presented here to a number of other data sets. A comparison between BrO mixing ratios obtained from LP-DOAS (this work) and chemical ionization mass spectrometer (CIMS) was published in Liao *et al.* (2011). In this study, an astonishingly well agreement (slope =1.10, r^2=0.74) was found between LP-DOAS and CIMS. The correlation could be even improved when measurements at moderate wind-speeds and low nitric oxide (NO) indicating local pollution were selected (r^2=0.85). The improved correlation is probably due to the elimination of horizontal inhomogeneities of the BrO distribution.

8.1. Spectral evaluation of the LP-DOAS

The DOAS analysis for BrO concentrations was performed on individual LP-DOAS measurements with an integration time between 1 s and 50 s depending on the signal strength (cf. Section 5.1.1). Prior to the DOAS fit analysis, the dispersion of the spectrometer was calibrated using the position of mercury emission lines (Figure 8.1a). The mercury emission line at 334.15 nm was used to derive the instrument slit function of the spectrometer (Figure 8.1b). The spectral analysis was performed in the wavelength interval between 315.5 nm and 348.0 nm and included the cross sections of the trace gases listed in Table 8.1. The applied wavelength interval includes seven strong absorption bands of BrO as depicted in Figure 8.2.

[1] Parts of this chapter are already published in Liao *et al.* (2011), Frieß *et al.* (2011), and Helmig *et al.* (2012).

(a) *spectrograph calibration* (b) *instrument slit function*

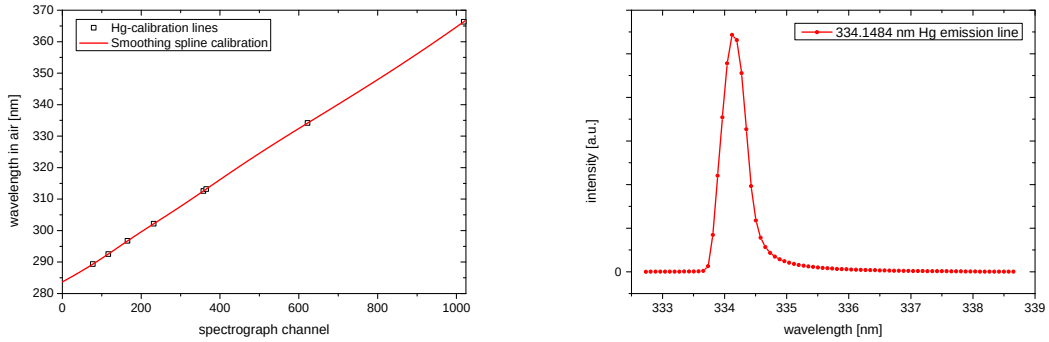

Figure 8.1.: *Spectrometer calibration and instrument slit function of the Acton 300i spectrometer applied in the LP-DOAS measurements at Barrow.*

Usually, the trace gas column densities are determined by fitting a linear combination of the narrow band trace gas absorption structures to the measured optical density spectra $\tau = \ln(I/I_0)$ using a non-linear Levenberg-Marquardt algorithm (Kraus, 2004). In this work, however, the standard evaluation scheme needed to be altered in order to overcome a still relatively large residual background signal. The disadvantageous influence of the high intensity of scattered sunlight on the background signal was amplified by a malfunction of the camera software, which slightly altered the exposure time of measurements and the readout frequency of the different lines depending on the illumination of the CCD. As a result, the effective dispersion of each CCD readout changed slightly when light intensity or exposure time changed, e g. between atmospheric and background measurement, leading to malicious structures in the retrieval.

Three additional correction spectra were therefore added to the set of trace-gas absorption spectra for the analysis. The initial intensity $\ln(I_0)$ (denoted SC) is fitted to the measurement spectrum $\ln(I)$ in order to compensate some of the exposure artefacts. The additional correction spectra consisted of the logarithm of the actual atmospheric background spectrum ln(BG) as well as the squared spectra $\ln(\mathrm{BG}^2)$ (denoted BG2) and $\ln(I_0^2)$ (denoted SC2), which represent the second term of the Taylor expansion of the exponential Beer-Lambert Law. This approach improves the modelling of non-linear artefacts within the otherwise linear DOAS algorithm and was first published by Pukite *et al.* (2010). The calculated optical density as well as the absorption cross sections adapted from the literature were filtered using a binomial high-pass filter with 1000 iterations prior to the analysis. A third-order polynomial accounted for residual broadband structures. Finally, the amplitude of the residual spectrum was used as a quality criterion in order to filter unsuccessful fit results due to poor signal quality. An example evaluation is shown in Figure 8.2.

The spectral analysis yields the column density of each fitted absorber. The path averaged concentration of a particular trace gas is then calculated by dividing its column density by the optical path length. The mixing ratio is calculated from the

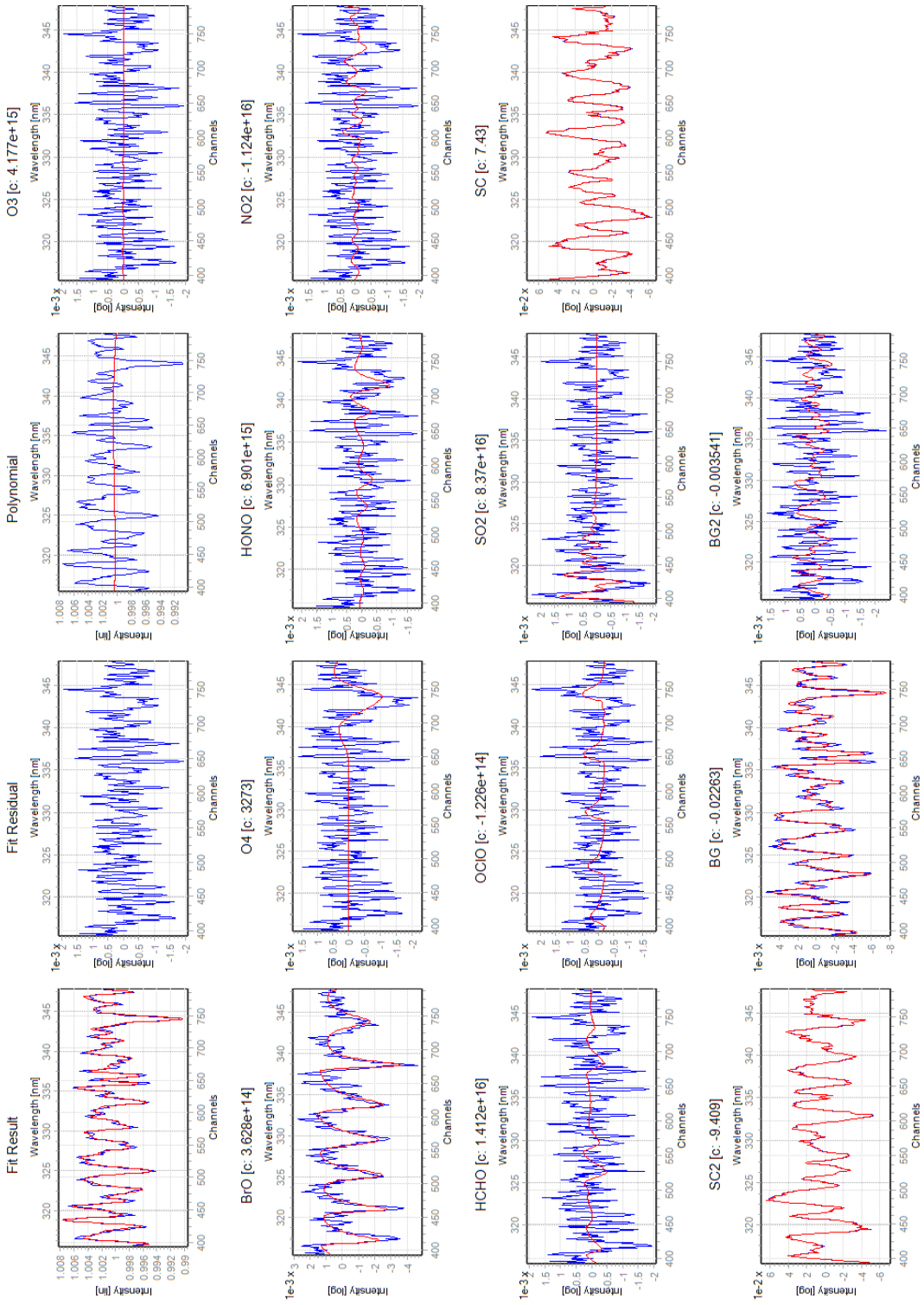

Figure 8.2.: *DOAS fit of an absorption spectrum recorded by the active LP-DOAS instrument at 15:45:55 Alaska Standard Time on April 7, 2009 (7248 m total path length). The BrO result corresponds to a concentration of 5.0×10^8 molec cm^{-3} and a mixing ratio of 17 pmol mol^{-1}.*

Species	Reference	Temperature
O_3	Burrows *et al.* (1999)	241 K
BrO	Wilmouth *et al.* (1999)	228 K
O_4	Greenblatt *et al.* (1990)	
HONO	Stutz *et al.* (2000)	298 K
NO_2	Burrows *et al.* (1998)	241 K
HCHO	Meller & Moortgat (2000)	298 K
OClO	Bogumil *et al.* (2003)	293 K
SO_2	Bogumil *et al.* (2003)	243 K

Table 8.1.: *Compilation of the literature absorption cross-sections applied in the LP-DOAS evaluation.*

concentration using the ideal gas law for air and using on-site temperature and pressure measurements (Section 5.1.3).

8.1.1. Discussion of systematic errors of LP-DOAS measurements

The quality of the DOAS retrieval of the here performed measurements was found to suffer from strong systematic spectral structures. At least three possible causes of these structures could be identified.

1. It was found out after the campaign that the camera software altered the read-out speed of the 2D CCD sensor depending on the illumination. In the applied spectrograph, the dispersion varies over the height of the CCD sensor. One CCD readout is performed by shifting the collected charges vertically into the read-out register of the analog-to-digital converter (ADC). The CCD was still illuminated during read-out. A shutter was omitted in order to increase the effective area of the chip and to use the read-out time for further exposure. However, changes of the readout speed depending on the intensity may have influenced the dispersion between scans. As the intensity varied strongly between atmospheric, background, and reference spectrum, the dispersion between these spectra may have changed due to a varying read-out speed of the ADC. The varying read-out time influences the effective dispersion of the spectra and possibly lead to malicious structures in the retrieval.

2. Varying spectral structures originated from fluctuations of the light source and of ambient illumination (scattered sun light), which was an issue during the day due to reflecting surfaces close to the retro-reflector arrays.

3. The instrument setup relied on the mode-mixing capabilities of the single receiving fibre. An active mode-mixer as proposed by Stutz & Platt (1997) was omitted as it severely reduced the light throughput of the system during tests at Barrow. During previous measurements, Pöhler *et al.* (2010b) applied almost the same instrument also without active mode-mixing without encountering the

structures observed here. Probably the most important difference between the LP-DOAS setup at Barrow and the one by Pöhler *et al.* (2010b) is that another fibre bundle was applied. Whereas Pöhler *et al.* (2010b) applied a bundle whose single fibres had a diameter of 200 µm, at Barrow a fibre bundle consisting of 100 µm fibres was utilized because it delivered a higher light throughput compared to the 200 µm bundle. Comparison measurements later revealed that the mode-mixing capabilities of the applied 100 µm bundle are significantly reduced compared to the 200 µm bundle.

For the LP-DOAS measurements at Barrow, probably a combination of these effects led to inferior spectral quality when compared to the measurements by (Pöhler *et al.*, 2010b). However, it was possible to fine-tune the retrieval parameters in order to at least gain realistic BrO concentrations when compared to other instruments. The results of O_3 and NO_2 were found to be of minor quality but still applicable. The results for the other trace-gases included in the fit (HCHO, OClO, and SO_2) were unrealistic and are discarded.

As a result, the BrO measurements comprise an unknown systematic error arising from malicious narrow-band features in the measured optical density. The measurement error of BrO (σ) of the Levenberg-Marquardt analysis error needs to be multiplied by a scaling factor to account for remaining systematic structures in the residual (Stutz & Platt, 1996). In this work, however, a scaling factor of 1.8 between measurement and retrieval error is determined by comparing the retrieval error with the observed distribution of measurements. The detection limit is estimated to 3σ. This leads to an optimum nighttime detection limit of 2×10^7 molec^{-3}cm (0.7 pmol mol^{-1}) for the long light path and 6×10^7 molec^{-3}cm (2 pmol mol^{-1}) for the short light path. During the day, however, due to larger interferences with sun light scattered into the light path, the detection limits were usually higher depending on the viewing conditions and light-source used. Mean daytime detection limits are estimated to 5×10^7 molec^{-3}cm (2 pmol mol^{-1}) and 1.5×10^8 molec^{-3}cm (5 pmol mol^{-1}) for long and short light paths, respectively.

It is furthermore noted that the absolute calibration of the BrO absorption cross-section also contributes to the systematic error of the measurement. During the measurements of laboratory cross sections it is crucial to determine the exact concentration of the target trace gas (Wilmouth *et al.*, 1999; Fleischmann *et al.*, 2004). The differential cross sections of BrO differ significantly within the literature. Therefore, an additional systematic error of 10 % for the retrieved BrO concentration is a realistic assumption (Dorf, 2005).

8.2. Time-series at Barrow

The time-series of BrO, O_3, and NO_2 mixing ratios as well as the photolysis frequency of Br_2 measured at Barrow are shown in Figures 8.3 and 8.4.

Apart from sporadic outliers in the beginning of the time-series, the LP-DOAS shows significantly positive BrO abundances essentially every day. Measurements applying the shorter light path (green dots) show a larger scatter due to a smaller

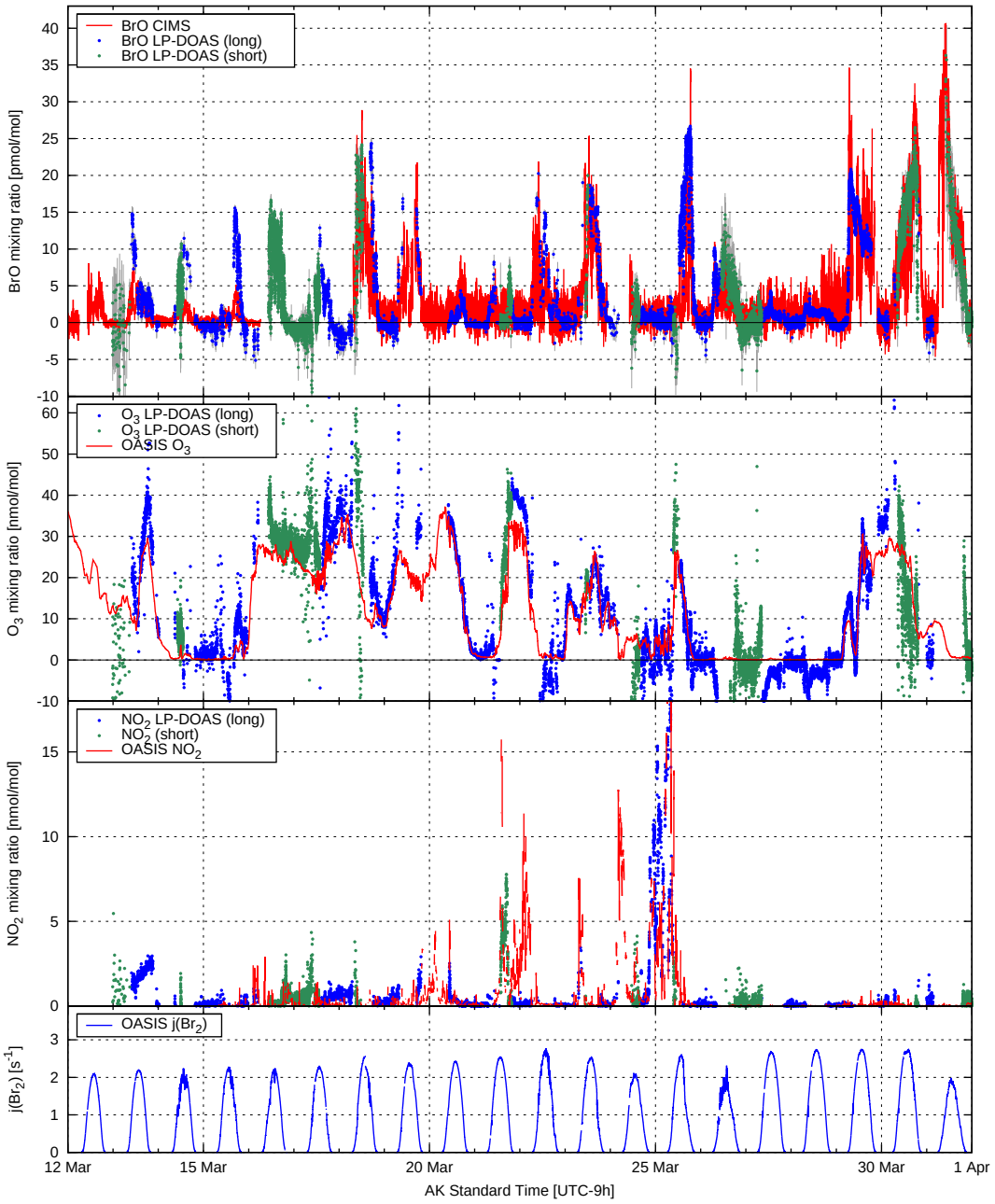

Figure 8.3.: *Results from LP-DOAS and complementary measurements at Barrow in March 2009. The blue and green dots denote LP-DOAS measurements along the short and the long light path, respectively. The red lines denote results form different in-situ instruments. The tick marks correspond to 00:00 Alaska Standard Time. Errorbars are omitted for the sake of clarity.*

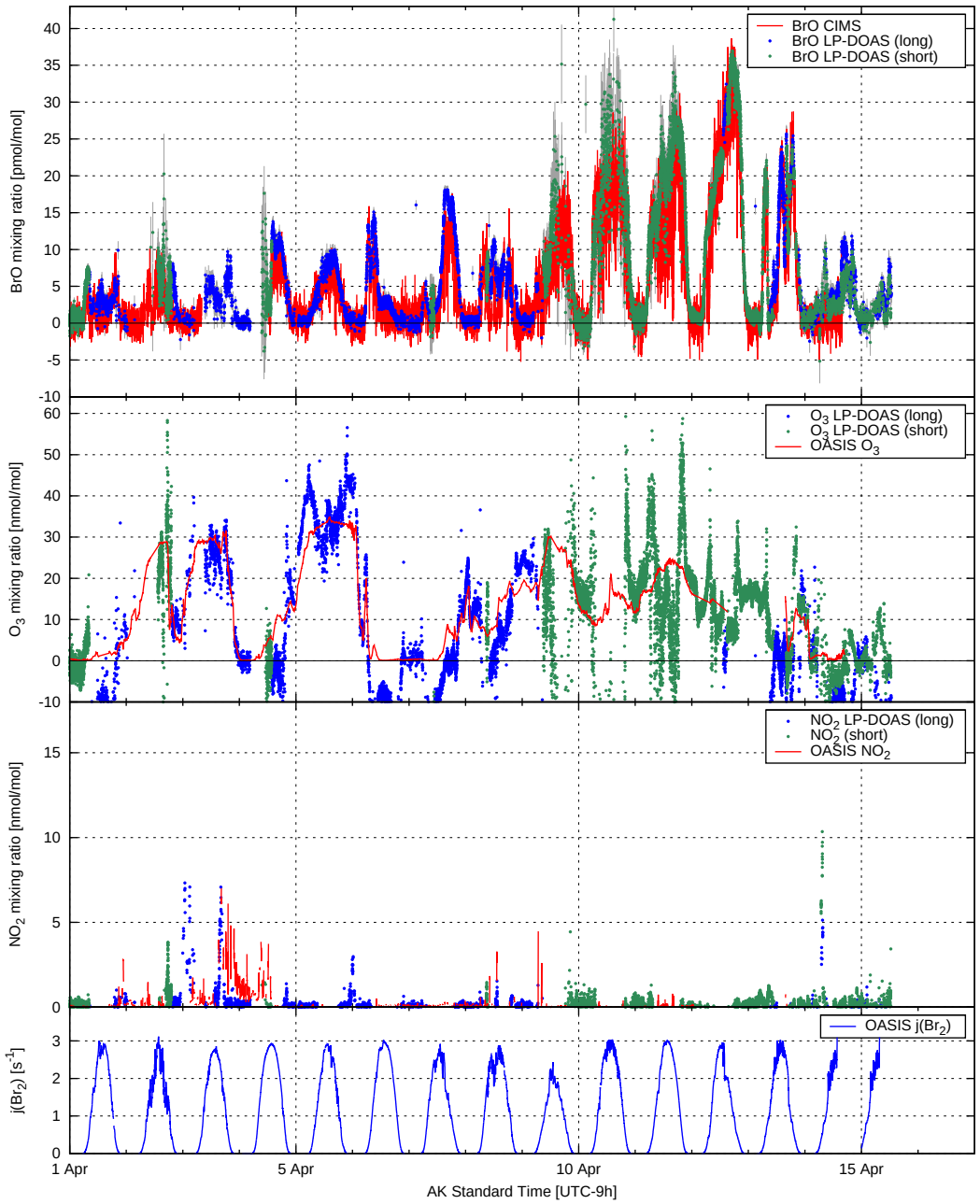

Figure 8.4.: *Continuation of Figure 8.3.*

averaging volume and hence a larger statistical column error. On several days in March peak mixing ratios of around 25 pmol mol^{-1} were reached and values above 35 pmol mol^{-1} could be observed in a succession of days between April 10 and April 12. Night-time mixing ratios are below the detection limit due to the absence of Br radicals production from Br_2 photolysis. The comparison to the CIMS measurements shows striking correlation between both data-sets (Liao *et al.*, 2011).

The O_3 mixing ratios measured by LP-DOAS shows significant scatter and systematic deviations from the in-situ O_3 monitors. Even though the both techniques match occasionally, like on March 20 and 21, the LP-DOAS regularly measures negative values when the in-situ instrument reported near-zero values. It is noted that the applied spectral range is not optimized for the retrieval of O_3. These discrepancies decrease the confidence into the LP-DOAS O_3 measurements and are therefore disregarded in the following discussion. The maximum O_3 mixing ratio during this campaign are between 35 to 40 nmol mol^{-1} depending on the applied instrument and sampling height (Helmig *et al.*, 2012). This background mixing ratio, however, was only reached occasionally. O_3 mixing ratios ranged around 20 nmol mol^{-1} when BrO was most abundant. On several occasions, O_3 was depleted below 100 pmol mol^{-1}. Between March 26 and 28, O_3 was almost completely destroyed and remained at a very low level. This event is discussed below in Section 8.3.

Surprisingly high mixing ratios of NO_2 were also detected at Barrow. On several days, mixing ratios exceeded 5 nmol mol^{-1} and a maximum value of 23 nmol mol^{-1} on March 25 (out of scale). The comparatively large mixing ratios for a presumably pristine Arctic environment are mostly due to local pollution originating from the town of Barrow as discussed in (Liao *et al.*, 2011). Again, there is some correlation between LP-DOAS measurements and in-situ observations. However, the LP-DOAS data has large systematic errors as mentioned above.

8.3. Correlation of O_3 and BrO at low O_3 mixing ratios

BrO cannot be produced from Br in the absence of ozone at very low ozone concentrations. Thus, the steady-state involving BrO and Br is shifted towards Br, which is subsequently converted to reservoir species, such as HBr, and a proportionality between BrO and ozone can be expected. This behaviour has been found during previous studies in Barrow (Simpson *et al.*, 2007b). However, a more detailed investigation of bromine chemistry at very low ozone concentrations was not possible owing to the lack of sensitivity of the ozone measurements at the sub-ppb level. The high sensitivity ozone measurements during the OASIS campaign and BrO measurements by LP-DOAS allow for a more in depth re-examination of this question. A zoom into the time-series of BrO and O_3 for the ozone depletion event (ODE) between March 25 and 29 is plotted in Figure 8.5.

The onset of ODE during the sunset of March 25 is characterized by a decrease in ozone mixing ratios from more than 20 nmol mol^{-1} to below 1 nmol mol^{-1} during less than 6 hours. The rate of ozone decrease was much higher than predicted by photochemical models. It is therefore likely that part of the observed drop in ozone was

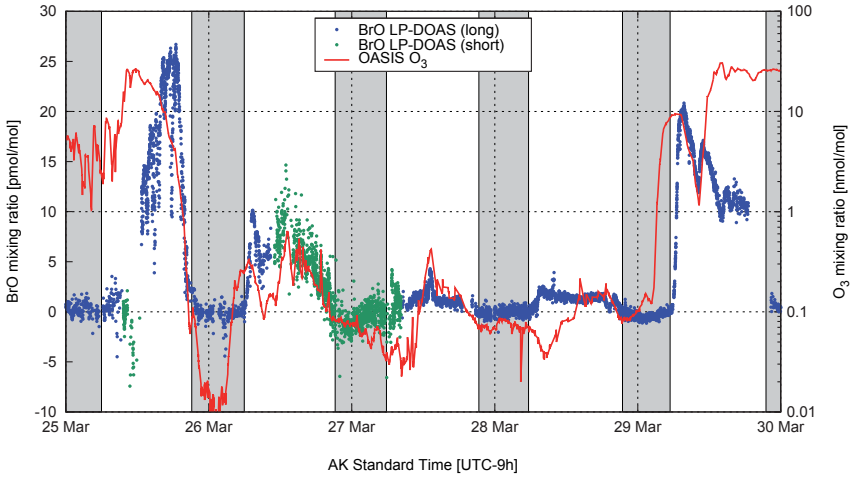

Figure 8.5.: *Time series of BrO and O_3 mixing ratios measured by LP-DOAS and in-situ instruments, respectively. Dark periods ($j_{Br_2} < 1 \times 10^{-5}\,s^{-1}$) are shaded grey. Note that O_3 is shown on logarithmic scale. The tick marks correspond to 00:00 Alaska Standard Time Errorbars are omitted for the sake of clarity.*

caused by advection of air masses already depleted in ozone rather than by in-situ photochemistry. The decrease in BrO mixing ratios from more than 25 pmol mol^{-1} to values below the detection limit was always observed during sunset and the simultaneous decline in ozone for March 25 is most likely coincidental. The same applies to the increase both in ozone and – with a delay of 4 hours – in BrO at the end of this ODE in the night from 28 to 29 March.

During most of this time, however, ozone and BrO are positively correlated. The diurnal variability of both species agrees remarkably well, indicating that, as expected, the formation of BrO is controlled by ozone concentrations at these low ozone levels. It is furthermore noted, that on March 26 BrO mixing ratios up to 10 pmol mol^{-1} could be observed when O_3 fluctuated around 0.5 nmol mol^{-1}. As pointed out by (Helmig *et al.*, 2012), the ozone growth seen in these data is probably from chemical production from NO_x (provided by local pollution) and not from advection of air from aloft with higher ozone into the surface layer at the site.

8.4. Comparison of long and short LP-DOAS light paths

Two light paths with two different lengths were established at Barrow in order to study the spatial variability of BrO distribution (cf. Section 5.1.2). However, an alternating measurement procedure utilizing both light-paths in a rapid succession was realized between April 13 and 15. Earlier attempts were prevented by either poor visibility, wind-stress on the telescope, or stepper-motor malfunction due to cold temperatures. Figure 8.5 shows the time-series of BrO and O_3.

The measurements on April 13 vary between 8 and 25 pmol mol^{-1} of BrO. These

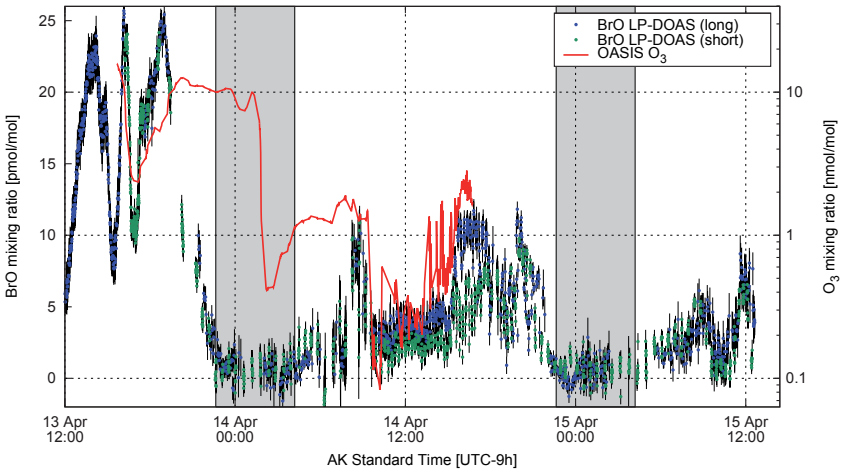

Figure 8.6.: *Time series of BrO and O_3 mixing ratios measured by LP-DOAS and in-situ instruments, respectively. Dark periods ($j_{Br_2} < 1 \times 10^{-5}\ s^{-1}$) are shaded grey. Note that O_3 is shown on logarithmic scale. Errorbars are denoted in black.*

variations are probably due to advection as the coincident decrease of O_3 are again faster than can be explained by photochemistry. On this day, the measurements of both light paths show a good agreement.

The next day, on April 14, O_3 was furthermore depleted leading to a situation similar to the one described in Section 8.3. While approximately the same BrO mixing ratio was measured along both light paths in the morning, the afternoon values again show larger mixing ratio along the longer light-path. However, from the presented measurements it is not possible to judge whether this observation is due to an actual BrO gradient or caused by spectral interferences in the retrieval. One the one hand, the DOAS retrieval for O_3 resulted in values more negative over the long path than over the short path (see Figure 8.4). Therefore, a negative correlation between BrO and O_3 absorption cross-sections can be suspected to cause the differences in the BrO mixing ratio. On the other hand, a BrO gradient can in fact be caused by a O_3 concentration gradient possibly due to a different O_3 production rate from NO_x and snow photochemistry in the snow pack. This hypothesis is supported by the variations of the O_3 mixing ratio measured at the trailers. However, a final conclusion can not be given and future measurement are needed to study horizontal BrO gradients on these spacial scales.

8.5. Correlation with retrieved surface concentrations from MAX-DOAS

Furthermore, MAX-DOAS measurements were performed at Barrow as described in Section 5.1.3 in page 51. The measured SCDs of BrO and O_4 were used to retrieve the vertical profiles of the aerosol optical density as well as the BrO mixing ratio using

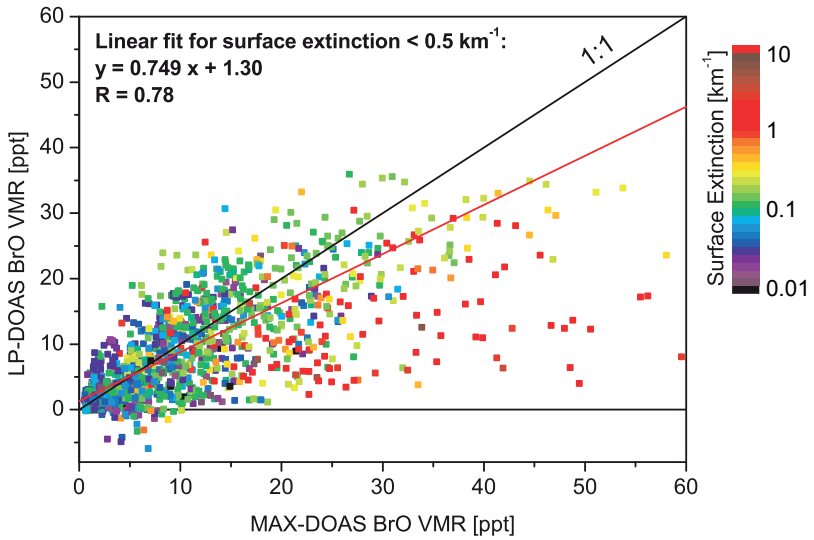

Figure 8.7.: *Correlation of BrO surface mixing ratio from LP-DOAS with the average BrO mixing ratio between 0 and 100 m from the MAX-DOAS retrieval. The color code indicates the surface extinction retrieved from MAX-DOAS. The 1:1 line is shown in black, and the red line shows the linear fit for data points with a surface extinction <0.5 km^{-1}. Adapted from (Frieß* et al.*, 2011).*

the optimal estimation method. The results of this retrieval are discussed in Frieß *et al.* (2011). Here, the BrO mixing ratio at the surface measured by LP-DOAS and retrieved from MAX-DOAS measurements are compared. The quality of this comparison is important for the discussion presented in Section 9.2 in the next chapter, in which also satellite measurements are included.

The correlation between BrO surface mixing ratio from LP-DOAS and from the MAX-DOAS profile retrieval is shown in Figure 8.7. The data points are color coded for the surface extinction retrieved from MAX-DOAS. Good agreement is only found for small to moderate extinction values <0.5 km^{-1}, whereas BrO surface mixing ratios are significantly overestimated by MAX-DOAS at high extinction. This illustrates the limitations of this technique under conditions of low visibility. For a surface extinction <0.5 km^{-1}, a linear fit yields a regression coefficient of R=0.78 and a slope of 0.75, which is caused by the aforementioned overestimation of the BrO concentration by MAX-DOAS at high extinction. The bias between MAX-DOAS and LP-DOAS is only 1.3 pmol mol^{-1}. At this point, it is important to emphasize that LP-DOAS and MAX-DOAS represent very different measurement techniques for BrO, and that a simple correlation analysis needs to be interpreted with caution. LP-DOAS observes the average concentration along a well defined light path, whereas MAX-DOAS observes the average concentration in a layer of several hundred meters thickness. The vertical resolution varies with time, since it is a function of visibility. Furthermore, both instruments do not measure exactly the same air mass, and small delays in the observed temporal variability can reduce the correlation significantly.

9. Comparison of satellite to ground-based measurements

In this chapter, tropospheric BrO VCDs from GOME-2 are compared to both LP-DOAS and MAX-DOAS measurements of BrO obtained during two Arctic field campaigns, respectively. The data of the first campaign to the Amundsen Gulf are described in Section 7.1 and partly published by Pöhler *et al.* (2010b). These include LP-DOAS as well as MAX-DOAS measurements. The data set of the second campaign was obtained at Barrow, Alaska as a part of this thesis. The LP-DOAS measurements were presented in the previous chapter and are already published in Liao *et al.* (2011). Vertical profiles of BrO and aerosols were retrieved from MAX-DOAS data using optimal estimation as described by Frieß *et al.* (2011). Tropospheric BrO VCDs were determined by integrating the retrieved MAX-DOAS profiles (cf. Section 8.5).[1]

Both, ground-based and satellite measurements offer their particular advantages and disadvantages to study the same phenomenon. Resolution and coverage differ between both approaches spatially and temporally. Ground-based instruments usually offer a higher spatial and temporal resolution whereas satellite measurements observe the same property over a vast area at moderate spatial and temporal resolution. In conclusion, a high correlation may only be expected if both techniques sample the same volume of air and spatial as well as temporal variabilities are small. The algorithm for collocating satellite and ground-based measurements is described in Section 7.2.

9.1. Results from comparing satellite with ground-based measurements

This section summarizes the results from both field campaigns which are then discussed in Section 9.2.

For the Amundsen measurements, the time series of MAX-DOAS and LP-DOAS are shown together with the GOME-2 overpass data (cf. Section 7.2) using a sensitivity threshold of $\mathrm{AMF}_{500}^{\mathrm{min}}=1$ in Figures 9.1 and 9.2. The corresponding correlation plots shown in Figures 9.6a and 9.6b, respectively, where the slope a and y-intercept b of a linear bi-variate model (Cantrell, 2008) are calculated based on overpass averages obtained by the collocation scheme described in Section 7.2. The comparison to the MAX-DOAS measurements encompasses more than a month beginning on 9 March 2008. Both instruments, MAX-DOAS and GOME-2, captured several events of elevated tropospheric BrO VCDs including one major event around 14 March. Figure 9.3

[1] Parts of this chapter have been accepted for publication in Sihler *et al.* (2012).

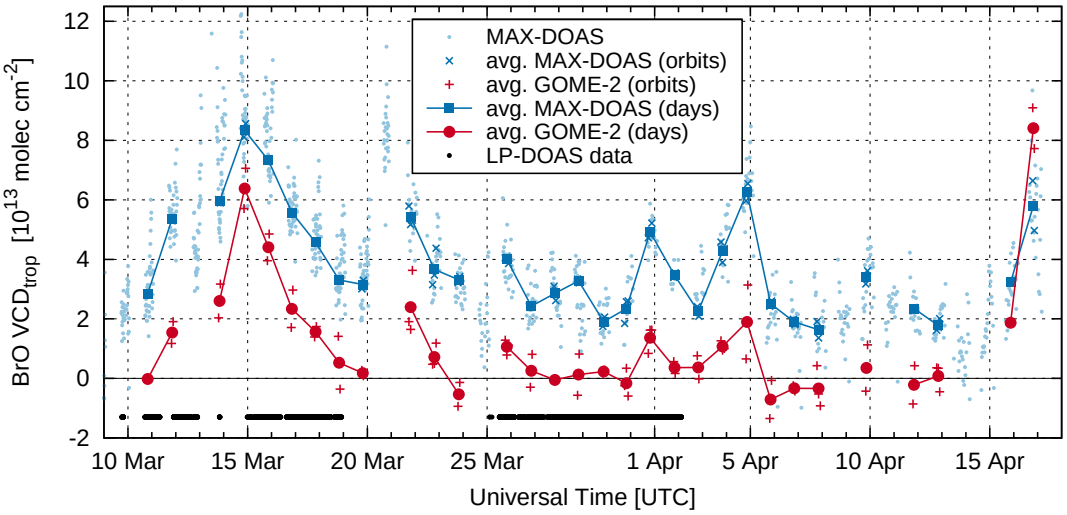

Figure 9.1.: *Time-series of MAX-DOAS BrO VCDs from aboard the Amundsen research icebreaker in 2008 compared to retrieved tropospheric BrO VCDs from GOME-2 (AMF_{500}^{min}=1), same data as in Figure 9.6a. The black dots denote periods of LP-DOAS measurements. Error bars are omitted for the sake of clarity.*

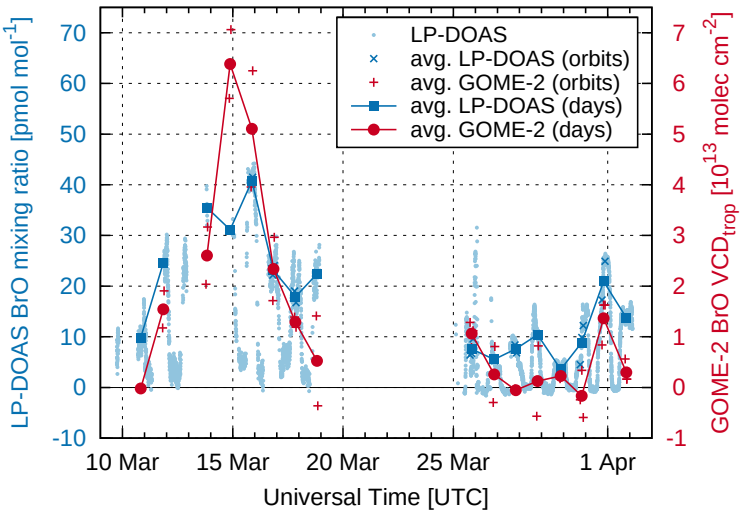

Figure 9.2.: *Same as Figure 9.1 but showing BrO mixing ratios measured by LP-DOAS. Both ordinates are scaled corresponding to a mixing height of 345 m. Correlation in Figure 9.6b.*

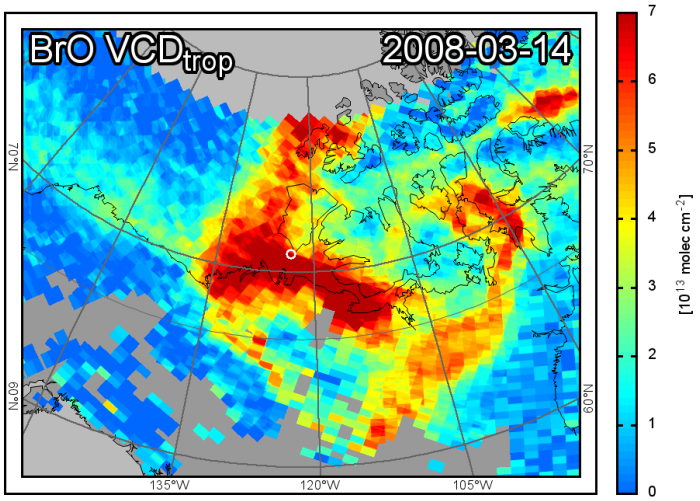

Figure 9.3.: *Satellite map of tropospheric BrO VCDs measured by GOME-2 on 14 March 2008. The circle denotes the position of the Amundsen icebreaker. Further maps of the Amundsen campaign are shown in Appendix C.1.*

shows a map of this particular event. The GOME-2 data furthermore reveal another particularly strong enhancement on 16 April 2008. The amplitudes of the collocated MAX-DOAS VCD time series are almost identical (slope close to unity), but there is a significant bias. The tropospheric column densities retrieved from GOME-2 measurements are systematically smaller by approx. 3×10^{13} molec cm^{-2} than measured by MAX-DOAS (Figure 9.6a). The LP-DOAS measurements of the BrO mixing ratio, however, encompass only 16 days with collocated GOME-2 measurements interrupted by 5 days of cruise. The LP-DOAS measured up to 42 pmol mol^{-1} of BrO on 15 March when major enhancements were also observed by GOME-2 (see supplement). The slope in Figure 9.6b is approx. 500 m which represents an estimate for the BrO layer thickness.

The time series of both MAX-DOAS and LP-DOAS measurements at Barrow are shown in Figures 9.4 and 9.5, respectively. More than a month of collocated measurements with GOME-2 from mid March to mid April 2009 are available. Compared to the measurements form aboard the Amundsen, the amplitudes of BrO enhancements (VCDs and mixing ratios) were generally smaller at Barrow. The correlations between GOME-2 and MAX-DOAS (Figure 9.6c) as well as GOME-2 VCD and LP-DOAS mixing ratio (Figure 9.6d) are weaker but statistically significant (n=77, r^2=0.1, p=0.005). The slope in Figure 9.6c reveals that the BrO VCDs retrieved from MAX-DOAS measurements are approx. twice as high as the collocated GOME-2 measurements. However, the offset between both data sets is significantly smaller than for the Amundsen measurements.

It is important to note that the temporal variability of LP-DOAS mixing ratios at Barrow occasionally deviates from GOME-2 tropospheric VCDs (Figure 9.5). There are several days where the LP-DOAS measured above 10 pmol mol^{-1} while the GOME-2 VCDs are close to zero (16, 23, 29 March, and 11 April). On 14 March, however,

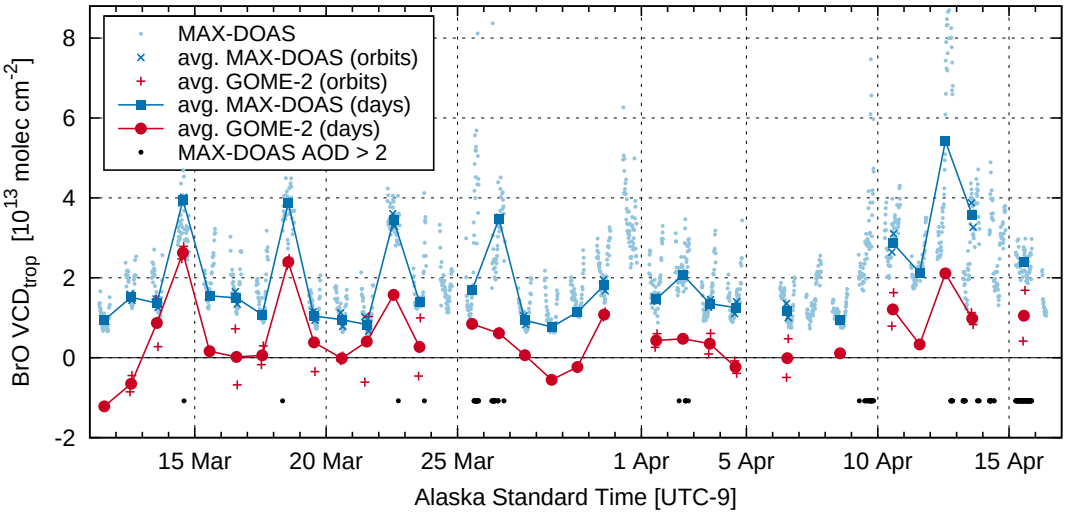

Figure 9.4.: *Time-series of retrieved BrO VCDs from ground-based MAX-DOAS measurements at Barrow, Alaska, 2009 compared to retrieved tropospheric BrO VCDs from GOME-2 (AMF_{500}^{min}=1), same data as in Figure 9.6c. Black dots denote MAX-DOAS measurements, where the surface aerosol optical density (AOD) exceeded 2. Error bars are omitted for the sake of clarity.*

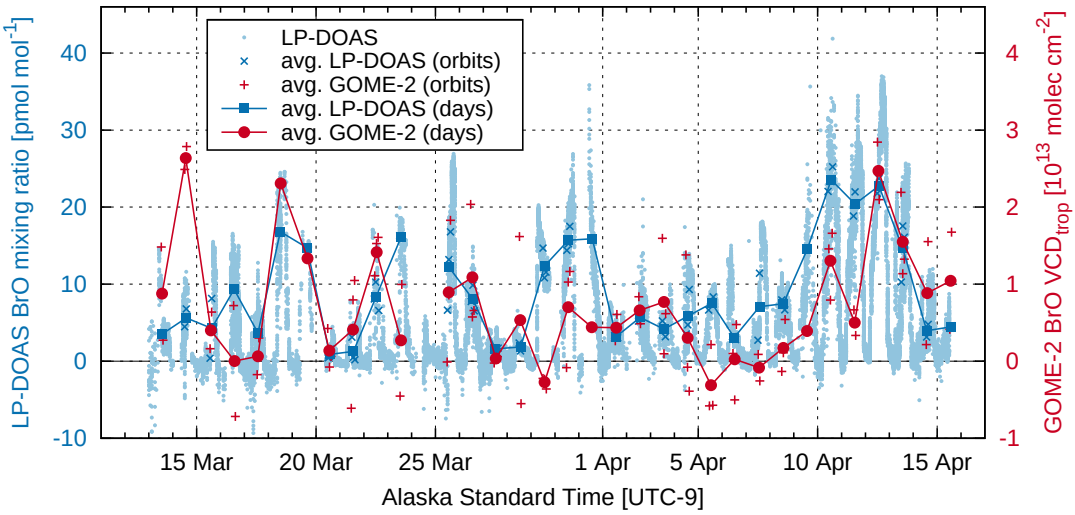

Figure 9.5.: *Same as Figure 9.4 but showing BrO mixing ratios measured by LP-DOAS. Both ordinates are scaled corresponding to a mixing height of 345 m. Correlation in Figure 9.6d.*

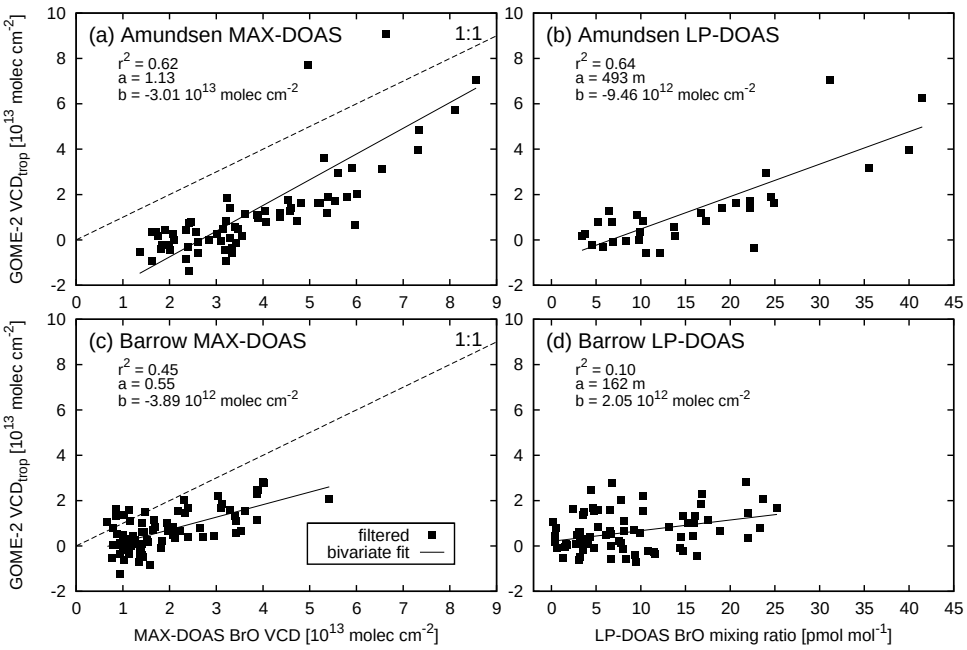

Figure 9.6.: *Correlation and orthogonal fit of the different ground-based data-sets with VCD_{trop} measured by GOME-2 (AMF_{500}^{min}=1). Note that the slopes in (b) and (d) are given in unit meter comparable to the height of the mixing-layer (assuming ρ_{air}=2.9×10^{19} molec cm^{-3}). Error bars are omitted for the sake of clarity.*

both GOME-2 and MAX-DOAS show significantly elevated BrO columns while the LP-DOAS measured comparatively moderate 7 pmol mol^{-1}. These differences are discussed in Section 9.2.

Finally, the dependence on the sensitivity threshold $\mathrm{AMF}_{500}^{\mathrm{min}}$ is studied. The correlation coefficient r^2 is calculated for all four ground-based data sets and collocated GOME-2 measurements for different $\mathrm{AMF}_{500}^{\mathrm{min}}$ between 0.5 and 4 (Figure 9.7). Furthermore, the respective number of remaining collocated measurements are shown. As already mentioned, the correlation between satellite and ground-based measurements is larger for the Amundsen than for the Barrow data. The increase in r^2 with $\mathrm{AMF}_{500}^{\mathrm{min}}$ is consistent for both MAX-DOAS comparisons indicating that the proposed sensitivity filter in fact identifies measurements with ambiguous sensitivity (Figures 9.7a and 9.7c). For the LP-DOAS measurements, however, the trend for r^2 is less clear. For the Amundsen data, the correlation with LP-DOAS mixing ratios decreases significantly for $\mathrm{AMF}_{500}^{\mathrm{min}}$>2. At Barrow, r^2 increases only for rather high thresholds $\mathrm{AMF}_{500}^{\mathrm{min}}\geq$3 when more than half of the collocated measurements are filtered. For $\mathrm{AMF}_{500}^{\mathrm{min}}$=3.2 the correlation between LP-DOAS and GOME-2 is r^2=0.19 (see discussion bellow).

Gridded maps of daily satellite measurements corresponding to both time-series can be found in the supplement to this paper.

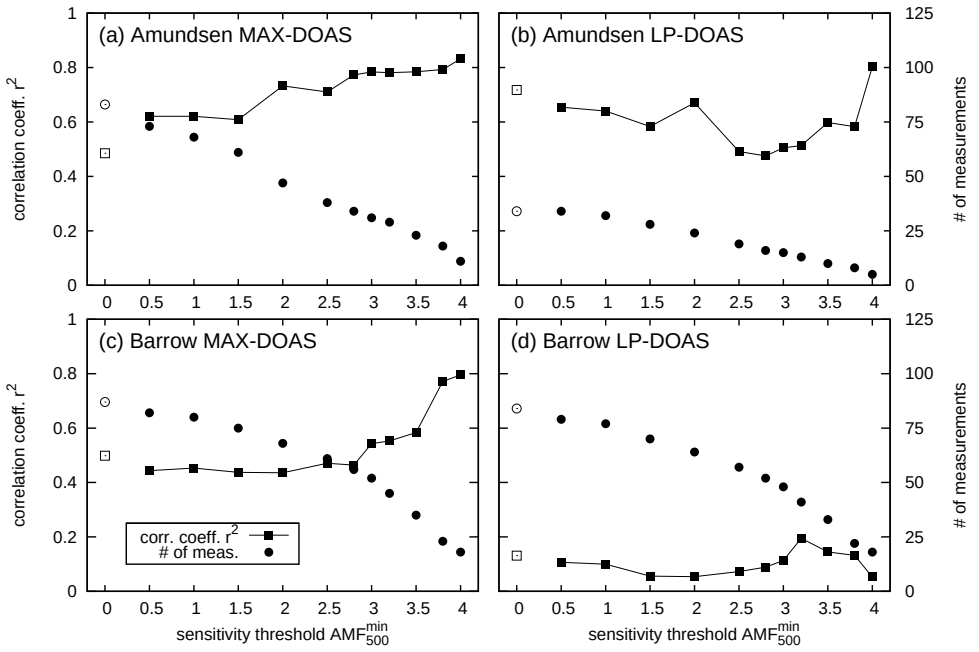

Figure 9.7.: *Correlation coefficient r^2 and number of collocated measurements depending on the applied sensitivity threshold AMF_{500}^{min}. Empty symbols denote correlations without sensitivity filter and geometric AMF applied.*

9.2. Discussion of comparison with ground-based measurements

The comparisons between ground-based and satellite measurements of BrO show a good agreement, demonstrating the capability of the presented method to retrieve realistic tropospheric BrO column densities from GOME-2 measurements. The deviation from unity slopes for the correlation between GOME-2 VCDs and ground-based MAX-DOAS measurements for Amundsen and Barrow may be explained by a systematic difference of the sensitivity of both techniques with respect to the real distribution of BrO. The negative offset of GOME-2 VCDs compared to both MAX-DOAS time series possibly indicates that the presented algorithm underestimates the integrated tropospheric column. This systematic difference may be a result of the column separation algorithm (Section 6.4) for which it was assumed that the tropospheric column enhancement may reach zero. Hence, the negative offset indicates that there might be some residual BrO present almost everywhere in the Arctic during spring when also both presented LP-DOAS time series report significant BrO abundances every day (Pöhler *et al.*, 2010b; Liao *et al.*, 2011). However, it is difficult to give a quantitative interpretation because both MAX-DOAS data sets were evaluated using different algorithms with different systematic errors. Furthermore, both MAX-DOAS and the GOME-2 retrieval apply different AMFs which may furthermore lead to systematic differences. E. g., the AMFs applied for the Amundsen measurements did not account

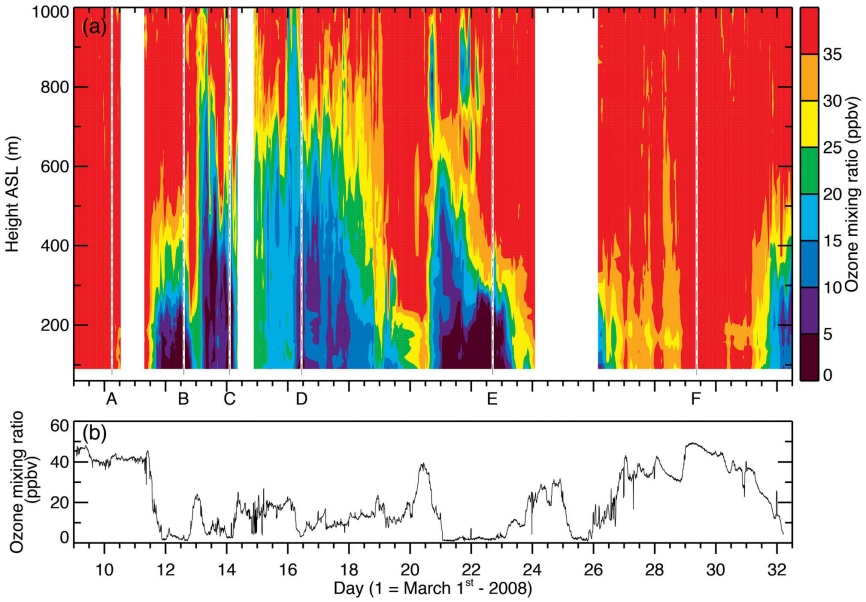

Figure 9.8.: *Ozone measurements aboard the Amundsen near the onset of polar sunrise (9 March to 2 April 2008). (a) LIDAR measurements as a function of time and height above sea level. Omitted data includes periods of repair time on the DIAL, as well as periods of low-level clouds or ice fog that interfered with the ozone retrieval. (b) In situ ozone measurements with air sampling on the top deck of the ship, 25 m above sea level. Adapted from (Seabrook* et al.*, 2011).*

for aerosol scattering which alters the sensitivity of the MAX-DOAS measurement with respect to GOME-2.

The comparison of LP-DOAS measurements aboard the Amundsen in spring 2008 and GOME-2 VCDs clearly indicates that surface concentrations of BrO may provide significant contributions to the BrO column of more than 6×10^{13} molec cm^{-2} on 14 March. This corresponds to a surface BrO column extending to approx. 500 m altitude (Figure 9.6b) in agreement with the height of the simultaneously measured O_3-depleted layer reported by Seabrook *et al.* (Figure 9.8 2011). The map of tropospheric BrO column densities (Figure 9.3) shows a particularly large area affected by bromine activation. It is hence concluded, that this particular "BrO cloud" is located at the surface but not in elevated layers, at least not at the location of the Amundsen vessel.

At Barrow, however, the correlation between LP-DOAS and GOME-2 measurements was much weaker than seen on the Amundsen vessel. There are several potential explanations for this behaviour.

1. The Barrow time series is much longer and the correlation comprises several strong events of elevated BrO levels. The height of the chemically perturbed boundary-layer varied strongly between these events (Frieß *et al.*, 2011; Helmig *et al.*, 2012). Therefore the assumption of a linear correlation may not be ap-

propriate.

2. Located onshore, the local meteorology as well as surface processes related to bromine activation at Barrow may differ fundamentally from that over the sea ice. Furthermore, ground-based O_3 measurements at Barrow revealed large horizontal heterogeneities (Liao *et al.*, 2011; Helmig *et al.*, 2012) which may bias the LP-DOAS measurements with respect to the satellite.

3. The uncertainties of the sensitivity of the satellite measurement to the surface due to the nearby opening in the sea ice are large (cf. Section 6.5.3). In fact, increasing AMF_{500}^{min} at Barrow resulted in an increased r^2 supporting this hypothesis. However, the comparison between MAX-DOAS and GOME-2 measurements at Barrow shows a good agreement despite the offset. Furthermore, the correlation of surface concentrations as measured by LP-DOAS and retrieved from MAX-DOAS measurements is significant as shown in Figure 8.7 on page 129.

This indicates that the VCDs measured by GOME-2 are realistic and, hence, the variations of the BrO profile at Barrow were probably larger than during the Amundsen campaign where only one major event was captured by LP-DOAS. Occasionally enhanced near-surface BrO concentrations correspond to a shallower average mixing height of BrO as reproduced in Figure 9.6d. In the following, two example days are selected in order to illustrate the vertical variability of the BrO profile.

As mentioned above, the LP-DOAS data in Figure 9.5 show on several days considerably higher enhancements than GOME-2. This discrepancy can be explained by a very shallow layer of BrO (Figure 9.9b). All shown MAX-DOAS profiles decrease to background values at altitude above 250 m.

Another interesting event was captured at Barrow on 14 March 2009. GOME-2 observed a significantly elevated BrO column while the LP-DOAS shows only moderate levels of bromine activation. However, the comparison with the integrated tropospheric VCD from MAX-DOAS again shows good agreement and the apparent discrepancy between LP-DOAS and GOME-2 therefore indicates the presence of an elevated layer of enhanced BrO concentrations as suggested by e. g. Hönninger & Platt (2002), Wagner *et al.* (2007), and Frieß *et al.* (2011). In this context, the term elevated denotes a layer of enhanced BrO at a few hundred metres which are still within the boundary-layer. On this day, O_3 levels were below 1 nmol mol^{-1} suggesting a limited production of BrO at the surface (Helmig *et al.*, 2012). As sampled by an ozonesonde launched at Barrow (Figure 9.9a), the O_3 mixing ratio increases with altitude allowing for a more efficient BrO production at these altitudes. Furthermore, the potential temperature gradient profile suggests a highly stratified boundary layer as well as a strong temperature inversion at the surface ($\sim$50 m) hampering O_3 mixing from aloft. This conclusion is supported by BrO profiles retrieved from MAX-DOAS measurements from the same day as depicted in Figure 9.9a (Frieß *et al.*, 2011). Despite one outlier retrieved from measurements around 11:30 AST, all retrieved profiles feature a positive BrO gradient close to the surface. However, most BrO is still located within the boundary layer.

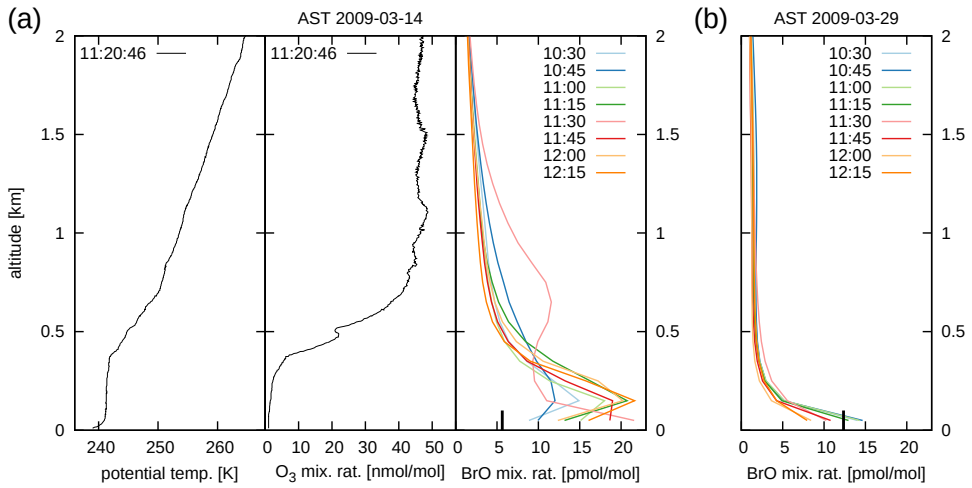

Figure 9.9.: *(a) Profiles of potential temperature, O_3, and BrO mixing ratio at Barrow on 14 March 2009. (b) BrO profile on 29 March 2009. The marks at the bottom of the BrO profiles denote the values measured by LP-DOAS. Potential temperature and O_3 are measured by ozonesonde (courtesy of NOAA Earth System Research Laboratory). BrO profiles are retrieved from MAX-DOAS measurements (Frieß* et al.*, 2011).*

From the data presented in this chapter, it is concluded that events of enhanced BrO are well captured by satellite measurements, and that ground-based observation and tropospheric VCDs retrieved from GOME-2 data are significantly correlated. The surface-near concentrations measured by LP-DOAS furthermore indicate, that the satellite observations in turn are linked to surface processes as observed from aboard the Amundsen. At Barrow, however, deviations from this general dependence could be explained by local meteorological perturbations and variations of the surface BrO column height. Occasionally, satellite measurements may underestimate the influence by bromine activation when the surface BrO layer is extremely shallow and horizontal gradients of both the chemistry and the surface sensitivity are large. The general applicability of this observation, however, needs to be tested further because the presented study comprises only a relatively small number of ground-based observations over the sea-ice.

10. Distribution of BrO in the polar atmosphere

One of the greatest advantages of satellite measurements is the possibility to map the distribution of trace-gases on a global scale. While the last chapter was dedicated to the comparison between ground-based and satellite measurements, this chapter extends the focus on the whole Arctic and Antarctic utilizing the advantageous coverage provided by satellites. However, since the developed retrieval for polar tropospheric BrO VCDs (see Chapter 6) is at present not applicable to the southern hemisphere most of the presented observations are limited to the northern hemisphere. Here, satellite measurements of polar bromine activation are presented which are compared to additional data sources in the subsequent Chapter 11.

This chapter begins with observations of the annual cycle of total BrO column densities in both hemispheres (Section 10.1). After that, tropospheric BrO VCDs are presented (Section 10.2) and the seasonal pattern of Arctic regions frequently witnessing bromine activation is investigated (Section 10.3).

10.1. Total BrO columns in the Arctic and Antarctic

In this section, the distribution of total BrO column densities in both polar regions are investigated. Maps of total BrO column densities are calculated from normalized total BrO SCDs (Section 6.4) using the stratospheric AMF shown in Figure 6.7 for a tropopause height of 12 km. The presented data are based on of GOME-2 measurements obtained between February 2007 and June 2010 at an SZA below 80°.

As discussed in Section 6.4, maps of total BrO VCDs are potentially biased by systematic variations of the tropopause height. Furthermore, variations of the surface albedo due to snow and sea-ice alter the sensitivity for near-surface layers leading to interferences with the total BrO column. Both major influences on the total column are corrected for in the developed retrieval for tropospheric BrO (Chapter 6). However, the new algorithm is only applicable to the northern hemisphere and tropospheric VCDs may only be calculated for areas with a significant sensitivity for near-surface absorbers. Total BrO column densities, on the contrary, can be calculated for both hemispheres.

The presented maps of monthly mean BrO distribution show similar spatial and temporal patterns as previously published observations by the GOME instrument Wagner (e.g. 1999); Wagner *et al.* (e.g. 2001); Richter *et al.* (e.g. 2002); Hollwedel *et al.* (e.g. 2004). GOME-2, however, features a fourfold higher spatial resolution than GOME (80 instead of 320 km across-track pixel size) improving the possibility to identify smaller structures like the sea-ice edge and topographic features.

(a) *the Arctic* (b) *the Antarctic*

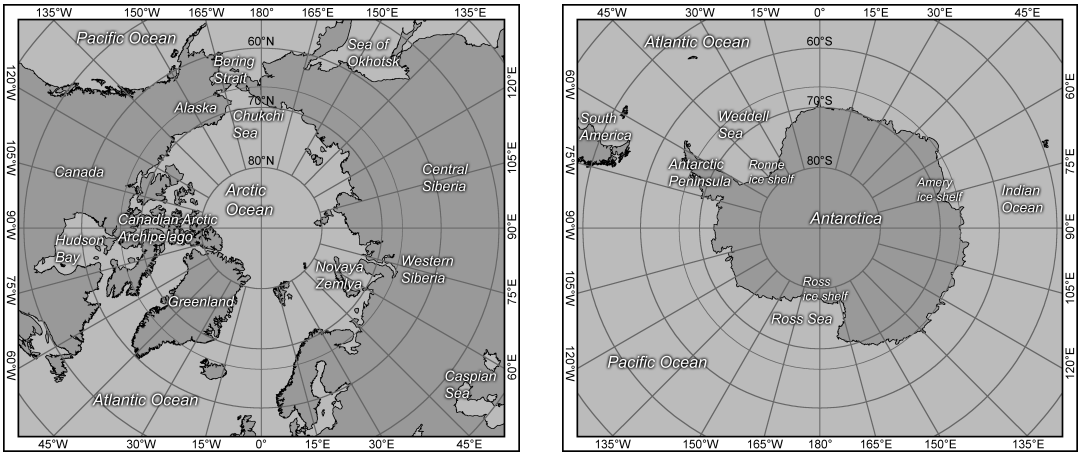

Figure 10.1.: *Names of geographical regions in both hemispheres which are discussed in the text.*

10.1.1. Total BrO column densities in the Arctic

Maps of the monthly mean BrO distribution over the Arctic are shown in Figure 10.2.

Beginning in mid-winter with January, there are already some areas of enhanced BrO columns visible at the northern edge defined by the SZA threshold of 80°. The sea-ice covered Hudson Bay (see Figure 10.1a for geographical names in the northern hemisphere) shows the earliest BrO mean column density enhancement between 5 and 6×10^{13} molec cm^{-2}. In February, also the Sea of Okhotsk, the Chukchi Sea and areas at the northern coast of Western Siberia show significantly enhanced levels. As the sun continues to rise in spring, essentially the entire atmosphere over the sea-ice covered Arctic show enhanced BrO VCDs in March and April. In March the Canadian Arctic Archipelago appears to show the largest enhancements of more than 7×10^{13} molec cm^{-2}, while in April, however, the largest enhancement can be found over the Chukchi Sea and the East Siberian coast. Furthermore, there appears to be some BrO enhancement north of the Caspian Sea and continued to the east. In the second half of the year, the BrO VCD over the Arctic Ocean and adjacent land masses are not considerably enhanced.

Furthermore, the VCDs over Greenland show an interesting behaviour: During the first five months, the BrO VCDs over Greenland are smaller than over the adjacent Arctic Ocean. Between July and September, however, the BrO VCDs over Greenland are comparatively larger. From the measurements presented here, it cannot be judged if this observation is real because the observations over Greenland are prone to systematic errors due to the high ground elevation and large surface albedo. On the one hand, however, ground-based measurements by LP-DOAS conducted at Summit, Greenland on top the Greenland ice sheet in May 2007 and June 2008 reported BrO mixing ratios of up to 5 ppt (Stutz *et al.*, 2011). The BrO is suspected to be produced by snow photochemistry and peaks in morning and evening hours while a drop of

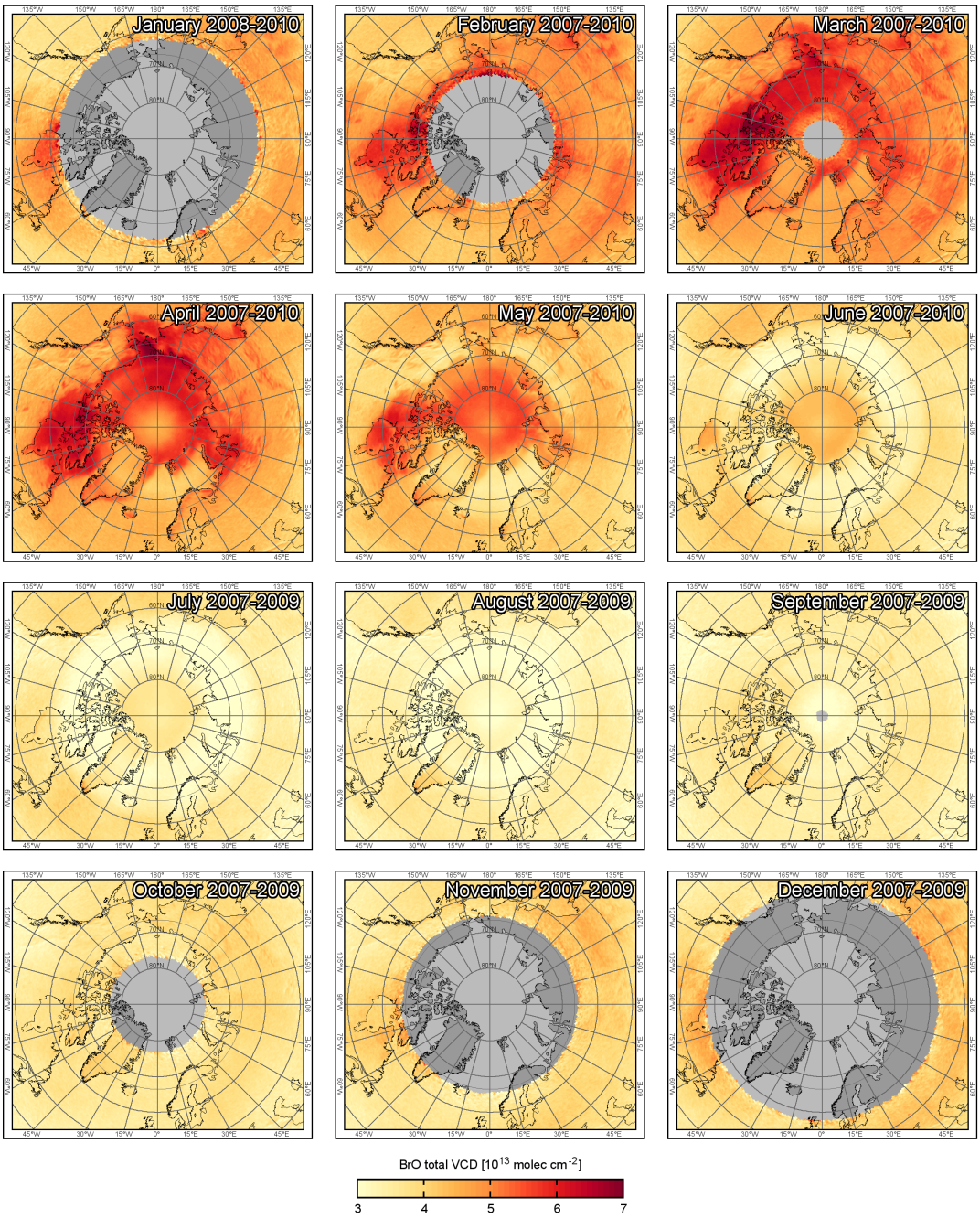

Figure 10.2.: *Monthly means of BrO total column densities in the Arctic. Total columns calculated using a purely stratospheric AMF. Areas without measurements with an SZA below 80° are left gray.*

BrO during the day is explained by a dilution of BrO into the open troposphere. On the other hand, the large surface albedo of Greenland increases the sensitivity to tropospheric BrO and thus increasing the total observed column which may also explain this weak signal.

Finally, the maps of total BrO VCDs also reveal systematic errors and problems of the BrO retrieval. First of all, the spring maps feature strong gradients visible especially in the Atlantic ice-edge. One the one hand, these gradients may be caused by large sensitivity gradient between the open and ice-covered ocean. On the other hand, however, these gradients between ocean and sea-ice may be in fact due to the chemistry as observed from ship-borne measurements in the Antarctic by Wagner *et al.* (2007). Furthermore, the surface relief seems to produce some structures (e. g. Rocky Mountains in Northern America, the Central Siberian Plateau, and the Caucasus Mountains west of the Caspian Sea).

10.1.2. Total BrO column densities in the Antarctic

Maps of the monthly mean BrO distribution over the Antarctic are shown in Figure 10.3. The time-series is shifted by six months in order to account for shifted seasons of the southern hemisphere.

The season of enhanced BrO columns in the southern hemisphere starts in August. Even though there are almost no observations over the Antarctic continent available, the mean BrO VCDs clearly show enhanced columns over the sea-ice adjacent to the Weddell Sea, the Ross Sea, and at the coast close to the Amery ice shelf (see Figure 10.1b for geographical names in the southern hemisphere). During September and October, there are enhanced mean BrO VCDs essentially present over the entire Antarctic sea-ice whose extent is exemplary shown in Figure 10.4a for October 1, 2007. The enhancements over the sea-ice continue until as late as January or even sporadically February which is considerably longer than in the Arctic. When compared to the sea-ice extent as measured by AMSR-E on February 1, 2008 (Figure 10.4b), the distribution of the enhanced BrO VCDs over the ocean is clearly confined to the areas potentially covered by sea-ice. However, whether this confinement is either due to the increased sensitivity over sea-ice or the realistic BrO distribution, can not be inferred from satellite measurements alone. As published by Wagner *et al.* (2007), ground-based measurements like MAX-DOAS offer a much higher sensitivity to near-surface BrO and are therefore suitable to answer this question. Furthermore, Wagner *et al.* (2007) conclude from their measurements a high probability that BrO is in fact confined to the area covered by first-year sea-ice.

Furthermore, it is interesting to note that the mean BrO columns over the Antarctic continent again show a strong correlation to the surface elevation, e. g. high BrO columns over the relatively low shelf-ice regions of the Ronne ice shelf and the Ross shelf ice. But also the mountain ridge of the Antarctic Peninsula can be identified in the BrO maps by comparatively low VCDs. As discussed above for Greenland, enhanced BrO VCDs are also visible inland ($\varphi \leq 80°$S) even until March. This is a puzzling observation because the probable source of bromine, the sea-ice, is more than 1000 km away from these enhanced areas. It may only be speculated here that again

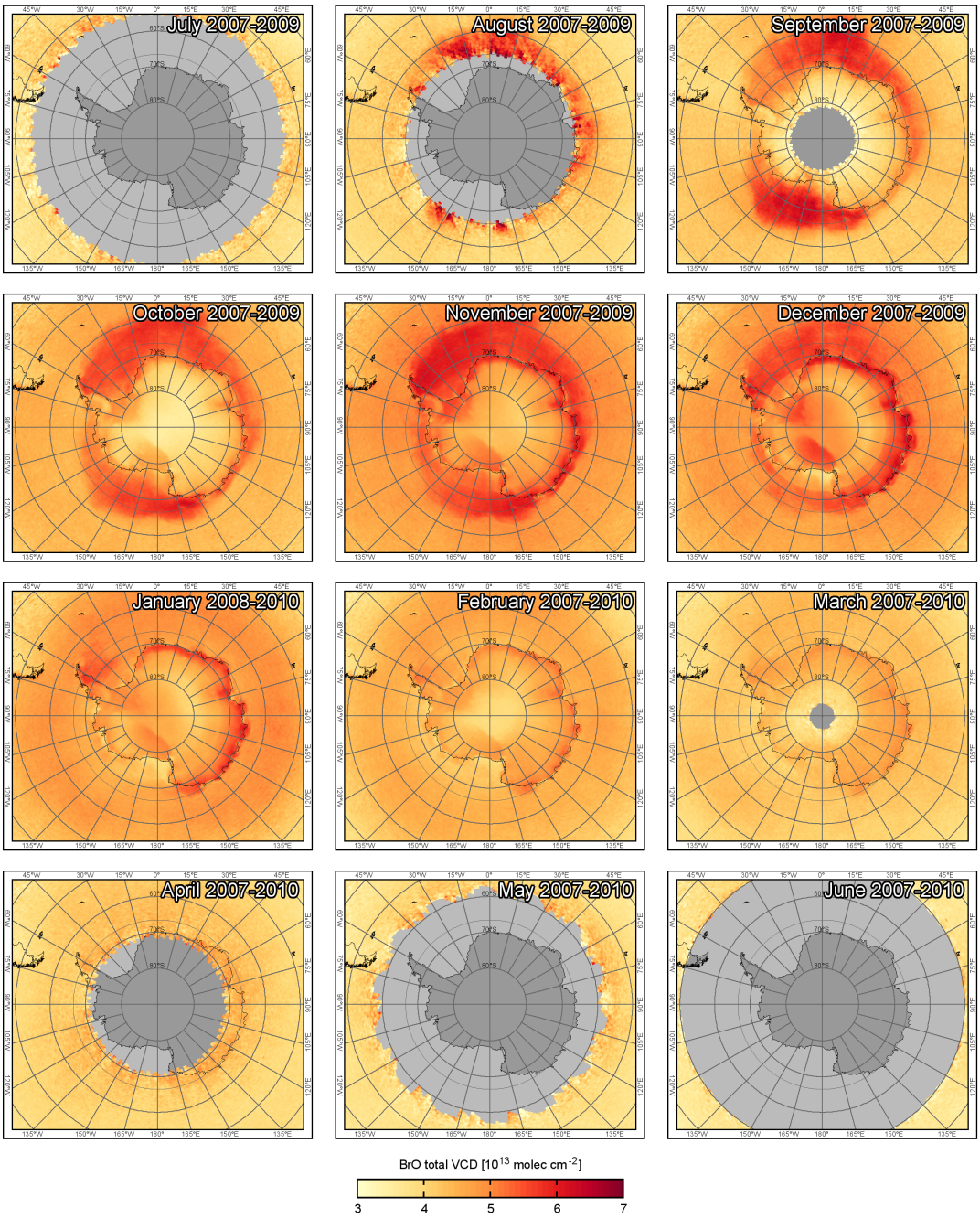

Figure 10.3.: *Monthly means of BrO total column densities in the Antarctic. Total columns calculated using a purely stratospheric AMF. Areas without measurements with an SZA below 80° are left gray.*

(a) *October 1, 2007*

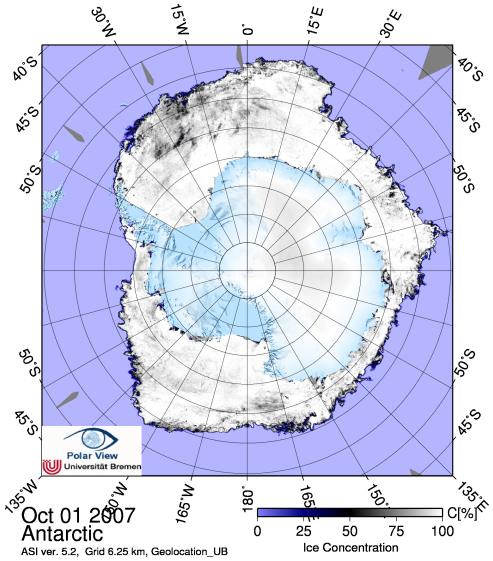

(b) *February 1, 2008*

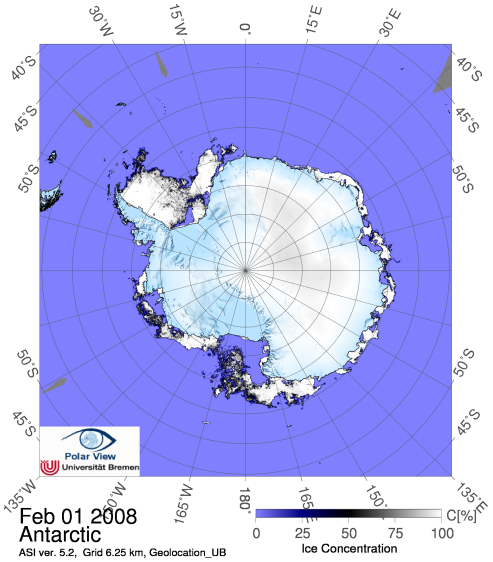

Figure 10.4.: *Sea-ice concentration around Antarctica measured by AMSR-E microwave sounder on (a) October 1, 2007 and (b) February 1, 2008. Courtesy of University of Bremen, Germany (Spreen* et al.*, 2008).*

snow photochemistry potentially recycles bromide from transported sea-salt aerosols to form BrO. Ground-based measurements would be required in order to confirm this hypothesis and to study the underlying processes.

10.2. Tropospheric BrO column densities in the northern hemisphere

In this section, it is switched from total to tropospheric BrO VCD as retrieved by the newly developed algorithm presented in Chapter 6. With this algorithm it is possible to select measurements with an assured surface sensitivity. Again, the data consists of GOME-2 measurements obtained between February 2007 and June 2010 at an SZA below 80°. Figure 10.5 shows the resulting monthly mean tropospheric BrO VCDs using the calculated AMF_{500} for $\mathrm{AMF}_{500}^{\mathrm{min}}$=1.

The distribution of surface sensitive measurements is discussed first. Then, the amplitude of the tropospheric BrO VCD enhancements are discussed for mid-latitudes and the Arctic separately below.

In polar regions, there are no measurement possible in the UV/vis spectra range due to the absence of sun light. This leads to the large data gaps in the center of the maps. In December and January, the largest areas of surface sensitive measurements are the snow-covered plains of Central Siberia and Northern America. From February on, the maximum latitude of sensitive measurements increases enabling measurements over Scandinavia, the Canadian Arctic Archipelago and the coast of the Arctic Ocean. As

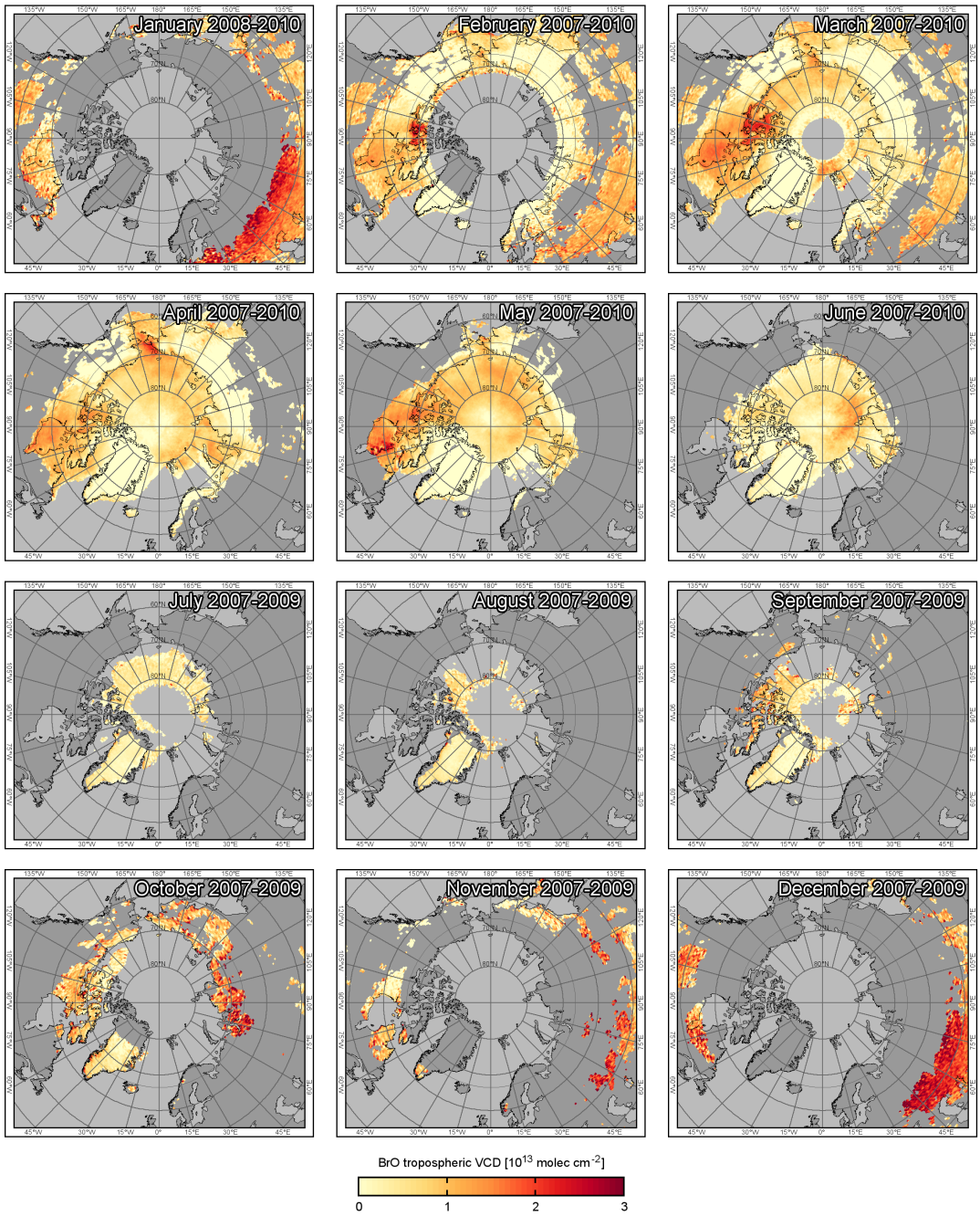

Figure 10.5.: *Monthly means of BrO tropospheric column densities in the Arctic. Areas without measurements sensitive to the surface (AMF_{500}^{min}=1) are left gray. Singular outliers are filtered.*

snow and sea-ice thaw during summer, there are less and less sensitive measurements available. During April and May, the area of sensitive measurements shows a reasonable pattern defined by the sea-ice edge (e. g. North Atlantic and Bering Strait) and snow-covered continents (North America and Siberia).

10.2.1. Tropospheric BrO column densities in mid-latitudes

It may be surprising to note, that the Central Siberian plains exhibit enhanced columns of up to approx. 2.5×10^{13} molec cm^{-2} during winter (December, January, and February). The BrO enhancements over Siberia are rather large and may be due to the bromine released from sea-ice on the Caspian Sea as discussed by Wagner *et al.* (2001). However, the area exhibiting enhanced tropospheric BrO reaches from Central Siberia to Europe suggesting a much larger bromine source than previously assessed. Therefore, it needs to be tested if the observed tropospheric BrO columns are plausible in order to formulate a justified conclusion (Figure 10.6).

The first question to be addressed is whether the tropospheric enhancement is visible in the total columns as well. Figures 10.6a and 10.6b show the total BrO VCD without and with the surface sensitivity filter applied, respectively. A careful inspection of the spatial structures reveals that similar patterns of slightly elevated total VCDs around 50°N also pass the surface sensitivity filter (e. g. areas denoted with ellipses in Figure 10.6b). On the one hand, these structures are possibly due to stratospheric BrO whose AMF is slightly also depending on the surface albedo as illustrated in Figures 6.6 and 6.7 on pages 72 and 73, respectively. On the other hand, these structures may also be due to BrO concentrations in the free troposphere or even in the boundary layer ground as (Fitzenberger *et al.*, 2000; Wagner *et al.*, 2001; Richter *et al.*, 2002; Van Roozendael *et al.*, 2002; Hendrick *et al.*, 2007; Theys *et al.*, 2007, 2011).

The second question to be addressed is why the tropospheric VCDs for January (Figure10.5) are significantly more enhanced over Eurasia than over North America despite the same latitude band. This question may be answered by the longitudinal asymmetry of the stratospheric BrO VCDs retrieved from total O_3 VCDs as depicted in Figures 10.6c and 10.6d, respectively. Retrieved stratospheric BrO VCDs are significantly smaller over Eurasia than over North America due to a smaller O_3 VCD over this area which may again have at least two reasons. One reason could be a statistically higher tropopause over Eurasia, the other reason could be that the stratospheric chemistry is longitude-dependent potentially leading to systematic errors. However, measurements potentially within the polar vortex were discarded, and, hence, the chemistry should be similar. Therefore, the influence of systematic errors due to the stratospheric correction at different tropopause heights remains unanswered. In RT simulations presented in Figure 6.7 it was shown that the ratio of stratospheric BrO AMF and O_3 AMF depends only slightly on the tropopause height over bright surfaces. However, the ratio is <1.05 for an SZA$<80°$ which would result in a smaller BrO VCD compared to the O_3 VCD. The effect of the tropopause height is therefore negligible if not even resulting in systematically smaller tropospheric VCDs.

In conclusion, the enhanced tropospheric BrO VCDs over Siberia/Eurasia at lati-

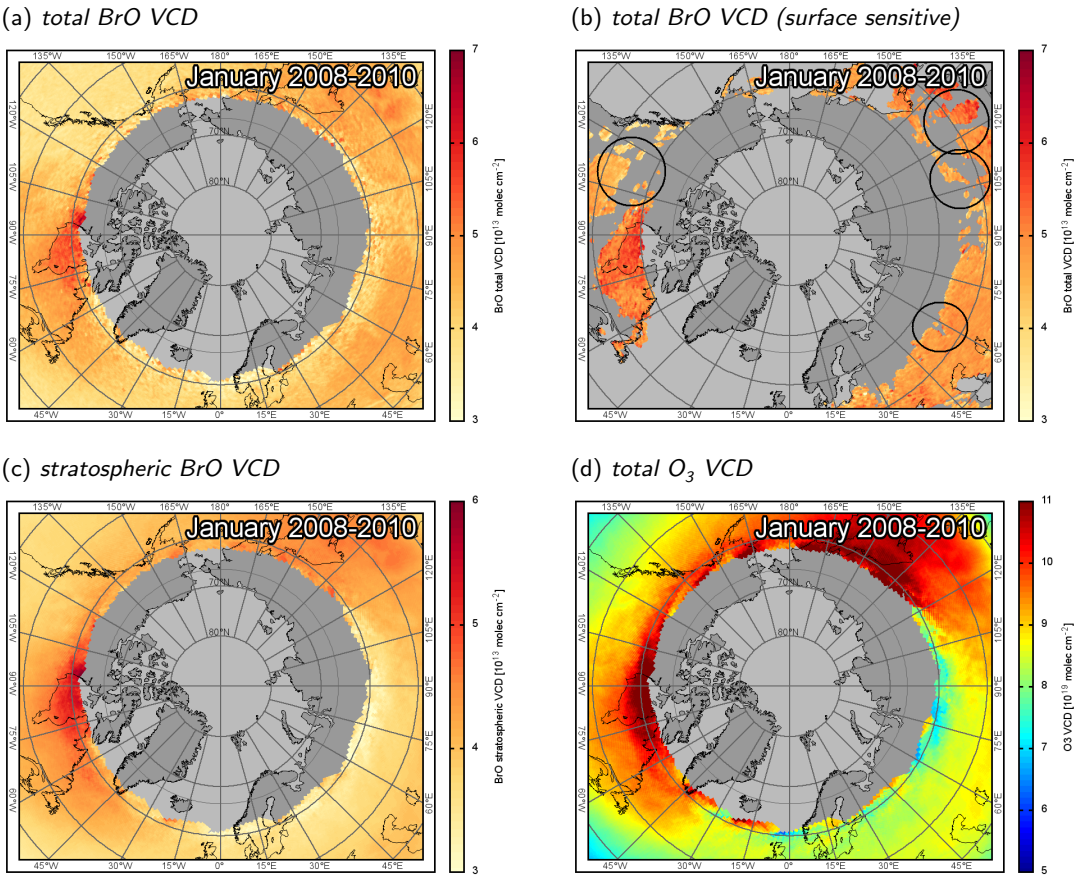

Figure 10.6.: *Mean BrO and O_3 column densities in January between 2008 and 2010. (a) total BrO VCD (same as in Figure 10.2 but without measurements within the polar vortex), (b) total BrO VCD with AMF_{500}>AMF_{500}^{min}=1 (same pixel selection as in Figure 10.5), (c) retrieved BrO stratospheric VCD, and (d) total O_3 VCD. The ellipses in (b) denote example regions exhibiting spatial structures also visible in (a).*

tudes around 50°N in January seem to be realistic, even though a possible interference from a longitude-dependent stratospheric chemistry outside the polar vortex may not completely be ruled out. The reason for the enhancement are likely to be either BrO in the free troposphere or in the boundary layer. However, some questions remain open: (1) If the enhancement is due to BrO in the free troposphere, why is it then larger over Siberia than over North America? (2) If the enhancement is due to the boundary layer chemistry, what are then the sources of reactive bromine far away from oceanic sources such as sea-ice? Ground-based measurements are required in order to further investigate the nature of the observed tropospheric BrO enhancement at mid-latitudes and to investigate the vertical distribution of BrO in winter.

10.2.2. Tropospheric BrO column densities in the Arctic high-latitudes

Finally, turning again to higher latitudes, the months February till June (depicted in Figure 10.5) are investigated towards tropospheric BrO in the Arctic. During July through January, tropospheric BrO columns are either very low ($<1\times10^{13}$ molec cm^{-2}) or there are no surface sensitive measurements in the entire high Arctic. In February, the areas most enhanced in BrO are those most north and limited by the SZA threshold ($\leq80°$) in the Chukchi Sea, the southern waterways within the Canadian Archipelago, and Western Siberia. Also in March, the largest tropospheric BrO VCDs are retrieved over the Canadian Archipelago. This observations is studied in detail in Section 11.1. In April, however, the largest BrO VCDs are measured in the Bering Strait. Mean tropospheric BrO VCD above 1.5×10^{13} molec cm^{-2} are detected over the Arctic sea-ice throughout April and May but decrease towards June. In addition to the areas covered by sea-ice, the land surfaces adjacent to the sea-ice show enhanced BrO values, in particular between the Canadian Archipelago and the Hudson Bay as well as the West Siberian coast.

10.3. Areas of significantly elevated BrO column densities and seasonal evolution

In this section, the distribution of elevated BrO levels in the Arctic spring is studied on a more general level than in the previous section. In Section 6.4, a criterion for significantly elevated BrO SCDs was defined which is used here to study the seasonality of elevated measurements over an area relative to the number of measurements of the same area. In the following, a tropospheric BrO SCD larger than two standard deviations (2σ) of the stratospheric mode (cf. Figure 6.19 on page 88) is assumed to be significantly elevated due to tropospheric bromine activation. The threshold for a significantly elevated measurement can be set arbitrarily and also 3σ is frequently used. As shown in Appendix B, however, the qualitative probability distribution of significantly elevated BrO SCDs for the presented data is, despite the amplitude, almost independent from the significance threshold.

The spatial distribution of significantly elevated tropospheric BrO SCDs is studied using the following five categories

1. the number of measurements at a certain location
2. the number of measurements with a significantly elevated BrO SCD
3. probability to observe a significantly elevated BrO SCD, i. e. the fraction of 2 and 1
4. probability for measurements sensitive to boundary layer (as 3 but only sensitive measurements)
5. probability for possibly obscured and significantly elevated measurements (as 3 but only measurements that are not sensitive to the boundary layer)

The complete GOME-2 data set between 2007 and 2010 is divided into periods. Each period contains all measurements of half a month and of all four years. The distribution of all five categories and for eight half month periods are shown in Figures 10.7 till 10.10 on pages 152 till 155, respectively. The selection of data between 14 February and 15 June is chosen because there is only a limited number of observations prior to this period (polar night) and there are almost no observations of elevated BrO columns after mid-June. The choice of half month periods presents a trade-off between high temporal resolution and still good statistics without producing too many plots.

The number of all measurements (left column in Figures 10.7 and 10.8) show a radial structures whose symmetry is slightly altered in March and April due to asymmetry of the polar vortex which is more frequently located over the Eurasian sector and which is discarded during the retrieval process (cf. Section 6.4). The high values above 73°N indicate that this area is sampled more frequently due to the orbit parameters of MetOp-A and the swath width of GOME-2. The number of significantly elevated BrO columns (middle column in Figures 10.7 and 10.8) can be compared to the probability density distribution (right column in Figures 10.7 and 10.8, left column in Figures 10.9 and 10.10).

Most dominantly in the early phase of the season between February and the end of March, the sea-ice waterways of the Canadian Arctic Archipelago exhibit the highest probability to observe elevated BrO SCDs. Up to 50 % of the measurements in this region are significantly elevated. Other regions showing enhanced probabilities are Hudson Bay (and the land between Hudson Bay and the Archipelago) and Siberia. However, when comparing the probability distribution depending on the retrieved surface sensitivity (Figures 10.9 and 10.10) one notes a clear difference between both regions. The right column of Figures 10.9 shows that in Period 2 there are almost no significantly elevated measurements over the sea-ice meaning that practically all measurements of enhanced BrO are also sensitive to the surface-near BrO. However, most significantly elevated measurements over Siberia are flagged possibly obscured indicating that these elevated column potentially have a different vertical distribution which might be underestimated by the 500 m box-profile assumed for the sensitivity filter (cf. 6.3.2).

In April, the probability distribution of significantly enhanced BrO SCDs is different. Highest probabilities can now be found in the Bering Strait as well as over the central Arctic Ocean. The comparison to the sensitivity flag exhibits, that especially over the Arctic Ocean, the probabilities are much higher for the possibly obscured measurements than for the sensitive measurements. This is a puzzling observation, especially because it vanishes toward Period 8, in which sensitive measurements over sea-ice again have a higher probability to be significantly elevated compared to possibly obscured measurements. Possibly, either uplift above clouds or, more complex, processes linked to the production of BrO are linked to processes generating thick cloud or aerosol layers higher up triggering the sensitivity filter in the middle of the season. These processes may include condensation of clouds due to air-mass uplift or uplifted windblown snow due to high wind-speeds at the surface. Finally, the last significant BrO enhancements are most probably observed over the sea-ice in the Siberian sector of the Arctic until the beginning of June. This asymmetry may be

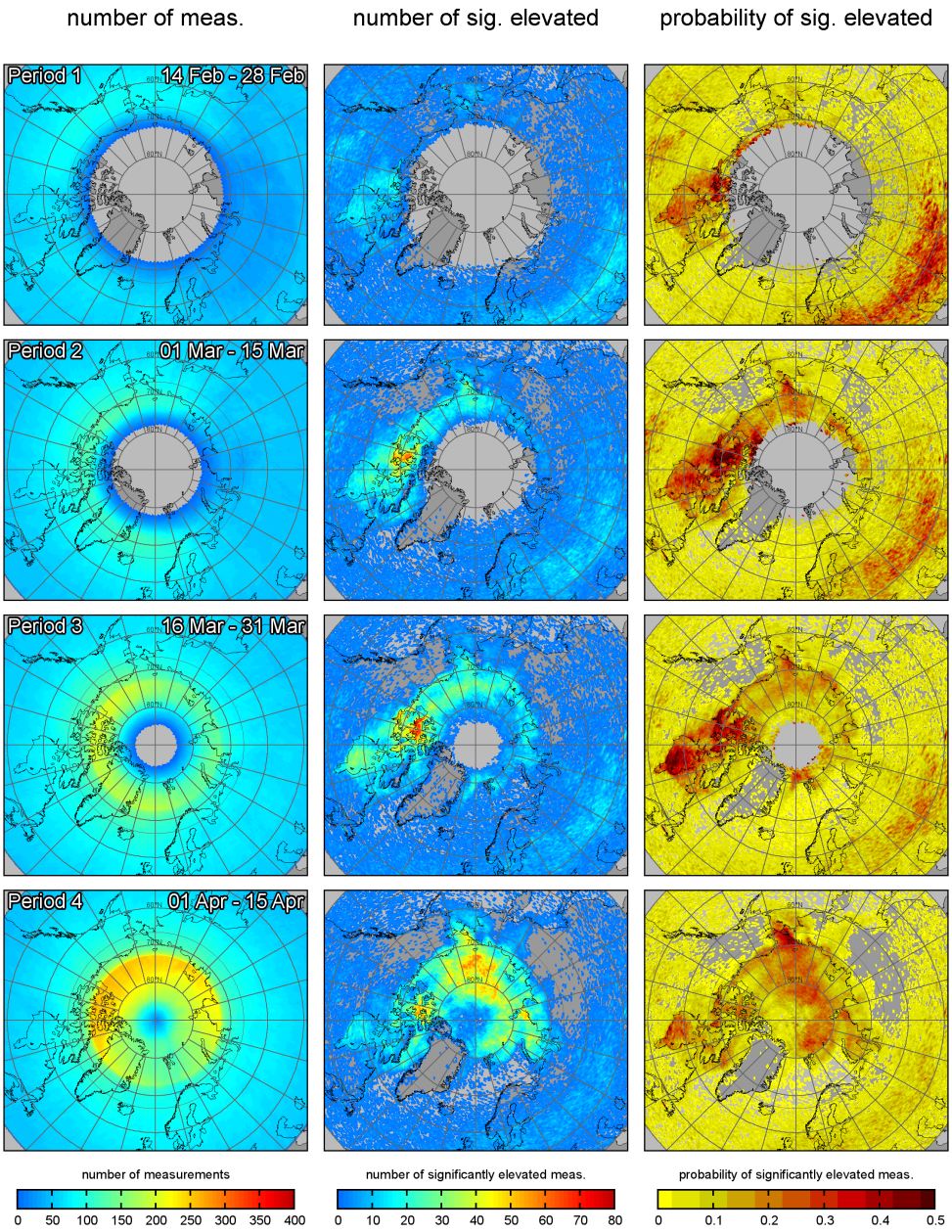

Figure 10.7.: *Distribution of all BrO measurements in Arctic Spring between 14 February and 15 April combining the years 2007 to 2010. Left column: number of measurements. Middle column: number of significantly elevated BrO columns. Right column: probability for measurements with a significantly elevated column. Areas without measurements and above 80° SZA are left gray. The asymmetric distribution of measurements (left column) is due to the ozone hole filter criterion (see Section 6.4).*

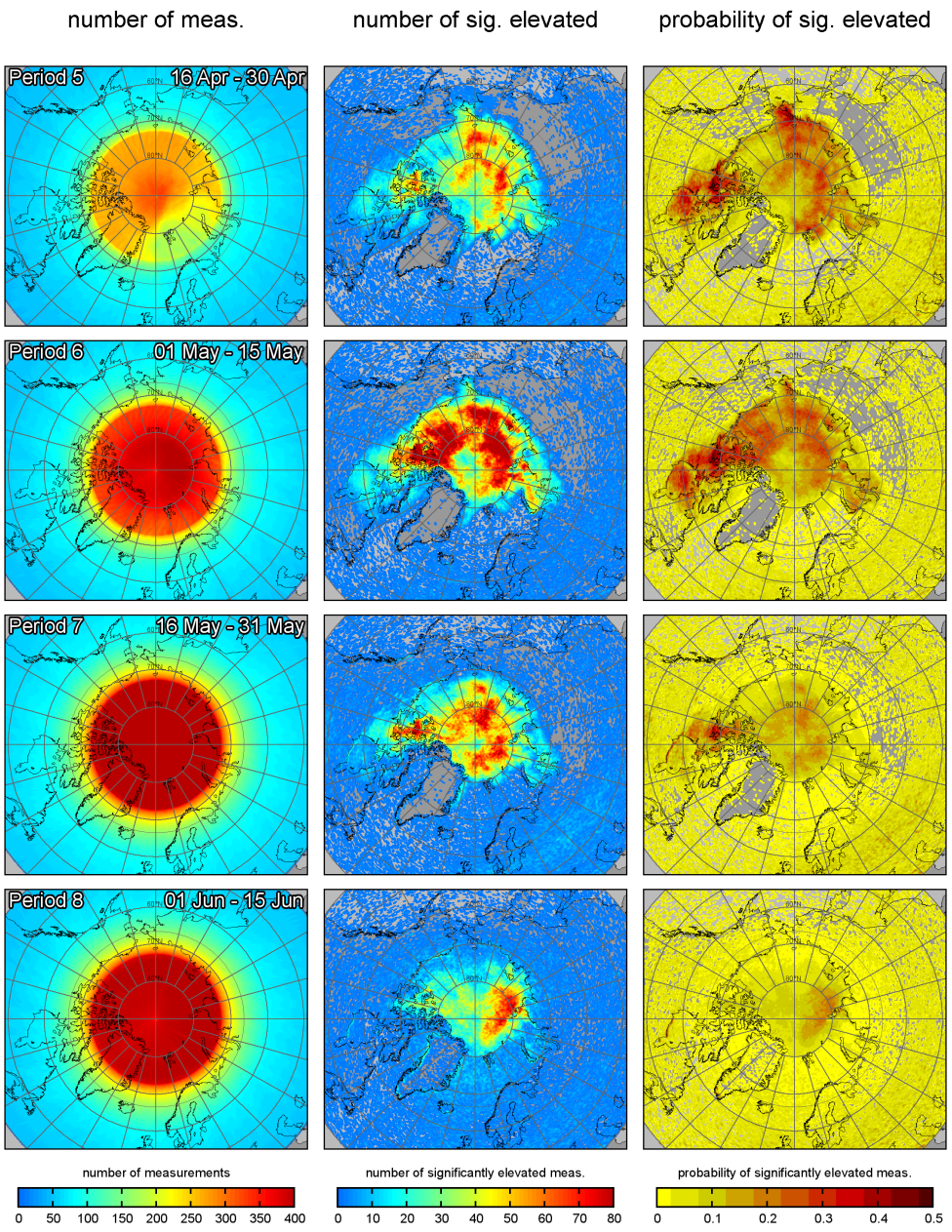

Figure 10.8.: *Continuation of Figure 10.7 but showing measurements between 16 April and 15 June.*

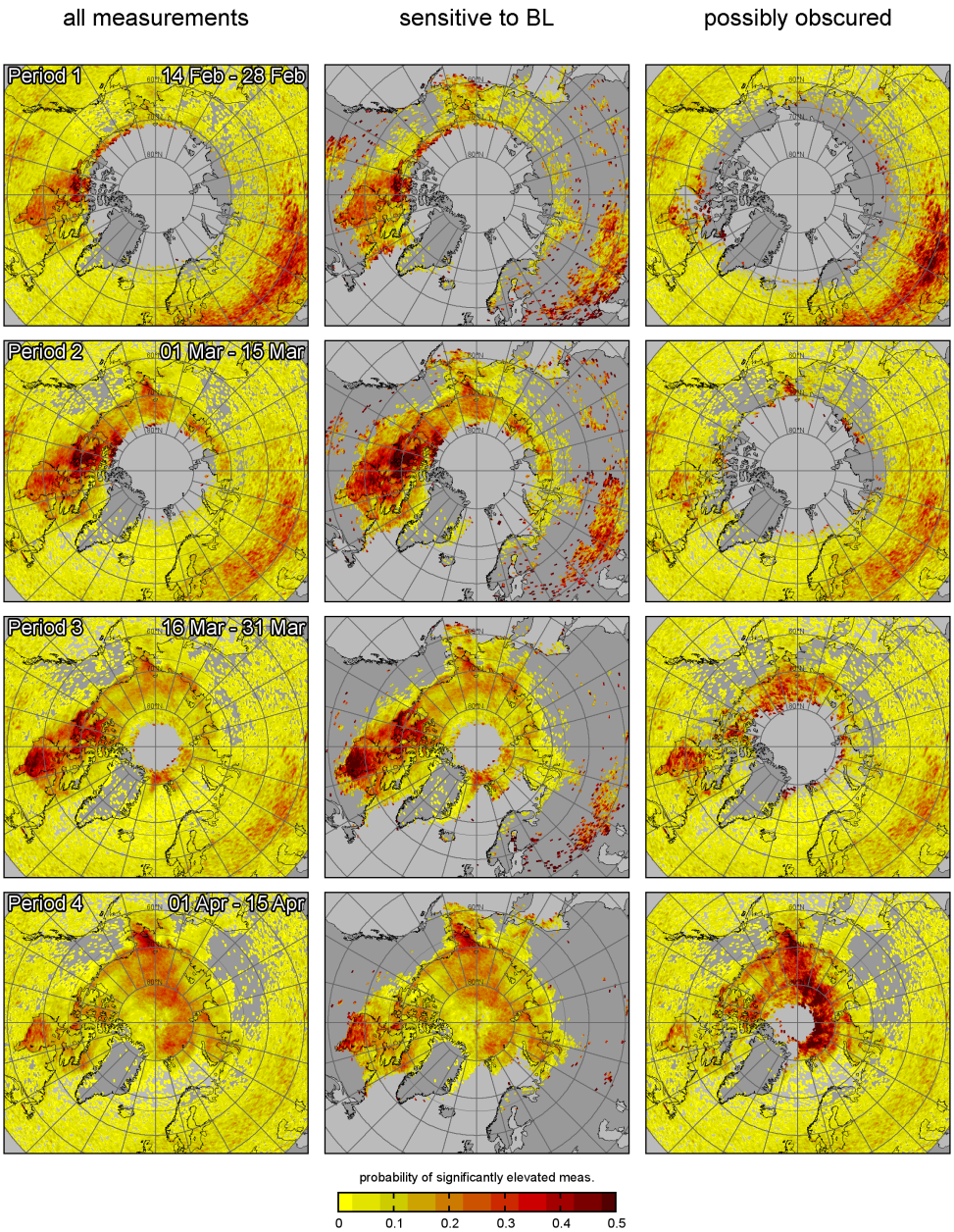

Figure 10.9.: *Probability distribution for significantly elevated BrO SCD measurements in the Arctic between 14 February and 15 April and the years 2007 to 2010. Left column: all measurements (same as in right column of Figure 10.7). Middle column: probability of measurements sensitive to the boundary-layer ($AMF_{500}>AMF_{500}^{min}=1$). Right column: probability of possibly obscured measurements. Areas without measurements and above 80° SZA are left gray.*

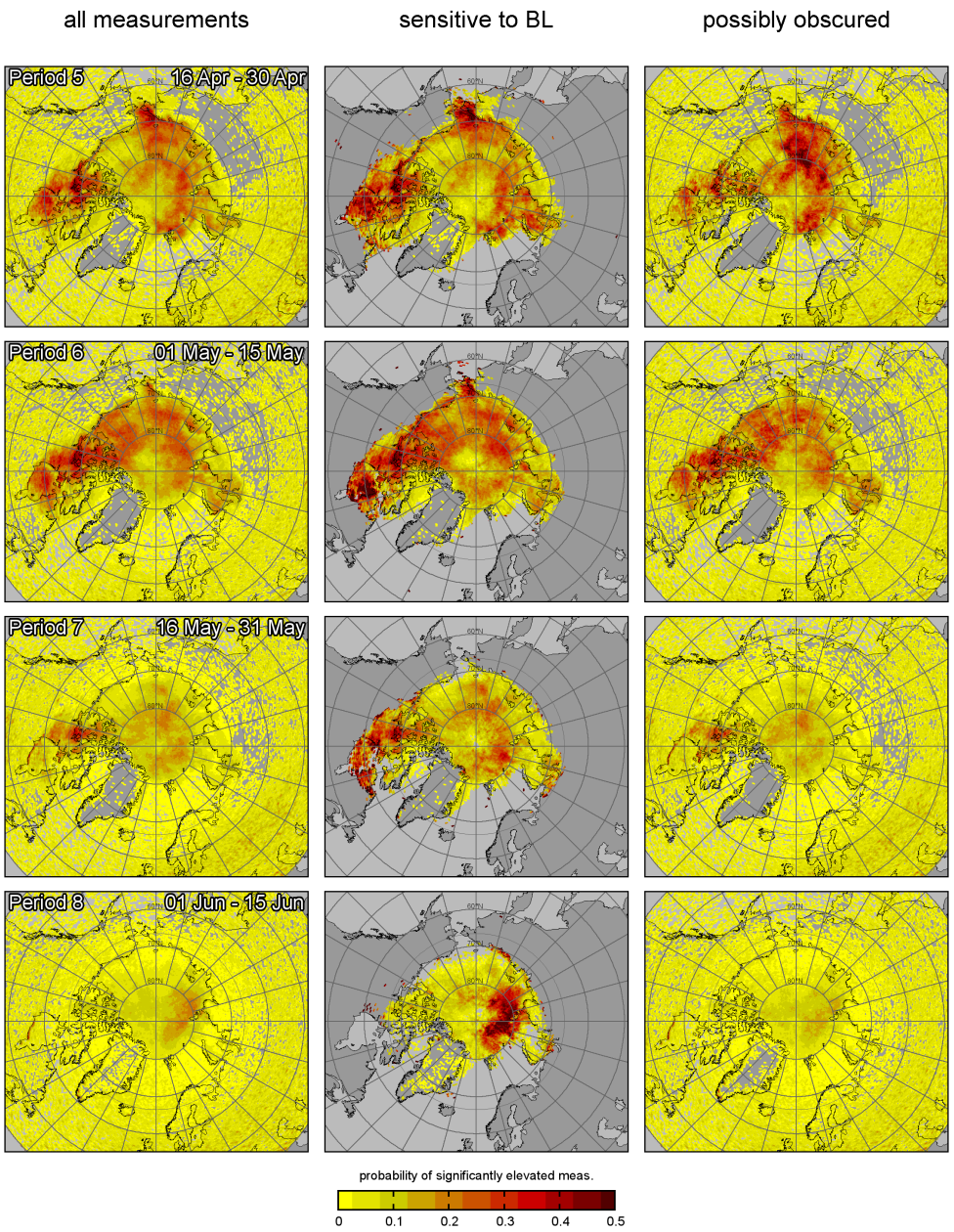

Figure 10.10.: *Continuation of Figure 10.9 but showing measurements between 16 April and 15 June.*

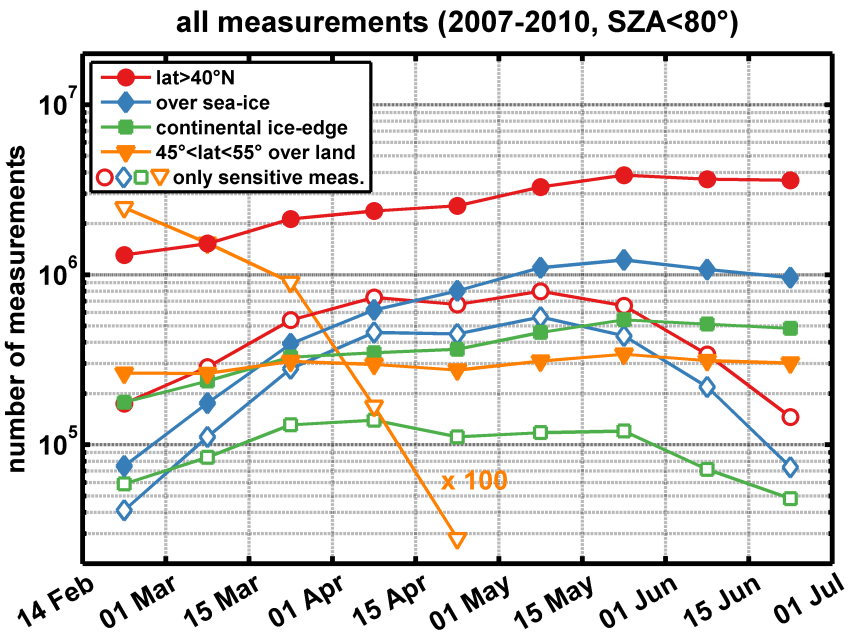

Figure 10.11.: *Number of GOME-2 measurements in the northern hemisphere at latitudes above 40°N during spring in the years 2007 through 2010. The number of measurements in the base population (red circles) and three subsets are displayed: (blue diamonds) measurements over sea-ice (coverage > 50 %), (green squares) measurements at least 100 km off the ice-edge and within 500 km from the coast, and (yellow triangles) measurements within a 10°-wide latitude band over land. Note that the empty symbols denote the number of measurements sensitive to the surface (AMF_{500}^{min}=1). The number of sensitive measurements in mid-latitudes is multiplied by 100.*

due to the distribution of multi- and first-year sea-ice. Multi-year sea-ice is usually located between the North Pole, Greenland, and the Canadian Archipelago. First-year sea-ice, in contrary, may then be the reason for enhanced BrO SCDs as suspected in many earlier studies (Section 2.4).

10.3.1. Conclusions from the probability distribution study

In the light of statistical measures applied on the distribution of BrO SCDs, the Canadian Arctic Archipelago is found to be the region of the highest probability for elevated BrO SCDs in the beginning of the season. This observation is in agreement with the observations from analysing mean total and tropospheric VCDs in the Sections 10.1.1 and 10.2, respectively. Furthermore, the Bering Strait as well as the Hudson Bay area exhibit a generally high probability for significantly elevated columns. Interestingly, the probability is observed to be increased for possibly obscured observations over the sea-ice between mid-March and end-April.

In conclusion, Figure 10.11 shows the total number of observations above 40°N latitude and three subsets in the years 2007 through 2010. The number of measurements

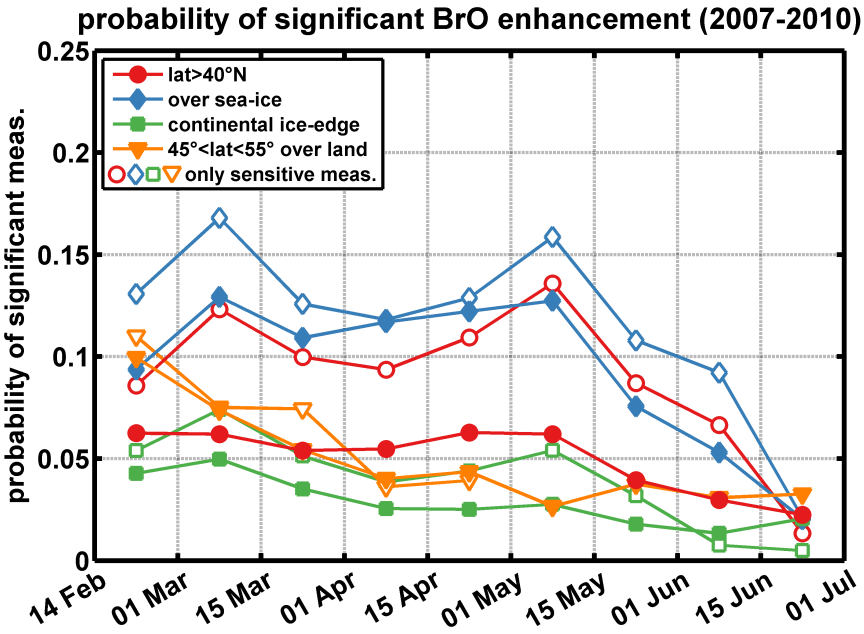

Figure 10.12.: *Same as Figure 10.11 but showing the probability for a significant BrO SCD enhancement with all four categories.*

are binned in half months periods. The total number of measurements (red solid circles) increases due to the rising sun in spring allowing more measurements below the SZA-threshold of 80°. The number of measurements connected to the sea-ice (blue and green curves) are even more dependent on time as these areas are located at very high latitudes where the SZA is relatively large early in the season. The number of measurements at mid-latitudes (cf. Section 10.2.1) is almost constant whereas the number of sensitive measurements at mid-latitudes are quickly decreasing during snow-melt between March and April.

The probabilities for significantly enhanced BrO SCD for the different subsets are shown in Figure 10.12, respectively. Significantly elevated observations are up to about four times more probable for measurements over sea-ice than over the continental sea-ice edge reaching about 500 km inland. The probability for all measurements above 40°N is generally larger than over the sea-ice edge because the measurements over the sea-ice have a large statistical weight as shown in Figure 10.11. The probability for BrO enhancements at mid-latitudes decreases to the level of the continental sea-ice edge within the first four investigated periods in accordance to the maps shown in Figure 10.7 as discussed in Section 10.2.1. It is furthermore noted that measurements sensitive to the surface are more likely also enhanced in BrO than those possibly obscured. However, the probabilities for measurements at mid-latitudes are less depending on the surface sensitivity indicating that these enhancements are probably due to BrO in the free troposphere.

11. Relationship between tropospheric BrO and environmental parameters

The BrO retrieval algorithm presented in Chapter 6 is not depending on input from external data sets and climatologies and thus avoids the influence of systematic biases from these sources. The resulting tropospheric BrO VCDs are therefore ideal to be compared to additional (e. g. meteorological) data which may be considered independent. In this chapter, the retrieved tropospheric BrO VCDs are compared to different environmental parameters suspected to modulate the release and distribution of BrO during Arctic spring as reviewed in Section 2.4. Firstly, the comparisons are conducted with a regional focus using satellite measurements averaged over selected periods as well as single overpass data. Thereafter, the entire GOME-2 data-set between 2007 and 2010 is used to study the correlation between enhanced tropospheric BrO VCDs and different environmental parameters.

The first section is dedicated to the mean distribution of BrO in the Canadian Arctic Archipelago, which was found to be particularly important in the previous chapter. The tropospheric BrO VCDs measured in this region are compared to surface data which are probably related to the observed distribution (Section 11.1). In the two subsequent sections, two case studies are presented where tropospheric BrO VCDs are related to the residence time in the boundary layer (Section 11.2) as well as the meteorology of a cold front (Section 11.3), respectively. Both case studies illustrate the interconnection between meteorology and bromine activation. The conclusions drawn are important for the interpretation of the results presented in the following sections where tropospheric BrO VCDs are more systematically correlated to a variety of environmental parameters. Firstly, the correlation with the type of sea-ice is studied (Section 11.4). Secondly, the correlation to meteorological parameters – surface temperature, surface wind-speed, boundary layer height, and residence time in the boundary layer – is investigated for measurements over sea-ice (Section 11.5). The possible influence of aerosol and cloud particles on the recycling efficiency of bromine is studied from the correlation with CALIPSO measurements (Section 11.6). Finally, the different studied environmental parameters and their connection to tropospheric BrO VCDs are summarized at the end of the chapter (Section 11.7).

Throughout this chapter, the season of tropospheric BrO activation during Arctic spring is divided into periods of half a month. This approach provides still a good temporal resolution as well as statistical quality and limits the number of intervals to be considered. The data analysis is based on observations of the years 2007 to 2010 unless otherwise noted.

11.1. Mean tropospheric BrO in the Canadian Arctic Archipelago

The Canadian Arctic Archipelago (cf. Figure 10.1a) has been identified in Section 10.3 as the region where GOME-2 measures enhanced BrO column densities with the highest probability of bromine activation during the onset of the "activated season" during February and March. Furthermore, the highest tropospheric BrO VCDs are observed in the waterways (fjords and channels) between the numerous islands which may now be resolved due to the improved spatial resolution of GOME-2 compared to the older GOME instrument. In this section, the mean tropospheric BrO VCDs between 1 and 15 March are detailed and compared to meteorological ECMWF data (cf. Section 7.3) in order to derive the mean regional horizontal and vertical distribution of BrO. This period is chosen because it is the earliest period of two weeks in which the satellite measurements provide a good coverage of the investigated area.

Figure 11.1 compiles the mean tropospheric BrO VCD and complementary data (convolved with the spatial resolution of GOME-2) between 1 March and 15 March in the years 2008 through 2010 (the year 2007 is excluded in this case study due to an anomaly in the ECMWF data in the studied spatial and temporal domain). As described before, GOME-2 observes systematically larger tropospheric BrO VCDs over the waterways between the islands than over land (Figure 11.1a). Especially the sea-ice south-east of Victoria Island and north of Melville Island exhibit very high column densities. Furthermore, the tropospheric BrO VCD over some larger islands, e. g. Banks Island, Victoria Island, and Baffin Island, reveal a VCD depending on the island topography shown in Figure 11.1c. This pattern deserves a detailed investigation.

First of all, it is necessary to check whether the distribution of tropospheric BrO VCDs is an artefact of a varying sensitivity for surface near layers. The retrieved O_4 AMFs (Figure 11.1b), however, reveal that the sensitivity is homogeneously distributed throughout the Archipelago. (Only in the north of Baffin Island and towards the North American continent, the O_4 AMF decreases indicating a lower sensitivity.) Hence, it is very likely that the observed BrO column distribution following the topography and surface type is realistic. Furthermore, Figure 11.1f shows that the mean tropopause height is more than 1 km lower over the Archipelago than over the adjacent oceanic and land surfaces. An influence on the column separation algorithm is rather unlikely to explain this coincidence as daily maps of the tropopause height usually show structures different from the distribution of BrO. The comparatively low tropopause can be explained from the special meteorology of the Arctic dome (cf. Section 2.2) and the very cold mean surface temperatures regularly observed in this region (e. g. Maxwell, 1981; Rigor *et al.*, 2000). However, this observation furthermore indicates that there is a higher probability for low pressure systems (leading to a lower, warmer tropopause) in the Arctic Archipelago which may, in turn, lead to conditions favourable to bromine activation like higher wind-speeds or frontal passages. From the obvious strong correlation between surface type and topology it is concluded that most tropospheric BrO chemistry is actually located in the boundary layer (BL) as

(a) *tropospheric BrO VCD*

(b) *sensitivity (O_4 AMF)*

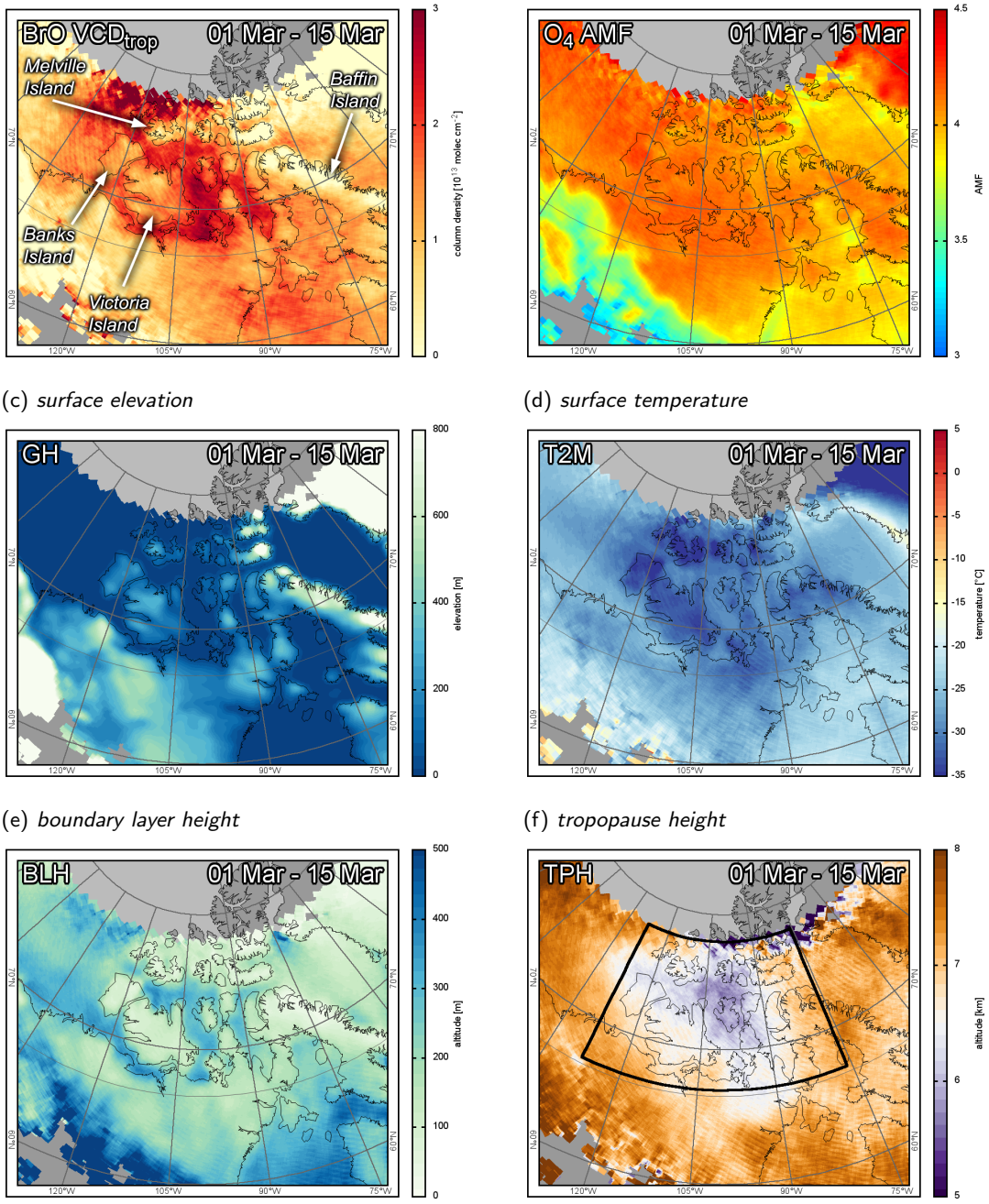

(c) *surface elevation*

(d) *surface temperature*

(e) *boundary layer height*

(f) *tropopause height*

Figure 11.1.: *Tropospheric BrO VCDs and ECMWF parameters over the Canadian Arctic Archipelago during the the first half of March in the years 2008 to 2010. (a) tropospheric BrO VCD, (b) O_4 AMF, (c) surface elevation, (d) surface temperature, (e) boundary layer height, and (f) tropopause height. Measurements within the highlighted domain in (f) are used for the correlation study.*

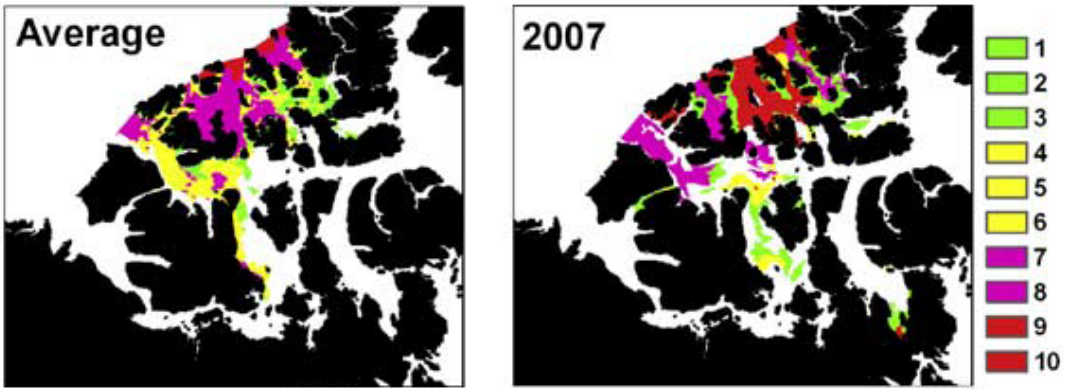

Figure 11.2.: *Spatial distribution of multi-year ice concentration in the Canadian Arctic Archipelago on the first week of April (left) averaged between 2000 and 2007 and (right) for 2007. Legend is ice concentration in tenths. Adapted from Howell* et al. *(2008).*

it is unlikely that uplifted air-masses would show such a strong feedback from the surface. This confirms many previous observations on the vertical distribution of BrO (e. g. Wagner *et al.*, 2001; Hönninger & Platt, 2002; Richter *et al.*, 2002; Hönninger *et al.*, 2004; Wagner *et al.*, 2007; Prados-Roman *et al.*, 2010; Frieß *et al.*, 2011).

Another particularity of the Canadian Arctic Archipelago is the prevailing ice-type covering its many waterways (Figure 11.2 (Howell *et al.*, 2008)). Due to its bathymetry and geographical location, a large fraction of the waterways is covered by multi-year sea-ice. Multi-year sea-ice from the Arctic Ocean replenishes the ice-melt during summer leading to a flux of multi-year sea-ice into the Archipelago. Large fractions of the northern Archipelago as well as Arctic Ocean to the north-west (not included in Figure 11.2) are covered by multi-year sea-ice. This is an at first sight surprising finding, because the current understanding of bromine activation over sea-ice is that multi-year sea ice plays a minor role compared to the saltier first-year sea-ice (cf. Section 2.4) (e. g. Wagner *et al.*, 2001; Bottenheim & Chan, 2006; Simpson *et al.*, 2007a). This apparent contradiction may be resolved by expecting the fractionation into multi-year and first-year sea-ice as indicated in Figure 11.2. Even a small fraction of first-year sea-ice (multi-year sea-ice is seldom 100 %) or a few newly-formed leads may still provide a sufficiently large area to provide the necessary amount of bromine as it is estimated in Section 2.3. Frost-flower growth on sea-ice may furthermore increase the efficiency of the bromine release (Kaleschke *et al.*, 2004). Another explanation could be that the bromine is advected into the Archipelago which, however, would require efficient recycling during transport as pointed out by Begoin *et al.* (2010).

11.1.1. Regional correlation with surface parameters

Finally, the distribution of tropospheric BrO VCDs over the Canadian Arctic Archipelago between 2008 and 2010 is correlated to different surface parameters possibly explaining the observed tropospheric BrO VCD gradients. The data originates from

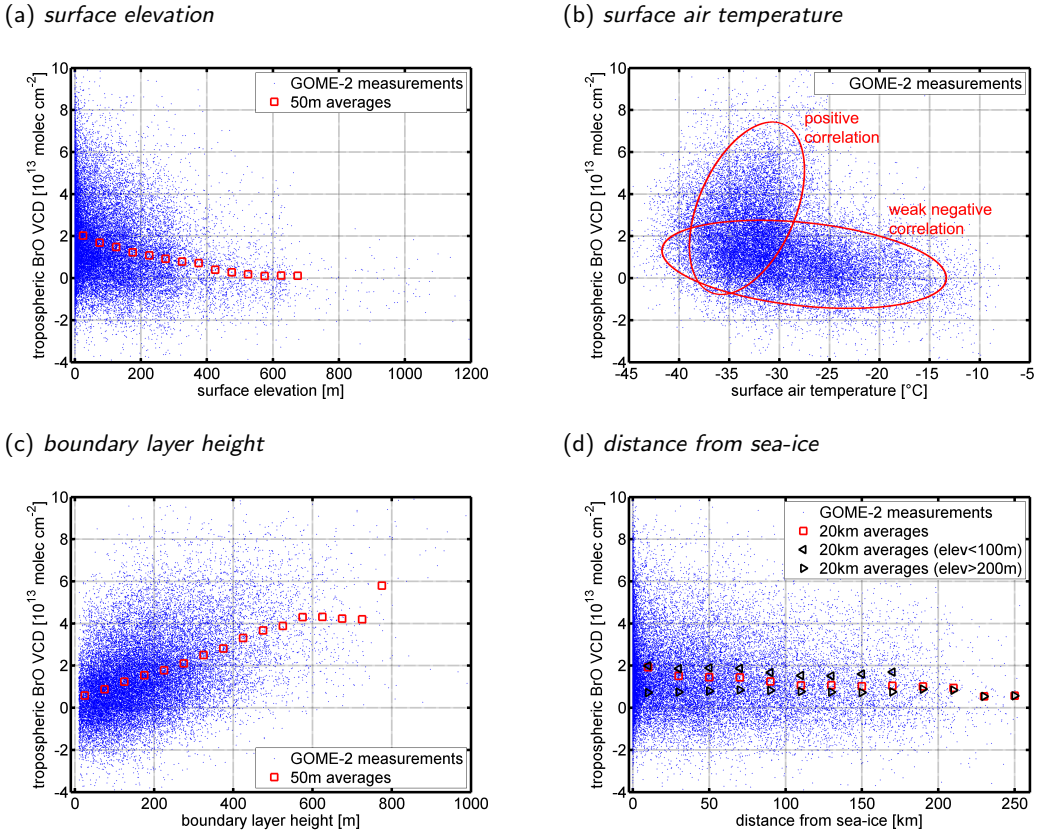

Figure 11.3.: *Correlation between tropospheric BrO VCD and (a) surface elevation, (b) surface temperature, (c) boundary layer height, and (d) distance from sea-ice at different surface elevations. Note that the ellipses in (b) are manually fitted to highlight two branches of the correlation with surface temperature. Errorbars are omitted for the sake of clarity.*

within the domain highlighted in Figure 11.1f.

Figure 11.3 shows the correlations between tropospheric BrO VCD (Figure11.1a) and surface elevation (Figure11.1c), surface temperature (Figure11.1d), boundary layer height (Figure11.1e), and distance from sea-ice, which are discussed in the following. These parameters are interpolated from ECMWF data whose calculation includes parametrizations of surface heat-flux over sea-ice and land as well as the parametrization of the boundary-layer stratification (cf. Section 2.2).

The strongest correlations are found for the comparison between tropospheric BrO VCD and parameters describing the vertical extent of the surface column (Figures 11.3a and 11.3c). On the one hand, the comparison with the surface elevation (Figure 11.3a) reveals that the mean tropospheric BrO VCD decreases with a higher surface altitude. This decrease may be due to a compression of the real BL height due to higher wind-speeds over higher ground or a reduction of the surface column height due to an elevated surface in analogy to island peaks sticking out of a “sea of BrO” located in

the lowest few hundred meters over sea level. On the other hand, an almost linear dependency is found between ECMWF boundary layer height and the tropospheric BrO VCD (Figure 11.3c). This observation again confirms that most BrO is located in the BL. The almost linear slope of the running mean calculation corresponds to an average BrO mixing ratio in the BL of 23 pmol mol^{-1} ($c_{\mathrm{BrO}} \approx 4\times10^{13}$ molec cm^{-2}/60000 cm, $c_{\mathrm{air}}=2.9\times10^{19}$ cm^{-3}). This estimate is large compared to most ground-based measurements. However, the measurements by (Pöhler *et al.*, 2010b) in the Amundsen Gulf (Sections 7.1 and 9.1) also revealed comparatively high average values for the BrO mixing ratio over the sea-ice confirming that this estimate is realistic. Hence, it can be concluded that the Amundsen measurements of BrO may be representative also for the average Canadian Archipelago.

Another aspect is the dependence on temperature altering the efficiency of the bromine explosion chemistry. However, the correlation to the surface air temperature is less clear (Figure 11.3b). There is one branch showing a strong positive and one branch showing a weak negative correlation with temperature. The largest tropospheric BrO VCDs are found in the positively correlated branch which is probably not caused by a varying chemistry because the efficiency of the bromine explosion mechanism exhibits a negative correlation to temperature. Recent studies showed that cold temperatures are at least a prerequisite for an efficient release of bromine. The positive correlation may therefore be a result from boundary-layer meteorology because higher surface temperatures lead to higher boundary layer heights which, in turn, are found to be highly correlated to tropospheric BrO VCDs.

Finally, it is studied how the tropospheric BrO VCDs depend on the distance from the sea-ice (Figure 11.3d). Assuming that sea-ice is the BrO source, one would expect a decrease of the BrO concentrations as the air-mass enriched in BrO travels inland. And in fact, the average tropospheric BrO VCD computed from all data (red squares) exhibits a clear decrease with increasing distance form the sea-ice. However, the BrO decay is possibly a result of the stronger correlations with both the surface elevation and boundary layer height. For instance, the averages calculated from subsets of surface elevations below 100 m and above 200 m, respectively, exhibit a much weaker trend (black symbols). Hence, a correlation of tropospheric BrO VCDs with the distance from the sea-ice edge for distances below 200 km is unlikely.

11.1.2. Conclusion of the regional correlation study

By comparing the correlations of tropospheric BrO VCDs to different environmental parameters, a strong correlation between boundary layer height and tropospheric BrO VCDs is found. Furthermore, the surface elevation shows a high negative correlation possibly intercorrelated with the boundary layer height. The correlation to the surface air temperature and the distance form the sea-ice are less distinct.

The correlation to the boundary layer height further leads to the conclusion that the average concentration of BrO in the surface column is independent from the boundary layer height. Hence, the source of BrO is supposed to be large enough to support a constant average concentration independent from the volume. This may indicate that the average BrO source strength of sea-ice is not limiting the measurable

concentrations. Rather, one may hypothesize that at a certain level of BrO the ozone destruction (which increases with the square of the BrO concentration) becomes so rapid that lack of O3 prevents further liberation of reactive bromine. This observation can be compared to BrO measurements by LP-DOAS performed at Summit, Greenland on top the ice-sheet by Stutz *et al.* (2011). At Summit, the concentrations of BrO were correlated to the boundary-layer height suggesting a constant BrO surface column distributed over a varying BL height. In conclusion, the BrO concentrations are controlled by the release process at Summit whereas the release of BrO over sea-ice in March is highly efficient. Maximum BrO concentrations are controlled by the O_3 destruction which increases with the square of the BrO concentration. Decreased O_3 thus limits the production of BrO at an increased probability of the BrO-BrO self-reaction.

11.2. Case study I – comparison to the boundary layer residence time

In this section, measured tropospheric BrO VCDs are compared to the meteorological condition east of Novaya Zemlya on 6 April 2009 (see Figure 11.4). The sea-level pressure (Figure 11.4b) shows a combination of two low pressure systems, from which the stronger one is located around 70°N and 75°E. The tropospheric BrO VCDs exhibit a characteristic hook-shape which can also be identified in the boundary layer height and surface air temperature plots, respectively (Figures 11.4c and 11.4d).

The tropospheric BrO VCDs are compared to the residence times of trajectories in the boundary-layer over sea-ice ending at different altitudes for each satellite pixel (cf. Section 7.4). Figure 11.6 shows the residence time of trajectories ending at 100, 200, 400, 600, 800, 1000, 1500, and 2000 m altitude and for the first, second, third, and fourth day prior to the GOME-2 overpass, respectively. When compared to the respective tropospheric BrO VCDs (Figure 11.6a using the same colormap), it is possible to identify a good spatial correlation between the residence time and the BrO column for altitudes between 200 and 1500 m and times up 48 h prior to the GOME-2 overpass. The residence time plots of 100 m arrival altitude (first row) and those calculated for more than two days earlier (last two columns) the spatial correlation is less apparent. In fact, the complete left arm of the hook may be reproduced by integrating the heights between 400 and 1000 m for the first day, while the thin filament in the center seems to be best matched by the BL residence times between 1 and 2 days prior to the overpass and at altitudes of 800 and 1000 m (plots highlighted in green).

The highlighted residence times are subsequently averaged and correlated to tropospheric VCDs of BrO. The is illustrated in Figure 11.6b showing a distribution strikingly similar to BrO. This agreement is also reproduced by the pixel-to-pixel correlation shown in Figure 11.6c. Obviously, there is a strong link between the spatial structures of BrO as detected by GOME-2 and atmospheric motion linked to surface processes. This observation may lead to the following implications:

1. The correlation to the average sea-ice contact time of the probed column possi-

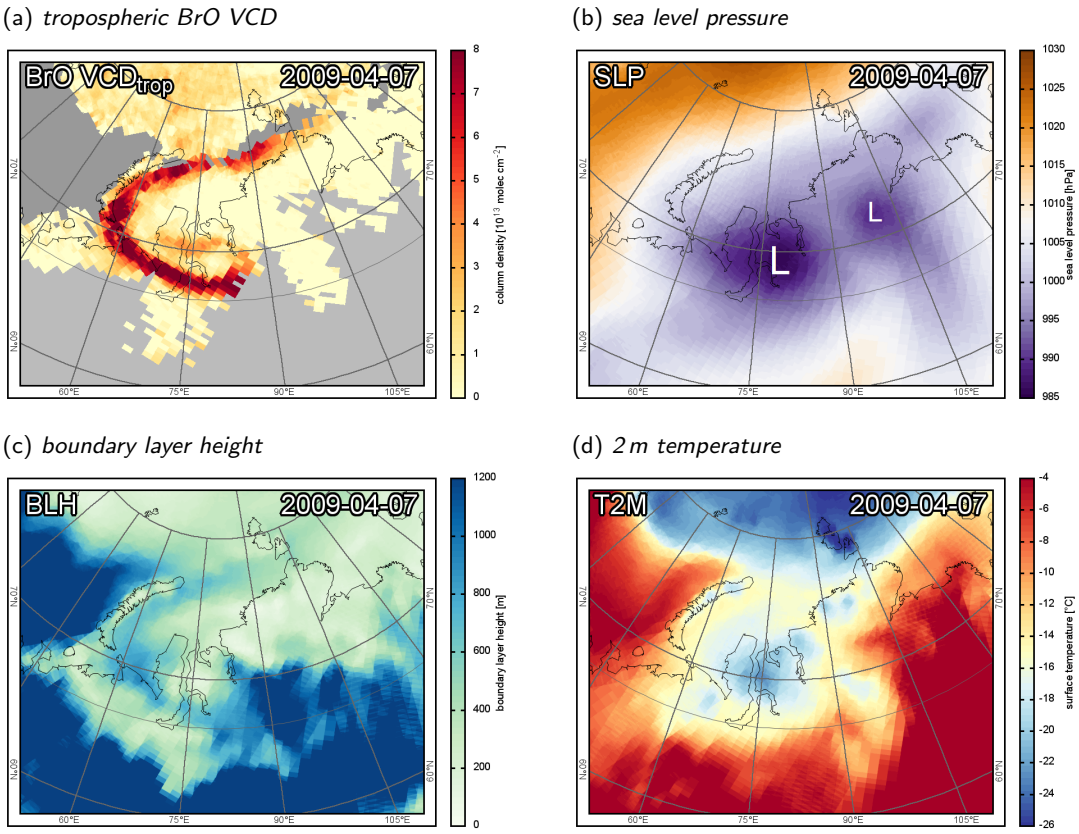

Figure 11.4.: *Case study of (a) BrO distribution in connection with (b) a low pressure cyclone. (c) boundary layer height and (f) 2 m temperature. The map shows the area east of Novaya Zemlya for 7 April 2009.*

bly indicates that the longer an air-mass has contact with the sea-ice, the more BrO is produced within this air-mass.

2. In general,a thick boundary layer may also result in a larger residence time in the boundary layer. However, the spatial pattern is less accurately reproduced for trajectories ending at 100 and 200 m. This observation contradicts the hypothesis that an air-mass is simply "charged" with BrO by processes at the sea-ice surface. A possible explanation is that O_3 is almost depleted in the air close to the surface leading to a decreased production of BrO there, but when lifted upwards it may mix with ozone rich air from aloft producing BrO.

3. In order to yield a large residence time in the boundary layer as well as a comparatively high altitude at an end-point, the considered air-masses have to have witnessed an upward motion prior to the measurement. This upward motion is probably the result of the vertical motion within a cyclone as described above and which may also be observed in this example. Hence, the observed BrO distribution may either be the results of this upward motion in connection with

vertical mixing of O_3 rich air from aloft. Or, as a second possibility, air enriched in reactive bromine (exclusive BrO) is lifted into air richer in O_3 and thus BrO is produced. The difference between both possibilities is that the BrO is either located at the ground and O_3 is mixed from aloft as indicated by vertical motion, or the BrO is produced aloft where it mixes with O_3 rich air. However, the close correlation to trajectories ending at elevated altitudes strongly suggests that the measured BrO is located in elevated layers, but originates from within the boundary layer.

4. A further, more speculative, explanation could be, that the upward motion is the result of two opposing fronts possibly leading to horizontal diffusion between one air-mass rich in O_3 and another almost depleted in O_3 close to the surface. Colder air more likely originates from higher latitudes where sea-ice concentrations are high and O_3 is more likely depleted hampering the production of BrO (cf. Section 2.5). Warmer air, in contrary, probably originates from lower latitudes and therefore contains more O_3 which, if bought in contact with bromine radicals, may produce BrO similar to the model calculations presented in Section 2.5.

11.3. Case study II – enhanced tropospheric BrO VCDs in a cold front

In this section, a case study of the BrO distribution in a Arctic cold front is presented as well. Compared to the case study presented in the previous section, the cyclone is captured at a younger stage exhibiting a textbook-like cold front. Hence, the comparison to the distinct frontal meteorology may be studied in more detailed here. Figures 11.7 and 11.8 show maps as well as cross-sections of tropospheric BrO VCDs and several meteorological parameters of an Arctic cyclonic system with a characteristic warm front occlusion north of Alaska on 6 April 2009. The ECMWF meteorological fields correspond to the 18:00 UTC simulation output whereas the BrO data is from a GOME-2 overpass at 19:55 UTC. The BrO cross section (Figure 11.7b) includes pixels between 77.5°N and 78.5°N latitude which may be shifted to the East with respect to the ECMWF data due to the time difference of almost two hours and considering the frontal evolution (the front moves eastward).

The pressure minimum of the cyclone is located approx. 1000 km north of Alaska at 150°W longitude (denoted L in Figure 11.7f). The low attracts warmer air from the south forming a comma-shaped sector surrounded by relatively cold air below -22°C(Figure 11.7e). The horizontal distribution of the warm air-mass spatially correlates with the distribution of BrO (Figures 11.7a and 11.7b). However, the maps of surface wind speed (Figure 11.8a) as well as boundary layer height (Figure 11.8b) show a pattern less correlated with BrO. All shown meteorological parameters conclusively illustrate the dynamics of the frontal system.

The potential temperature cross section (Figure 11.7g) shows the occlusion of a warm front formed by a cold front west of 145°W (denoted C_1, strong gradient in

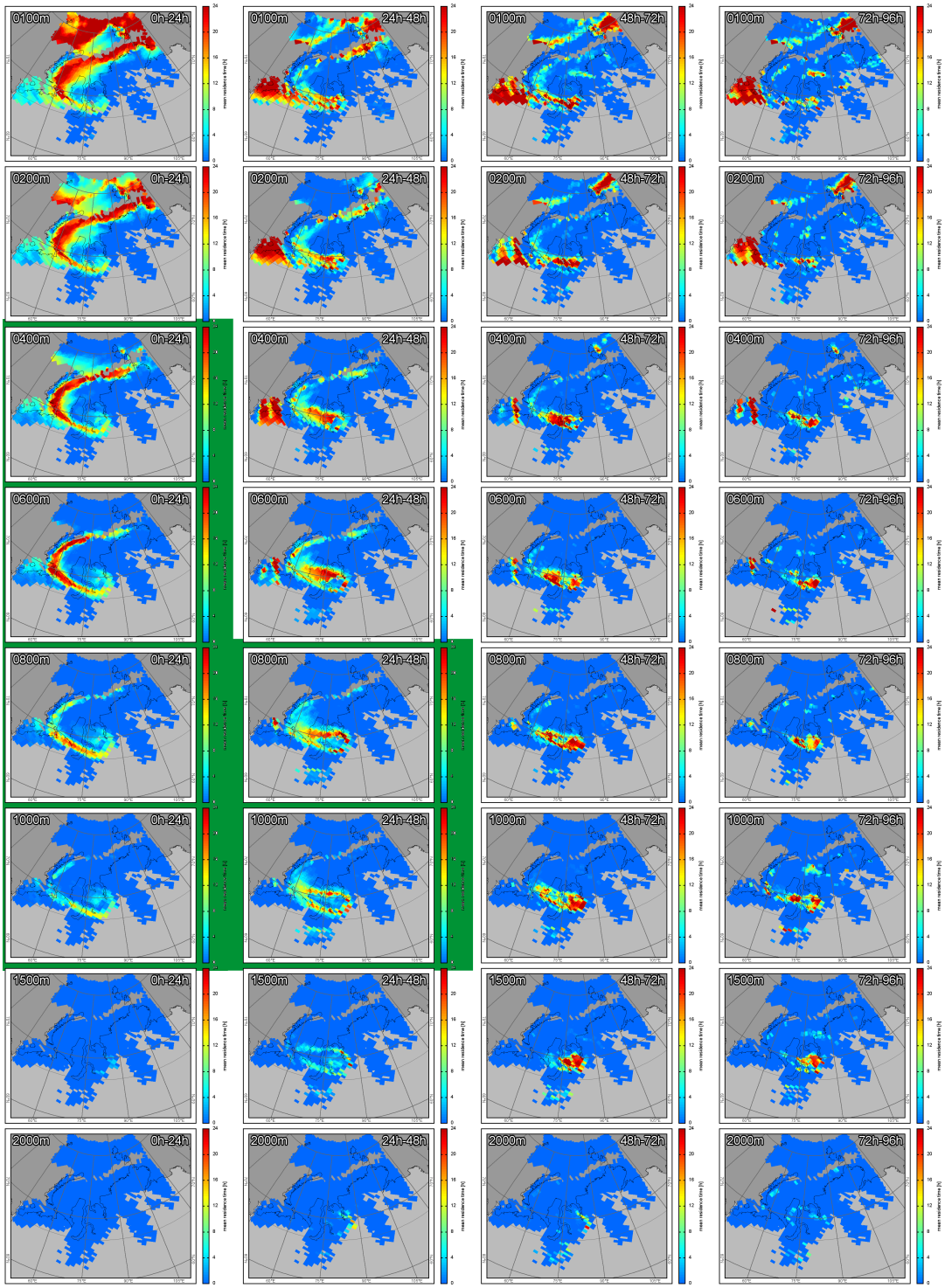

Figure 11.5.: *Same as Figure 11.4 but showing the residence time of backward trajectories depending on the end-point altitude in each GOME-2 pixel (rows) and the time prior to the satellite overpass (columns). The images highlighted in green are averaged in Figure 11.6b.*

(a) *tropospheric BrO VCD* (b) *residence time in boundary layer*

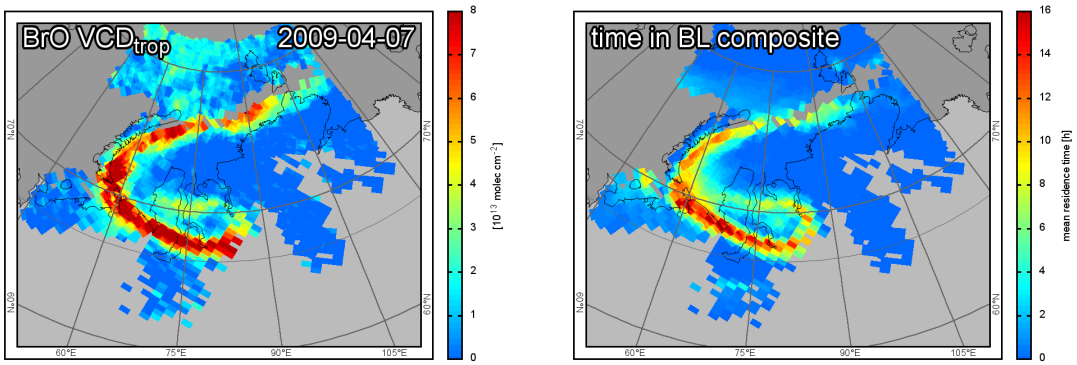

(c) *tropospheric BrO VCD vs. time in BL*

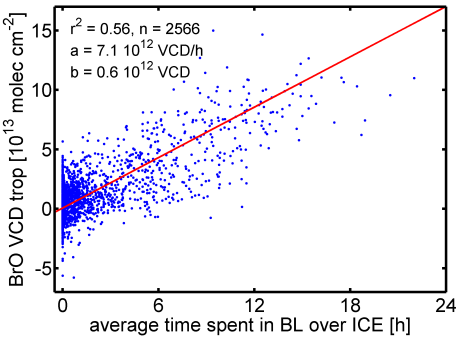

Figure 11.6.: *Comparison between (a) tropospheric BrO VCD measured by GOME-2 (same as Figure 11.4a) and (b) average residence time in boundary layer of the highlighted images shown in Figure 11.5 (see text). (c) correlation and covariant fit of (a) and (b).*

wind direction in Figure 11.7d) and a colder air mass east of 135°W (denoted C_2). This occlusion is characterized by a neutrally stratified surface layer (θ=const.) and hence enhanced vertical motion (Figure 11.7c). This meteorological situation most likely leads to an enhanced vertical as well as horizontal mixing between 143°W and 134°W longitude which would be typical for an occlusion (e. g. Rohli & Vega, 2011).

It is furthermore noted, that the horizontal wind-speed (Figure 11.8c) is significantly larger east of 140°W due to the larger pressure gradient shown in Figure 11.7h, and that the boundary layer height steadily decreases from west to east (Figure 11.8d). The boundary layer height clearly results from the stratification shown in the potential temperature cross section (Figure 11.7g). As for longitudes west of 135°W near-surface air-masses are neutrally stratified leading to an enhanced boundary layer height, whereas east of 135°W a strong temperature inversion caused by the occluded warmer air (denoted W) leads to a more stratified surface layer and a much decreased boundary layer height.

The meteorological observations can be compared to the BrO cross-section in Figure 11.7b. The tropospheric BrO VCDs rise quickly between 145°W and 140°W collocated

(a) *tropospheric BrO VCD*

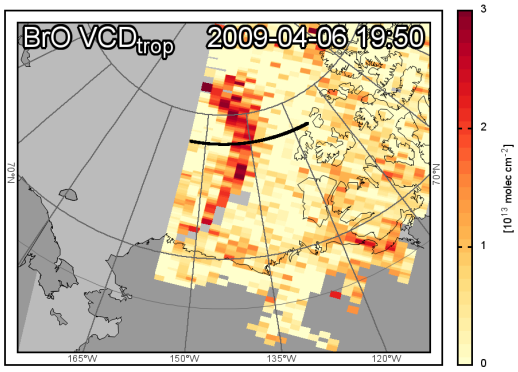

(b) *trop. BrO VCD cross-section*

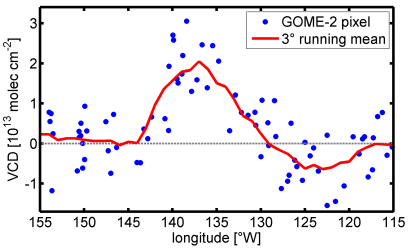

(c) *vertical velocity cross-section*

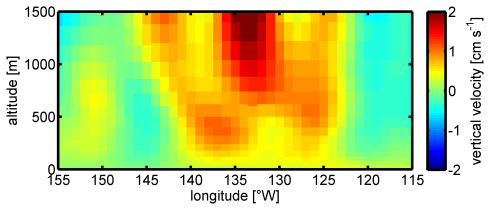

(d) *wind direction cross-section*

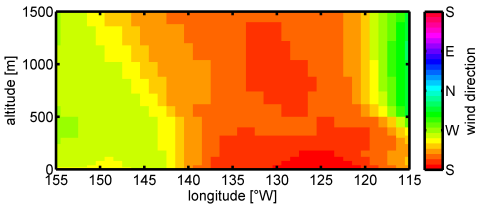

(e) *surface temperature*

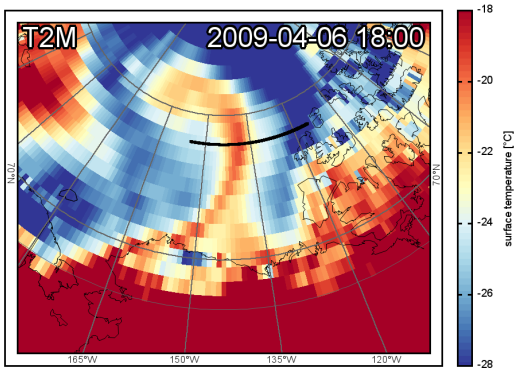

(f) *sea level pressure*

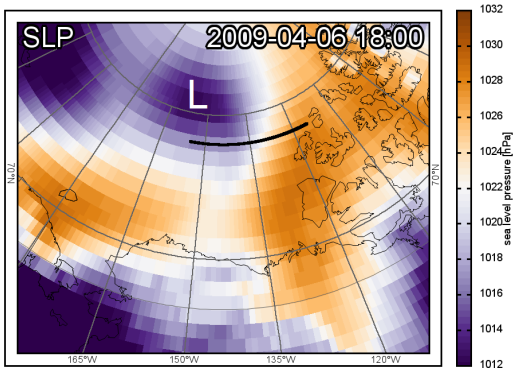

(g) *potential temperature cross-section*

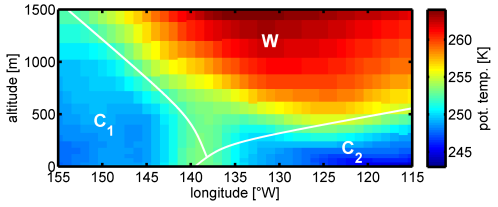

(h) *sea level pressure cross-section*

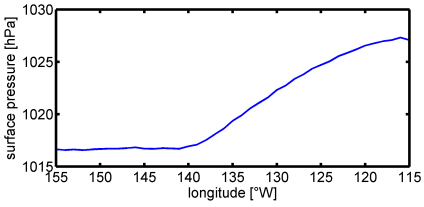

Figure 11.7.: *Distribution of BrO (a) retrieved from GOME-2 measurements compared to the meteorology of a cold front as provided by ECMWF. (b) tropospheric BrO VCDs measured along the 920 km long longitudinal cross-section at 78°N denoted in (a). (c) Vertical wind velocity, (d) horizontal wind direction, (e) 2 m-temperature, (f) sea level pressure, (g) cross-section of potential temperature, and (h) sea level pressure. The evolution of this BrO enhancement on 6 April 2009 is illustrated in Appendix C.2 on page 232. Note the striking similarity between (a) and (e) originating from entirely different data sources.*

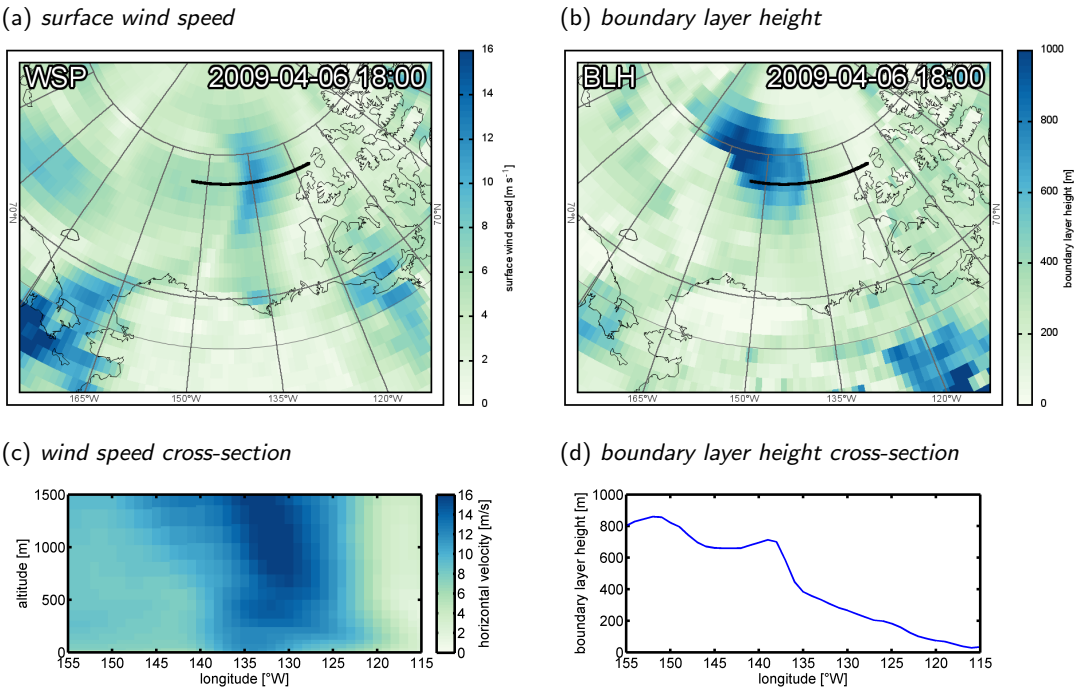

Figure 11.8.: *Continuation of Figure 11.7. (a) Surface wind-speed, (b) boundary layer height, (c) cross-section of horizontal wind-speed, and (d) cross-section of boundary layer.*

with the frontal system and decrease east of 135°W, probably due to a shallower surface column as indicated by the boundary layer height drop in Figure 11.8d. The data in particular reveal a striking similarity of patterns between two quantities originating from entirely different data sources: (1) tropospheric BrO VCDs (Figure 11.7a, GOME-2 BrO retrieval from this work) and (2) surface temperature (Figure 11.7e, ECMWF weather model). Two possible explanations for this behaviour are:

1. If we assume the surface air being almost depleted in O_3 but still rich in reactive bromine, turbulent mixing with O_3-rich air would produce large amounts of BrO. Ozone can be mixed into the surface layer either from aloft through vertical mixing or regional-scale turbulent mixing in the horizontal direction. Both options, or a combination of both, are possible for the presented case study. Warmer air masses from the south may be richer in O_3 than the colder air which is probably depleted in O_3 due to a longer residence time over the sea-ice (e. g. Bottenheim *et al.*, 2009; Jacobi *et al.*, 2010; Toyota *et al.*, 2011).

2. The observed BrO enhancement may be due to an increased wind speed triggering an increased production of aerosols (providing an increased area for heterogeneous recycling processes to occur) or increase the wind-pumping of the snow-pack over the sea-ice (releasing more activated bromine species). However, as the spatial correlation between BrO and wind-speed is not perfect – there are areas increased in BrO but the wind is comparatively calm – this explana-

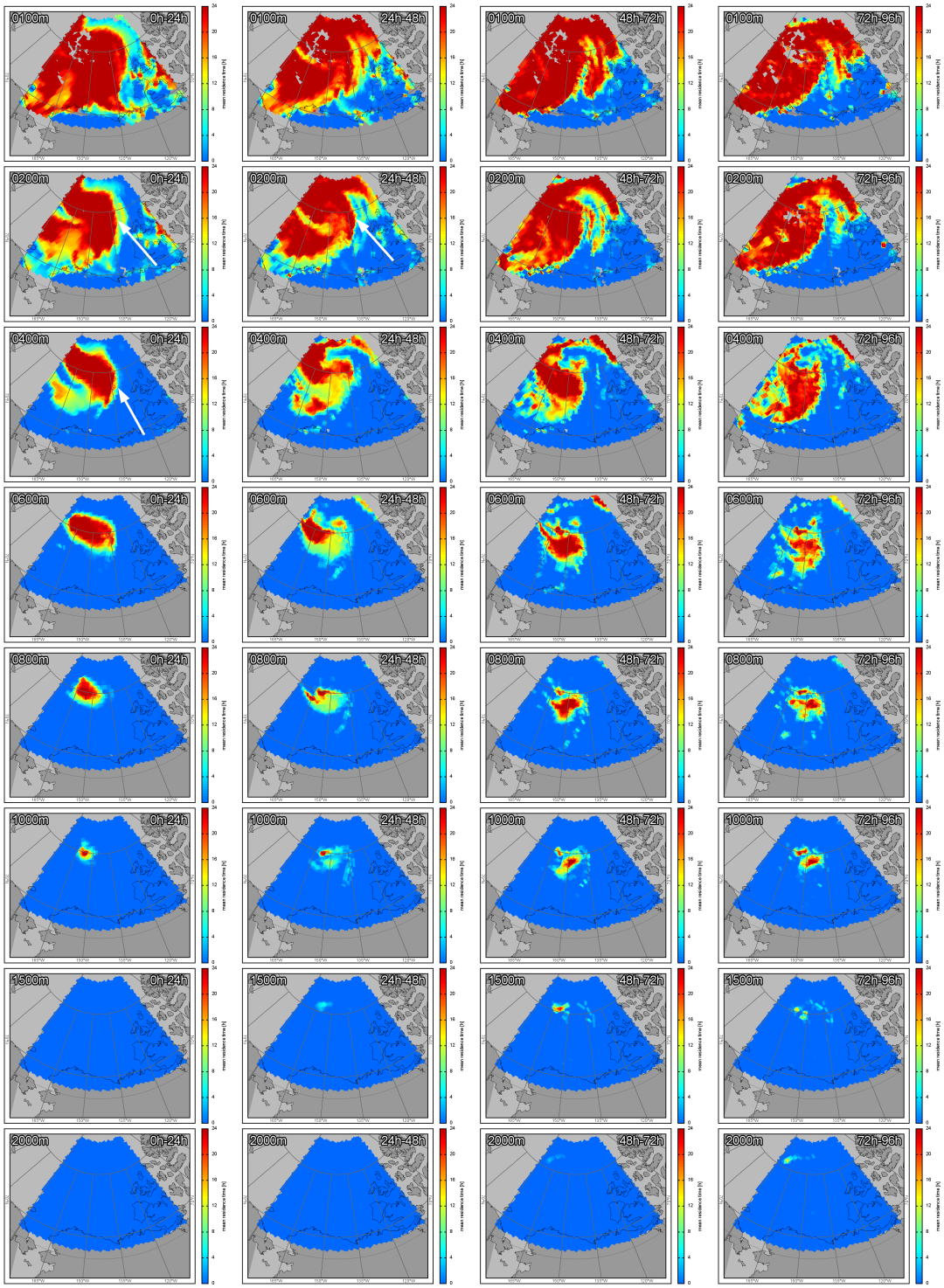

Figure 11.9.: *Residence time of backward trajectories depending on the end-point altitude in each GOME-2 pixel (rows) and the time prior to the satellite overpass (columns). The map shows the area north of Barrow, Alaska for 6 April 2009. The corresponding tropospheric BrO VCDs are depicted in Figure 11.10.*

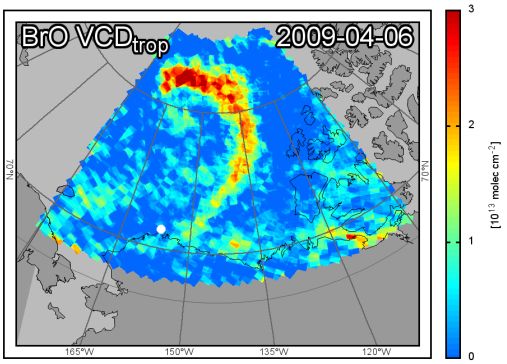

Figure 11.10.: *Tropospheric BrO VCD measured by GOME-2 (as Figure 11.7a but averaging all measurements of that day) corresponding to the residence times shown in Figure 11.9. The white circle denotes the location of the ground-based measurements at Barrow, Alaska (Chapter 8).*

tion for increased tropospheric BrO VCDs is less likely than the alternatives described above (e. g. Fan & Jacob, 1992; Frieß *et al.*, 2004, 2011).

It is emphasized that all discussed parameters are intercorrelated and it is difficult to separate the different influences on the observed tropospheric BrO VCDs. E. g., high wind speeds and higher surface temperatures cause a higher boundary layer, but may also produce more aerosol particles on which heterogeneous reactions may occur. Therefore, the optional mixing of O_3 into the boundary layer from aloft is not necessarily the only explanation for this dynamically complex phenomenon.

Finally, the distribution of tropospheric BrO VCDs is compared to the residence time in the boundary layer in analogy to the previous case study (Section 11.2). The residence times in the last four days of trajectories ending at ten different heights are depicted in Figure 11.9. A map showing the respective GOME-2 measurements of BrO is depicted in Figure 11.10. This time, the correlation between the residence time in the boundary layer and the tropospheric BrO VCDs is almost negligible which is puzzling when compared to the excellent agreement found in the first case study (Figure 11.6). The reasons for this disagreement are unclear at this stage of studying the boundary layer resident times and satellite measurements of the tropospheric BrO VCD. A different chemistry of the involved air masses may potentially explain the observed behaviour.

The chemical boundary conditions, especially the ozone concentration, may alter the correlation between residence time and tropospheric BrO VCD. Ground-based measurements conducted at Barrow, Alaska (cf. BrO and O_3 timeseries in Figure 8.4, location denoted in Figure 11.10) are available at the lowest tail of the cold front. The surface observations show a rapid depletion from O_3 concentrations above 30 nmol mol^{-1} to approx. 1 nmol mol^{-1} in the morning hours. As soon as the O_3 concentration becomes very small, the BrO concentration changes from up to 15 pmol mol^{-1} to below 3 pmol mol^{-1}. BrO concentrations during this transition are correlated to the slope of O_3. If we assume that the measurements at Barrow are to some extent

representative for the chemistry within the entire front whose southern tip touched Barrow (Figure 11.10), we may conclude that the surface concentrations of both O_3 and BrO in the cold air sector behind the front (denoted C_1 in Figure 11.7g) are very low. The air in this sector shows large residence time in the boundary layer over the sea-ice for trajectories arriving at altitudes $\leq$200 m which potentially contains high concentrations of reactive bromine. However, the production of BrO is low due to the absence of O_3. Meanwhile, the right edge of the area featuring large residence times (white arrows in Figure 11.9) correlates well with the right edge of the BrO enhancement in the cold front. It may hence be concluded, that the correlation to the residence time in the boundary layer may only be observed if there is enough O_3 present to produce BrO. In the presented case, the air-mass behind the front is probably depleted in O_3 leading to smaller tropospheric BrO VCDs than predicted by the residence time. However, further studies on this correlation are required to sufficiently explain the observed discrepancy between both properties.

11.4. Correlation with ice type

First-year sea-ice is suspected to be the dominant source of bromine in the Arctic. This hypothesis is mainly supported by backward trajectory analysis of both ODE and BrO times-series (e. g. Frieß *et al.*, 2004; Bottenheim & Chan, 2006; Simpson *et al.*, 2007a; Wagner *et al.*, 2007; Frieß *et al.*, 2011). The salinity and hence the bromine content of first-year sea-ice is much higher than multi-year sea-ice. As pointed out by Kaleschke *et al.* (2004), frost-flowers forming on frozen-over ice-cracks are another potential source.

In this section, the distribution of tropospheric BrO VCDs is systematically correlated to the microwave backscatter coefficient (MWBC) as measured by QuickScat (Section 5.3.1). The MWBC can be used as a measure to distinguish between first-year and multi-year sea-ice due to its different grain size. Multi-year sea-ice has a larger MWBC. The swath of QuickScat has two beams. However, only the vertically polarized MWBCs measured at the outer beam at 45° are used here. Furthermore, QuickScat measurements after 15 April are discarded because water clouds are beginning to interfere with the sea-ice signal when air temperature rises and water clouds become more probable. A complete analysis of the correlation between tropospheric BrO VCD and MWBC in four periods between mid-February and mid-April is shown in Figure 11.11.

The correlation analysis contains three properties evaluated for all measurements sensitive to the surface and over sea-ice: (1) the total number of all MWBC measurements over sea-ice and the subset of measurements featuring a significantly elevated BrO SCD, (2) the probability to measure a significantly elevated BrO SCD depending on the MWBC, and (3) the distribution of measurements in the (MWBC,BrO VCD)-plane with the linear correlation coefficient r^2 and a linear fit of both data-sets. This scheme is repeated throughout this chapter in order to provide the possibility for inter-comparison of the correlations.

For the comparison with the MWBC, only weakly positive and negative correla-

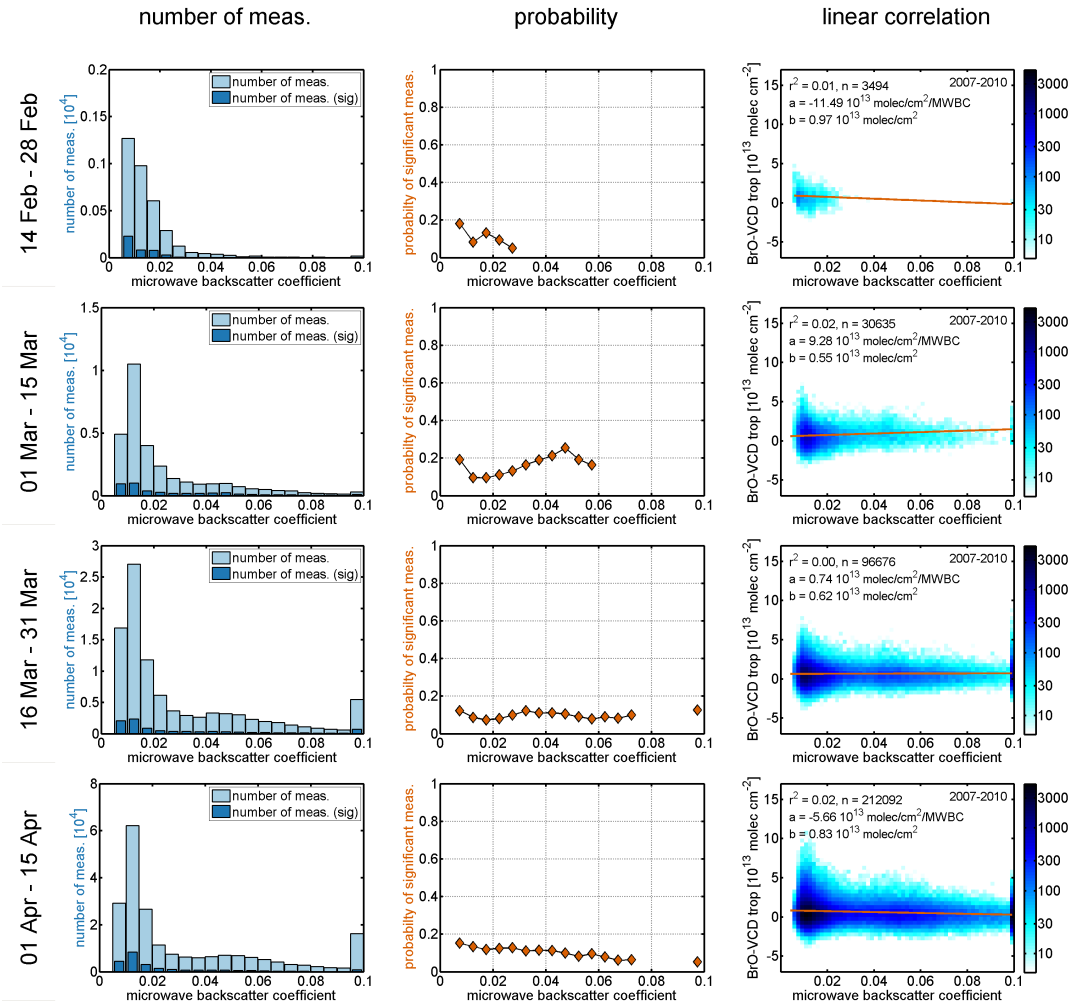

Figure 11.11.: *Correlation between QuickScat microwave backscatter coefficient (MWBC) and tropospheric BrO measurements in four half month periods between mid-February and mid-April. Left column: number of surface sensitive measurements over sea-ice binned according to the MWBC, dark blue denotes the number of significantly elevated BrO SCDs measured. Middle column: probability of measuring a significantly elevated BrO SCD depending on the MWBC. Right column: distribution of measurements and linear regression between MWBC and tropospheric BrO VCD. A higher MWBC indicates areas more likely to be covered by multi-year sea-ice rather than by first-year sea-ice.*

tions with tropospheric BrO VCD are found in the second and fourth period, respectively. The correlations in the first and third period are probably not significant. The histogram shows that most measurements exhibit a MWBC below 0.03 indicating first-year sea-ice. The slightly positive correlation in the beginning of March (period 2) as displayed in the probability as well as the linear correlation plot in Figure 11.11 is probably due to the high probability of significantly elevated BrO columns in the Canadian Arctic Archipelago as discussed in Section 11.1. There, a comparatively large fraction of the waterways are covered by multi-year sea-ice. Furthermore, in the beginning of March, the number of measurements over the open Arctic Ocean are under-represented due to the large SZAs in that time of the season (cf. Section 10.3). The slightly negative correlation in April is based on more distributed measurements and may indicate that enhanced tropospheric BrO VCDs above multi-year sea-ice are in fact less probable.

From this comparison, a clear influence of the sea-ice type on the instantaneously measured tropospheric BrO VCD cannot be concluded. However, it needs to be noted that past studies were mostly depending on back-ward trajectory calculations taking the history of the probed air-mass into account (e. g. Frieß *et al.*, 2004; Kaleschke *et al.*, 2004; Bottenheim & Chan, 2006; Simpson *et al.*, 2007a; Frieß *et al.*, 2011). The residence time over a certain surface is an important parameter for release processes and is discussed below in Section 11.5.4.

11.5. Correlation with meteorology

Meteorological factors are supposed to play an important role in the release mechanism of reactive bromine as introduced in Chapter 2. Furthermore, the meteorology of the boundary layer may also create situations under which the satellite can detect tropospheric BrO. In Chapter 9, GOME-2 measurements were compared to ground-based measurements and a high correlation was found. At Barrow, however, the LP-DOAS and the GOME-2 tropospheric BrO VCD deviated occasionally. These deviations could be explained considering the vertical structure of the boundary layer and the vertical distribution of BrO as measured by MAX-DOAS. Hence, the meteorology alters the probability for significantly enhanced tropospheric BrO VCDs by changing the release processes, the entrainment of O_3 into the boundary layer, as well as the integrated BrO surface column density. Despite the inter-correlation of these influences, different meteorological parameters are compared to tropospheric BrO VCD measurements in this section.

Firstly, the influence of the surface air temperature is studied in order to test the observed temperature dependency of bromine activation found in previous studies (Section 11.5.1) Secondly, a correlation with the surface wind-speed is performed (Section 11.5.2). Then, the boundary layer height is compared to the tropospheric BrO VCDs over entire Arctic Ocean (Section 11.5.3). Finally, the residence times over sea-ice and land are compared to the tropospheric BrO VCD using LAGRANTO backward trajectories (Section 11.5.4).

11.5.1. Surface temperature over sea-ice

The temperature is an important parameter influencing the efficiency of the bromine explosion and hence the release of reactive bromine into the gaseous phase (cf. Section 2.4). Several processes potentially lead to a higher amplification rate at colder temperatures. These processes include an increased carbonate precipitation in brine, an increased frost-flower growth-rate, and a higher Br_2 to BrCl ratio leading to a higher net release in reactive bromine (e. g. Kaleschke *et al.*, 2004; Sander *et al.*, 2006). However, the temperature also influences the meteorology (cf. Section 11.3) which alters the vertical distribution of BrO: E. g., higher surface air temperatures potentially lead to a higher boundary layer and increased turbulent mixing.

In this section, the dependence between 2 m-temperature fields from ECWMF and tropospheric BrO VCDs measured by GOME-2 is studied during Spring between mid-February and mid-June. The number of measurements, probability for elevated BrO SCDs, and correlation analysis of data over sea-ice and sensitive to the surface are depicted in Figures 11.12 and 11.13, respectively.

Apart from February, a steady increase in the mean temperature is evident for the transition from late Winter to early Summer from the histograms (left column). (The higher temperatures in February are probably due to more measurements at lower latitudes in this period.) More surprising are the evolution of the probability as well as correlation plots. A clear negative correlation between tropospheric BrO VCD and temperature can be observed in the beginning (until mid-March) and the end of the season (from mid-May). In between, however, the correlation is less clear and April shows even a positive correlation between both properties. The probability curves in the four periods in April and May exhibit a maximum between -20°C and -5°C.

The probability curves of all periods are compiled in Figure 11.14. The plots shows a bi-modal dependence between the probability of a significantly elevated BrO SCD and the ECMWF 2 m temperature. Early in the season, the probability increases towards low temperatures. From April on, the probability maximum lays above -20°C.

Discussion of the comparison with surface air temperatures

The negative correlation with temperatures early in the season agrees well with previous observations of BrO activation and ODEs (e. g. Tarasick & Bottenheim, 2002; Zeng *et al.*, 2003; Bottenheim & Chan, 2006) who reported that temperatures below -20°C may be a prerequisite for O_3 depletion to occur (cf. Section 2.3). Furthermore, this finding correlates with the observation of comparatively high tropospheric BrO VCDs in the Canadian Archipelago (cf. Section 11.1) where, together with Siberia, also the lowest surface temperatures of the whole Arctic prevail (cf. Figure 2.5 on page 13).

Figure 11.14 furthermore depicts a second probability maximum at higher temperatures below -5°C. This is an unexpected finding and therefore needs to be argued. Obviously, halogen activation occurs at temperatures larger than -20°C as can be seen in the histograms for times after early-April (Figures 11.12 and 11.13). This observation agrees with Bottenheim *et al.* (2009) who also reported ODEs at temperatures

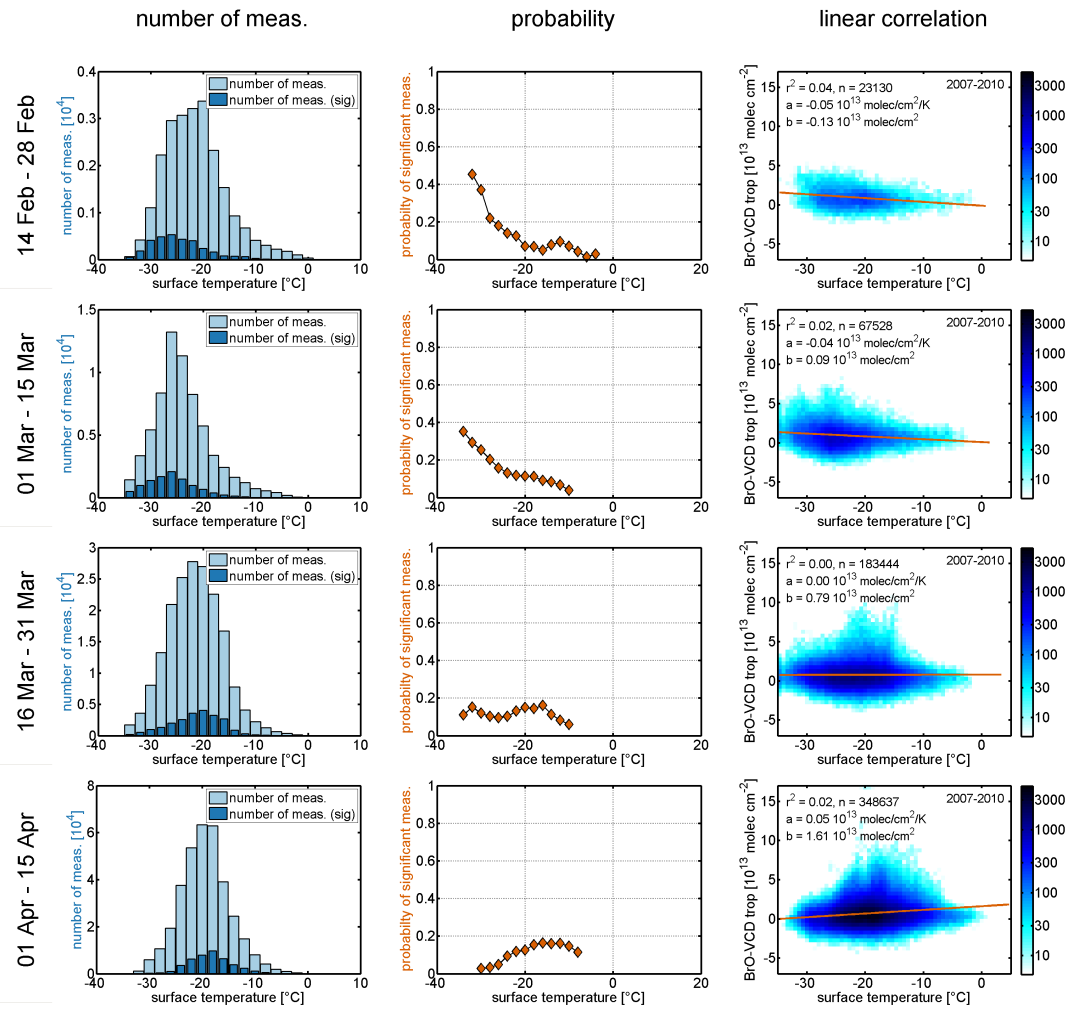

Figure 11.12.: *Correlation between 2 m-temperature and tropospheric BrO measurements in four half month periods between mid-February and mid-April. Left column: number of surface sensitive measurements over sea-ice, dark blue denotes the number of significantly elevated BrO SCDs measured. Middle column: probability of measuring a significantly elevated BrO SCD. Right column: distribution of measurements and linear regression between surface air temperature and tropospheric BrO VCD.*

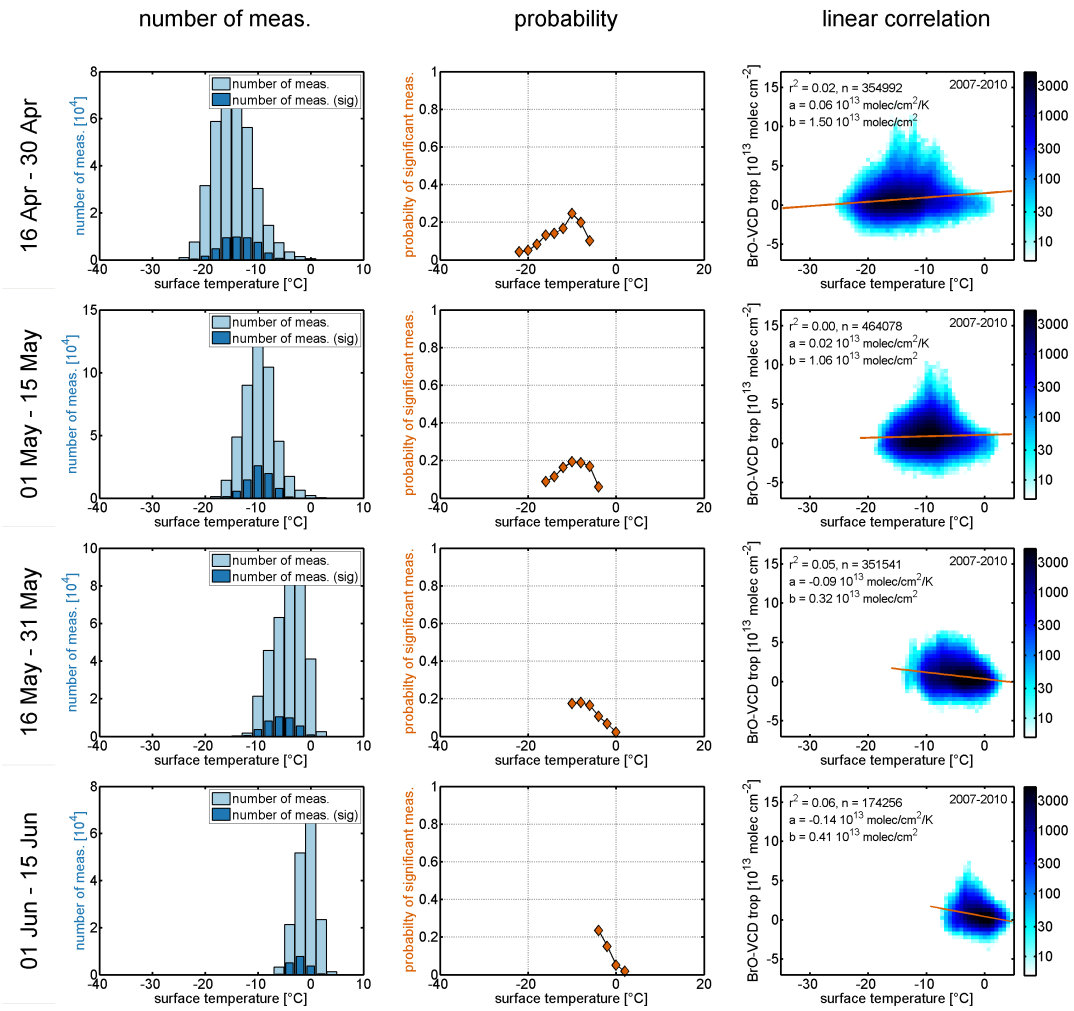

Figure 11.13.: *Continuation of Figure 11.12. Displayed are the results from four periods between mid-April and mid-June.*

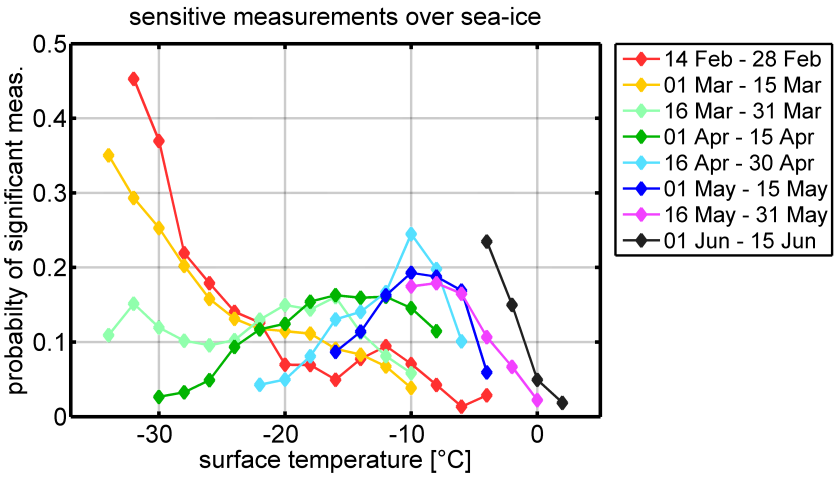

Figure 11.14.: *Period-summary of temperature dependence of the probability to measure a significantly elevated tropospheric BrO VCD. The data contains all measurements over sea-ice sensitive to near-surface BrO of the years 2007 to 2010.*

above this value. However, the link between an ODE and halogen activation may be less direct as the primary bromine release may also have happened elsewhere and the BrO is subsequently advected to the location of the satellite measurement.

On the one hand, a larger probability at higher temperatures may indicate that there are bromine release processes which are more efficient at higher temperatures. On the other hand, and this is more likely, systematic meteorological perturbations may be linked to high BrO levels. The temperature may either be the result or cause of a meteorological condition leading to enhanced tropospheric BrO VCDs.

- A low pressure system causing high wind-speeds and an increased boundary layer height also attracts warmer air from the south as depicted in Figure 11.7a. Then, warmer surface temperature would be the result of low pressure systems.

- Higher surface temperatures certainly decrease the stratification of the boundary layer and increase the height of the surface column. Thus, the tropospheric BrO VCD may increase assuming a constant mixing ratio and given the presence of a BrO source. Then, warmer surface temperatures would be the cause.

- Another possible explanation for a higher probability for higher surface temperatures is the development of cold fronts increasing vertical turbulence and hence mixing of ozone rich air from aloft into the boundary layer potentially void of O_3. The case study presented in Section 11.3 illustrates this hypothesis.

- Furthermore, warm surface air can also be associated to air originating from lower latitudes (cf. Figure 11.7e). The warmer air is attracted by polar cyclones transporting air potentially richer in O_3 over the sea-ice. Active bromine released from the sea-ice and/or snowpack may then continue to catalyse O_3 leading to

BrO concentrations larger than under conditions where O_3 concentrations are very low (cf. Section 8.3).

The negative correlation to temperature found again after 15 May is possibly caused by a less efficient release mechanism at temperatures this high.

11.5.2. Surface wind speed over sea-ice

Another parameter discussed in connection with bromine observations from space is the surface wind speed over sea-ice (e. g. Yang *et al.*, 2008; Jones *et al.*, 2009, 2010; Frieß *et al.*, 2011; Theys *et al.*, 2011). High surface winds produce wind-blown particles (e. g. blowing snow) providing an increased surface for heterogeneous recycling processes. Furthermore, high surface winds may increase the mixing between the snow-pack air and the overlying atmosphere through wind-pumping.

The comparison between ECMWF surface wind-speed and tropospheric BrO VCD measured by GOME-2 is shown in Figures 11.15 and 11.16, respectively. The wind-speed histogram shows an almost constant distribution for all analysed periods. The probabilities for significantly elevated BrO SCDs increase slightly with increasing wind-speeds as expected. This trend is especially developed for the periods between mid-March until the end of May. However, the calculated linear-correlation coefficients are surprisingly low for all periods ($r^2 \leq 0.04$). The last analysed period in June does not show any dependence on wind speed.

Even though the correlations are low, the probability study still indicates a higher probability at higher wind speeds for periods after mid March. This time interval may be correlated to the aforementioned bimodal behaviour regarding the surface temperature. In the first two periods, low temperatures increase the probability for elevated BrO columns, while from April on, a correlation to higher surface temperatures and higher wind-speeds is found.

Furthermore, it is noted that the presented analysis does not exhibit two maxima for different wind speeds (one at stable/calm conditions, one at high wind speeds and with blowing snow) favouring ODEs as discussed by Jones *et al.* (2009). This observation, however, does not contradict the hypothesis by (Jones *et al.*, 2009), but may rather be due to the different conditions leading to either significantly enhanced tropospheric BrO VCDs or effective O_3 destruction.

11.5.3. Boundary layer height over sea-ice

In Section 11.1, retrieved tropospheric BrO VCDs were compared to the boundary layer height (BLH) from ECMWF over the Canadian Arctic Archipelago and a strikingly linear dependence was found. Here, this comparison is extended to the whole Arctic but taking only sensitive measurements over sea-ice into account. The results from the eight periods from mid-February to mid-June are shown in Figures 11.17 and 11.18, respectively.

The BLH histograms of all measurements show an asymmetric distribution whose maximum and mean values increase from period to period. This behaviour of the

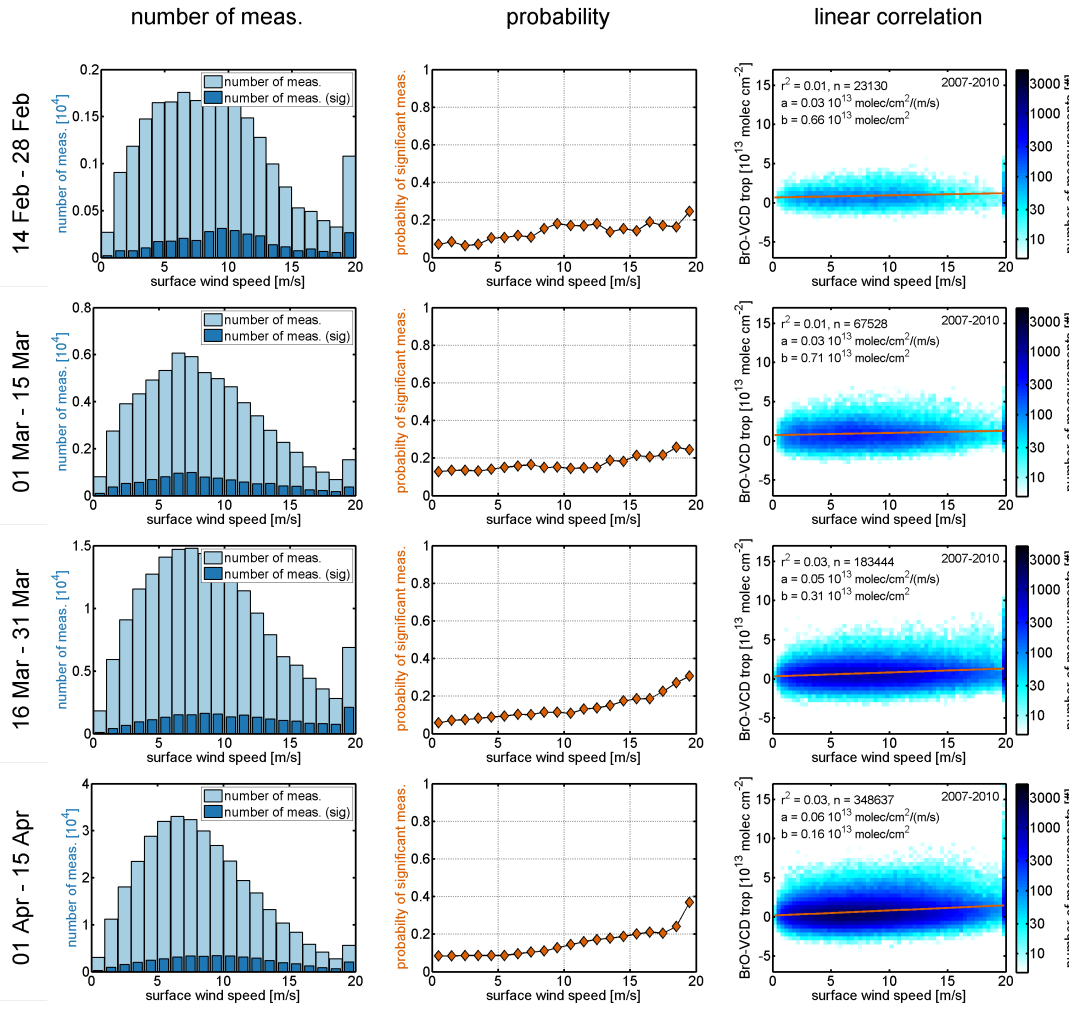

Figure 11.15.: *Correlation between surface wind-speed and tropospheric BrO measurements in four half month periods between mid-February and mid-April. Left column: number of surface sensitive measurements over sea-ice, dark blue denotes the number of significantly elevated BrO SCDs measured. Middle column: probability of measuring a significantly elevated BrO SCD. Right column: distribution of measurements and linear regression between wind-speed at the surface and tropospheric BrO VCD.*

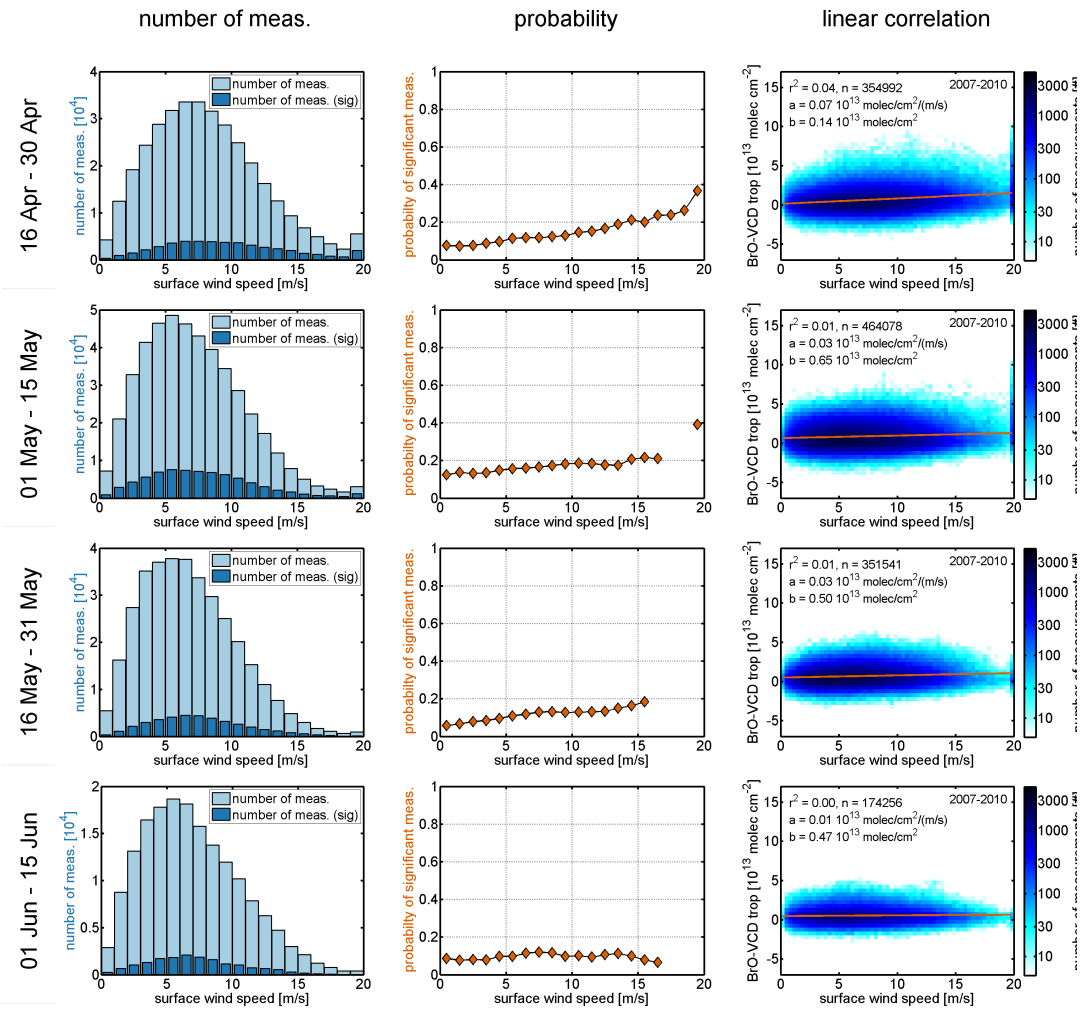

Figure 11.16.: *Continuation of Figure 11.15. Displayed are the results from four periods between mid-April and mid-June.*

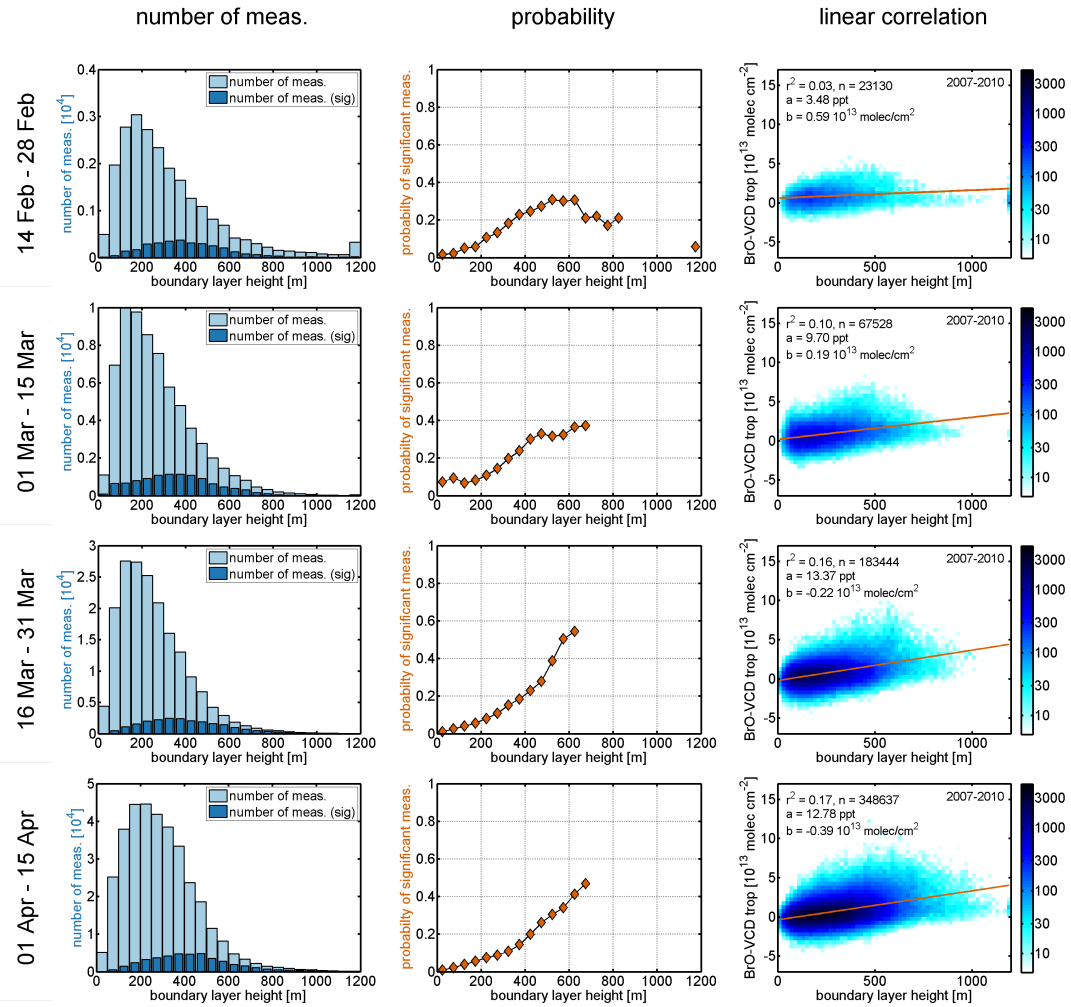

Figure 11.17.: *Correlation between modelled boundary layer height (BLH) and tropospheric BrO measurements in four half month periods between mid-February and mid-April. Left column: number of surface sensitive measurements over sea-ice, dark blue denotes the number of significantly elevated BrO SCDs measured. Middle column: probability of measuring a significantly elevated BrO SCD. Right column: distribution of measurements and linear regression between boundary layer height and tropospheric BrO VCD.*

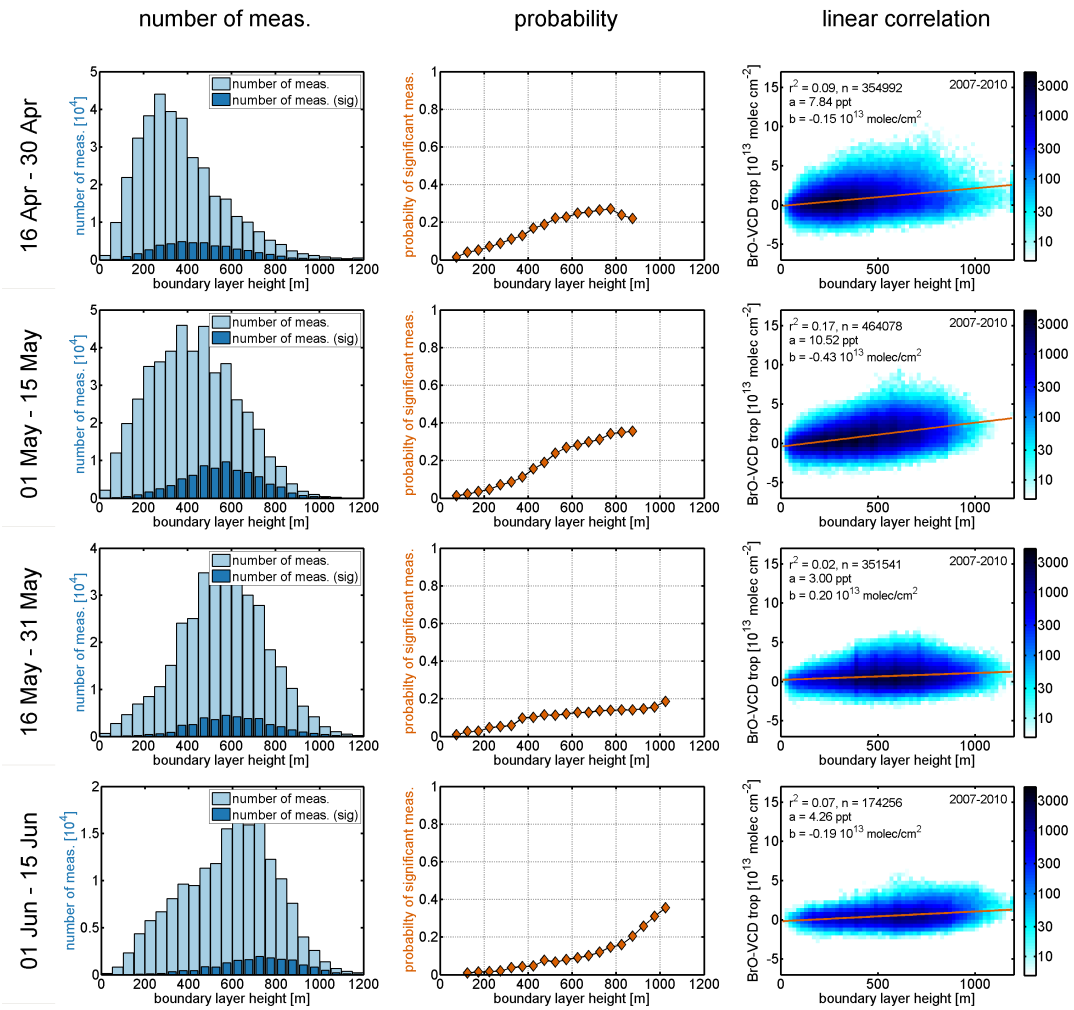

Figure 11.18.: *Continuation of Figure 11.17. Displayed are the results from four periods between mid-April and mid-June.*

BLH is probably related to the seasonal trend already discussed for the distribution of surface temperatures (see Section 11.5.1 above). However, the distribution of measurements with a significantly elevated tropospheric BrO VCD show a different distribution whose maximum is always shifted towards larger BLH. This observation yields for all analysed periods. As a result, the probability to observe a significantly elevated BrO SCD always increases for larger BLHs. The first and fifth period (end of February and end of April) both display the only exceptions to this rule, where the probability drops for BLHs larger than 600 m and 800 m, respectively. Even though the number of measurements is comparatively low, this may indicate that enhanced bromine levels are less likely in regions featuring higher BLHs during this time of the season. Alternatively, conditions leading to high BLHs, such as very high surface temperatures, may suppress the production of bromine.

For the periods from the beginning of March to mid May, tropospheric BrO VCD and BLH exhibit a clear correlation (cf. Section 11.1). The correlation coefficients $r^2 \gtrsim 0.1$ are generally larger than calculated above for all microwave backscatter coefficient, surface temperature, and wind speed. The slope of the linear regression corresponds to average mixing ratios of approx. 10 pmol mol^{-1} (c_{air}=2.9×10^{19} cm^{-3}) which is significantly less than the 23 pmol mol^{-1} found in the Canadian Arctic Archipelago in the beginning of March (cf. Section 11.1). This surprisingly good correlation justifies the attempt to calculate the average BrO mixing ratios in the Arctic. The results from this experiment are presented in Section 11.5.5 below.

11.5.4. Boundary layer residence time of backward trajectories

The mean residence time in the boundary layer is the last meteorological parameter to be considered in this study. It is the only parameter which takes the history of the probed air-mass into account instead of using the instantaneous meteorological conditions (cf. Section 11.2). The residence time is selected from the many possible proxies to be evaluated from backward trajectories because it reproduces the contact time with the surface underneath assuming a well mixed boundary layer allowing for sufficient turbulent diffusion from the surface. However, as the vertical distribution of BrO is unknown a priori, it is necessary and useful to calculate trajectories for different heights and compare the result with the observations as pointed out by Begoin *et al.* (2010). Therefore, backward trajectories were calculated for different end-heights and for every single satellite pixel as described in Section 7.4. Firstly, the modelled average residence times are compared to measured tropospheric BrO VCDs for two different height intervals for arriving trajectories. Secondly, the influence of the surface type is investigated using residence times over sea-ice and land.

Residence time of near-surface trajectories over sea-ice

In this section, surface sensitive tropospheric BrO VCDs over sea-ice are correlated to the average residence time over sea-ice calculated from trajectories ending in the respective satellite pixel at altitudes of 100, 200 and 400 m. These heights were chosen in order to model the near-surface column motion. The results of this correlation study

are compiled in Figures 11.19 and 11.20.

In general, a positive correlation between residence time over sea-ice and the measured tropospheric BrO VCD is found for all periods. The probability curves indicate a similar relationship between both properties. The probability of measuring a significantly elevated BrO column is always larger for higher average residence times in the boundary layer. However, the changing histograms indicate that the height selection criterion of the trajectories was maybe not perfect. In the beginning of the season, most trajectories were not inside the boundary layer at all, while almost all trajectories spent all the time within the boundary layer in the second half of the season. This behaviour indicates that the calculation of average residence times probably interferes with the seasonal trend of the BLH.

Residence time of elevated trajectories over sea-ice

In this section, average residence times over sea-ice are calculated from trajectories arriving at 600, 800, and 1000 m altitude, in contrary to the analysis presented in the previous section. This altitude range is assumed to be above the boundary layer. Hence, trajectories with a larger average boundary-layer residence time witnessed a significant upward motion previous to the measurement. The results of this study are compiled in Figures 11.21 and 11.22.

This time, the histograms (left columns) indicate that almost all trajectories ending at elevated altitudes did not spend any time in the boundary layer during the 24 h prior to the GOME-2 overpass. However, the probability for an increased residence time increases after April indicating that the trajectory ensemble partially ended within the boundary layer. However, at least in the first four periods, the distribution of measurements in the correlation plots (right columns in Figures 11.21 and 11.22) indicate that the small fraction of trajectories that actually witnessed an uplift from within the boundary layer to an elevated altitude also exhibits an enhanced tropospheric BrO VCD. This positive correlation is also visible in the second half of the season, even thought the effect is smaller – probably due to a generally higher boundary layer over sea-ice during the end of the season.

Comparison with residence time over land and ocean

The results presented in the previous two sections were dedicated to observations over sea-ice and the residence time of trajectories over sea-ice. In this section, it is turned to the question whether the residence time over land and ocean shows a similar correlation to measured tropospheric BrO VCDs as the residence time over sea-ice. The complete analysis compiled in Appendix E shows that the correlation to the residence time over land as well as ocean for measurements over both, sea-ice and land, is negligible. Here, only an example of the correlation with the residence time over land is presented.

Figure 11.23 compares the correlation of the residence time over sea-ice and land to the tropospheric BrO VCD for the third period, the end of March. The comparison does not reveal a significant correlation of tropospheric BrO VCDs measured over the

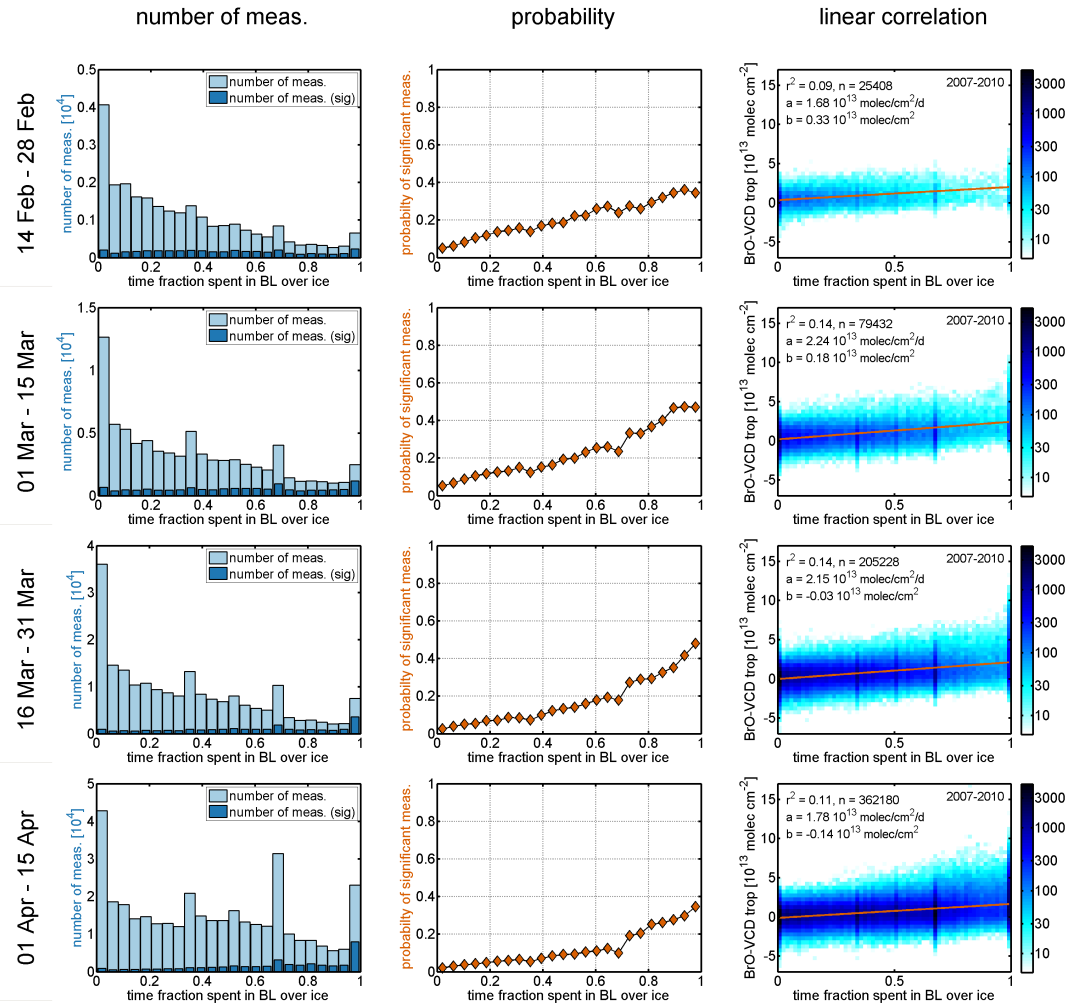

Figure 11.19.: *Correlation between residence of trajectories arriving at 100 m, 200 m and 400 m in the last 24 h in the boundary layer over sea ice and tropospheric BrO measurements in four half month periods between mid-February and mid-April. Left column: number of surface sensitive measurements over sea-ice, dark blue denotes the number of significantly elevated BrO SCDs measured. Middle column: probability of measuring a significantly elevated BrO SCD. Right column: distribution of measurements and linear regression between residence time over sea-ice and tropospheric BrO VCD.*

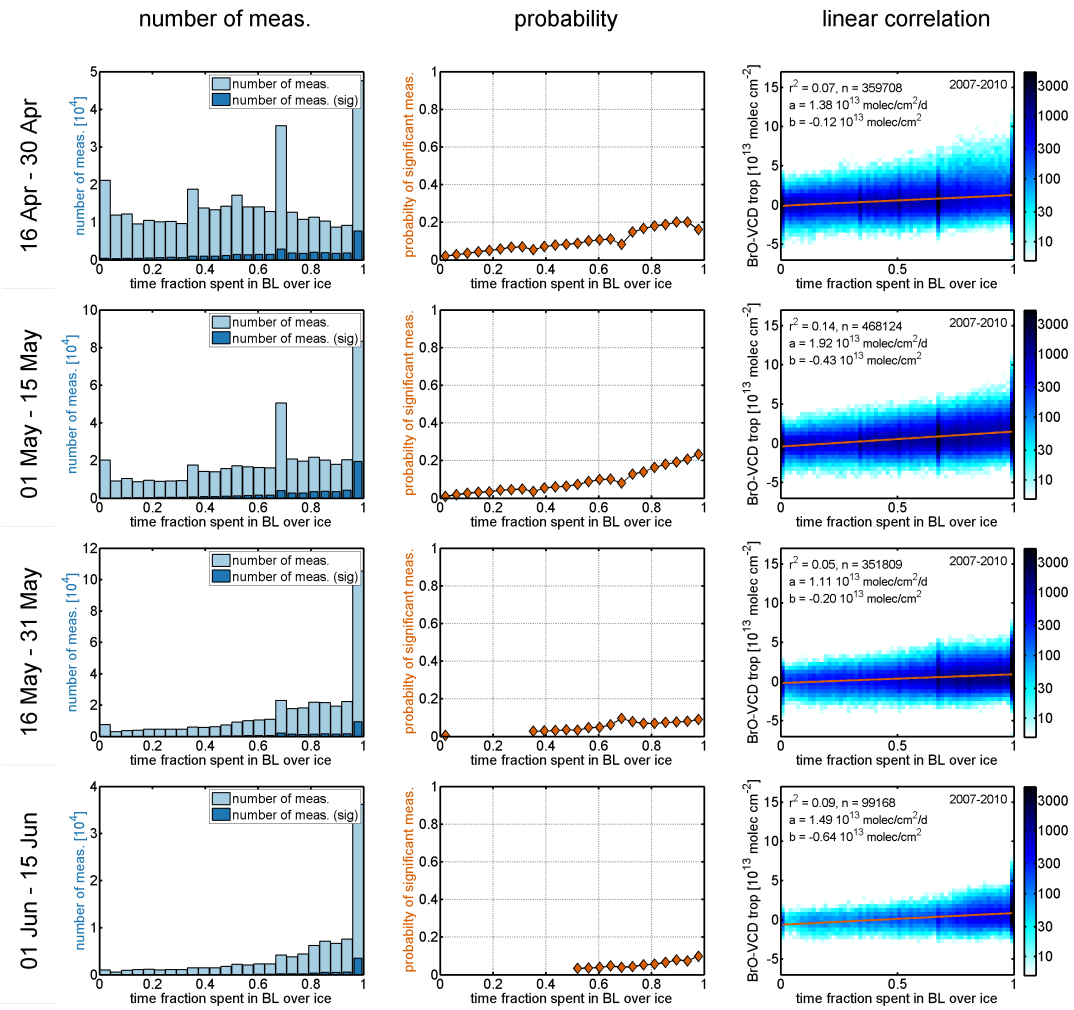

Figure 11.20.: *Continuation of Figure 11.19. Displayed are the results from four periods between mid-April and mid-June.*

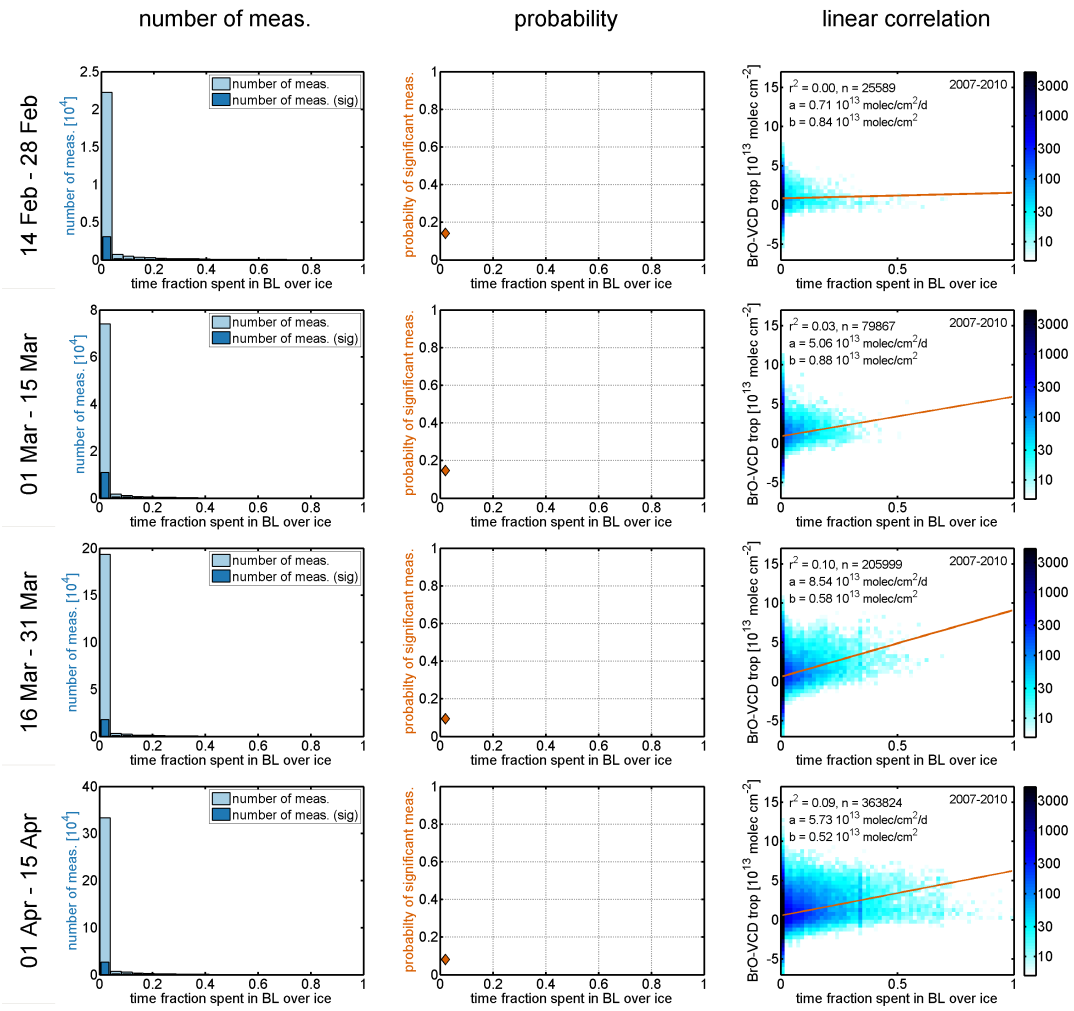

Figure 11.21.: *As Figure 11.19 but for trajectories arriving at 600 m, 800 m and 1000 m in the last 24 h in the boundary layer over sea ice.*

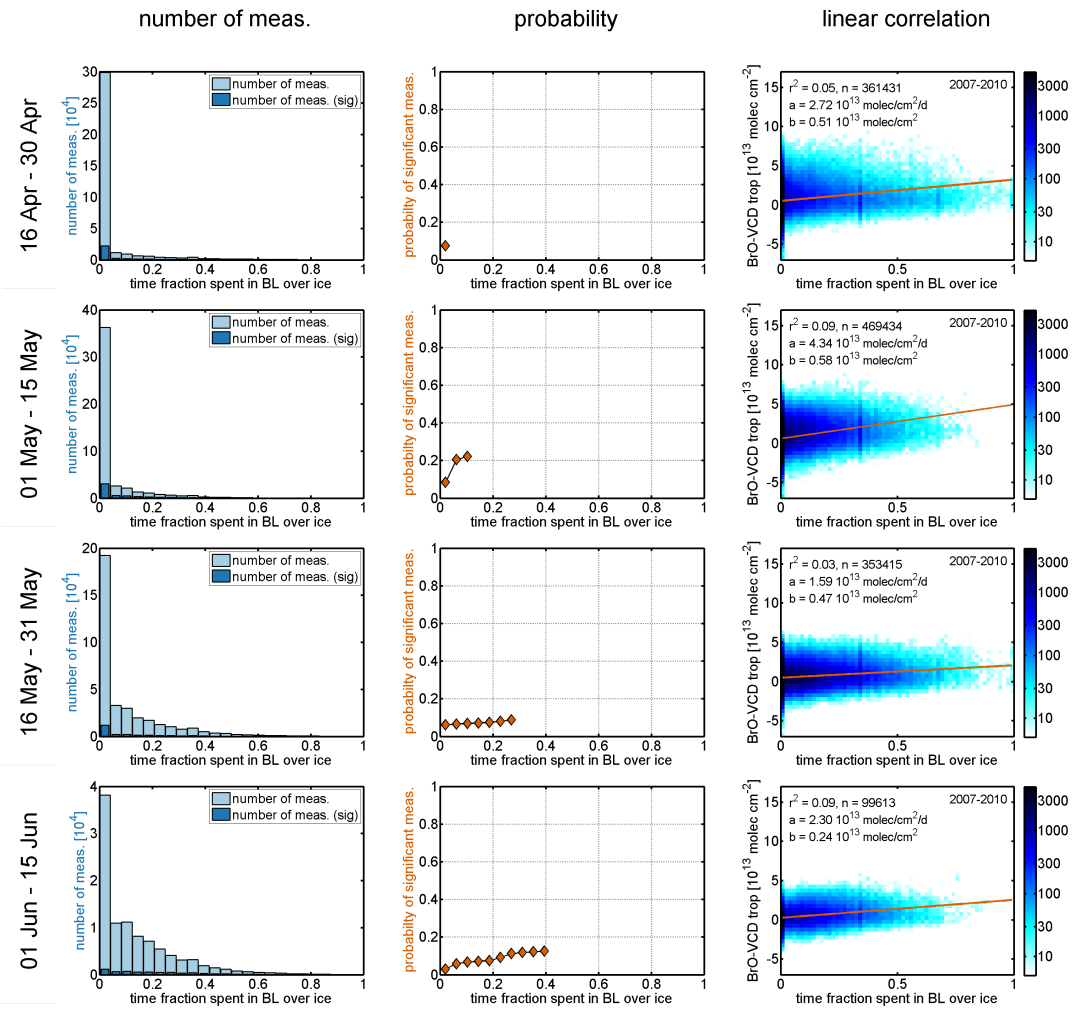

Figure 11.22.: *Continuation of Figure 11.21. Displayed are the results from four periods between mid-April and mid-June.*

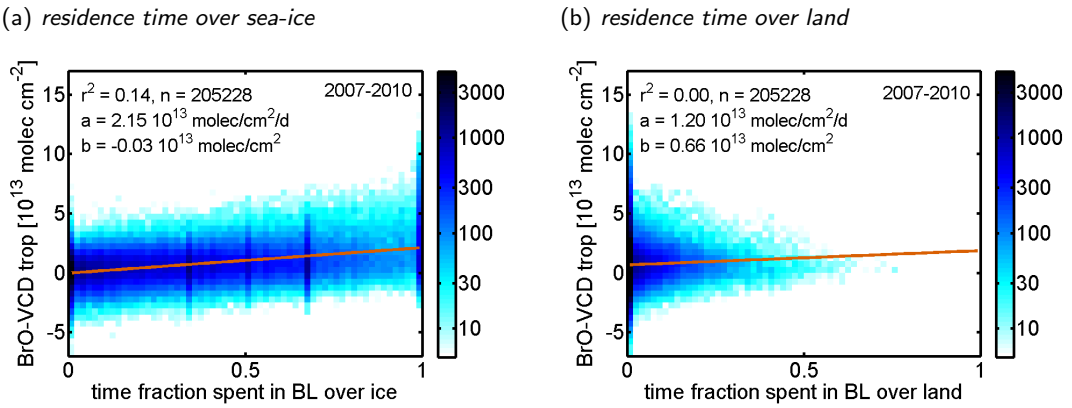

Figure 11.23.: *Correlation between BrO measurements and the average residence time of trajectories arriving at 100 m, 200 m and 400 m in the last 24 h in the boundary layer over (a) sea-ice and (b) land in period 3 in the second half of March. The complete period analysis of the residence time over land is compiled in Appendix E.1.1.*

sea-ice to the residence time over land while the residence time over sea-ice shows a clear positive correlation. It is therefore concluded that the land presents at most a minor source for active bromine compared to the sea-ice. This conclusion agrees with the conclusion of previous trajectory studies (e. g. Frieß *et al.*, 2004; Bottenheim & Chan, 2006; Simpson *et al.*, 2007a; Begoin *et al.*, 2010; Frieß *et al.*, 2011).

Furthermore, as shown in Appendix E.1.2, the residence time over ocean even showed a negative correlation with tropospheric BrO VCDs indicating that sea-salt aerosols produced from sea-spray generally have only a minor impact on bromine activation as seen from space. Furthermore, this negative correlation may be inter-correlated with the influence of the temperature. Air that comes from over the ocean is generally warmer than air that resided over the sea-ice and land over a longer time. As discussed above and in the literature, too warm temperatures are hampering the release of reactive bromine which may explain the observed anti-correlation.

Discussion of trajectory calculation experiments

The results from systematic backward trajectory calculations exhibited a significant correlation between the average residence times over sea-ice and the tropospheric BrO VCD retrieved from GOME-2 measurements. Two different altitude intervals were evaluated, one between 100 and 400 m and the other between 600 and 1000 m. The choice of these intervals was motivated by the assumption that these intervals either represent measurements within or above the boundary layer. However, the results exhibited some interferences with the actual boundary layer height which was found to be also correlated to the tropospheric BrO VCD in Section 11.5.3. Eventually, an altitude mesh adapting to the boundary layer height is necessary in order to eliminate these interferences. However, a recalculation applying this improvement could not be performed during the course of this thesis due to the available computing capacity

and the amount of data to be processed.

Despite the above mentioned interferences, it was still possible to identify a correlation for possibly elevated air-masses for the beginning of the season when the boundary layer is comparatively low. In conclusion, air-masses that spent sufficient time in the boundary layer over sea-ice and then rose prior to the GOME-2 overpass exhibited a larger tropospheric BrO VCD than those measurements without this upward movement. This observation may be confirmed by case study presented in Section 11.2, where a striking correlation between the boundary-layer residence time and the tropospheric BrO VCD was found.

11.5.5. The distribution of BrO surface mixing ratios

Both presented studies comparing tropospheric BrO VCDs and the ECMWF boundary layer height (Sections 11.1 and 11.5.3) revealed a significant linear correlation. Hence, it should be possible to calculate average BrO surface mixing ratios assuming a well mixed boundary layer with evenly distributed BrO. This assumption may not always be valid, as was shown in the comparison between ground-based and satellite measurements at Barrow (Chapter 9). However, the comparison of measurements over the sea-ice from aboard the Amundsen exhibited a close-to linear correlation between LP-DOAS and GOME-2 (Figure 9.6b on page 135).

The result for the third period (second half of March) as well as the respective tropospheric BrO VCDs, boundary layer height, surface temperature, and wind speed are shown in Figure 11.24. Figure 11.24d depicts the average surface mixing ratio of BrO calculated from GOME-2 tropospheric BrO VCDs and ECMWF boundary layer heights. Boundary layer heights below 100 m are excluded in order to reduce noise induced by the division by a small number. Furthermore, these results must be interpreted with caution as they are produced from two different data sources and possibly there are systematic biases influencing the calculation of the boundary layer height over land, where different fraction coefficients for different surface types and sloped need to be assumed.

The spatial pattern of BrO mixing ratios is similar to that of the VCDs (Figure 11.24a) but exhibits a stronger contrast over land where variations of the boundary layer height are larger that over sea-ice. Especially the on-shore regions around Barrow north of the Brooks Range, the Canadian Arctic Archipelago as well as the land surface in the south towards the Hudson Bay, North East Siberia, and the West Siberian Plain show enhanced average BrO surface mixing ratios. These regions have in common that they are north of the tree line and feature a flat terrain at low altitude.

Finally, the spatial coincidence of low average tropopause heights (Figure 11.24f) and the relatively high tropospheric VCDs and mixing ratios of BrO over the Canadian Arctic Archipelago are discussed. Salawitch *et al.* (2010) argued that the systematic longitudinal trend of the tropopause height may interfere with plots of average tropospheric BrO VCDs. This is probably true for total BrO columns as mentioned by Salawitch *et al.* (2010), but here tropospheric BrO VCDs were considered which are corrected for the effect of a varying tropopause height (cf. Section 6.4). There-

(a) *tropospheric BrO VCD*

(b) *boundary layer height*

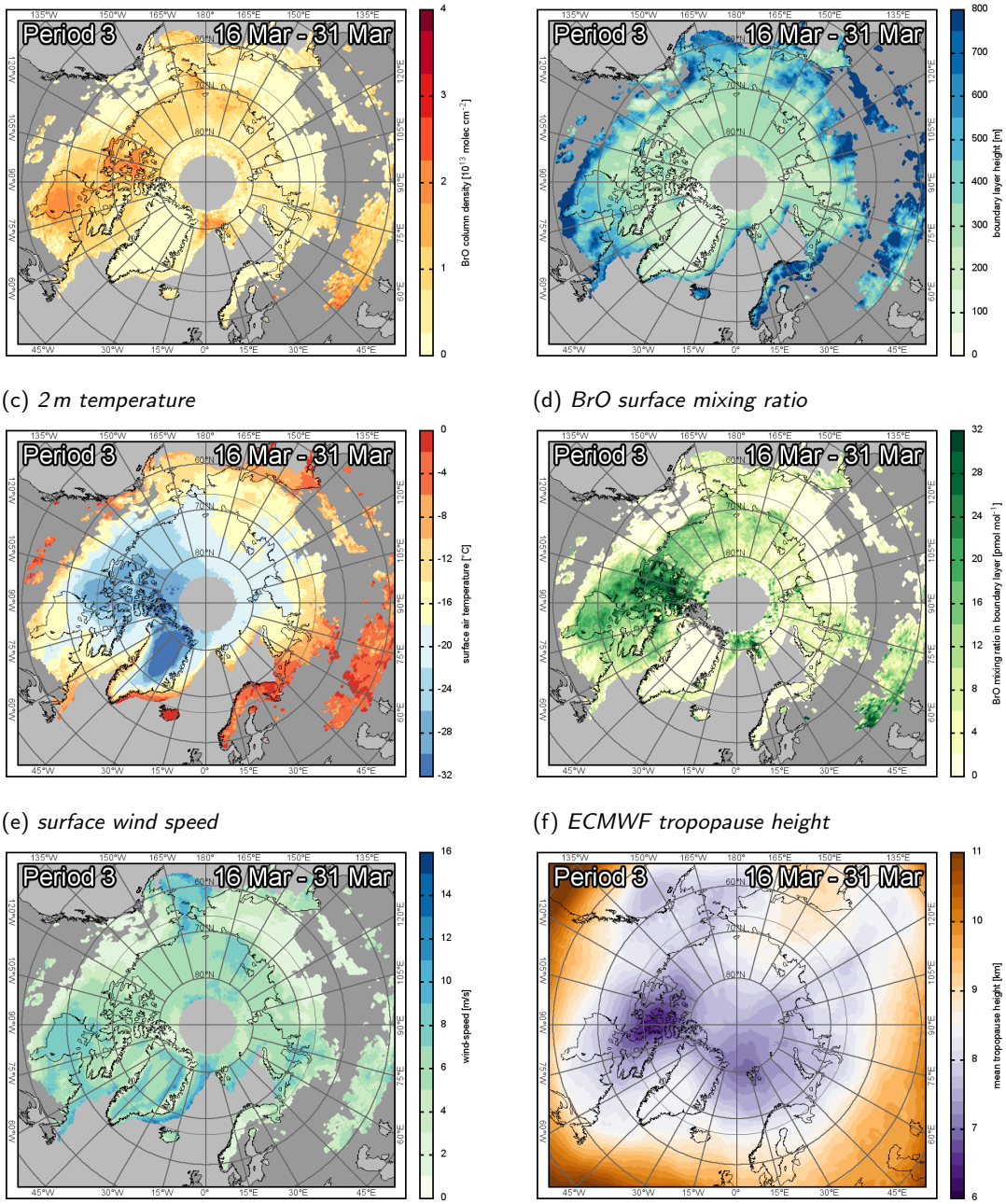

(c) *2 m temperature*

(d) *BrO surface mixing ratio*

(e) *surface wind speed*

(f) *ECMWF tropopause height*

Figure 11.24.: *GOME-2, ECMWF, and combined data obtained in the second half of March between 2007 and 2010: (a) GOME-2 tropospheric BrO VCD, (b) ECMWF boundary layer height, (c) ECMWF 2 m temperature, (d) BrO mixing ratio calculated from GOME-2 VCDs and ECMWF boundary layer heights, (e) ECMWF surface wind speed, and (f) ECMWF tropopause height. For (a)–(e) only measurements sensitive to the surface are considered.*

fore, it is likely that the spatial coincidence over the Canadian Arctic is rather the effect of meteorological conditions leading to enhanced tropospheric BrO VCDs than a stratospheric effect. This interpretation is further supported by the observations of only minor offsets in the correlation plots of VCD and boundary layer height (Figures 11.3c, 11.17, and 11.18). A possible systematic error in the stratospheric correction would lead to either an over- or an underestimated tropospheric column. If this was the case and a constant BrO column in the boundary layer is assumed, the offsets in these plots would be probably larger.

11.6. Correlation with optical cloud and aerosol properties

This section presents a comparison between CALIPSO measurements and collocated tropospheric BrO VCDs measured by GOME-2 in order to study the correlation to aerosols and cloud properties which possibly indicate the influence of heterogeneous chemistry (e. g. Fan & Jacob, 1992; Frieß *et al.*, 2004, 2011). In Section 6.5.3, cloud optical densities (CODs) and layer top altitudes (LTAs) measured by CALIPSO were used to validate the sensitivity filter developed in this thesis. Here, aerosol optical densities (AODs) as well as CODs are compared to the remaining sensitive tropospheric BrO VCD measurements over sea-ice as well as measurements over land located less than 500 km off the sea-ice edge. The CALIPSO data and the scheme to extract measurements collocated with GOME-2 is described in Section 6.5.3. The results are presented in tables, the corresponding plots are compiled in Appendix D.

11.6.1. Sensitive measurements over sea-ice

The first analysis is restricted to collocated measurement over sea-ice. In the case of COD, two probabilities $p_{nc} = \Sigma_{\mathrm{nc,sig}}/\Sigma_{\mathrm{nc}}$ and $p_c = \Sigma_{\mathrm{c,sig}}/\Sigma_{\mathrm{c}}$ for measuring a significantly elevated BrO SCD are calculated for not-cloudy (indexed nc) and cloudy (indexed c) scenes as determined by CALIPSO. The classification into not-cloudy and cloudy is done by comparing the mean COD measured within one GOME-2 pixel with an arbitrary COD threshold of 0.1. COD larger than the threshold are flagged cloudy. It is noted that the threshold may be shifted towards slightly higher CODs without changing the conclusions drawn from these observations. Table 11.1 compiles the results for each analysed half month period.

It shows that by looking at the number of measurements Σ, that the choice of the COD thresholds leads to larger number of measurements flagged cloudy than not-cloudy ($\Sigma_c > \Sigma_{nc}$). However, the probabilities for significantly elevated BrO SCDs reveals a higher probability for the cloudy pixels ($p_c > p_{nc}$) for each period. This result indicates a correlation between cloud particles detected by CALIPSO and elevated BrO columns.

In analogy, AODs are compared to GOME-2 measurements. In this case, a threshold level of AOD=0.01 is chosen to discriminate between pixels with aerosols (indexed a) and without aerosols (na). The results are compiled in Table 11.2. This time, however, the number of measurements with an AOD above this threshold is smaller than below ($\Sigma_a < \Sigma_{na}$). The calculated probabilities of finding an elevated BrO SCD

			COD≤0.1			COD>0.1		
ID	period	Σ	Σ_{nc}	$\Sigma_{\mathrm{nc,sig}}$	p_{nc}	Σ_{c}	$\Sigma_{\mathrm{c,sig}}$	p_c
1	14 Feb – 28 Feb	101	41	2	4.9 %	60	7	11.7 %
2	01 Mar – 15 Mar	360	187	32	17.1 %	173	34	19.7 %
3	16 Mar – 31 Mar	1911	1029	74	7.2 %	882	105	11.9 %
4	01 Apr – 15 Apr	2383	1127	93	8.3 %	1256	254	20.2 %
5	16 Apr – 30 Apr	2412	841	38	4.5 %	1571	304	19.4 %
6	01 May – 15 May	3139	674	33	4.9 %	2465	473	19.2 %
7	16 May – 31 May	3093	362	9	2.5 %	2731	251	9.2 %
8	01 Jun – 15 Jun	2162	424	8	1.9 %	1738	91	5.2 %

Table 11.1.: *Summary of collocated GOME-2 and CALIPSO measurements over Arctic sea-ice for the years 2007–2010. Significantly elevated BrO columns correlate to the elevated column cloud optical density (COD). In all periods, the probability p_c to find significantly elevated BrO when there are clouds detected (COD>0.1,* c*) when compared to the probability p_{nc} of cloud-free cases (COD≤0.1,* nc*).*

			AOD≤0.01			AOD>0.01		
ID	period	Σ	Σ_{na}	$\Sigma_{\mathrm{na,sig}}$	p_{na}	Σ_{a}	$\Sigma_{\mathrm{a,sig}}$	p_a
1	14 Feb – 28 Feb	64	52	3	5.8 %	12	2	16.7 %
2	01 Mar – 15 Mar	295	227	29	12.8 %	68	33	48.5 %
3	16 Mar – 31 Mar	1458	1125	92	8.2 %	333	63	18.9 %
4	01 Apr – 15 Apr	1801	1432	172	12.0 %	369	90	24.4 %
5	16 Apr – 30 Apr	1285	1064	122	11.5 %	221	45	20.4 %
6	01 May – 15 May	1443	1352	254	18.8 %	91	27	29.7 %
7	16 May – 31 May	886	834	92	11.0 %	52	7	13.5 %
8	01 Jun – 15 Jun	220	211	18	8.5 %	9	5	55.6 %

Table 11.2.: *Summary of collocated GOME-2 and CALIPSO measurements over Arctic sea-ice for the years 2007–2010. Significantly elevated BrO columns correlate to the elevated column aerosol optical density (AOD). In all periods, the probability p_a to find significantly elevated BrO when there are aerosols measured (AOD>0.01,* a*) when compared to cases without aerosols (AOD≤0.01,* na*).*

			COD≤0.1			COD>0.1		
ID	period	Σ	Σ_{nc}	$\Sigma_{\mathrm{nc,sig}}$	p_{nc}	Σ_{c}	$\Sigma_{\mathrm{c,sig}}$	p_c
1	14 Feb – 28 Feb	454	218	11	5.0 %	236	12	5.1 %
2	01 Mar – 15 Mar	491	217	23	10.6 %	274	28	10.2 %
3	16 Mar – 31 Mar	1493	626	56	8.9 %	867	44	5.1 %
4	01 Apr – 15 Apr	1602	719	30	4.2 %	883	65	7.4 %
5	16 Apr – 30 Apr	1588	529	17	3.2 %	1059	89	8.4 %
6	01 May – 15 May	1850	511	22	4.3 %	1339	119	8.9 %
7	16 May – 31 May	1865	455	6	1.3 %	1410	62	4.4 %
8	01 Jun – 15 Jun	1194	252	8	3.2 %	942	25	2.7 %

Table 11.3.: *Summary of collocated GOME-2 and CALIPSO measurements over the land adjacent to the Arctic sea-ice for the years 2007–2010. The correlation between column BrO and column cloud optical density (COD) is weaker than over sea-ice (Table 11.1). Apparently, the probabilities p_c and p_{nc} to find a significantly elevated BrO column are not depending on whether there are clouds or not, respectively.*

for pixels identified to contain aerosols are again enhanced compared to the opposite ($p_a > p_{na}$). This observation indicates a correlation between enhanced BrO SCDs and the presence of aerosols over sea-ice. Possibly, however, thin clouds may also increase the sensitivity to near-surface BrO thus leading to an overestimation of the tropospheric BrO VCD in the presence of clouds.

11.6.2. Sensitive measurements over land

In a second analysis, solely the collocated measurements over land are considered. The choice of COD and AOD thresholds is identical to the study conducted over sea-ice. Both, COD and AOD results are compiled in Tables 11.3 and 11.4, respectively.

The number of measurements show a similar behaviour than over sea-ice: A larger fraction of measurements are flagged cloudy than not-cloudy ($\Sigma_c > \Sigma_{nc}$) and vice versa for the aerosols ($\Sigma_a < \Sigma_{na}$). However, while the calculated probabilities of significantly enhanced BrO SCDs seem to be independent from an enhanced COD ($p_c \approx p_{nc}$), aerosols still appear to be positively correlated to BrO column enhancements ($p_a > p_{na}$). This is an interesting result compared to the correlation over sea-ice where both COD and AOD exhibited a positive correlation.

11.6.3. Discussion of the comparison with CALIPSO measurements

Both comparisons of CALIPSO AOD and GOME-2 BrO measurements over sea-ice and land close to the sea-ice revealed a positive correlation between the presence of aerosols and enhanced BrO. For COD measurements, a positive correlation was only found for collocated measurements over sea-ice. The correlation with COD over land was found to be ambiguous.

These results indicate that the presence of aerosols is linked to the observation

			AOD≤0.01			AOD>0.01		
ID	period	Σ	Σ_{na}	$\Sigma_{\mathrm{na,sig}}$	p_{na}	Σ_{a}	$\Sigma_{\mathrm{a,sig}}$	p_a
1	14 Feb – 28 Feb	248	196	11	5.6 %	52	5	9.6 %
2	01 Mar – 15 Mar	320	251	21	8.4 %	69	20	29.0 %
3	16 Mar – 31 Mar	1041	805	60	7.5 %	236	35	14.8 %
4	01 Apr – 15 Apr	1013	825	47	5.7 %	188	28	14.9 %
5	16 Apr – 30 Apr	647	556	52	9.4 %	91	22	24.2 %
6	01 May – 15 May	680	600	79	13.2 %	80	12	15.0 %
7	16 May – 31 May	503	465	43	9.2 %	38	2	5.3 %
8	01 Jun – 15 Jun	94	89	9	10.1 %	5	0	0.0 %

Table 11.4.: *Summary of collocated GOME-2 and CALIPSO measurements over the land adjacent to the Arctic sea-ice for the years 2007–2010. Significantly elevated BrO columns correlate to the elevated column aerosol optical density (AOD). In all periods, the probability p_a to find significantly elevated BrO when there are aerosols measured (AOD>0.01,* a*) when compared to cases without aerosols (AOD≤0.01,* na*). This behavior is comparable to the measurements over sea-ice Table 11.2.*

of enhanced BrO columns. However, this conclusion does not prove that aerosols increase the abundance of BrO in the atmosphere because there may be other causal links between both observations. For instance, high wind-speeds may increase the production of aerosols but also increase the boundary layer height decreasing the detection limit for BrO concentrations evenly mixed in the boundary layer.

The different correlations to COD for observations over sea-ice and over the adjacent land seems to pose more questions than giving answers. The positive correlation to the presence of clouds may be explained by the apparent cyclonic nature of "BrO clouds" because upward movement of air potentially also creates clouds through condensation. However, the question why this is not the case over land remains open. Possibly, open leads on the sea-ice provide the moisture for the production of clouds in the front. The land does not provide such a source for moisture.

11.7. Summary of relationship to environmental parameters

In this chapter, tropospheric BrO VCDs retrieved from GOME-2 measurements were compared to different environmental parameters such as the relief, meteorological parameters from the ECMWF weather model, and cloud properties measured by CALIPSO. The comparisons were performed in case studies with a regional focus as well as more systematically using the entire data-set of GOME-2 observations between 2007 and 2010 in the northern hemisphere. The presented studies were conducted in order to test the dependence of tropospheric bromine activation in polar regions on different environmental factors already discussed in the literatures (cf. Section 2.4).

On the one hand, cross-correlations between the surface meteorology altering the column height within the boundary-layer are evident in the presented GOME-2 mea-

surement which were found to correlate surprisingly well to the boundary layer height as provided by ECMWF. This observation indicates that BrO observations from space are in general strongly dependent on meteorology because the amplitude of the enhancement of tropospheric BrO concentrations is primarily a function of the column height of the mixing layer. Furthermore, the processes leading to increased boundary layer heights may also be responsible for the production of BrO in the first place because a less stratified boundary-layer (smaller potential temperature gradient) also increases the entrainment of O_3 into the boundary-layer where the concentration of reactive bromine is probably high.

On the other hand, the observed correlation between ECMWF boundary layer height and tropospheric BrO VCD allows to calculate an average boundary layer mixing ratio of BrO. This calculation revealed that the highest average BrO surface concentrations probably prevail in the Canadian Arctic Archipelago in the second half of March. Furthermore, it may be concluded from the observed inhomogeneous distribution of BrO mixing ratios that further factors influencing the occurrence of significantly elevated tropospheric BrO VCDs in satellite measurements may be separated from the influence of the boundary layer height. The different hypotheses linked to ozone depletion events and bromine activation are discussed in the light of the presented GOME-2 measurements in the following.

Surface temperature

The correlation between tropospheric BrO VCDs and the surface temperature extracted from ECMWF data revealed a bimodal dependence on temperature. In the beginning of the season, a clear negative correlation between both properties was found. This observation indicates that the primary release processes of reactive bromine is more efficient at lower temperatures. This observation agrees well with previously published studies. After March, however, a second maximum probability for enhanced tropospheric BrO VCDs is found for temperatures between -20°C and -5°C. This second maximum is most probably due to enhanced horizontal and vertical mixing present above areas with higher surface temperatures. The warm temperatures either indicate a low potential temperature gradient allowing for increased vertical mixing or warmer air-masses which potentially originate from lower latitudes and therefore contain more O_3 than air which resided for a longer period over the central Arctic where O_3 is depleted at the surface most of the time (e. g. Hopper *et al.*, 1998; Tarasick & Bottenheim, 2002; Jacobi *et al.*, 2010; Toyota *et al.*, 2011). The measurements presented here suggest that both the release as well as the mixing of two air-masses – one enriched in bromine but depleted in ozone and the other still containing background ozone concentrations – are the reason for the observed correlation between to bromine activation and temperature depending on the season.

Surface wind speed

The correlation between tropospheric BrO VCDs and the surface wind speed is less definite. There is a slight positive correlation between tropospheric BrO VCDs and the

surface wind speed between March and May. It remains however unclear whether this correlation is due to a causal relationship (wind pumping, aerosol production from frost-flowers, blowing snow, etc.) as identified in previous studies or an apparent cross-correlation to the meteorological condition (frontal activity, increased vertical mixing, higher boundary layer) increasing the probability for an enhanced tropospheric BrO column.

Aerosols and clouds

From the comparison between CALIPSO aerosol and cloud optical density measurements and retrieved tropospheric BrO VCDs from GOME-2 it may be concluded that the presence of clouds and aerosols are probably linked to the occurrence of enhanced tropospheric BrO VCDs over sea-ice. The observations over land were less conclusive. Hence, further studies also taking the vertical distribution of aerosols/clouds in to account are necessary to clarify the connection between satellite measurements of BrO and the effect of airborne particles on bromine activation.

Surface type and origin

The comparison of the residence time of backward trajectories in the boundary layer reveals a clear correlation between contact with sea-ice and tropospheric BrO VCDs. The correlation was increased for trajectories ending at higher altitudes indicating that a large residence time in the boundary layer over sea-ice in connection with vertical mixing (upward motion prior to the satellite measurement) are a prerequisite for enhanced tropospheric BrO VCDs. However, no significant correlation was found for the residence time in the boundary layer over land indicating that the snowpack is probably only a minor source for reactive bromine.

Furthermore, the comparison to microwave backscatter measurements revealed only a slight dependence between the ice type and an enhanced tropospheric BrO VCD. The previously published positive correlation to first-year sea-ice and negative correlation to multi-year sea-ice could neither be confirmed nor disproved by the measurements presented in this thesis. The presented study even exhibited a positive correlation with potential multi-year sea-ice concentrations in the beginning of March. This positive correlation is probably due to a cross-correlation to the high probability for significantly enhanced tropospheric BrO VCDs in the Canadian Arctic Archipelago whose waterways typically contain at least some multi-year sea-ice. Hence, the instantaneous correlations between BrO and ice type is ambiguous. Further studies combining the ice type with the backward trajectories are required in order to assess the influence of either ice-type on BrO enhancements observed from space.

Synoptic patterns of BrO enhancements

Several previous studies suggested that horizontal and vertical mixing at synoptic scales are a prerequisite for ozone depletion events and enhanced BrO concentrations (Gong *et al.*, 1997; Hopper *et al.*, 1998; Strong *et al.*, 2002; Jacobi *et al.*, 2010; Toyota *et al.*, 2011). The data presented above confirms these observations. In Section

11.3, it was possible to precisely locate a "BrO cloud" in an occluding cold front also leading to the conclusion that vertical and horizontal mixing are a prerequisite for elevated BrO columns. It is hence concluded that the cold air over the sea-ice surface (i. e. the air within the Arctic Dome) is presumably void of ozone (e. g. Jacobi *et al.*, 2010; Toyota *et al.*, 2011). The availability of O_3 limits the production of BrO observable from space. However, the phenomenon of bromine activation may be even more widespread than seen in maps of tropospheric BrO VCD as large concentrations of reactive bromine in a very shallow surface layer are still possible, as discussed in Chapter 9.

Part IV.

Conclusions and Outlook

12. Conclusions

This thesis investigates the phenomenon of polar tropospheric halogen activation by applying both satellite and ground-based measurements. The concentrations and column densities of bromine monoxide (BrO) indicating tropospheric halogen activation were derived using the differential optical absorption spectroscopy (DOAS) technique taking advantage of narrow-band features in the BrO absorption cross-section. The main focus of this thesis was to retrieve tropospheric BrO vertical column densities (VCDs) from satellite measurements and to interpret the obtained data using various additional data sources including ground-based measurements, complementary satellite measurements, and meteorological data from a weather model. In contrast to satellite measurements delivering a complete coverage of the polar regions every day, ground-based measurements are more accurate and may provide information about the chemistry of further trace-gases, the vertical profile of BrO, as well as a much higher temporal resolution – but only at one place which may not be representative for the entire Arctic.

Ground-based measurements were conducted at Barrow, Alaska in spring 2009, yielding an almost five week long continuous time-series of BrO surface concentrations obtained by LP-DOAS measurements and vertical profiles retrieved from MAX-DOAS measurements, respectively. The measurements exhibit highly variable surface concentrations of BrO and O_3 leading to the conclusion that both local chemistry and the origin of the air-mass are important factors influencing halogen activation. Furthermore, the striking correlation between both DOAS measurements as well as between DOAS and chemical ionization mass spectroscopy (CIMS) measurements indicates that all techniques provide a consistent description of the studied phenomenon. However, the principal findings of this thesis are based on the combination of both ground-based and satellite observations taking.

In order to correlate satellite measurements of BrO to ground-based data, a new satellite retrieval for tropospheric BrO VCDs was developed. The presented algorithm separates the measured total BrO column density into stratospheric and tropospheric partial columns. The stratospheric column is unknown a priori and depends on the tropopause height and stratospheric chemistry. Two important properties of the new algorithm are that it identifies measurements a) with significantly enhanced tropospheric BrO amounts which can not be explained by stratospheric processes and b) which are sensitive for near-surface layers. Unlike earlier attempts to solve this task, the presented retrieval, applied on measurements by the second Global Ozone Monitoring Experiment (GOME-2) instrument, does not depend on extensive chemistry models and climatological data. Both the decomposition of the total column of BrO into stratospheric and residual tropospheric contribution, as well as the surface sensitivity filter algorithm were validated through real measurements and simulated data.

The resulting tropospheric BrO columns retrieved from GOME-2 measurements were compared to independent BrO data-sets from ground-based measurements. Data from two field campaigns taking place at Barrow, Alaska as part of this work and offshore aboard the Amundsen research icebreaker in the Amundsen Gulf was utilized and near-surface processes were found to be the source of activated bromine compounds in agreement with previous studies. The major deviations between surface observations and GOME-2 data could be explained by the vertical profiles of both BrO and O_3 which are a result of the surface layer stratification controlling the flux of BrO and O_3. Moreover, as described in this thesis, it is occasionally possible that shallow surface layers and horizontal heterogeneities may obfuscate active bromine chemistry from satellite measurements.

As inferred in earlier studies, the distribution of BrO in the troposphere was found highly correlated to the presence of sea-ice. Furthermore, the high correlation to the surface elevation and boundary layer height strongly suggest a rather shallow layer enriched in BrO at the surface. Furthermore, significantly enhanced tropospheric BrO VCDs were also detected over large snow covered areas at mid-latitudes in central Eurasia during winter. While the influence of a comparatively high surface albedo may not be entirely ruled out, the observations indicate the presence of enhanced concentrations of BrO in the free troposphere. However, the major part of tropospheric BrO is located in the springtime polar boundary layer and the relationship between several environmental parameters and the occurrence of enhanced BrO VCDs was studied.

It is shown that the occurrence of enhanced tropospheric BrO VCDs are strongly related to boundary layer meteorology. The causality, however, is not always clear because meteorological conditions leading to an enhanced mixing depth (e. g. higher wind-speeds and surface temperatures) may also provoke an increased probability of measuring a significant enhancement of the near-surface BrO column density. However, an interesting bimodal correlation between tropospheric BrO VCDs and the surface air temperature over sea-ice was revealed. During the beginning of the season, the comparison exhibits a clear negative correlation whereas a secondary maximum probability for enhanced tropospheric BrO VCDs exist at temperatures above -20°C begiining in late-March. While rather low temperatures below -20°C are known to increase the release efficiency of active bromine from brine surfaces, the behaviour at higher temperatures adds a new aspect to the phenomenon. The correlation to higher temperatures is likely related to the production of BrO in meteorological fronts. The turbulent diffusion, which is typically enhanced through strong wind shear, leads to the mixing of two air-masses with a different chemistry: One is halogen-rich and ozone-poor (ozone depleted air originating from over the sea-ice) whereas the other is ozone-rich (background air). The result is an increased BrO production in the intermediate zone as illustrated in Section 2.5. Hence, there are at least two possible explanations for the observed correlation with temperature. Firstly, ozone-rich air may be mixed from aloft as warmer surface temperatures lead to increased vertical movement due to a decreased potential temperature profile. Secondly, air transported from lower latitudes, which potentially contains still sufficient amounts of O_3 to produce BrO, is warmer. Without the mixing, the production of BrO is hampered at low O_3 concentrations which probably prevail at the sea-ice surface throughout spring.

13. Outlook

The retrieval algorithm for tropospheric BrO VCDs developed in this thesis was solely applied on GOME-2 measurements. By design, however, the retrieval is applicable to measurements performed by other satellite instruments like GOME, SCIAMACHY, and OMI as well. Additionally, the algorithm to determine the sensitivity to trace-gas concentrations close to the surface is neither limited to retrievals of BrO nor to the Arctic. Any DOAS retrieval from satellites intended to study surface concentrations over bright surfaces may, in principle, apply the presented surface sensitivity filter, for instance retrievals of iodine monoxide (IO) in the Antarctic troposphere.

Besides the application of the developed retrieval algorithm, there are several scientific questions and tasks to be addressed in future studies using the satellite data presented here.

- Areas of enhanced vertical or horizontal turbulent diffusion may be identified by additional meteorological parameters in order to improve the correlation and to identify cases which are possibly not so much affected by meteorological processes. Similarly, published transport patterns of reactive bromine species in elevated layers should be compared to other meteorological parameters in order to find a conclusive explanation including both BrO production in meteorological fronts and long-range transport.

- The comparison of tropospheric BrO VCDs to backward trajectories may be improved after studying the influence of the maximum height assumed to represent contact with the surface. In the future, the study should be repeated using microwave data in order to identify possible source regions and the predominant ice-type in this region.

- Trajectory calculations may also be used to estimate the flux of bromine compounds from the polar boundary layer into the free troposphere and lower latitudes.

- The measurements presented here are limited to measurements below 80° SZA. Hence, the atmosphere may not be probed earlier in the season during which the principal release of reactive bromine species occurs. This restriction is impaired by the comparatively early Equator crossing time of GOME-2 resulting in even lower maximum latitudes. In order to fill the afternoon measurement gap, the data of other satellite missions such as OMI may be included in the study.

- The comparison studies involving CALIPSO column data may be improved by using the profile information provided by this instrument.

In addition, ground-based and air-borne measurements as well as laboratory studies are required in order to investigate the underlying chemistry and to determine the vertical distribution of reactive halogen species.

- The generation of BrO occurring in frontal mixing needs to be fast in order to explain the high spatial and temporal correlation between meteorology and chemistry. However, chemistry models implementing the bromine explosion mechanism are still not capable to explain the speed under which the observed BrO patterns evolve. Hence, either a modified bromine explosion mechanism, which also includes reactions with nitrogen oxide compounds, or even an alternative production scheme is required. It may be speculated if rather high Br_2 and Br-atoms concentrations persist in the boundary-layer most of the time potentially explaining the rapid BrO production. In this case, HBr, HOBr, and possibly also $BrONO_2$ accumulating on aerosols and the snow-pack would only be produced from a fraction of the reactive bromine stock.

- Measurements from low-flying aircrafts as, for instance, conducted during the recent BROMEX campaign are necessary to improve our understanding of the vertical profile of O_3, BrO and further species close to the surface and within the boundary-layer. These measurement may be used to study the possible long-range transport of bromine species and furthermore determine the exact distribution of BrO in fronts.

- The identification of the Canadian Arctic Archipelago as well as the Siberian Coast as the regions most affected by bromine activation in the beginning of the season strongly suggests to conduct future field campaigns in these regions. It is furthermore noted, that the concentrations of BrO in the troposphere over central Eurasia were probably increased during winter. Here, ground-based measurements are required in order to confirm the satellite observations.

Finally, the results from this thesis may lead to even broader implications. On the one hand, model studies are required to improve our understanding of polar tropospheric halogen activation and the impact on a global scale. The results presented in this thesis highly suggest that future chemistry models need to implement meteorological dispersion processes as well in order to be able to reproduce the observed strong cross-correlation between chemistry and meteorology. On the other hand, satellite measurements of BrO may as well be used to study diffusion processes within occluding fronts, which are yet difficult to measure at synoptic scales. This approach, however, requires that the chemistry in the transition zone is sufficiently quantified. The simple chemistry and diffusion model presented in the introduction part of this thesis may serve as a starting point.

Appendix

A. Abbreviations and symbols

A.1. Abbreviations

ACIA	Arctic Climate Impact Assessment
AICI	Air Ice Chemical Interactions
AMAP	Arctic Monitoring and Assessment Program
AMAX-DOAS	Airborne Multi AXis Differential Optical Absorption Spectroscopy
AMF	Air Mass Factor
AMSR-E	Advanced Microwave Scanning Radiometer-EOS
AOD	Aerosol Optical Density
AOT	Aerosol Optical Thickness
ARCPAC	Aerosol, Radiation, and Cloud Processes affecting Arctic Climate
ARCTAS	Arctic Research of the Composition of the Troposphere from Aircraft and Satellites
ARCTOC	ARCtic Tropospheric Ozone Chemistry
ASTAR	Arctic Study of Tropospheric Aerosol, Clouds and Radiation
AVHRR	Advanced Very High Resolution Radiometer
BASCOE	Belgian Assimilation System for Chemical ObsErvations
BL	Boundary Layer
BLH	Boundary Layer Height
CALIOP	Cloud-Aerosol Lidar with Orthogonal Polarization
CALIPSO	Cloud-Aerosol Lidar & Infrared Pathfinder Satellite Observations
CARIBIC	Civil Aircraft for the Regular Investigation of the Atmosphere Based on an Instrument Container
CCGS	Canadian Coast Guard Ship
CF	Cloud Fraction
CFC	ChloroFluoroCarbon
CFL	Circumpolar Flaw Lead
CH	Cloud Height
CIMS	Chemical Ionization Mass Spectroscopy
COD	Cloud Optical Density
COT	Cloud Optical Thickness
CS	Cross-Section
CTM	Chemistry and Transport Model
DLR	Deutsches zentrum für Luft- und Raumfahrt
DMS	DiMethyl Sulfide

continued on next page

continued from last page

DOAS	Differential Optical Absorption Spectroscopy
DOASIS	DOAS Intelligent System
DOD	Differential Optical Density
ECHAM	ECmwf HAMburg global climate model
ECMWF	European Centre for Medium-Range Weather Forecasts
EMAC	ECHAM/MESSy Atmospheric Chemistry
EOS	Earth Observing System
ERS	European Remote-sensing Satellite
ESA	European Space Agency
f-Br	Filterable Bromine
FWHM	Full-Width Half-Maximum
FYI	First-Year sea-Ice
GCM	Global Climate Model
GH	Ground Height
GMES	Global Monitoring for Environment and Security
GOME	Global Ozone Monitoring Experiment
HAF	High Albedo Fraction
HIRLAM	HIgh Resolution Limited Area Model
HYSPLIT	HYbrid Single Particle Lagrangian Integrated Trajectory model
IGAC	International Global Atmospheric Chemistry
IPCC	Intergovernmental Panel on Climate Change
IPY	International Polar Year
JPL	Jet Propulsion Laboratory
LAGRANTO	LAGRangian ANalysis TOol
LIDAR	LIght Detection And Ranging
LOS	Line Of Sight
LP-DOAS	Long Path Differential Optical Absorption Spectroscopy
LSM	Land Sea Mask
LTA	Layer Top Altitude
LUT	Look Up Table
MARS	Meteorological Archival and Retrieval System
MAX-DOAS	Multi AXis Differential Optical Absorption Spectroscopy
McArtim	Monte Carlo Atmospheric Radiative Transfer Inversion Model
MECCA	Module Efficiently Calculating the Chemistry of the Atmosphere
MESSy	Modular Earth Submodel System
MWBC	MicroWave Backscatter Coefficient
MYI	Multi-Year sea-Ice
NASA	National Aeronautics and Space Administration
ND	Number Density
NIST	National Institute of Standards and Technology
NMHC	Non Methane HydroCarbon
NOAA	National Oceanic and Atmospheric Administration

continued on next page

continued from last page

OASIS	Ocean-Atmosphere-Sea Ice-Snowpack
OD	Optical Density
ODE	Ozone Depletion Event
OMI	Ozone Monitoring Experiment
OOTI	Out On The Ice
PBL	Polar Boundary Layer
PFF	Potential Frost Flower area
PSC	Polar Stratospheric Clouds
PSE	Polar Sunrise Experiment
PV	Potential Vorticity
PVU	Potential Vorticity Unit
QuikSCAT	Quik SCATterometer
RH	Relative Humidity
RHS	Reactive Halogen Species
RT	Radiative Transfer
RV	Research Vessel
SCD	Slant Column Density
SCIAMACHY	SCanning Imaging Absorption spectroMeter for Atmospheric CHartographY
SLIMCAT	Single Layer Isentropic Model of Chemistry And Transport
SLOE	Semi Low Ozone depletion Event
SLP	Sea Level Pressure
SODAR	SOnic Detection And Ranging
SOLAS	Surface Ocean Lower Atmosphere Study
SP-UV	Sun Photometer in UltraViolet
SRAA	Solar Relative Azimuth Angle
SHEBA	Surface Heat Budget of the Arctic Ocean
SSA	Sea Salt Aerosol
SZA	Solar Zenith Angle
T2M	2 m Temperature
TOA	Top Of Atmosphere
TOMCAT	Toulouse Off-line Model of Chemistry And Transport
TOPSE	Tropospheric Ozone Production about the Spring Equinox
TPH	TropoPause Height
UNIS	UNiversity centre In Svalbard
UV	UltraViolet radiation
VCD	Vertical Column Density
VOC	Volatile Organic Compound
VZA	Viewing Zenith Angle
WL	WaveLength
WMO	World Meteorological Organization
WSP	Wind Speed

A.2. Symbols

symbol	name	abbreviation	page
A_{500}	AMF for the lowest 500 m	AMF_{500}	93
A	(total) Air Mass Factor	AMF	45
$V_{j,m,n}$	3D vertical column density		47
$\hat{A}_{j,m,n}$	3D-Box-AMF		47
T	absolute temperature		14
σ	absorption Cross-Section	CS	39
k	asymmetry filter iteration step		86
a_k	asymmetry in step k		86
$\bar{\rho_i}$	averaged number density		43
S_{strat}	background stratospheric SCD		77
T_0	base population of measurements		80
h_{BL}	boundary layer height		16
$\hat{A}_j$	Box-AMF of atmospheric layer j		46
$\sigma_{i,0}$	broad-band cross-section of species i		41
I'_0	broad-band intensity		41
η_c	cloud fraction	CF	99
f	Coriolis parameter		16
$\mathrm{Ri_c}$	critical Richardson Number		16
δz	cropping threshold		86
σ_i	cross-section of species i		40
D	day		80
ρ	density of air		16
τ'	Differential Optical Density	DOD	42
j_z	diffusive flux		15
a_β	distribution asymmetry in partition β		85
Ω	domain for partitioning of T		83
L	Earth radiance, Earthshine radiance		96
z_α	element of T with index α		82
$\bar{z}$	estimator of $\bar{z}_0$		78
ζ_{σ_0}	Gaussian error of z		78
φ	geographical LATitude or parallel [°N]	LAT	56
λ	geographical LONGitude [°E]	LONG	56
A_{g}	geometric AMF		46
h_j	height of layer j		47
R_{high}	high albedo reflectance		99
α	index denoting the measurement		82
β	index denoting the partition		83
I_0	initial intensity		39
I	intensity		39

continued on next page

continued from last page

symbol	name	abbreviation	page
ψ	Line Of Sight angle	LOS	44
ψ_α	LOS of measurement α		82
R_{low}	low albedo reflectance		99
$\bar{z}_0$	mean of z_0		78
$\bar{z}$	mean of z		85
A_{500}^{meas}	measured air-mass factor	$\text{AMF}_{500}^{\text{meas}}$	96
$\tilde{z}$	median of z		85
v, v_y	meridional component of wind velocity		
ϵ_M	Mie scattering coefficient		40
σ_M	Mie scattering cross-section		40
D	molecular diffusion coefficient		15
σ_i'	narrow-band cross-section of species i		41
D'	narrow-band intensity variation		41
ρ_R	ND of Rayleigh scatterer		40
V_{N}	NO_2 VCD		79
$V_{\text{N}\alpha}$	NO_2 VCD of measurement α		82
ρ	number density	ND	39
ρ_M	number density of Mie scatterer		40
ρ_i	number density of species i		40
N_α	number of measurements in T		83
N_β	number of measurements in partition β		83
N_ψ	number of partitions in ψ-direction		83
N_ϑ	number of partitions in ϑ-direction		83
N_V	number of partitions in V_{N}-direction		83
τ	Optical Density	OD	40
S_j	partial SCD within atmospheric layer j		46
V_j	partial VCD within atmospheric layer j		46
i	partition index in ϑ-direction		83
j	partition index in V_{N}-direction		83
ψ_k	partition limit k in ψ-direction		83
Ω_β	partition of T		83
$\Delta\vartheta$	partitioning node displacement in ϑ-direction		84
ΔV_{N}	partitioning node displacement in V_{N}-direction		84
$\text{d}s$	path element		39
L	path length		39
P	period of days		80
$\mathcal{P}_r$	polynomial of order r		42
θ	potential temperature		14
PV	potential vorticity	PV	16
p	pressure		14
z'	ratio between S_{trop} and $S_{\text{strat},\text{O}_3}$		78

continued on next page

continued from last page

symbol	name	abbreviation	page
z	ratio of total BrO/O_3 SCD		78
ϵ_R	Rayleigh scattering coefficient		40
σ_R	Rayleight scattering cross-section		40
R	reflectance		96
R_{cc}	reflectance in the presence of clouds		99
R_{cf}	reflectance when cloud-free		99
S_{trop}	residual tropospheric SCD		77
Ri	Richardson Number		16
p_0	sea level pressure		14
$\mathrm{AMF}_{500}^{\mathrm{min}}$	sensitivity threshold		96
S	Slant Column Density	SCD	44
S_i	slant column density of species i		44
E	solar irradiance		96
β	Solar Relative Azimuth Angle	SRAA	44
θ, ϑ	Solar Zenith Angle	SZA	44
R	specific gas constant		14
c_p	specific heat at constant pressure		14
σ_β	standard deviation in partition β		87
σ_{strat}	standard deviation of S_{strat}		87
σ	standard deviation of z, estimator of σ_0		85
$S_{\mathrm{strat},\mathrm{O}_3}$	stratospheric O_3 SCD		78
z_0	stratospheric BrO/O_3 SCD ratio		78
T	subset of T used for stratospheric correction		82
$T_{i,j}$	subset of T, measurements in $\Omega_{i,j}$		84
B	substituting sum of broad-band absorber terms		41
η_s	surface High Albedo Fraction	HAF	99
ϑ_α	SZA of measurement α		82
t	time		
Θ	Top Of Atmosphere	TOA	45
S_{O_3}	total O_3 SCD		78
A_{trop}	tropospheric air-mass factor		93
S_{trop}	tropospheric BrO slant column density		93
V_{trop}	tropospheric BrO vertical column density		93
V	Vertical Column Density	VCD	45
V_i	vertical column density of species i		45
w, v_z	vertical component of wind velocity		
K_z	vertical turbulent diffusion coefficient		15
λ	WaveLength	WL	39
$\vec{v}$	wind velocity		16
u, v_x	zonal component of wind velocity		

B. Distribution of significantly elevated columns depending on threshold

The distribution of the probability to observe a significantly elevated BrO column density is plotted assuming different significance thresholds: 2σ, 3σ, and 4σ where σ is the standard deviation of the stratospheric mode as described in Section 6.4. The displayed data is calculated from GOME-2 measurements between February 2007 and June 2010 and divided into two periods a month (cf. Section 10.3). In conclusion and despite the amplitude, the qualitative probability distribution of significantly elevated BrO SCDs measurements is almost independent from the significance threshold for all eight investigated periods.

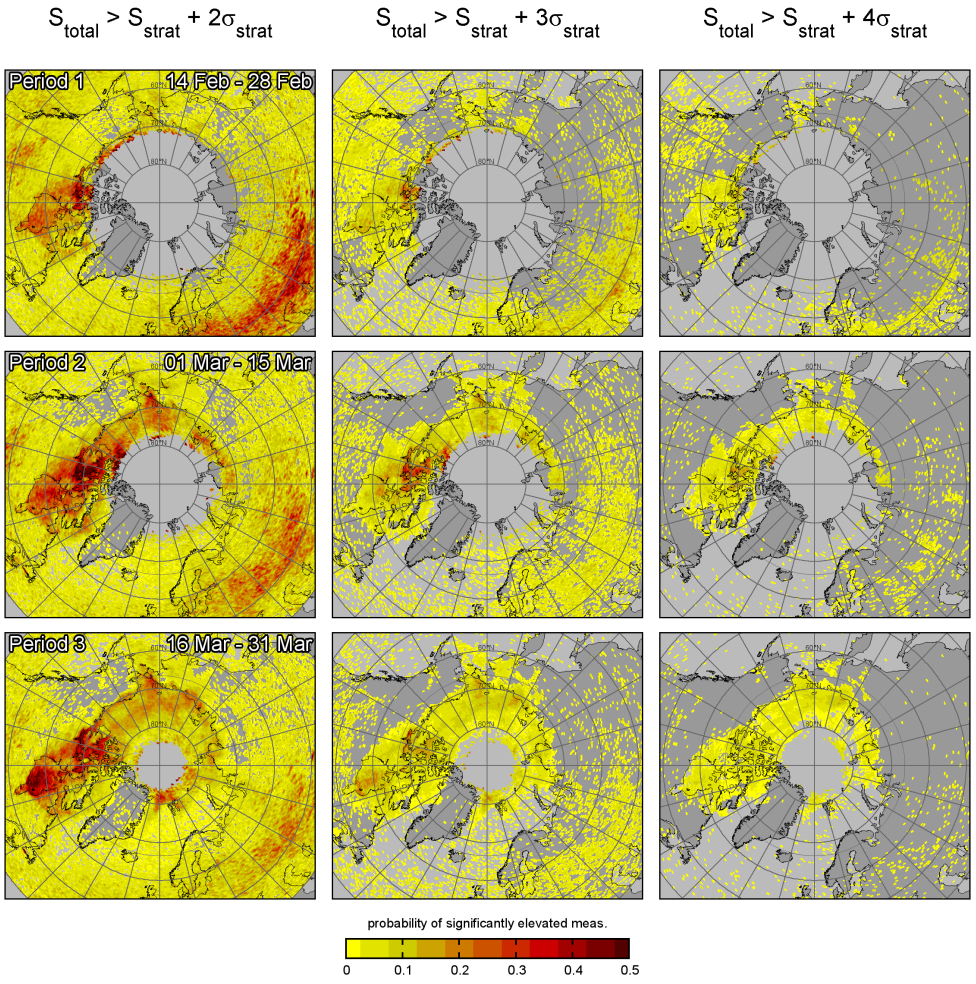

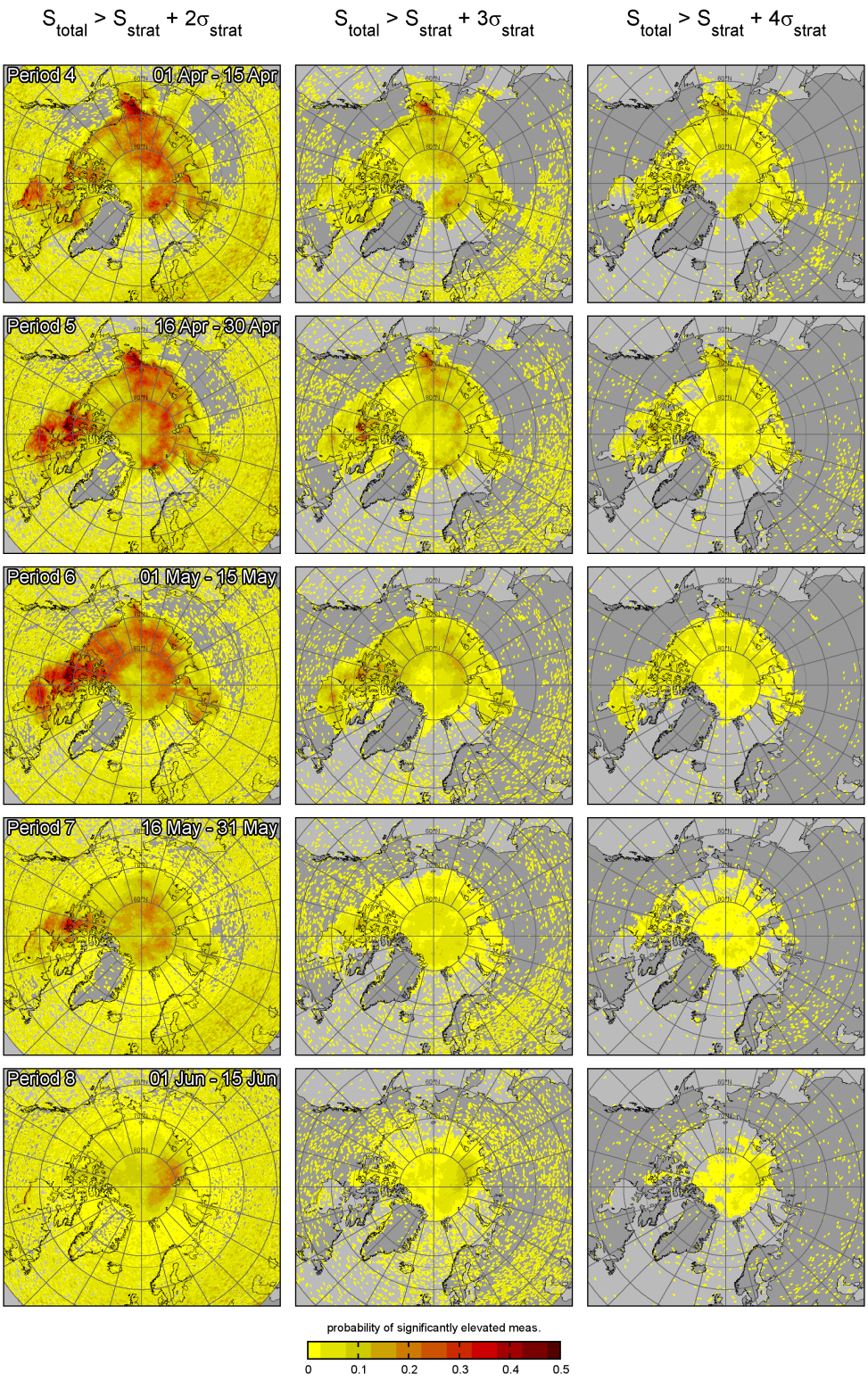
$S_{total} > S_{strat} + 2\sigma_{strat}$
$S_{total} > S_{strat} + 3\sigma_{strat}$
$S_{total} > S_{strat} + 4\sigma_{strat}$
Period 4
01 Apr - 15 Apr
Period 5
16 Apr - 30 Apr
Period 6
01 May - 15 May
Period 7
16 May - 31 May
Period 8
01 Jun - 15 Jun
probability of significantly elevated meas.
0
0.1
0.2
0.3
0.4
0.5

C. Daily maps of tropospheric BrO

This appendix contains two sets of maps corresponding to two field campaigns conducted in the course of the International Polar Year 2007–2008. The maps show gridded tropospheric column densities of bromine monoxide (BrO) measured by the GOME-2 instrument in the vicinity of two different locations where ground-based measurements of BrO and many other trace-gas species were performed. In spring 2008, ship-based measurements were performed aboard the Amundsen research icebreaker south of Banks Island in the Amundsen Gulf (Section C.1). In spring 2009, ground-based measurements were performed at Barrow, Alaska (Section C.2). Both field initiatives were conducted in the scope of the Ocean – Atmosphere – Sea Ice – Snowpack (OASIS) project.[1]

The BrO maps are averaged tropospheric column densities retrieved from measurements within the denoted day. On some days, however, there is no valid data present. Furthermore, only those measurements are averaged, which feature a solar zenith angle (SZA) smaller than 80°, and a tropospheric air-mass factor (AMF) larger than 1. The location of the ground-based measurements – the Amundsen research vessel, or Barrow, respectively – are marked with a white circle in the center of the map.

[1]This appendix has been accepted for publication as a supplementary part of Sihler *et al.* (2012).

C.1. Tropospheric BrO during Amundsen 2008 campaign

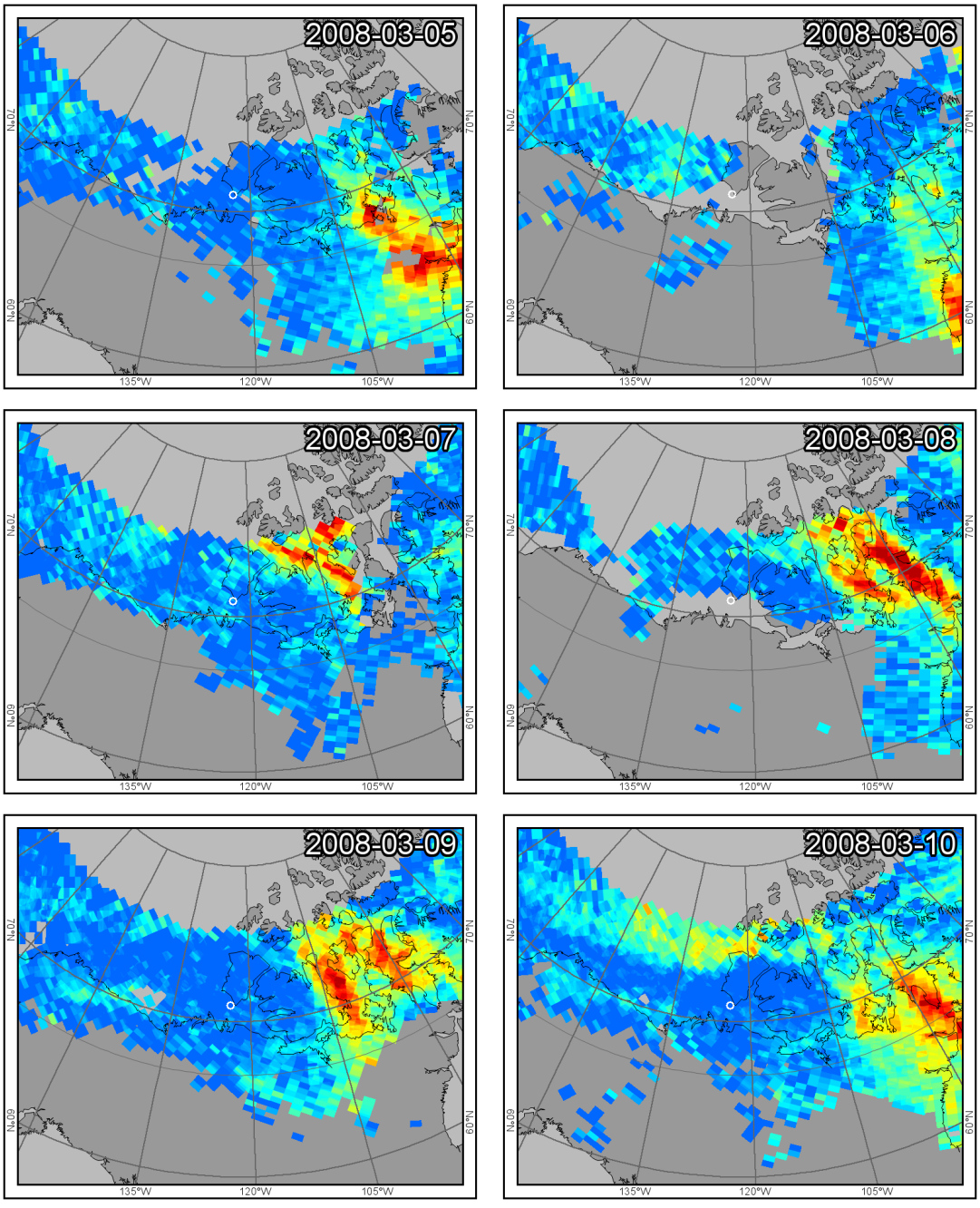

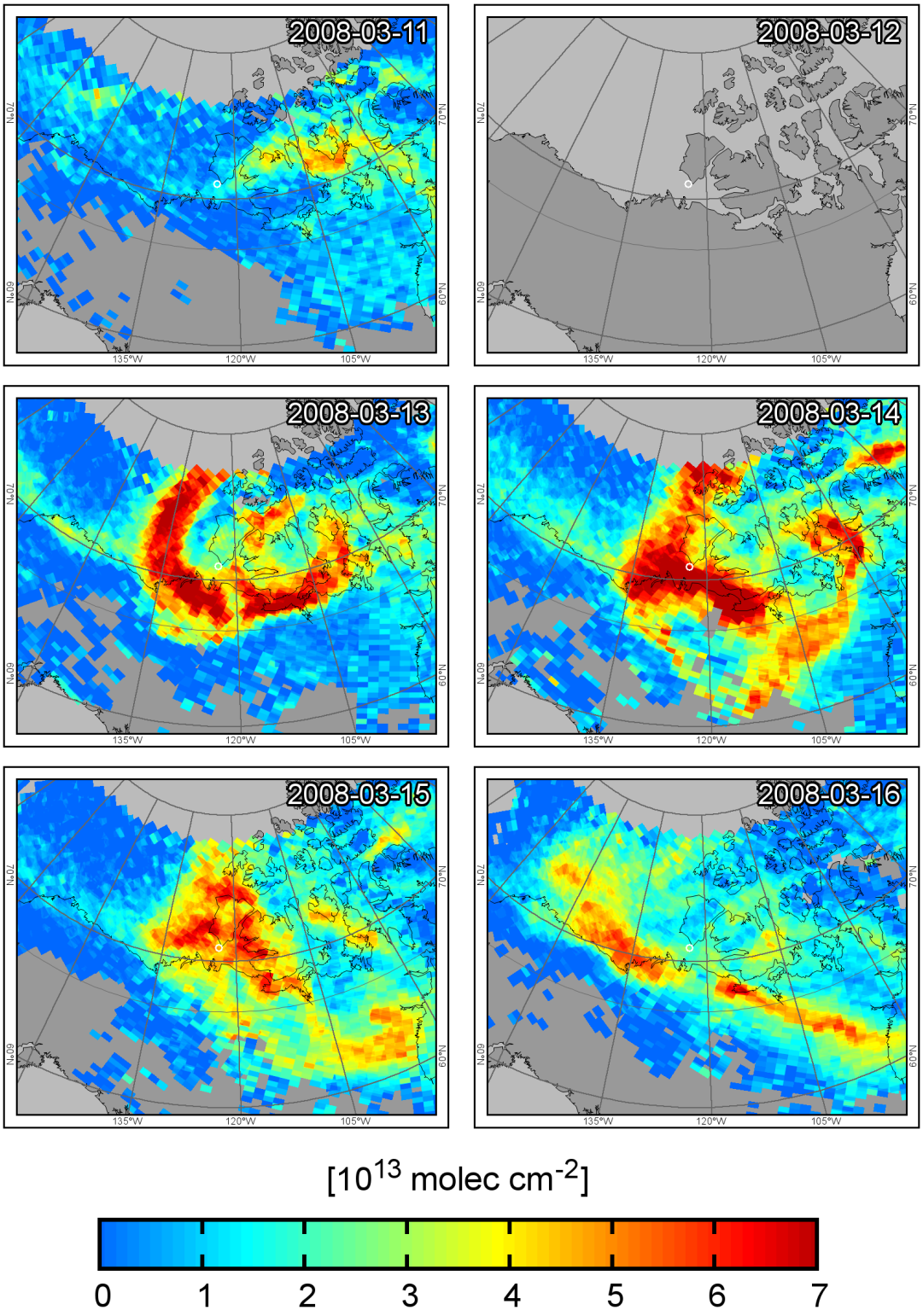
2008-03-11
2008-03-12
2008-03-13
2008-03-14
2008-03-15
2008-03-16
70°N
60°N
135°W
120°W
105°W
[10^13 molec cm^-2]
0
1
2
3
4
5
6
7

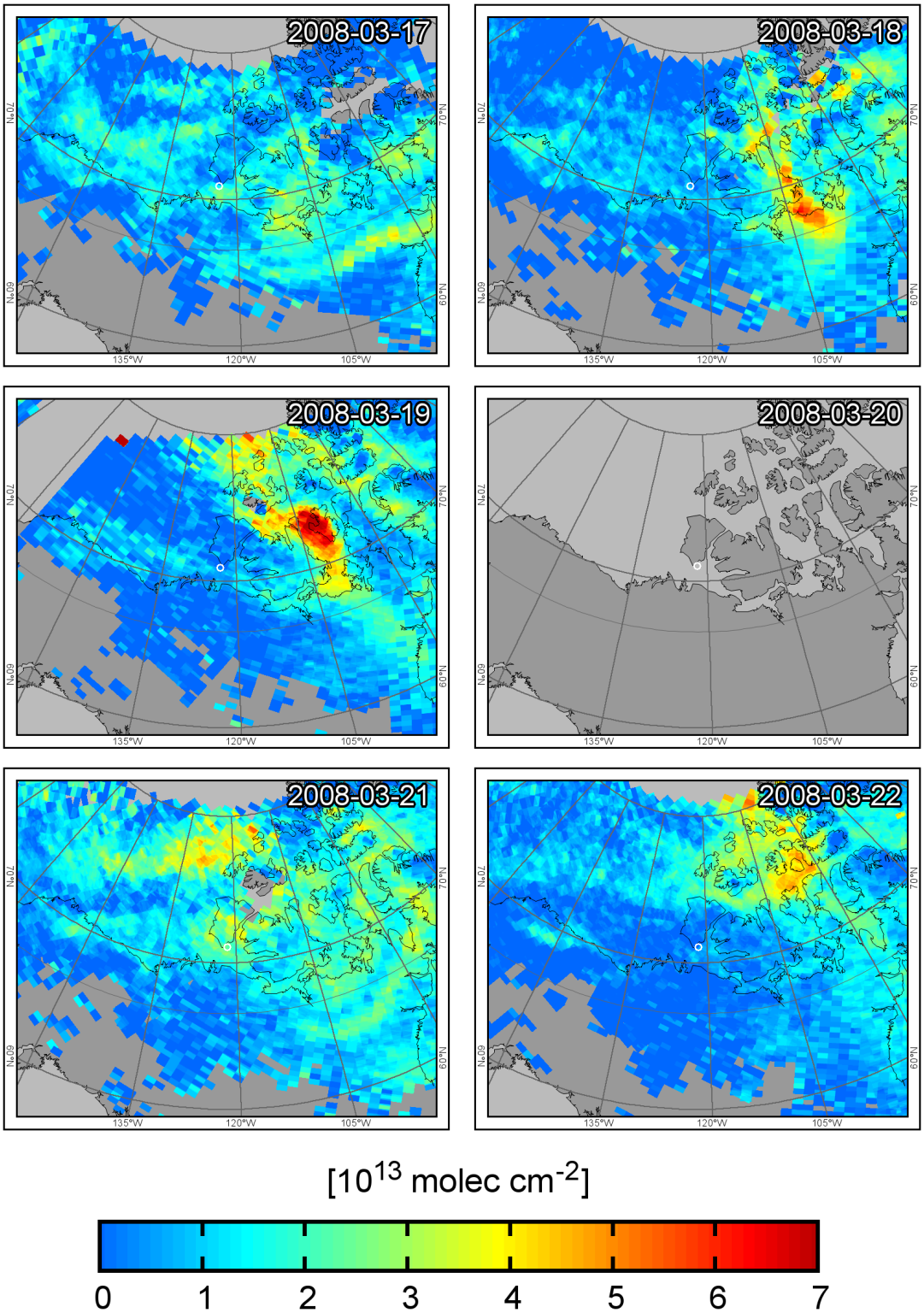
2008-03-17
2008-03-18
2008-03-19
2008-03-20
2008-03-21
2008-03-22
135°W
120°W
105°W
70°N
60°N
[10^13 molec cm^-2]
0
1
2
3
4
5
6
7

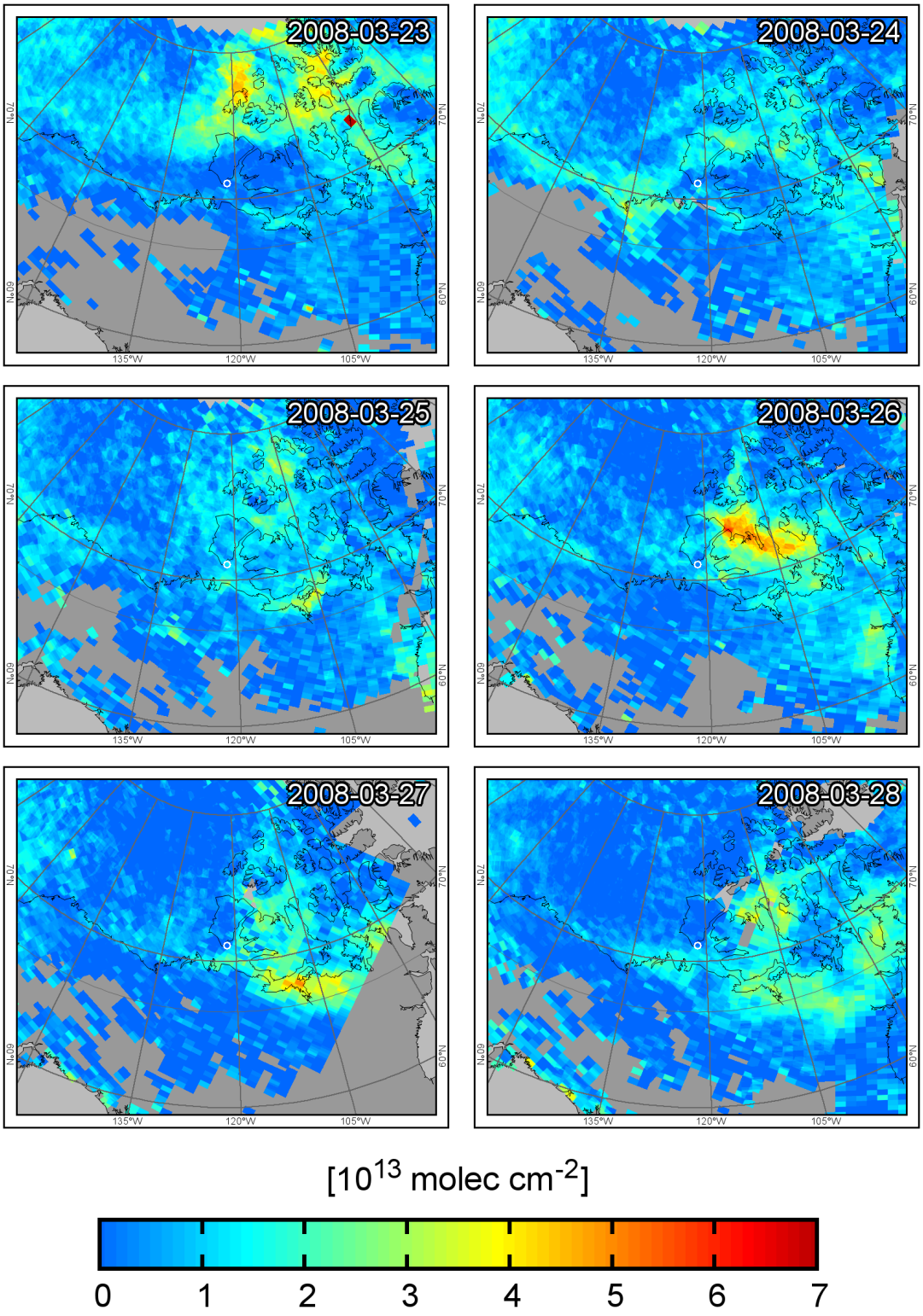
2008-03-23
2008-03-24
2008-03-25
2008-03-26
2008-03-27
2008-03-28
70°N
60°N
135°W
120°W
105°W
[10^13 molec cm^-2]
0
1
2
3
4
5
6
7

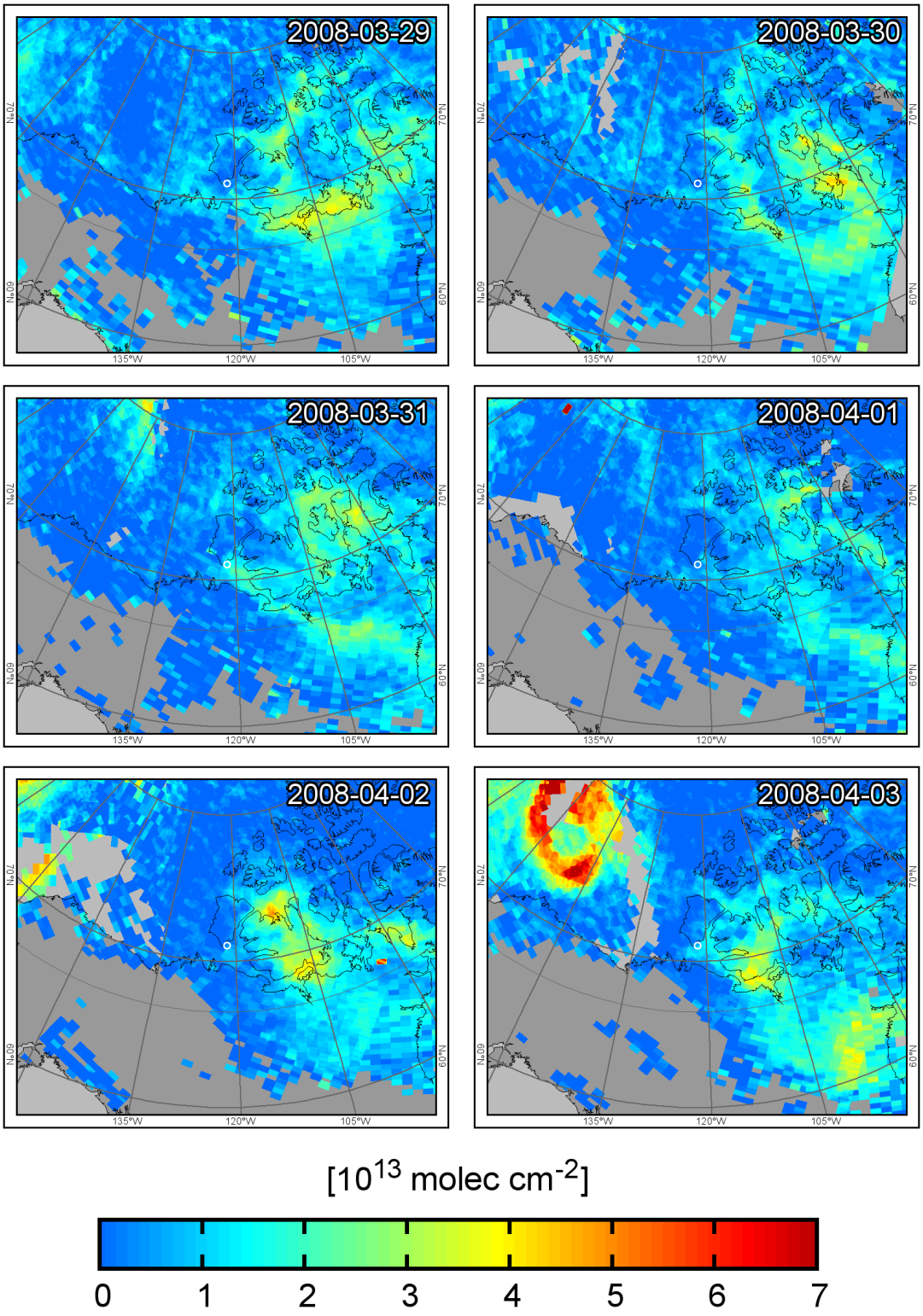
2008-03-29
2008-03-30
2008-03-31
2008-04-01
2008-04-02
2008-04-03
70°N
60°N
135°W
120°W
105°W
[10^13 molec cm^-2]
0
1
2
3
4
5
6
7

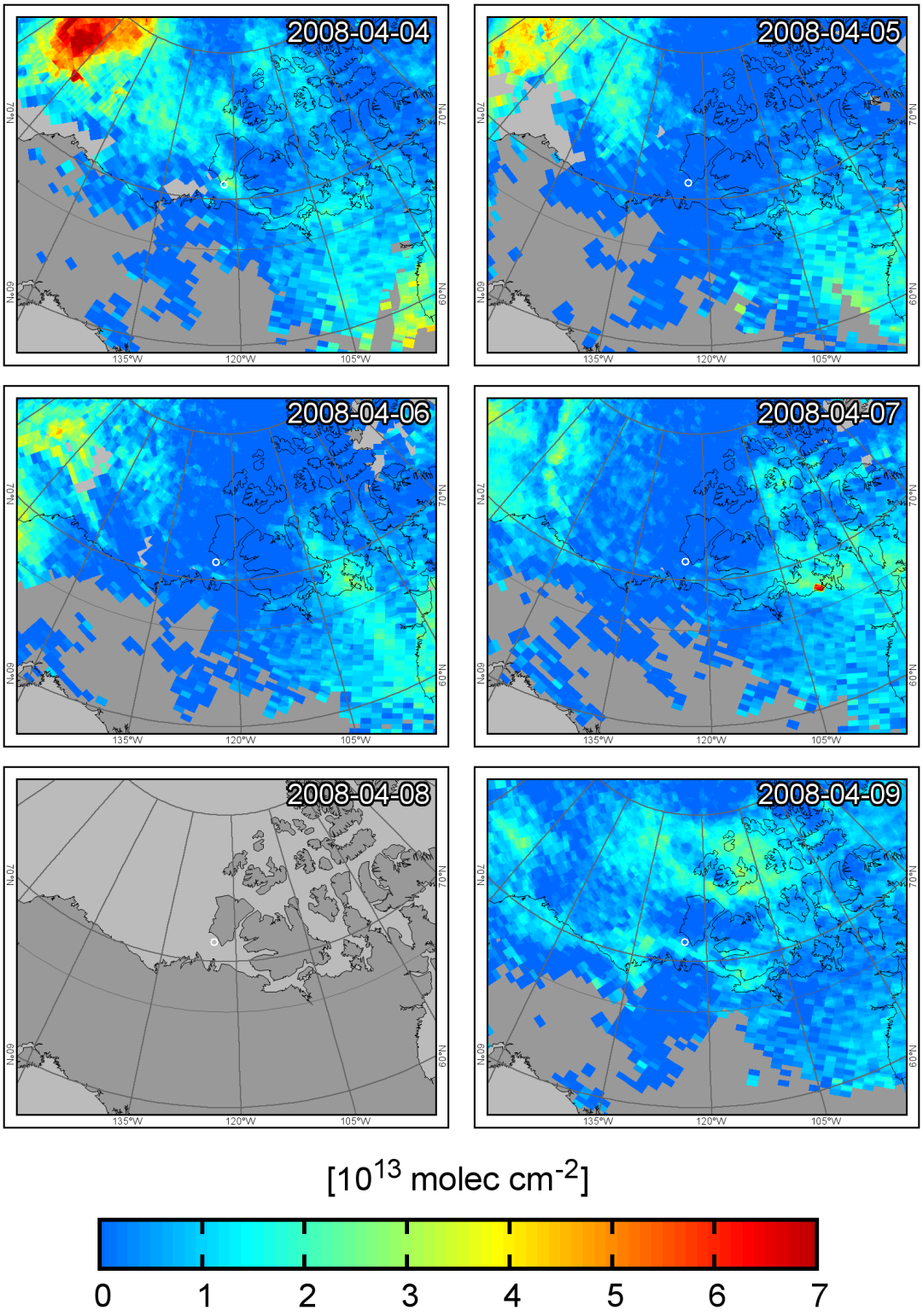
2008-04-04
2008-04-05
2008-04-06
2008-04-07
2008-04-08
2008-04-09
70°N
60°N
135°W
120°W
105°W
[10^13 molec cm^-2]
0
1
2
3
4
5
6
7

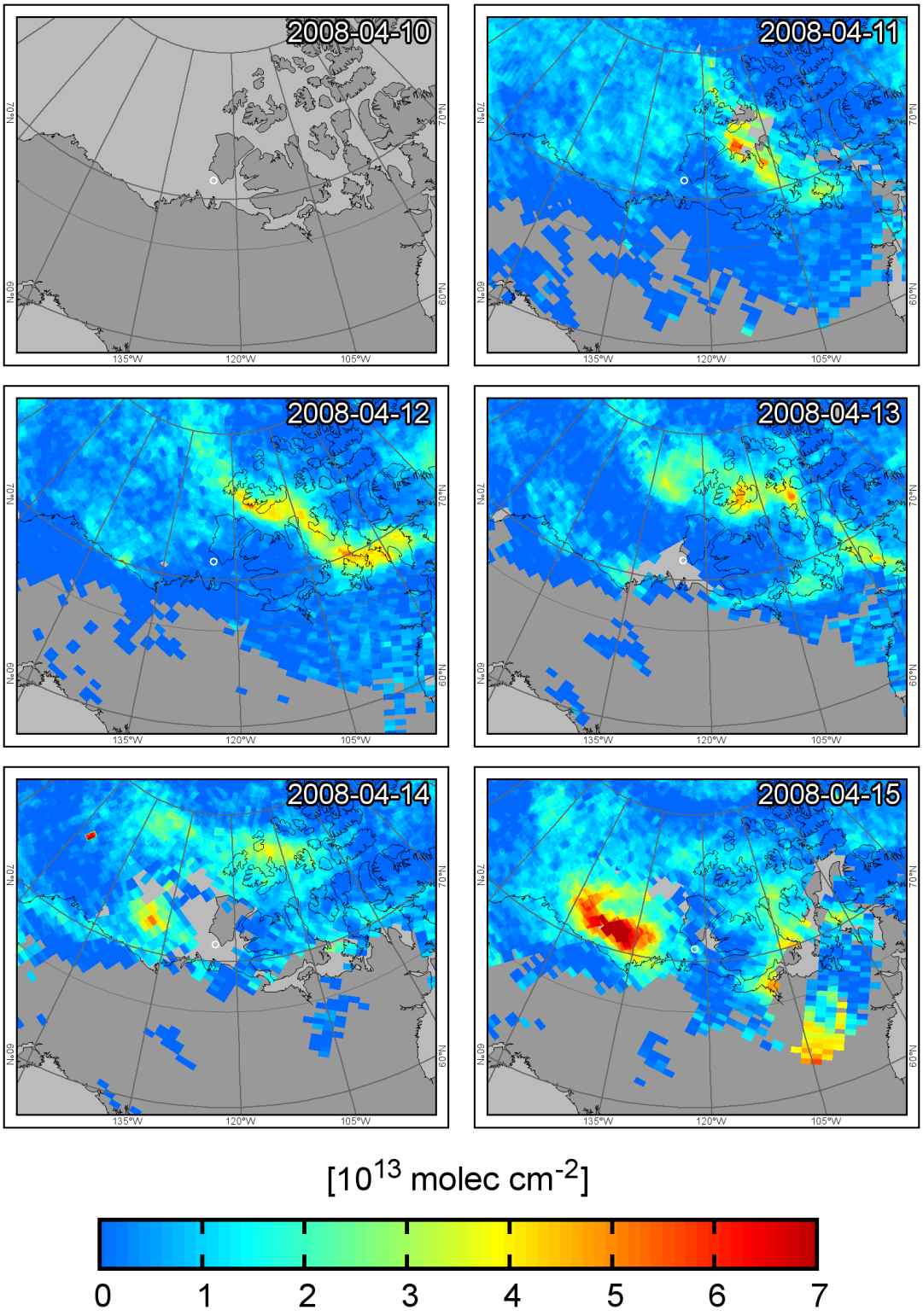
2008-04-10
2008-04-11
2008-04-12
2008-04-13
2008-04-14
2008-04-15
135°W
120°W
105°W
70°N
60°N
[10^13 molec cm^-2]
0
1
2
3
4
5
6
7

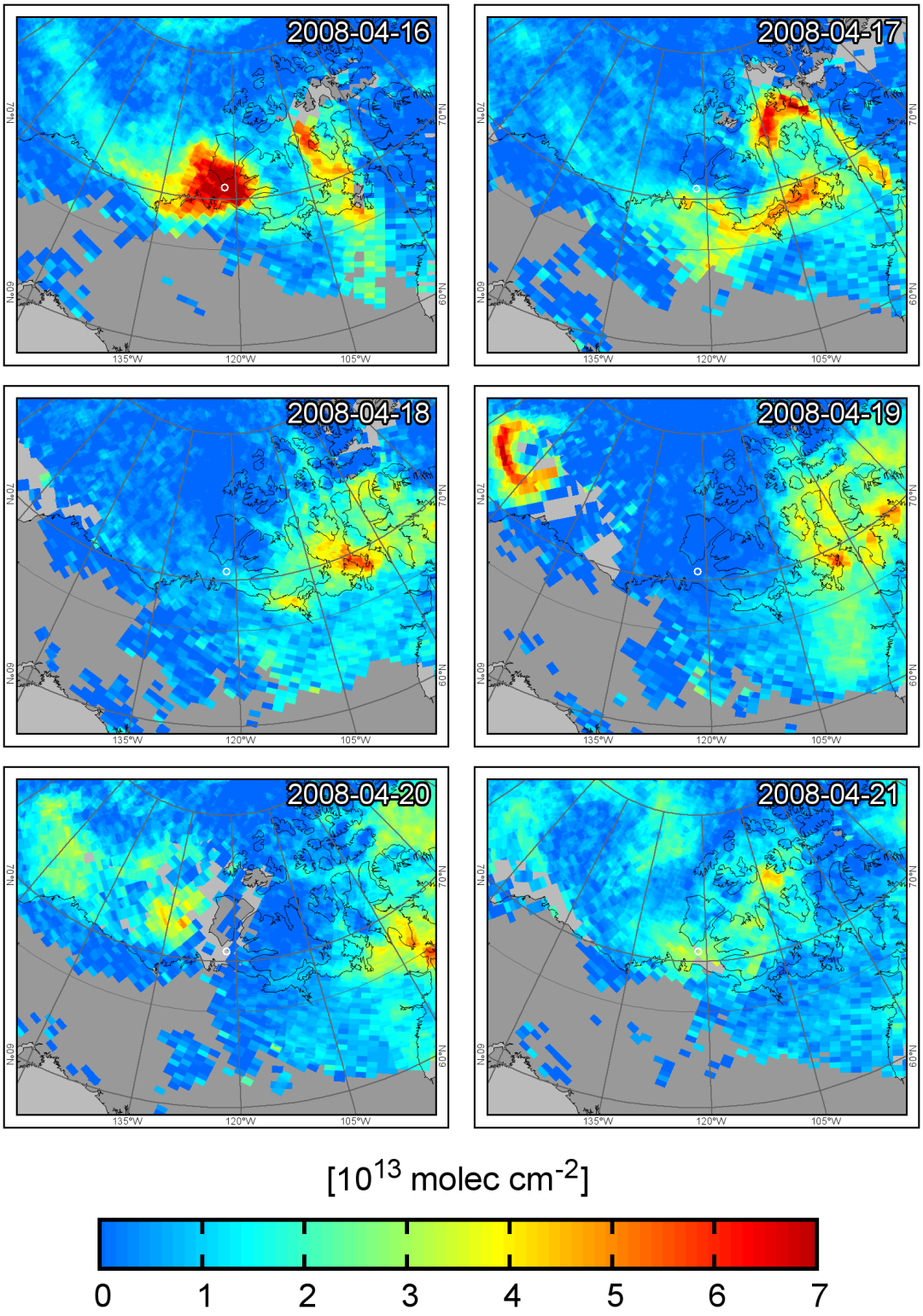
2008-04-16
2008-04-17
2008-04-18
2008-04-19
2008-04-20
2008-04-21
135°W
120°W
105°W
70°N
60°N
[10^13 molec cm^-2]
0
1
2
3
4
5
6
7

C.2. Tropospheric BrO during Barrow 2009 campaign

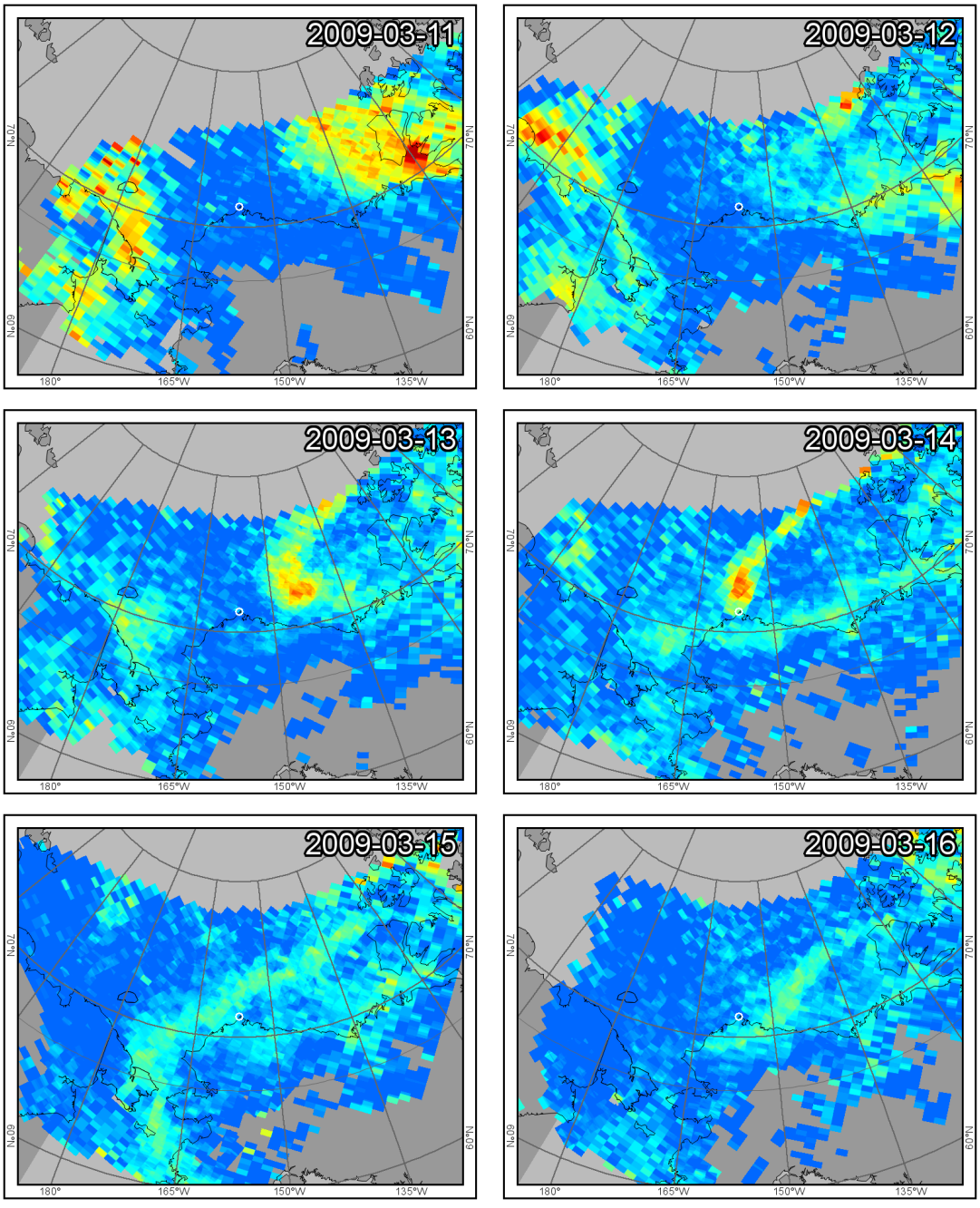

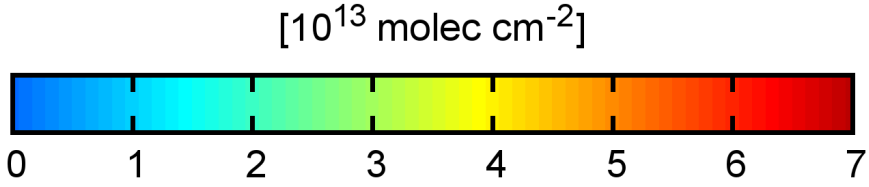

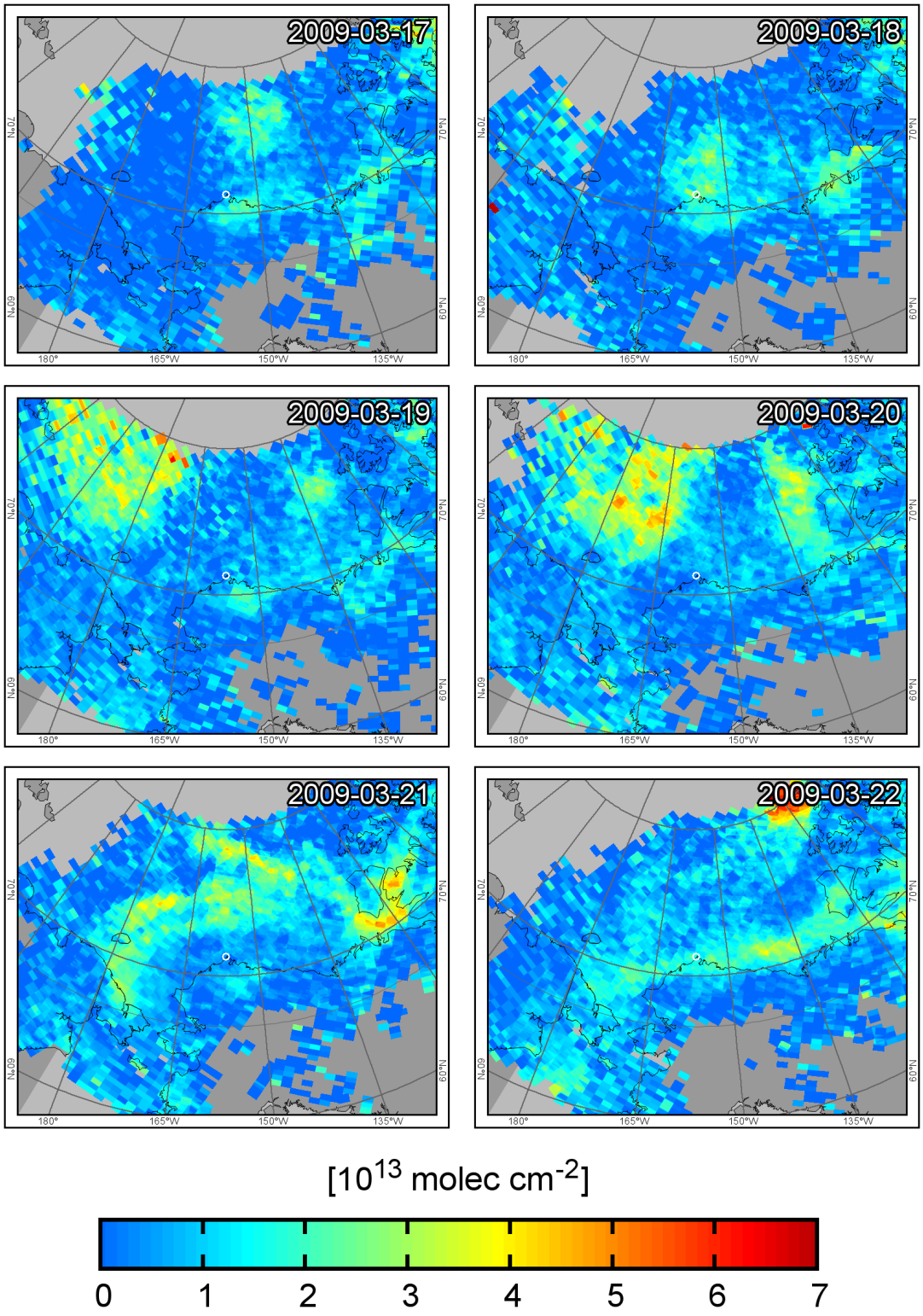
2009-03-17
2009-03-18
2009-03-19
2009-03-20
2009-03-21
2009-03-22
70°N
60°N
180°
165°W
150°W
135°W
[10^13 molec cm^-2]
0
1
2
3
4
5
6
7

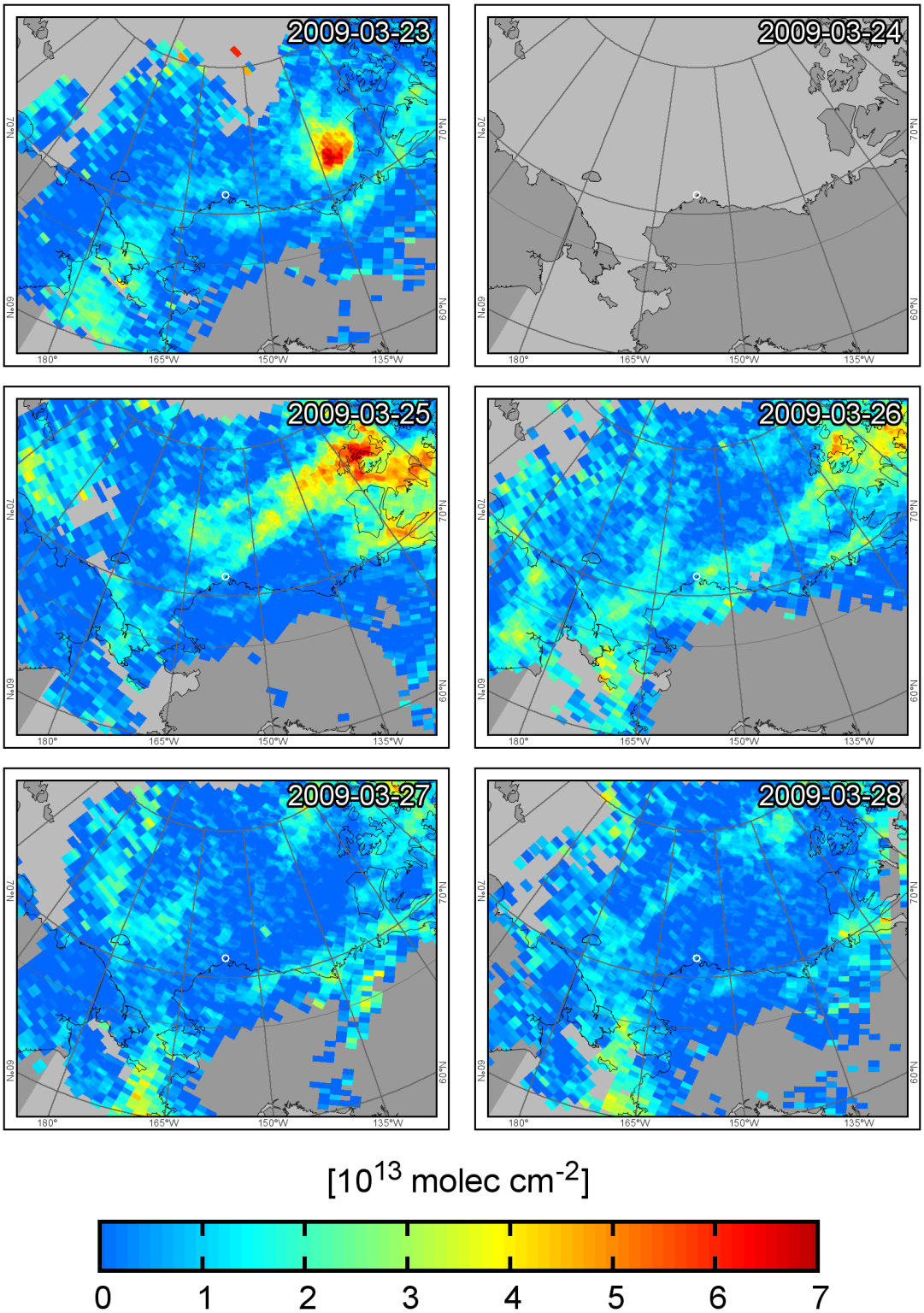
2009-03-23
2009-03-24
2009-03-25
2009-03-26
2009-03-27
2009-03-28
70°N
60°N
180°
165°W
150°W
135°W
[10^13 molec cm^-2]
0
1
2
3
4
5
6
7

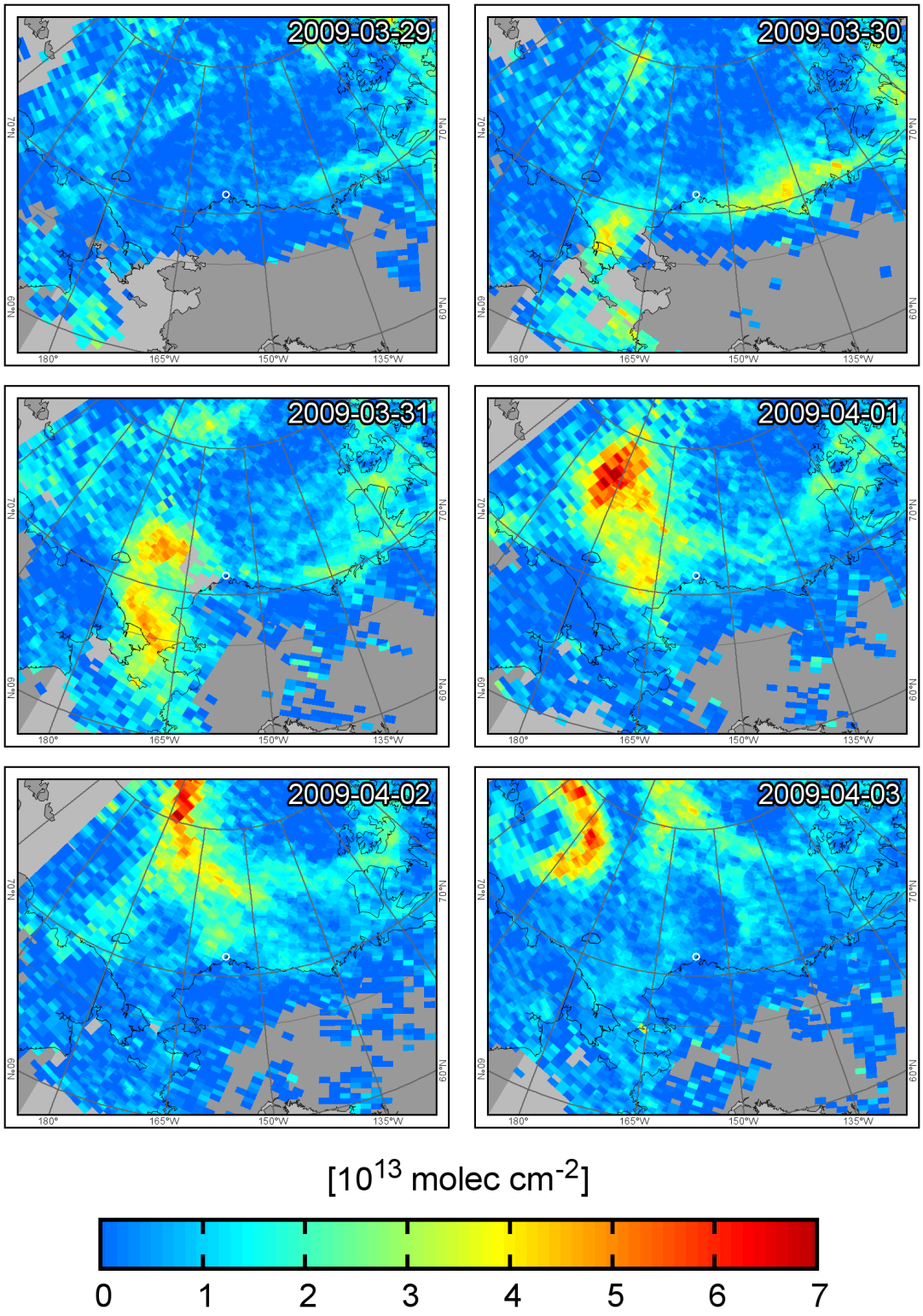
2009-03-29
2009-03-30
2009-03-31
2009-04-01
2009-04-02
2009-04-03
[10^13 molec cm^-2]
0
1
2
3
4
5
6
7

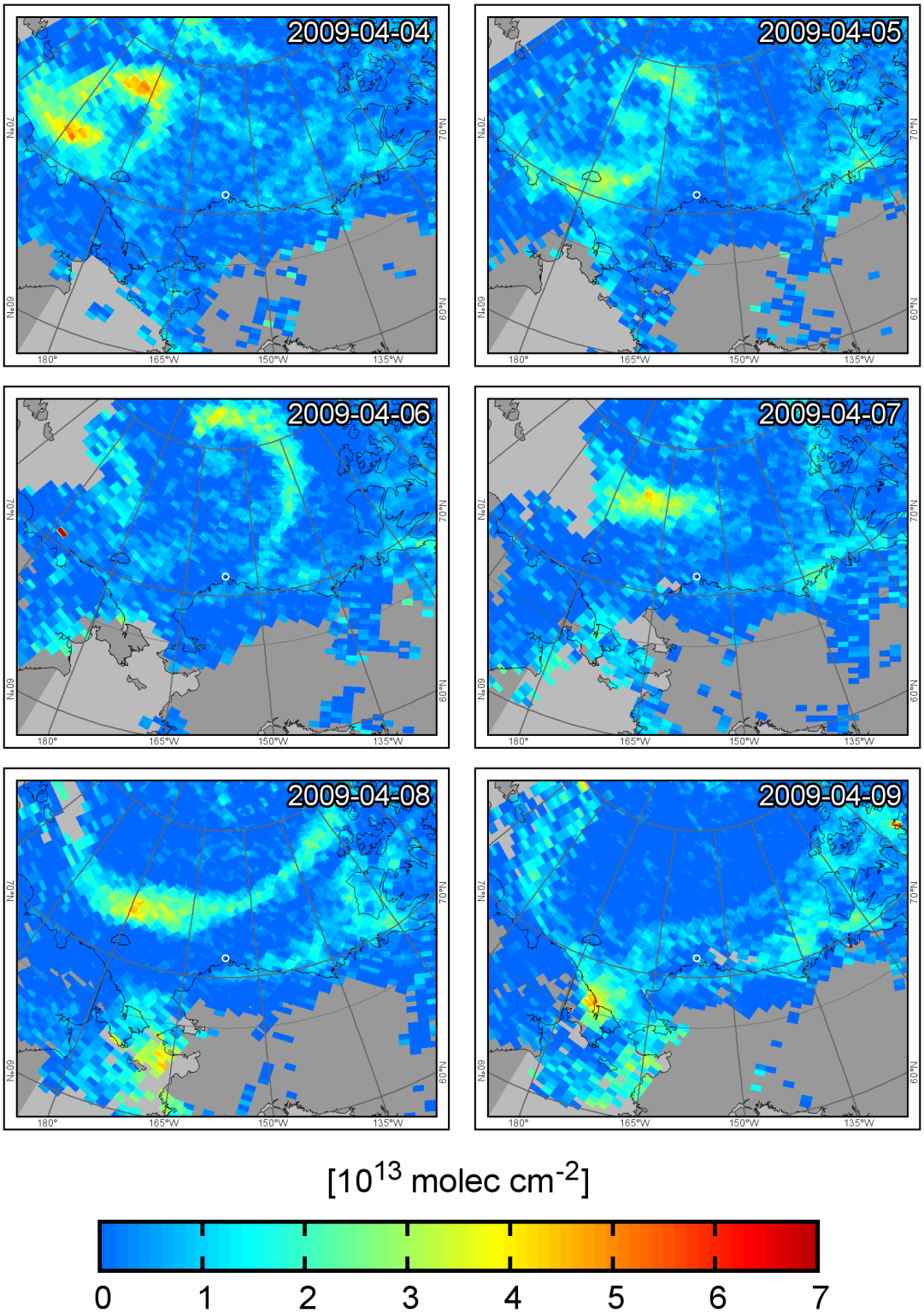
2009-04-04
2009-04-05
2009-04-06
2009-04-07
2009-04-08
2009-04-09
70°N
60°N
180°
165°W
150°W
135°W
[10^13 molec cm^-2]
0
1
2
3
4
5
6
7

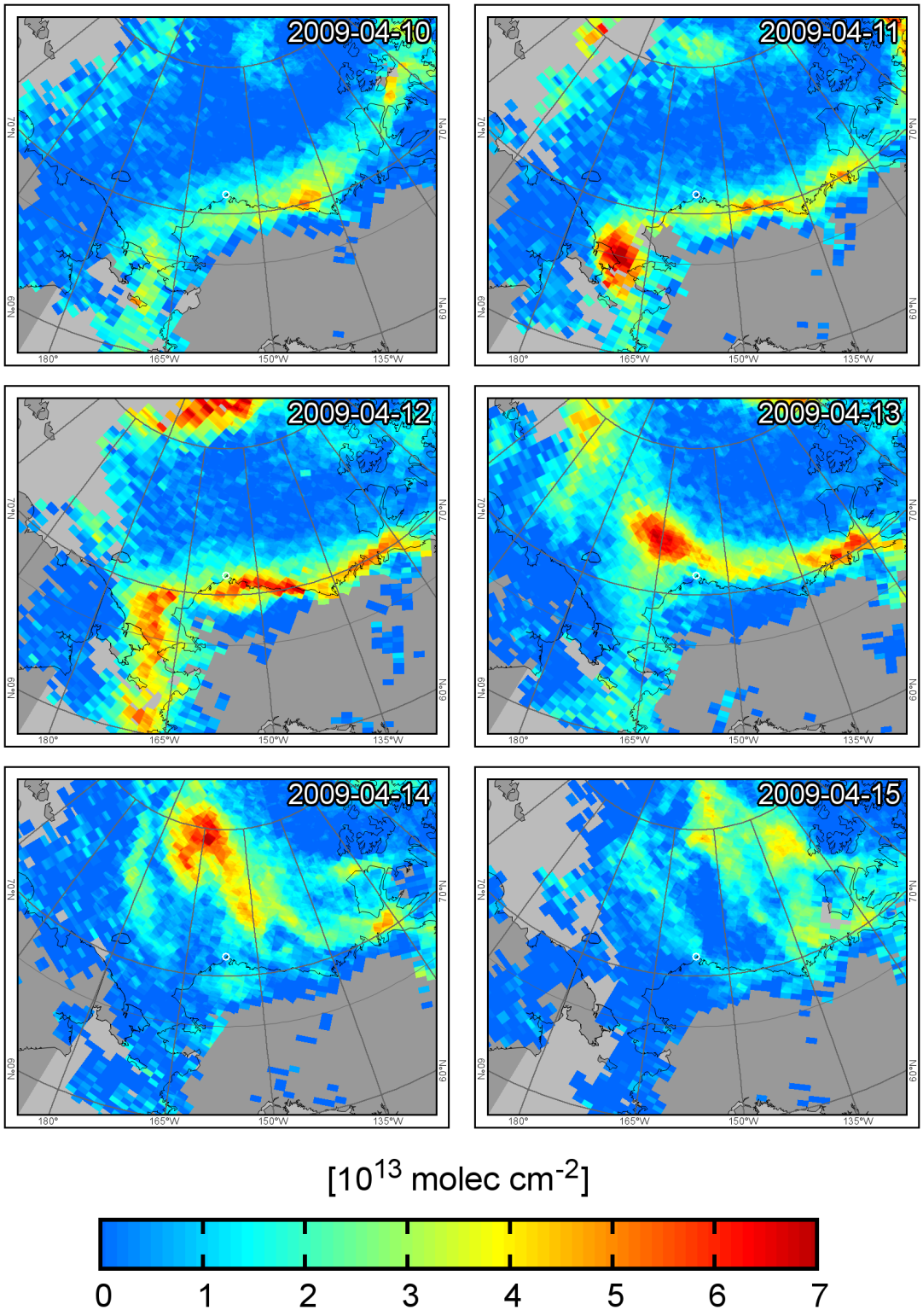
2009-04-10
2009-04-11
2009-04-12
2009-04-13
2009-04-14
2009-04-15
70°N
60°N
180°
165°W
150°W
135°W
[10^13 molec cm^-2]
0
1
2
3
4
5
6
7

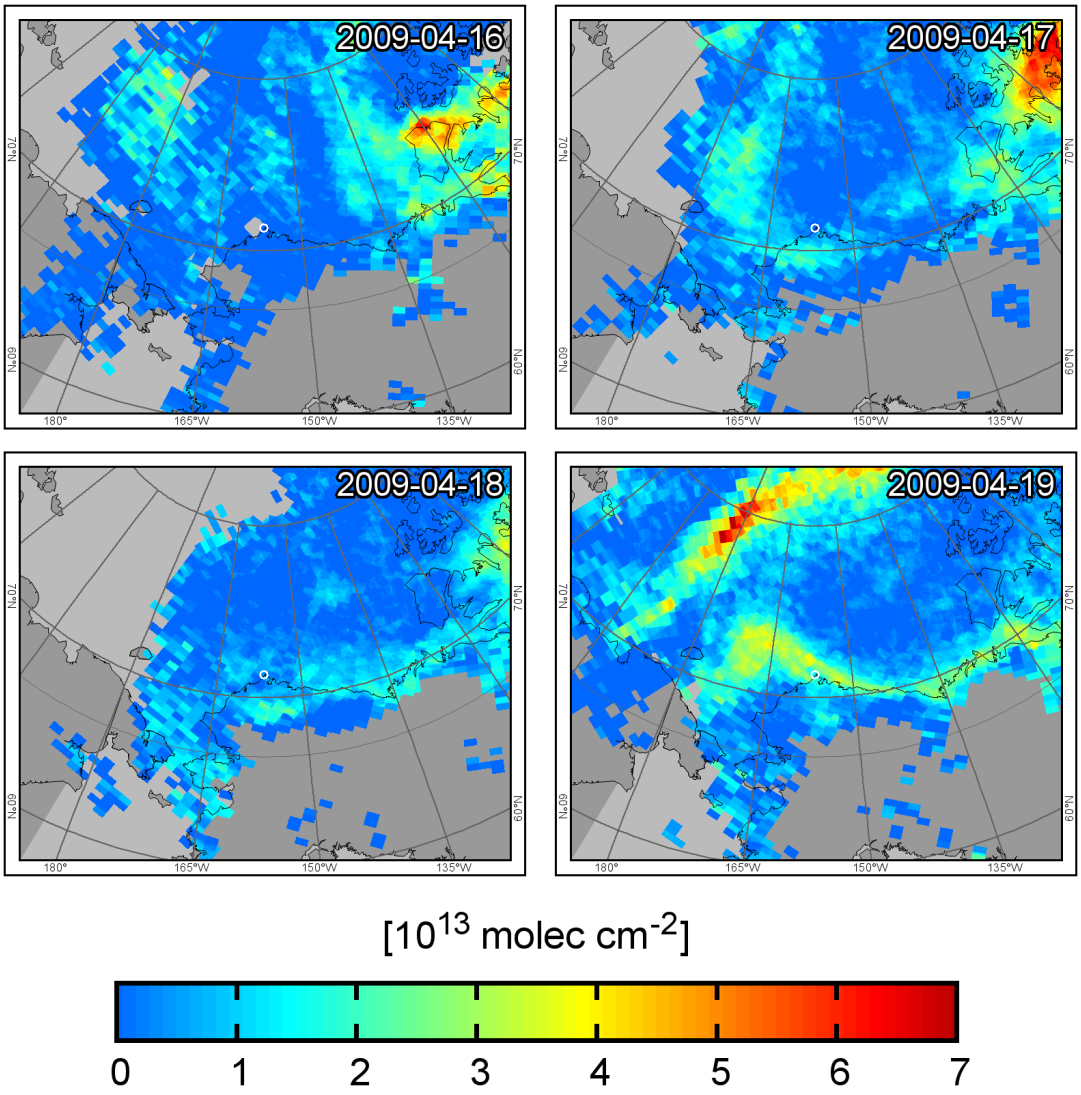
2009-04-16
2009-04-17
2009-04-18
2009-04-19
70°N
69°N
180°
165°W
150°W
135°W
[10^13 molec cm^-2]
0
1
2
3
4
5
6
7

D. Colocated measurements of GOME-2 and CALIPSO

This appendix compiles the illustrations comparing the occurrence of elevated BrO SCDs (Section 6.4) and CALIPSO aerosol and cloud column measurements (Section 5.3.2 which correspond to the results presented in Section 11.6. The number of collocated measurements depending on the column optical density measured by CALIPSO are separately evaluated over sea-ice (left columns) and land (middle columns), respectively. The maps (right columns) summarize the location of all collocated measurements taken into account where green and red dots denote measurements over sea-ice and land, respectively.

D.1. CALIPSO column aerosol optical density

Aerosols: Periods 1 to 3

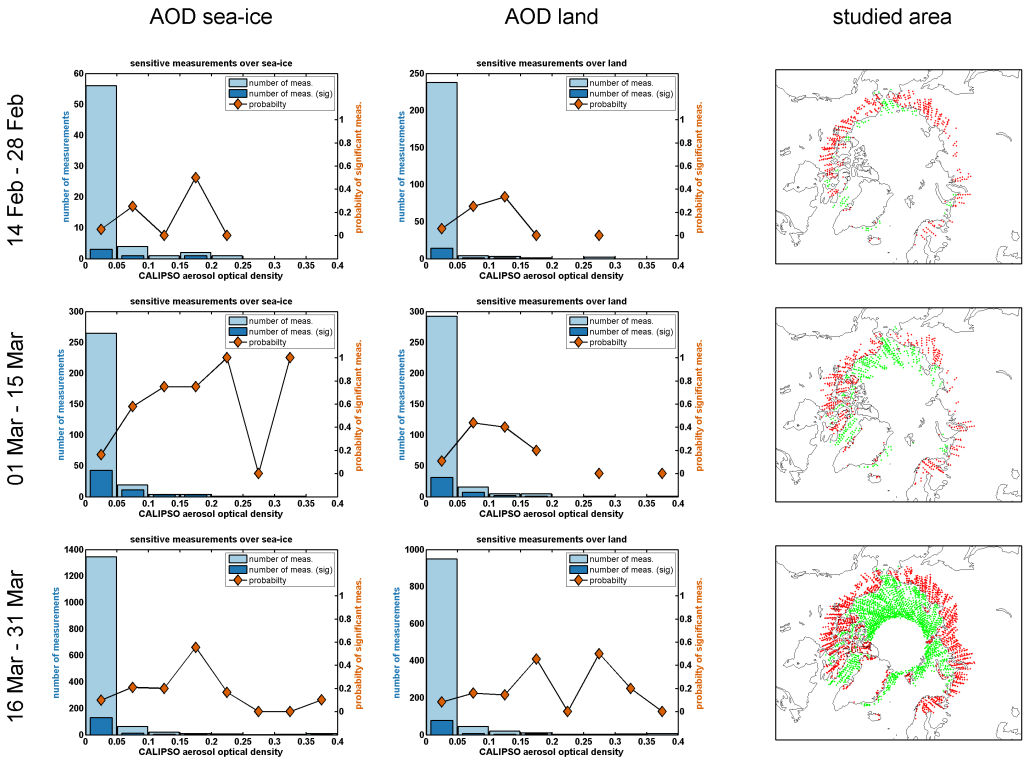

Aerosols: Periods 4 to 8

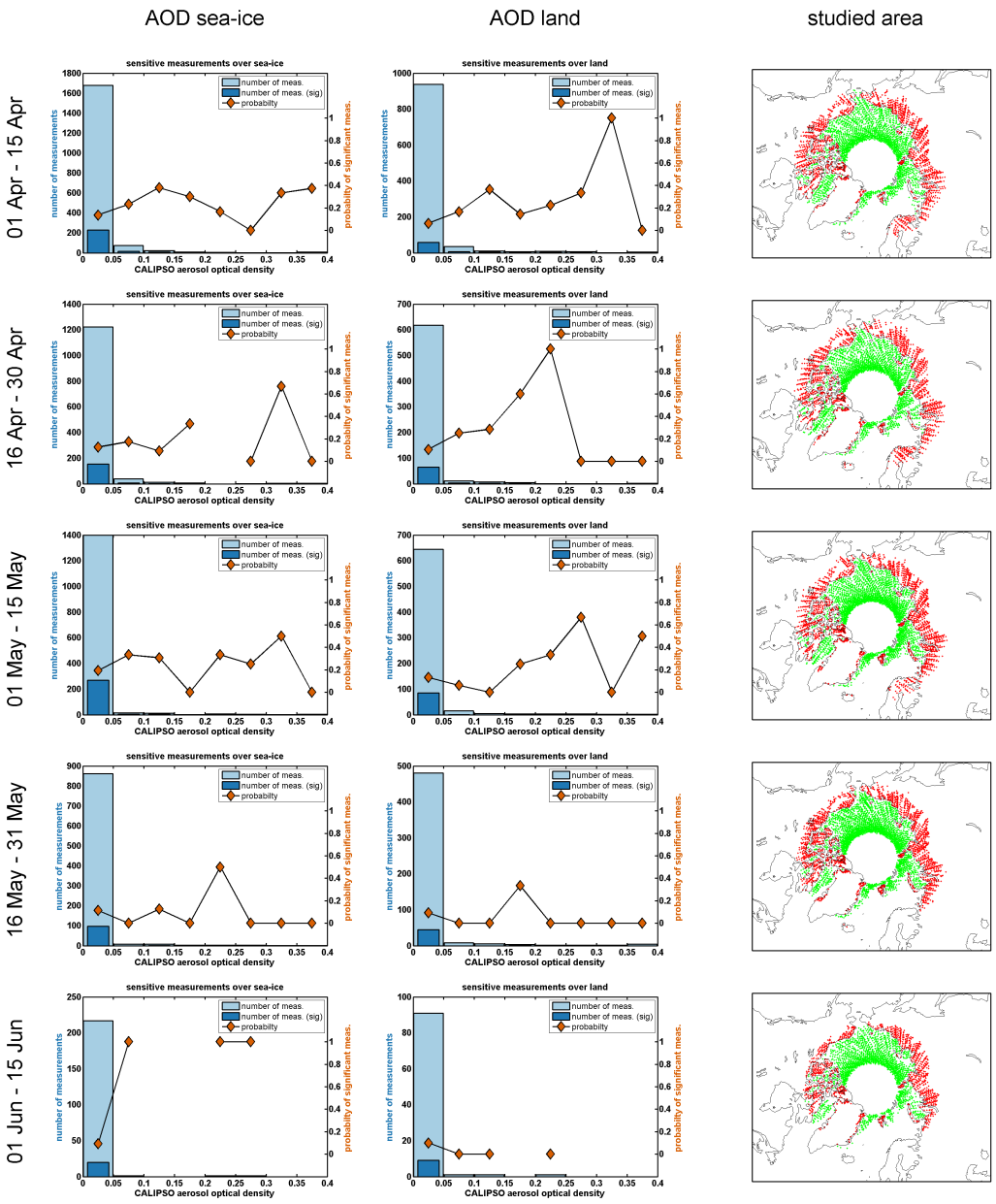

D.2. CALIPSO column cloud optical density

Clouds: Periods 1 to 4

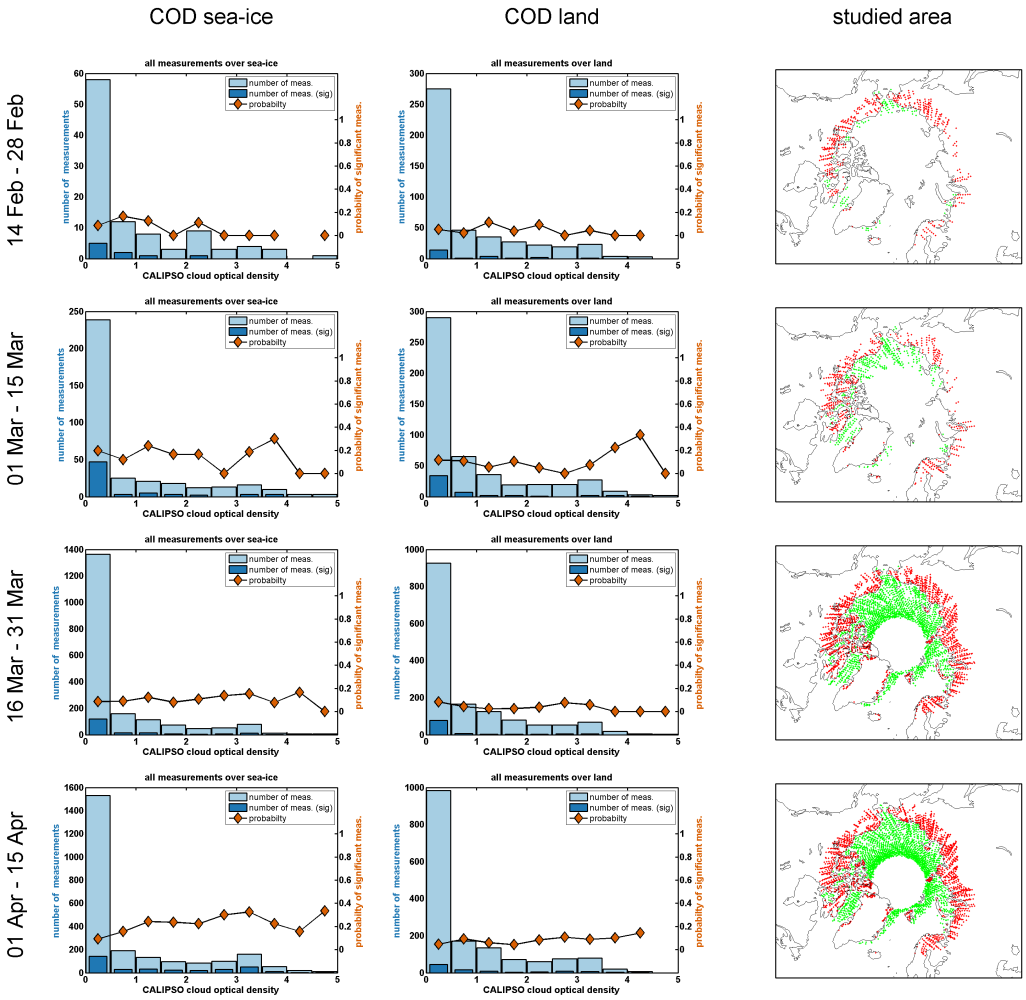

Clouds: Periods 5 to 8

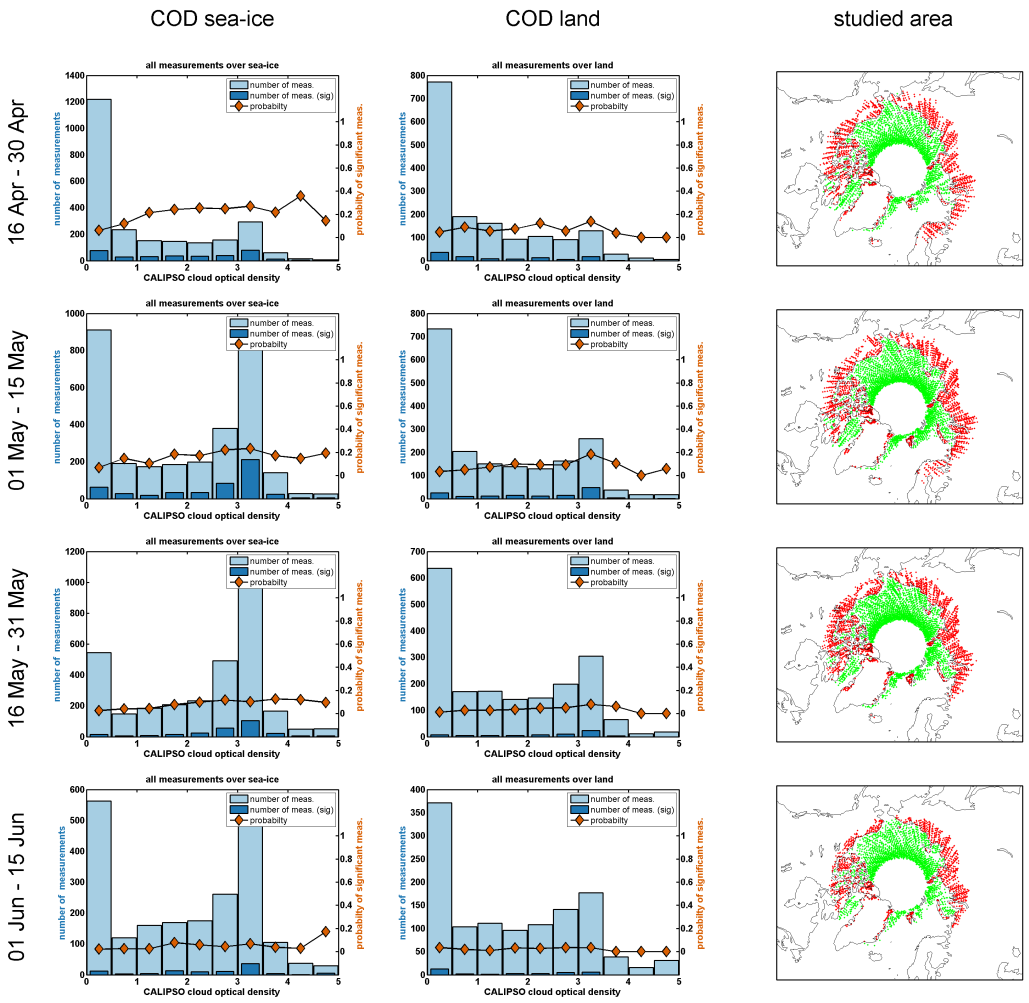

E. Results from Lagrangian source analysis

This appendix compiles the correlation plots between tropospheric BrO VCDs measured by GOME-2 and the residence times of backward trajectories in the boundary layer over different surface types (sea-ice, land, ocean). The GOME-2 measurements are distinguished into measurements over the sea-ice and land, respectively. The trajectories are calculated using LAGRANTO (Section 7.4) and end at 100, 200, and 400 m at the center of each GOME-2 pixel. The residence times are calculated for the 24 hours prior to the GOME-2 overpass.

The plots showing the residence time in the boundary layer over sea-ice for the observations over sea-ice are part of the main body (Section 11.5.4). The respective plots are shown in Figure 11.19 on page 188 and Figure 11.20 on page 189.

E.1. Observations over sea-ice

E.1.1. Residence time in boundary layer over land

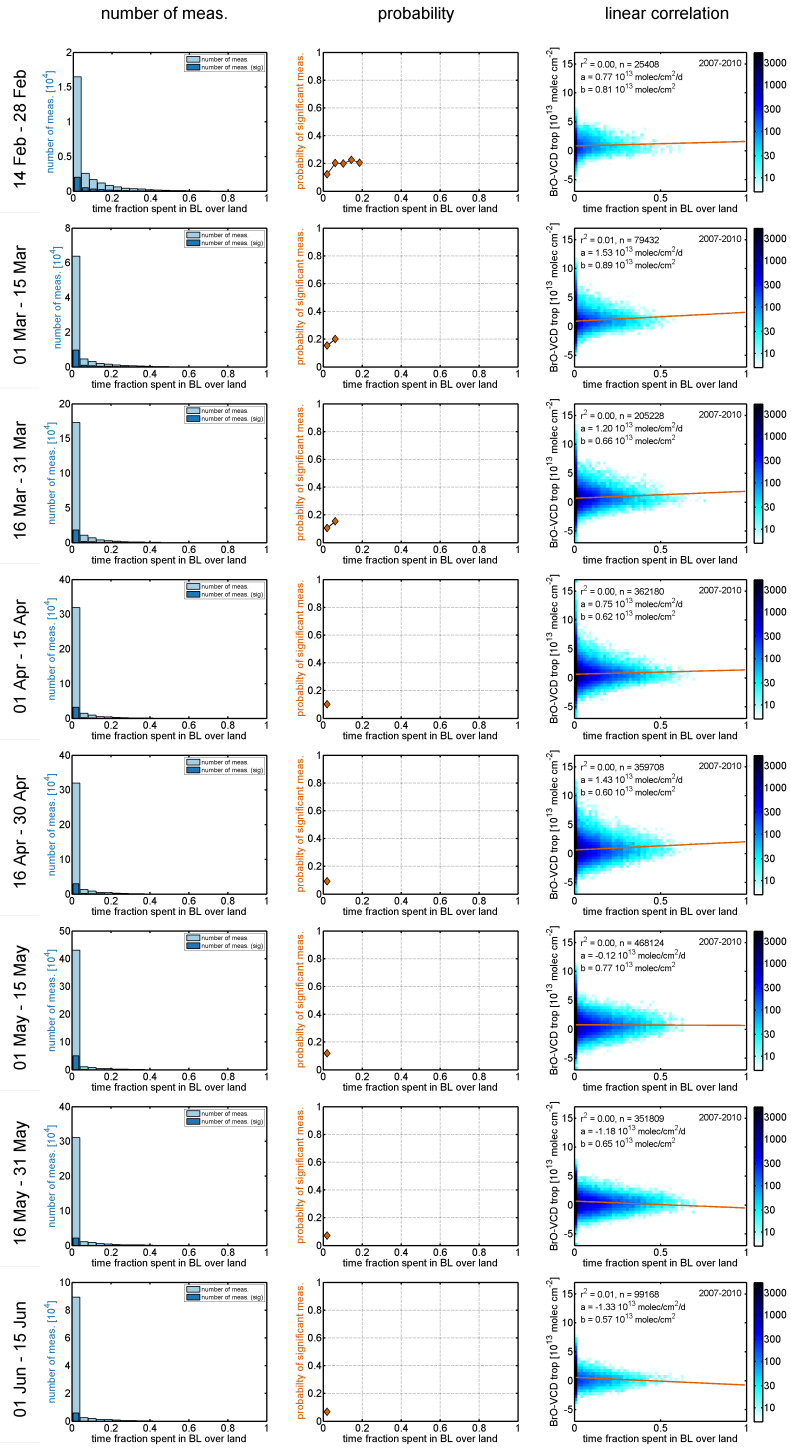

E.1.2. Residence time in boundary layer over ocean

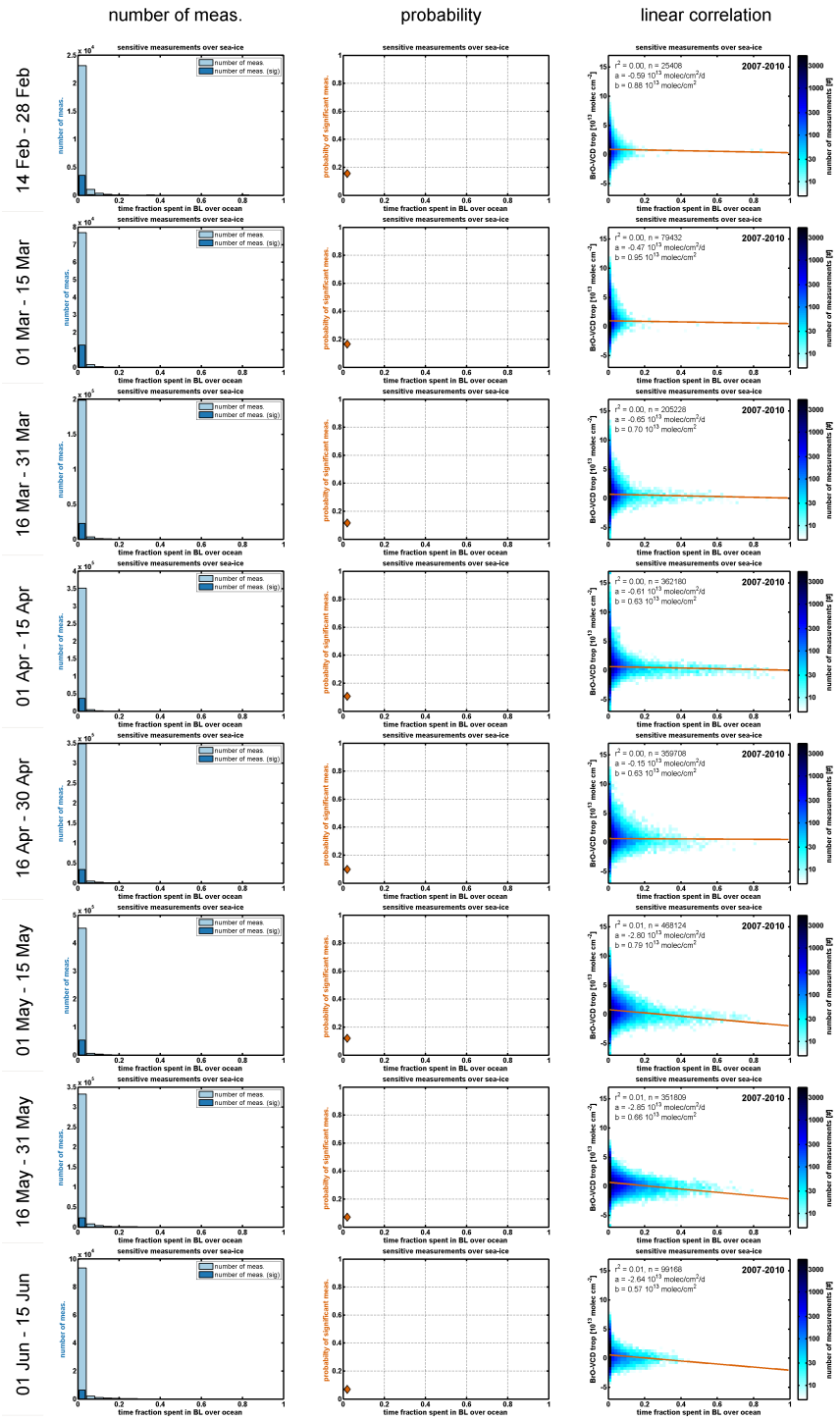

E.2. Observations over land adjacent to sea-ice

E.2.1. Residence time in boundary-layer over sea-ice

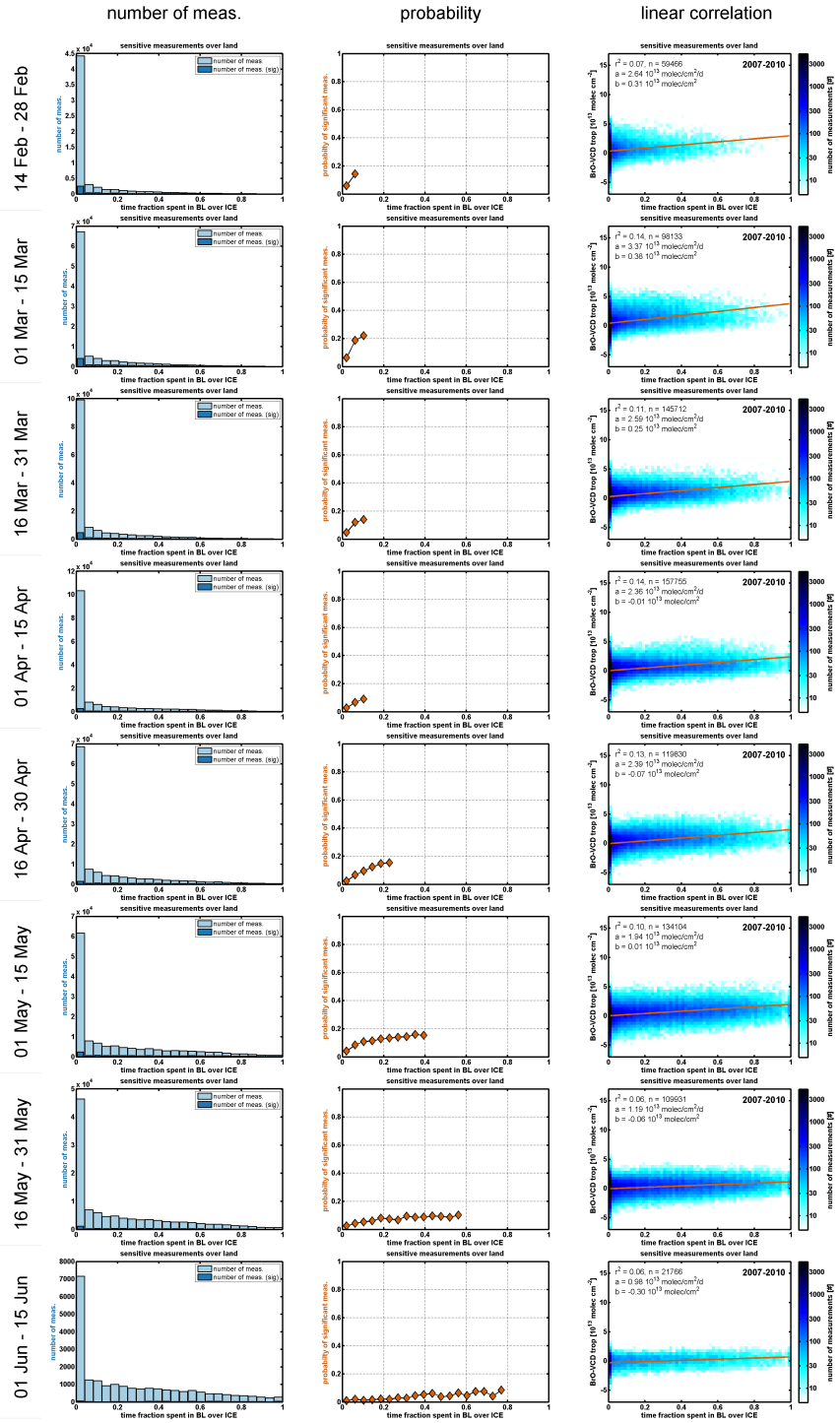

E.2.2. Residence time in boundary layer over land

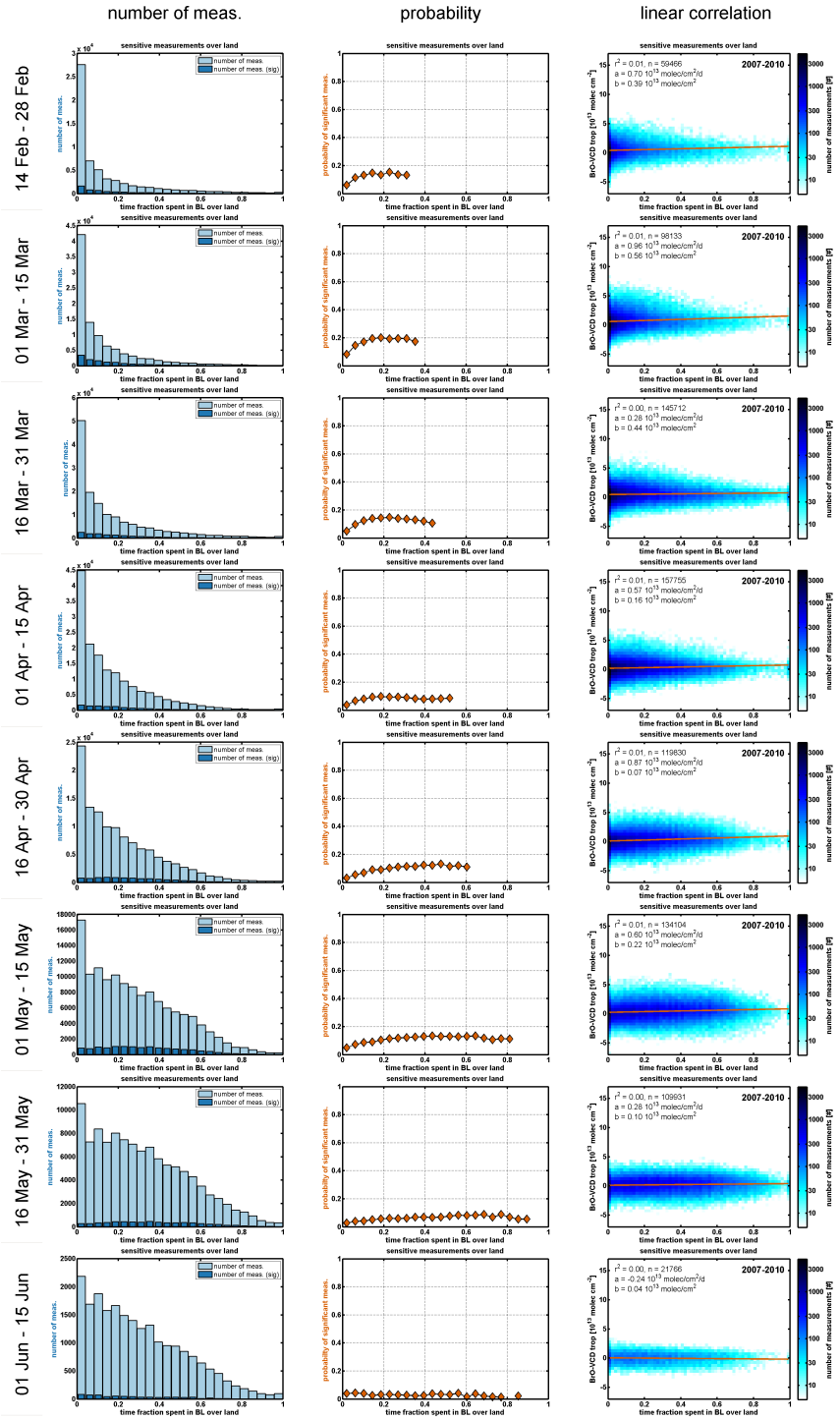

References

Acarreta, J. R., De Haan, J. F., & Stammes, P. 2004. Cloud pressure retrieval using the O_2-O_2 absorption band at 477 nm. *J. Geophys. Res.*, **109**(D5).

Afe, O., Richter, A., Sierk, B., Wittrock, F., & Burrows, J. 2004. BrO emission from volcanoes: A survey using GOME and SCIAMACHY measurements. *Geophys. Res. Lett.*, **31**(24), L24113.

Aliwell, S, Roozendael, M Van, Johnston, P, Richter, A, Wagner, T, & Arlander, D. 2002. Analysis for BrO in zenith-sky spectra: An intercomparison exercise for analysis improvement. *J. Geophys. Res.*, **107**(D14).

Anderson, P. S., & Neff, W. D. 2008. Boundary layer physics over snow and ice. *Atmos. Chem. Phys.*, **8**(13), 3563–3582.

Anlauf, K. G., Mickle, R. E., & Trivett, N. B. A. 1994. Measurement of ozone during Polar Sunrise Experiment 1992. *J. Geophys. Res.*, **99D**, 25 345–25 354.

Atkinson, R., Baulch, D. L., Cox, R. A., Crowley, J. N., Hampson, R. F., Hynes, R. G., Jenkin, M. E., Rossi, M. J., & Troe, J. 2007. Evaluated kinetic and photochemical data for atmospheric chemistry: Volume III – gas phase reactions of inorganic halogens. *Atmos. Chem. Phys.*, **7**(4), 981–1191.

Barber, D. G., Asplin, M. G., Gratton, Y., Lukovich, J. V., Galley, R. J., Raddatz, R. L., & Leitch, D. 2010. The International Polar Year (IPY) Circumpolar Flaw Lead (CFL) System Study: Overview and the Physical System. *Atmos. Ocean*, **48**(4), 225–243.

Barrie, L. A., Bottenheim, J. W., Schnell, R. C., Crutzen, P. J., & Rasmussen, R.A. 1988. Ozone destruction and photochemical reactions at polar sunrise in the lower Arctic atmosphere. *Nature*, **334**, 138–141.

Beesley, J. A., Bretherton, C. S., Jakob, C., Andreas, E. L, Intrieri, J. M., & Uttal, T. A. 2000. A comparison of cloud and boundary layer variables in the ECMWF forecast model with observations at Surface Heat Budget of the Arctic Ocean (SHEBA) ice camp. *J. Geophys. Res.*, **105**(D10), 12 337–12 349.

Begoin, M., Richter, A., Weber, M., Kaleschke, L., Tian-Kunze, X., Stohl, A., Theys, N., & Burrows, J. P. 2010. Satellite observations of long range transport of a large BrO plume in the Arctic. *Atmos. Chem. Phys.*, **10**(14), 6515–6526.

Bevington, P. R. 1969. *Data reduction and error analysis for the physical sciences.* New York: McGraw-Hill.

Bjerknes, J. 1919. On the structure of moving cyclones. *Geophys. Publ.*, **I**(2).

Bobrowski, N., Hönninger, G., Galle, B., & Platt, U. 2003. Detection of bromine monoxide from a volcanic plume. *Nature*, **423**, 273–276.

Bogumil, K., Orphal, J., Homann, T., Voigt, S., Spietz, P., & Fleischmann, O. 2003. Measurements of molecular absorption spectra with the SCIAMACHY pre-flight model: instrument characterization and reference data for atmospheric remote-sensing in the 230-2380 nm region. *J. Photochem. Photobiol. A-Chem.*, **157**(2-3), 167–184.

Bottenheim, J., & Chan, E. 2006. A trajectory study into the origin of spring time Arctic boundary layer ozone depletion. *J. Geophys. Res.*, **111**(D19), D19301.

Bottenheim, J., Gallant, A. J., & Brice, K. A. 1986. Measurements of NO_y species and O_3 at 82°N latitude. *Geophys. Res. Lett*, **13**, 113–116.

Bottenheim, J. W., Fuentes, J. D., Tarasick, D. W., & Anlauf, K. G. 2002. Ozone in the Arctic lower troposphere during winter and spring 2000 (ALERT2000). *Atmos. Environ.*, **36**(15–16), 2535–2544.

Bottenheim, J. W., Netcheva, S., Morin, S., & Nghiem, S. V. 2009. Ozone in the boundary layer air over the Arctic Ocean: measurements during the TARA transpolar drift 2006-2008. *Atmos. Chem. Phys.*, **9**(14), 4545–4557.

Brasseur, G., & Solomon, S. 2005. *Aeronomy of the middle atmosphere*. 3rd edn. Atmospheric and oceanographic sciences library ; 32. Dordrecht: Springer.

Bruns, M., Buehler, S. A., Burrows, J. P., Heue, K. P., & Platt, U. 2004. Retrieval of profile information from airborne multiaxis UV-visible skylight absorption measurements. *Appl. Opt.*, **43**(22), 4415–4426.

Burrows, J., Dehn, A., Deters, B., Himmelmann, S., Richter, A., & Voigt, S. 1998. Atmospheric remote-sensing reference data from GOME: Part 1. Temperature-dependent absorption cross-sections of NO_2 in the 231-794 nm range. *J. Quant. Spectrosc. Radiat. Transfer*, **60**(6), 1025–1031.

Burrows, J., Richter, A., Dehn, A., Deters, B., Himmelmann, S., & Orphal, J. 1999. Atmospheric remote-sensing reference data from GOME – Part 2. Temperature-dependent absorption cross sections of O-3 in the 231-794 nm range. *J. Quant. Spectrosc. Radiat. Transfer*, **61**(4), 509–517.

Byrkjedal, O., Esau, I., & Kvamsto, N. G. 2008. Sensitivity of simulated wintertime Arctic atmosphere to vertical resolution in the ARPEGE/IFS model. *Clim. Dynam.*, **30**(7–8), 687–701.

Callies, J., Corpaccioli, E., Eisinger, M., Hahne, A., & Lefebvre, A. 2000. GOME-2 – MetOp's Second-Generation Sensor for Operational Ozone Monitoring. *ESA Bulletin*, **102**, 28–36.

Cantrell, C. A. 2008. Technical Note: Review of methods for linear least-squares fitting of data and application to atmospheric chemistry problems. *Atmos. Chem. Phys.*, **8**(17), 5477–5487.

Chance, K. 1998. Analysis of BrO measurements from the Global Ozone Monitoring Experiment. *Geophys. Res. Lett.*, **25**(17), 3335–3338.

Chance, K., Kurosu, T., & Sioris, C. 2005. Undersampling correction for array detector-based satellite spectrometers. *Appl. Opt.*, **44**(7), 1296–1304.

Chapman, S. 1930. On ozone and atomic oxygen in the upper atmosphere. *Phil. Mag. Ser. 7*, **10**(64), 369–383.

Chipperfield, M. P. 1999. Multiannual simulations with a three-dimensional chemical transport model. *J. Geophys. Res.*, **104**, 1781–1805.

Chipperfield, M. P., Feng, W., & Rex, M. 2005. Arctic ozone loss and climate sensitivity: Updated three-dimensional model study. *Geophys. Res. Lett.*, **32**(11), L11813.

Choi, S., Wang, Y., Salawitch, R. J., Canty, T., Joiner, J., Zeng, T., Kurosu, T. P., Chance, K., Richter, A., Huey, L. G., Liao, J., Neuman, J. A., Nowak, J. B., Dibb, J. E., Weinheimer, A. J., Diskin, G., Ryerson, T. B., da Silva, A., Curry, J., Kinnison, D., Tilmes, S., & Levelt, P. F. 2011. Analysis of satellite-derived Arctic tropospheric BrO columns in conjunction with aircraft measurements during ARCTAS and ARCPAC. *Atmos. Chem. Phys.*, **12**(3), 1255–1285.

Clémer, K., Van Roozendael, M., Fayt, C., Hendrick, F., Hermans, C., Pinardi, G., Spurr, R., Wang, P., & De Mazière, M. 2010. Multiple wavelength retrieval of tropospheric aerosol optical properties from MAXDOAS measurements in Beijing. *Atmos. Meas. Tech.*, **3**(4), 863–878.

De Smedt, I., Van Roozendael, M., & Jacobs, T. 2004. *Optimization of DOAS settings for BrO fitting from SCIAMACHY nadir spectra – Comparison with GOME BrO retrievals.* Tech. rept. Belg. Inst. for Space Aeron., Brussels, Belgium. Available at http://www.oma.be/BIRA-IASB/Molecules/BrO/BIRA_SCIABrO.pdf.

Deutschmann, T., Beirle, S., Frieß, U., Grzegorski, M., Kern, C., Kritten, L., Platt, U., Prados-Román, C., Pukite, J., Wagner, T., Werner, B., & Pfeilsticker, K. 2011. The Monte Carlo atmospheric radiative transfer model McArtim: Introduction and validation of Jacobians and 3D features. *J. Quant. Spectrosc. Radiat. Transfer*, **112**(6), 1119–1137.

Dominé, F., Sparapani, R., Ianniello, A., & Beine, H. J. 2004. The origin of sea salt in snow on Arctic sea ice and in coastal regions. *Atmos. Chem. Phys.*, **4**(9/10), 2259–2271.

Dorf, M. 2005. *Investigation of inorganic stratospheric bromine using balloon-borne DOAS measurements and model simulations.* PhD thesis, University of Heidelberg.

Dorf, M., Butler, J. H., Butz, A., Camy-Peyret, C., Chipperfield, M. P., Kritten, L., Montzka, S. A., Simmes, B., Weidner, F., & Pfeilsticker, K. 2006. Long-term observations of stratospheric bromine reveal slow down in growth. *Geophys. Res. Let.*, **33**, L24808.

Dörner, S. 2010. *Comparison of Stratospheric Meteorology and Chemistry in Satellite Observations, EMAC simulations and ECMWF analysis data.* Diploma thesis, University of Mainz.

Drever, J. I. 1982. *The Geochemistry of Natural Waters.* New Jersey: Prentice Hall.

ECMWF. 2004 (March). *IFS DOCUMENTATION CY28r1 – Operational implementation 9 March 2004.* Internet. Available online at `http://www.ecmwf.int/research/ifsdocs/CY28r1/Physics/Physics-01-1.html`.

ECMWF. 2007 (Summer). *ECMWF newsletter No. 112.* Internet. Available online at `http://www.ecmwf.int/publications/newsletters/pdf/112.pdf`.

EUMETSAT. 2011 (Feb). *GOME-2 Level 1 Product Generation Specification.* Tech. rept. v7. EUMETSAT.

Fan, S. M., & Jacob, D. J. 1992. Surface ozone depletion in Arctic spring sustained by bromine reactions on aerosols. *Nature*, **359**(6395), 522–524.

Farman, J. C., Gardiner, B. G., & Shanklin, J. D. 1985. Large losses of total ozone in Antarctica reveal seasonal ClO_x/NO_x interaction. *Nature*, **315**, 207–210.

Finley, B. D., & Saltzman, E. S. 2008. Observations of Cl_2, Br_2, and I_2 in coastal marine air. *J. Geophys. Res.*, **113**, D21301.

Fitzenberger, R., Bösch, H., Camy-Peyret, C., Chipperfield, M. P., Harder, H., Platt, U., Sinnhuber, B.-M., Wagner, T., & Pfeilsticker, K. 2000. First profile measurements of tropospheric BrO. *Geophys. Res. Let.*, **27**, 2921–2924.

Fleischmann, O, Hartmann, M, Burrows, J, & Orphal, J. 2004. New ultraviolet absorption cross-sections of BrO at atmospheric temperatures measured by time-windowing Fourier transform spectroscopy. *J. Photochem. Photobiol. A*, **168**(1-2), 117–132.

Frieß, U. 2001. *Spectroscopic Measurements of Atmospheric Trace Gases at Neumayer-Station, Antarctica.* Ph.D. thesis, University of Heidelberg.

Frieß, U., Hollwedel, J., Konig-Langlo, G., Wagner, T., & Platt, U. 2004. Dynamics and chemistry of tropospheric bromine explosion events in the Antarctic coastal region. *J. Geophys. Res.*, **109**(D6).

Frieß, U., Sihler, H., Sander, R., Pöhler, D., Yilmaz, S., & Platt, U. 2011. The vertical distribution of BrO and aerosols in the Arctic: Measurements by active and passive differential optical absorption sprectroscopy. *J. Geophys. Res.*, **116**, D00R04.

Gayet, J.-F., Mioche, G., Dörnbrack, A., Ehrlich, A., Lampert, A., & Wendisch, M. 2009. Microphysical and optical properties of Arctic mixed-phase clouds. The 9 April 2007 case study. *Atm. Chem. Phys.*, **9**(17), 6581–6595.

Gong, S.L., Walmsley, J.L., Barrie, L.A., & Hopper, J.F. 1997. Mechanisms for surface ozone depletion and recovery during polar sunrise. *Atmos. Environ.*, **31**(7), 969–981.

Gür, B., Spietz, P., Orphal, J., & Burrows, J. 2005. *Absorption Spectra Measurements with the GOME-2 FMs using the IUP/IFE-UBs Calibration Apparatus for Trace Gas Absorption Spectroscopy CATGAS, Final Report.* Tech. rept. IUP University of Bremen, Germany.

Graf, J. E., Tsai, W.-Y., & Jones, W. L. 1998. Overview of the QuikSCAT mission – A quick deployment of a high resolution, wide swath scanning scatterometer for ocean wind measurement. *In: IEEE Proceedings Southeastcon '98.*

Grainger, J. F., & Ring, J. 1962. Anomalous Fraunhofer line profiles. *Nature*, **193**, 762.

Grannas, A. M., Jones, A. E., Dibb, J., Ammann, M., Anastasio, C., Beine, H. J., Bergin, M., Bottenheim, J., Boxe, C. S., Carver, G., Chen, G., Crawford, J. H., Dominé, F., Frey, M. M., Guzmán, M. I., Heard, D. E., Helmig, D., Hoffmann, M. R., Honrath, R. E., Huey, L. G., Hutterli, M., Jacobi, H. W., Klán, P., Lefer, B., McConnell, J., Plane, J., Sander, R., Savarino, J., Shepson, P. B., Simpson, W. R., Sodeau, J. R., von Glasow, R., Weller, R., Wolff, E. W., & Zhu, T. 2007. An overview of snow photochemistry: evidence, mechanisms and impacts. *Atmos. Chem. Phys.*, **7**(16), 4329–4373.

Greenblatt, G., Orlando, J., Burkholder, J., & Ravishankara, A. 1990. Absorption measurements of oxygen between 330 and 1140 nm. *J. Geophys. Res.*, **95**(D11), 18577–18582.

Grenfell, T. C., Warren, S. G., & Mullen, P. C. 1994. Reflection of solar radiation by the Antarctic snow surface at ultraviolet, visible, and near-infrared wavelengths. *J. Geophys. Res.*, **99**, 18 669–18 684.

Hartley, W. N. 1880. On the probable absorption of solar radiation by atmospheric ozone. *Chem. News*, **42**, 268.

Hausmann, M., & Platt, U. 1994. Spectroscopic measurement of bromine oxide and ozone in the high Arctic during the polar sunrise experiment 1992. *J. Geophys. Res.*, **99**(D12), 25399–25413.

Hegels, E., Crutzen, P. J., Klüpfel, T., Perner, D., & Burrows, J. P. 1998. Global distribution of atmospheric bromine-monoxide from GOME on earth observing satellite ERS-2. *Geophys. Res. Let.*, **25**(16), 3127–3130.

Helmig, D., Boylan, P., Johnson, B., Oltmans, S., Fairall, C., Staebler, R., Weinheimer, A., Orlando, J., Knapp, D. J., Montzka, D. D., Flocke, F., Frieß, U., Sihler, H., & Shepson, P. B. 2012. Ozone Dynamics and Snow-Atmosphere Exchanges During Ozone Depletion Events at Barrow, AK. *submitted to J. Geophys. Res.*

Hendrick, F., Van Roozendael, M., Chipperfield, M. P., Dorf, M., Goutail, F., Yang, X., Fayt, C., Hermans, C., Pfeilsticker, K., Pommereau, J.-P., Pyle, J. A., Theys, N., & De Mazière, M. 2007. Retrieval of stratospheric and tropospheric BrO profiles and columns using ground-based zenith-sky DOAS observations at Harestua, 60° N. *Atmos. Chem. Phys.*, **7**(18), 4869–4885.

Heue, K.-P., Brenninkmeijer, C. A. M., Baker, A. K., Rauthe-Schöch, A., Walter, D., Wagner, T., Hörmann, C., Sihler, H., Dix, B., Frieß, U., Platt, U., Martinsson, B. G., van Velthoven, P. F. J., Zahn, A., & Ebinghaus, R. 2011. SO_2 and BrO observation in the plume of the Eyjafjallajökull volcano 2010: CARIBIC and GOME-2 retrievals. *Atmos. Chem. Phys.*, **11**(6), 2973–2989.

Hidalgo, H., & Crutzen, P. J. 1977. The tropospheric and stratospheric composition pertubed by NO_x emissions of high altitude aircraft. *J. Geophys. Res.*, **83**, 5833–5866.

Hönninger, G. 2002. *Halogen Oxide Studies in the Boundary Layer by Multi Axis Differential Optical Absorption Spectroscopy and Active Longpath-DOAS*. PhD thesis, University of Heidelberg.

Hönninger, G, Leser, H, Sebastián, O, & Platt, U. 2004. Ground-based measurements of halogen oxides at the Hudson Bay by active longpath DOAS and passive MAX-DOAS. *Geophys. Res. Lett.*, **31**(4).

Hollwedel, J., Wenig, M., Beirle, S., Kraus, S., Kuhl, S., Wilms-Grabe, W., Platt, U., & Wagner, T. 2004. Year-to-year variations of spring time polar tropospheric BrO as seen by GOME. *Adv. Space Res.*, **34**(4), 804–808.

Hollwedel, J. C. 2005. *Observations of Tropospheric and Stratospheric Bromine Monoxide from Satellite*. PhD thesis, University of Heidelberg.

Hönninger, G., & Platt, U. 2002. Observations of BrO and its vertical distribution during surface ozone depletion at Alert. *Atmos. Environ.*, **36**, 2482–2489.

Hönninger, G., von Friedeburg, C., & Platt, U. 2004. Multi axis differential optical absorption spectroscopy (MAX-DOAS). *Atmos. Chem. Phys.*, **4**(1), 231–254.

Hopper, J. F., Barrie, L. A., Silis, A., Hart, W., Gallant, A. J., & Dryfhout, H. 1998. Ozone and meteorology during the 1994 Polar Sunrise Experiment. *J. Geophys. Res.*, **103**, 1481–1492.

Hörmann, C., Sihler, H., Bobrowski, N., Platt, U., & Wagner, T. 2012. Systematic investigation of bromine monoxide in volcanic plumes from space by using the GOME-2 instrument. *in preparation*.

Howell, S. E. L., Tivy, A., Yackel, J. J., & Scharien, R. K. 2006. Application of a SeaWinds/QuikSCAT sea ice melt algorithm for assessing melt dynamics in the Canadian Arctic Archipelago. *J. Geophys. Res.*, **111**, C07025.

Howell, S. E. L., Tivy, A., Yackel, J. J., Else, B. G. T., & Duguay, C. R. 2008. Changing sea ice melt parameters in the Canadian Arctic Archipelago: Implications for the future presence of multiyear ice. *J. Geophys. Res.*, **113**, C09030.

Jacobi, H.-W., Kaleschke, L., Richter, A., Rozanov, A., & Burrows, John P. 2006. Observation of a fast ozone loss in the marginal ice zone of the Arctic Ocean. *J. Geophys. Res.*, **111**(D15), D15309.

Jacobi, H.-W., Morin, S., & Bottenheim, J. W. 2010. Observation of widespread depletion of ozone in the springtime boundary layer of the central Arctic linked to mesoscale synoptic conditions. *J. Geophys. Res.*, **115**, D17302.

Jöckel, P., Kerkweg, A., Pozzer, A., Sander, R., Tost, H., Riede, H., Baumgaertner, A., Gromov, S., & Kern, B. 2010. Development cycle 2 of the Modular Earth Submodel System (MESSy2). *Geosci. Model Dev.*, **3**(2), 717–752.

Jones, A. E., Anderson, P. S., Begoin, M., Brough, N., Hutterli, M. A., Marshall, G. J., Richter, A., Roscoe, H. K., & Wolff, E. W. 2009. BrO, blizzards, and drivers of polar tropospheric ozone depletion events. *Atmos. Chem. Phys.*, **9**(14), 4639–4652.

Jones, A. E., Anderson, P. S., Wolff, E. W., Roscoe, H. K., Marshall, G. J., Richter, A., Brough, N., & Colwell, S. R. 2010. Vertical structure of Antarctic tropospheric ozone depletion events: characteristics and broader implications. *Atmos. Chem. Phys.*, **10**(16), 7775–7794.

Kaleschke, L., Lupkes, C., Vihma, T., Haarpaintner, J., & Bochert, A. 2001. SSM/I sea ice remote sensing for mesoscale ocean-atmosphere interaction analysis. *Can. J. Remote Sens.*, **27**(5), 526–537.

Kaleschke, L., Richter, A., Burrows, J., Afe, O., Heygster, G., Notholt, J., Rankin, A. M., Roscoe, H. K., Hollwedel, J., Wagner, T., & Jacobi, H.-W. 2004. Frost flowers on sea ice as a source of sea salt and their influence on tropospheric halogen chemistry. *Geophys. Res. Let.*, **31**, L16114.

Kercher, J. P., Riedel, T. P., & Thornton, J. A. 2009. Chlorine activation by N_2O_5: Simultaneous, in situ detection of $ClNO_2$ and N_2O_5 by chemical ionization mass spectrometry. *Atmos. Meas. Tech.*, **2**, 193–204.

Kern, C., Trick, S., Rippel, B., & Platt, U. 2006. Applicability of light-emitting diodes as light sources for active DOAS measurements. *Applied Optics*, **45**, 2077–2088.

King, M. D. 1987. Determination of the Scaled Optical Thickness of Clouds from Reflected Solar Radiation Measurements. *J. Atmos. Sci.*, **44**(13), 1734–1751.

Klonecki, A., Hess, P., Emmons, L., Smith, L., Orlando, J., & Blake, D. 2003. Seasonal changes in the transport of pollutants into the Arctic troposphere-model study. *J. Geophys. Res.*, **108**, 8367.

Koop, T., Kapilashrami, A., Molina, L. T., & Molina, M. J. 2000. Phase transitions of sea-salt/water mixtures at low temperatures: Implications for ozone chemistry in the polar marine boundary layer. *J. Geophys. Res.*, **105**, 26 393–26 402.

Kraus, G. 2006. *DOASIS – A Framework Design for DOAS*. PhD thesis, University of Mannheim.

Kraus, S. 2004. *DOASIS: DOAS Intelligent Sytem*. Software, Copyright 2004 Stefan Kraus. Institute of Environmental Physics, University of Heidleberg, Heidelberg. in cooperation with Hoffmann Messtechnik GmbH.

Kreher, K., Keys, J. G., Johnston, P. V., Platt, U., & Lui, X. 1996. Ground based measurements of ClO and HCl in austral spring 1993 at Arrival Heights, Antarctica. *Geophys. Res. Let.*, **23**, 1545–1548.

Kurucz, R. L., Furenlid, I., Brault, J., & Testermann, L. 1984. *Solar flux atlas from 296 to 1300 nm*. Natl. Sol. Obs. Atlas, Sunspot.

Kwok, R. 2004. Annual cycles of multiyear sea ice coverage of the Arctic Ocean: 1999–2003. *J. Geophys. Res.*, **109**, C11004.

Kwok, R., Cunningham, G. F., Zwally, H. J., & Yi, D. 2006. ICESat over Arctic sea ice: Interpretation of altimetric and reflectivity profiles. *J. Geophys. Res.*, **111**, C06006.

Kwok, R., Cunningham, G. F., Wensnahan, M., Rigor, I., Zwally, H. J., & Yi, D. 2009. Thinning and volume loss of the Arctic Ocean sea ice cover: 2003–2008. *J. Geophys. Res.*, **114**, C07005.

Lehrer, E. 1999. *Polar tropospheric ozone loss*. PhD thesis, University of Heidelberg.

Lehrer, E., Hönninger, G., & Platt, U. 2004. A one dimensional model study of the mechanism of halogen liberation and vertical transport in the polar troposphere. *Atm. Chem. Phys.*, **4**(11/12), 2427–2440.

Liao, J., Sihler, H., Huey, L., Neuman, J., Tanner, D., Friess, U., Platt, U., Flocke, F. M., Orlando, J. J., Shepson, P. B., Beine, H. J., Weinheimer, A. J., Sjostedt, S. J., Nowak, J. B., Knapp, D. J., Staebler, R. M., Zheng, W., Sander, R., Hall, S. R., & Ullmann, K. 2011. A comparison of Arctic BrO measurements by chemical ionization mass spectrometry and long path-differential optical absorption spectroscopy. *J. Geophys. Res.*, **116**, D00R02.

Lotter, A. 2006. *Field Measurements of Water Continuum and Water Dimer Absorption by Active Long Path Differential Optical Absorption Spectroscopy (DOAS)*. PhD thesis, University of Heidelberg.

Martin, R. V., Chance, K., Jacob, D.J., Kurosu, T. P., Spurr, R. J. D., Bucsela, E., Gleason, J. F., Palmer, P. I., Bey, I., Fiore, A. M., Li, Q., Yantosca, R. M., & Koelemeijer, R. B. A. 2002. An improved retrieval of tropospheric nitrogen dioxide from GOME. *J. Geophys. Res.*, **107**(D20), 4437.

Martin, S., Yu, Y., & Drucker, R. 1996. The temperature dependence of frost flower growth on laboratory sea ice and the effect of the flowers on infrared observations of the surface. *J. Geophys. Res.*, **101**(C5), 12 111–12 125.

Maxwell, J. B. 1981. Climatic Regions of the Canadian Arctic Islands. *Arctic*, **34**(3), 225–240.

McConnell, J. C., Henderson, G. S., Barrie, L., Bottenheim, J., Niki, H., Langford, C. H., & Templeton, E. M. J. 1992. Photochemical bromine production implicated in Arctic boundary-layer ozone depletion. *Nature*, **355**(6356), 150–152.

Meller, R., & Moortgat, G. K. 2000. Temperature dependence of the absorption cross sections of formaldehyde between 223 and 323 K in the wavelength range 225-375 nm. *J. Geophys. Res.-Biogeo.*, **105**(D6), 7089–7101.

Merten, A., Tschritter, J., & Platt, U. 2011. Design of differential optical absorption spectroscopy long-path telescopes based on fiber optics. *Appl. Opt.*, **50**(5), 738–754.

Mie, G. 1908. Beiträge zur Optik trüber Medien, speziell kolloidaler Metallösungen. *Annalen der Physik*, **330**, 377–445.

Molina, L. T., & Rowland, F. S. 1974. Stratospheric sink for chloro°uromethanes: chlorine atom catalyzed destruction of ozone. *Nature*, **249**, 820–822.

Morin, S., Honninger, G. H., Staebler, R. M., & Bottenheim, J. W. 2005. A high time resolution study of boundary layer ozone chemistry and dynamics over the Arctic Ocean near Alert, Nunavut. *Geophys. Res. Lett*, **32**(8).

Morin, S., Marion, G. M., von Glasow, R., Voisin, D., Bouchez, J., & Savarino, J. 2008. Precipitation of salts in freezing seawater and ozone depletion events: a status report. *Atmos. Chem. Phys.*, **8**, 7313–7324.

Munneke, P. K., & Reijmer, C. H. 2011. Assessing the retrieval of cloud properties from radiation measurements over snow and ice. *Int. J. Climatol.*, **31**(5), 756–769.

Munro, R., Eisinger, M., Anderson, C., Callies, J., Corpaccioli, E., Lang, R., Lefebvre, A., Livschitz, Y., & Albiñana, A. P. 2006. GOME-2 on MetOp. *Page 48 of: Proc. of The 2006 EUMETSAT Meteorological Satellite Conference, Helsinki, Finland, 12–16 June 2006, EUMETSAT.*

NASA. 2006 (Apr). *CloudSat-CALIPSO Launch.* Press Kit. National Aeronautics and Space Administration.

Neuman, J. A., Nowak, J. B., Huey, L. G., Burkholder, J. B., Dibb, J. E., Holloway, J. S., Liao, J., Peischl, J., Roberts, J. M., Ryerson, T. B., Scheuer, E., Stark, H., Stickel, R. E., Tanner, D. J., & Weinheimer, A. 2010. Bromine measurements in ozone depleted air over the Arctic Ocean. *Atmos. Chem. Phys.*, **10**(14), 6503–6514.

NIST. 2000. *NIST Kinetics Database*. Website. Online access in March 2012 under `http://kinetics.nist.gov/kinetics/index.jsp`.

Noxon, J. F. 1975. Nitrogen dioxide in the stratosphere and troposphere measured by ground-based absorption spectroscopy. *Science*, **189**, 547.

Noxon, J. F., Norton, R. B., & Henderson, W. R. 1978. Observation of Atmospheric NO3. *Geophys. Res. Lett.*, **5**, 675–678.

O'Byrne, G., Martin, R. V., van Donkelaar, A., Joiner, J., & Celarier, E. A. 2010. Surface reflectivity from the Ozone Monitoring Instrument using the Moderate Resolution Imaging Spectroradiometer to eliminate clouds: Effects of snow on ultraviolet and visible trace gas retrievals. *J. Geophys. Res.*, **115**.

Oltmans, S. J. 1981. Surface ozone measurements in clean air. *J. Geophys. Res.*, **86**, 1174–1180.

Oltmans, S. J., & Komhyr, W. 1986. Surface ozone distributions and variations from 1973 - 1984 measurements at the NOAA Geophysical Monitoring for Climate Change Baseline observatories. *J. Geophys. Res.*, **91**, 5229–5236.

Oltmans, S. J., Schnell, R. C., Sheridan, P. J., Peterson, R. E., Li, S. M., Winchester, J. W., Tans, P. P., Sturges, W. T., Kahl, J. D., , & Barrie, L. A. 1989. Seasonal surface ozone and filterable bromine relationship in the high Arctic. *Atmos. Environ.*, **23**, 2431–2441.

Palm, S. P., Yang, Y., Spinhirne, J. D., & Marshak, A. 2011. Satellite remote sensing of blowing snow properties over Antarctica. *J. Geophys. Res.*, **116**, D16123.

Pawlowicz, R. 2005. *M_Map: A mapping package for Matlab*. Website. Available online at `http://www.eos.ubc.ca/~rich/map.html`.

Perner, D., Ehhalt, D. H., Pätz, H. W., Platt, U., Röth, E. P., & Volz, A. 1976. OH-raidicals in the lower tropsosphere. *Geophys. Res. Lett*, **3**, 466–468.

Piot, M. 2007. *Modeling halogen chemistry during ozone depletion events in polar spring: a model study*. PhD thesis, University of Heidelberg.

Piot, M., & von Glasow, R. 2008. The potential importance of frost flowers, recycling on snow, and open leads for ozone depletion events. *Atmos. Chem. Phys.*, **8**(9), 2437–2467.

Platt, U., & Hönninger, G. 2003. The role of halogen species in the troposphere. *Chemosphere*, **52**(2), 325–338.

Platt, U., & Lehrer, E. 1996. Arctic Tropospheric Ozone Chemistry, ARCTOC, Final Report of the EU-Project NO. EV5V-CT93-0318.

Platt, U., & Stutz, J. 2008. *Differential Optical Absorption Spectroscopy – Principles and Applications.* Physics of Earth and Space Environments. Berlin Heidelberg: Springer. ISBN: 978-3-540-21193-8 e-ISBN: 978-3-540-75776-4.

Platt, U., Perner, D., & Pätz, H. W. 1979. Simultaneous measurements of atmospheric CH2O, O3 and NO2 by differential optical absortion. *J. Geophys. Res.*, **84**, 6329–6335.

Platt, U., Meinen, J., Pöhler, D., & Leisner, T. 2009. Broadband Cavity Enhanced Differential Optical Absorption Spectroscopy (CE-DOAS) – applicability and corrections. *Atmos. Meas. Tech.*, **2**(2), 713–723.

Pöhler, D., Sihler, H., Vogel, L., Frieß, U., & Platt, U. 2010a. *Characterization of Halogen Concentrations During Ozone Depletion Events from DOAS Observations in the Amundsen Bay.* IPY Oslo Science Conference.

Pöhler, D., Vogel, L., Frieß, U., & Platt, U. 2010b. Observation of halogen species in the Amundsen Gulf, Arctic, by active long-path differential optical absorption spectroscopy. *P. Natl. Acad. Sci. U. S. A.*, **107**(15), 6582–6587.

Prados-Roman, C. 2010. *Aircraft-borne spectroscopic limb measurements of trace gases absorbing in the UV-A spectral range – Investigations of bromine monoxide in the Arctic troposphere.* PhD thesis, University of Heidelberg.

Prados-Roman, C., Butz, A., Deutschmann, T., Dorf, M., Kritten, L., Minikin, A., Platt, U., Schlager, H., Sihler, H., Theys, N., Van Roozendael, M., Wagner, T., & Pfeilsticker, K. 2010. Airborne DOAS limb measurements of tropospheric trace gas profiles: case study on the profile retrieval of O_4 and BrO. *Atmos. Meas. Tech. Disc.*, **3**(4), 3925–3969.

Press, W. H., Flannery, B. P., Teukolsky, S. A., & Vettering, W. T. 1992. *Numerical Recipies in FORTRAN.* Cambridge University Press.

Press, W. H., Teukolsky, S. A., Vetterling, W. T., & Flannery, B. P. 2002. *Numerical Recepies in C++.* Vol. second edition. Cambridge University Press.

Pukite, J., Kühl, S., Deutschmann, T., Platt, U., & Wagner, T. 2010. Extending differential optical absorption spectroscopy for limb measurements in the UV. *Atmos. Meas. Tech.*, **3**(3), 631–653.

Quarteroni, A., Sacco, R., & Saleri., F. 2002. *Numerische Mathematik 2.* Berlin/Heidelberg: Springer Verlag.

Rankin, A. M. 2002. Frost flowers: Implications for tropospheric chemistry and ice core interpretation. *J. Geophys. Res.*, **107**(D23), 4683.

Rayleigh, L. 1899. On the transmission of light through an atmosphere containing many small particles in suspension, and on the origin of the blue of thesky. *Phil. Mag. Ser. 5*, **41**, 447–454.

Richardson, C. 1976. Phase relationships in sea ice as a function of temperature. *J. Glaciol.*, **17**, 507–519.

Richter, A., & Wagner, T. 2011. *The Remote Sensing of Tropospheric Composition from Space*. Physics of Earth and Space Environments. Berlin Heidelberg: Springer-Verlag. Chap. 2 – The Use of UV, Visible and Near IR Solar Back Scattered Raidation to Determine Trace Gases, pages 67–121.

Richter, A., Wittrock, F., Eisinger, M., & Burrows, J. 1998. GOME observations of tropospheric BrO in northern hemispheric spring and summer 1997. *Geophys. Res. Lett.*, **25**(14), 2683–2686.

Richter, A., Wittrock, F., Ladstätter-Weißenmayer, A., & Burrows, J. P. 2002. GOME measurements of stratospheric and tropospheric BrO. *Adv. Space Res.*, **29**(11), 1667–1672.

Rigor, I. G., Colony, R. L., & Martin, S. 2000. Variations in Surface Air Temperature Observations in the Arctic, 1979–97. *J. Climate*, **13**(5), 896–914.

Roedel, W. 2000. *Physik unserer Umwelt – Die Atmosphäre*. 3. edn. Berlin Heidelberg New York: Springer-Verlag.

Rohli, R. V., & Vega, A. J. 2011. *Climatology*. 2nd edn. Jones & Bartlett Publishers Canada.

Rothman, L., Gamache, R., Tipping, R., Rinsland, C., Smith, M., & Benner, D. 1992. The HITRAN molecular database – Editions of 1991 and 1992. *J. Quant. Spectrosc. Radiat. Transfer*, **48**(5–6), 469–507.

Salawitch, R. J., Canty, T., Kurosu, T., Chance, K., & Jacob, D. J. 2010. A New Interpretation of Total Column BrO during Arctic Spring. *Geophys. Res. Lett.*, **37**.

Sander, R., Burrows, J., & Kaleschke, L. 2006. Carbonate precipitation in brine – a potential trigger for tropospheric ozone depletion events. *Atmos.Chem. Phys.*, **6**(12), 4653–4658.

Schiller, C., Wahner, A., Platt, U., Dorn, H.-P., Callies, J., & Ehalt, D. 1990. Near UV atmospheric absorption measurements of column abundances during airborne Arctic stratospheric expedition, January - February 1989: 2. OClO observations. *Geophys. Res. Let.*, **17**, 501–504.

Schroeder, W. H., Steffen, A., Scott, K., Bender, T., Prestbo, E., Ebinghaus, R., Lu, J., & Lindberg, S. 2003. Summary report: first international Arctic atmospheric mercury research workshop. *Atmos. Environ.*, **37**(18), 2551–2555.

Seabrook, J. A., Whiteway, J., Staebler, R. M., Bottenheim, J. W., Komguem, L., Gray, L. H., Barber, D., & Asplin, M. 2011. LIDAR measurements of Arctic boundary layer ozone depletion events over the frozen Arctic Ocean. *J. Geophys. Res.*, **116**, D00S02.

Serreze, M. C., & Barry, R. G. 2005. *The Arctic Climate System.* Cambridge University Press.

Sihler, H. 2007. *Light-Emitting Diodes as Light Sources in Spectroscopic Measurements of Atmospheric Trace Gases.* Diploma thesis, University of Jena, Germany.

Sihler, H., Kern, C., Pöhler, D., & Platt, U. 2009. Applying light-emitting diodes with narrowband emission features in differential spectroscopy. *Opt. Lett.*, **34**(23), 3716–3718.

Sihler, H., Platt, U., Beirle, S., Marbach, T., Kühl, S., Dörner, S., Verschaeve, J., Frieß, U., Pöhler, D., Vogel, L., Sander, R., & Wagner, T. 2012. Tropospheric BrO column densities in the Arctic from satellite: Retrieval and comparison to ground-based measurements. *accepted for publication in Atmos. Meas. Tech. Disc.*

Simpson, W. R., Carlson, D., Hönninger, G., Douglas, T. A., Sturm, M., Perovich, D., & Platt, U. 2007a. First-year sea-ice contact predicts bromine monoxide (BrO) levels at Barrow, Alaska better than potential frost flower contact. *Atmos. Chem. Phys.*, **7**(3), 621–627.

Simpson, W. R., von Glasow, R., Riedel, K., Anderson, P., Ariya, P., Bottenheim, J., Burrows, J., Carpenter, L. J., Frieß, U., Goodsite, M. E., Heard, D., Hutterli, M., Jacobi, H.-W., Kaleschke, L., Neff, B., Plane, J., Platt, U., Richter, A., Roscoe, H., Sander, R., Shepson, P., Sodeau, J., Steffen, A., Wagner, T., & Wolff, E. 2007b. Halogens and their role in polar boundary-layer ozone depletion. *Atm. Chem. Phys.*, **7**(16), 4375–4418.

Sinnhuber, B.-M., Arlander, D. W., Bovensmann, H., Burrows, J. P., Chipperfield, M. P., Enell, C.-F., Frieß, U., Hendrick, F., Johnston, P. V., Jones, R. L., Kreher, K., Mohamed-Tahrin, N., Müller, R., Pfeilsticker, K., Platt, U., Pommereau, J.-P., Pundt, I., Richter, A., South, A. M., Tørnkvist, K. K., Roozendael, M. Van, Wagner, T., & Wittrock, F. 2002. Comparison of measurements and model calculations of stratospheric bromine monoxide. *J. Geophys. Res.-Biogeo.*, **107**(D19), 4398.

Sodemann, H., Pommier, M., Arnold, S. R., Monks, S. A., Stebel, K., Burkhart, J. F., Hair, J. W., Diskin, G. S., Clerbaux, C., Coheur, P.-F., Hurtmans, D., Schlager, H., Blechschmidt, A.-M., Kristjánsson, J. E., & Stohl, A. 2011. Episodes of cross-polar transport in the Arctic troposphere during July 2008 as seen from models, satellite, and aircraft observations. *Atmos. Chem. Phys.*, **11**(8), 3631–3651.

Solberg, S., Schmidbauer, N., Semb, A., Stordal, F., & Hov, Øystein. 1966. Boundary-layer ozone depletion as seen in the Norwegian Arctic in spring. *J. Atmos. Chem.*, **23**(3), 301–332.

Solomon, S., Garcia, R. R., Rowland, F. S., & Wuebbles, D. J. 1986. On the depletion of Antarctic ozone. *Nature*, **31**, 755–758.

Solomon, S., Schmeltekopf, A. L., & Sanders, R. W. 1987a. On the interpretation of zenith sky absorption measurements. *J. Geophys. Res.*, **92**, 8311–8319.

Solomon, S., Mount, G.H., Sanders, R.W., & Schmeltekopf, A.L. 1987b. Visible Spectrospcopy at McMurdo Station, Antarctica 2. Observations of OClO. *J. Geophys. Res.*, **93**, 8329–8338.

Solomon, S., Miller, H.L., Smith, J.P., Sanders, R.W., Mount, G.H., Smeltekopf, A.L., & Noxon, J.F. 1989. Atmospheric NO3 1. Measurement Technique and the Annual Cycle. *J. Geophys. Res.*, **94**, 11 041–11 048.

Spencer, M.W., Wu, C., & Long, D.G. 2000. Improved resolution backscatter measurements with the SeaWinds pencil-beam scatterometer. *IEEE Trans. Geosci. Remote Sens.*, **38**(1), 89–104.

Spreen, G., Kaleschke, L., & Heygster, G. 2008. Sea ice remote sensing using AMSR-E 89-GHz channels. *J. Geophys. Res.-Biogeo.*, **113**(C2), C02S03.

Steffen, A., Douglas, T., Amyot, M., Ariya, P., Aspmo, K., Berg, T., Bottenheim, J., Brooks, S., Cobbett, F., Dastoor, A., Dommergue, A., Ebinghaus, R., Ferrari, C., Gardfeldt, K., Goodsite, M. E., Lean, D., Poulain, A. J., Scherz, C., Skov, H., Sommar, J., & Temme, C. 2008. A synthesis of atmospheric mercury depletion event chemistry in the atmosphere and snow. *Atmos. Chem. Phys.*, **8**(6), 1445–1482.

Stöcker, H. (ed). 2004. *Handbuch der Physik*. Verlag Harri Deutsch.

Stohl, A. 2006. Characteristics of atmospheric transport into the Arctic troposphere. *J. Geophys. Res.*, **111**, D11306.

Stohl, A., Hittenberger, M., & Wotawa, G. 1998. Validation of the Lagrangian particle dispersion model FLEXPART against large scale tracer experiments. *Atmos. Environ.*, **32**, 4245–4264.

Stohl, A., Haimberger, L., Scheele, M. P., & Wernli, H. 2001. An intercomparison of results from three trajectory models. *Meteorol. Appl.*, **8**, 127–135.

Strong, C., Fuentes, J.D., Davis, R.E., & Bottenheim, J.W. 2002. Thermodynamic attributes of Arctic boundary layer ozone depletion. *Atmos. Environ.*, **36**(15–16), 2641–2652.

Stull, R. B. 1988. *An Introduction to Boundary Layer Meteorology*. Dodrecht / Boston/ London: Kluwer Academic Publishers.

Stutz, J., & Platt, U. 1996. Numerical analysis and estimation of the statistical error of differential optical absorption spectroscopy measurements with least-squares methods. *Appl. Opt.*, **35**(30), 6041–6053.

Stutz, J., & Platt, U. 1997. Improving long-path differential optical absorption spectroscopy with a quartz-fiber mode mixer. *Appl. Opt.*, **36**(6), 1105–1115.

Stutz, J., Kim, E. S., Platt, U., Bruno, P., Perrino, C., & Febo, A. 2000. UV-visible absorption cross sections of nitrous acid. *J. Geophys. Res.-Biogeo.*, **105**(D11), 14585–14592.

Stutz, J., Thomas, J. L., Hurlock, S. C., Schneider, M., von Glasow, R., Piot, M., Gorham, K., Burkhart, J. F., Ziemba, L., Dibb, J. E., & Lefer, B. L. 2011. Longpath DOAS observations of surface BrO at Summit, Greenland. *Atmospheric Chemistry and Physics*, **11**(18), 9899–9910.

Swan, A. M. 2011. *Multi-year Arctic Sea Ice Classification Using QuikSCAT*. Master thesis, Brigham Young University.

Tarasick, D. W., & Bottenheim, J. W. 2002. Surface ozone depletion episodes in the Arctic and Antarctic from historical ozonesonde records. *Atm. Chem. Phys.*, **2**(3), 197–205.

Theys, N., Van Roozendael, M., Hendrick, F., Fayt, C., Hermans, C., Baray, J.-L., Goutail, F., Pommereau, J.-P., & De Mazière, M. 2007. Retrieval of stratospheric and tropospheric BrO columns from multi-axis DOAS measurements at Reunion Island (21° S, 56° E). *Atmos. Chem. Phys.*, **7**(18), 4733–4749.

Theys, N., Roozendael, M. Van, Dils, B., Hendrick, F., Hao, N., & Maziere, M. De. 2009a. First satellite detection of volcanic bromine monoxide emission after the Kasatochi eruption. *Geophys. Res. Let.*, **36**.

Theys, N., Van Roozendael, M., Errera, Q., Hendrick, F., Daerden, F., Chabrillat, S., Dorf, M., Pfeilsticker, K., Rozanov, A., Lotz, W., Burrows, J. P., Lambert, J.-C., Goutail, F., Roscoe, H. K., & De Mazière, M. 2009b. A global stratospheric bromine monoxide climatology based on the BASCOE chemical transport model. *Atmos. Chem. Phys.*, **9**(3), 831–848.

Theys, N., Van Roozendael, M., Hendrick, F., Yang, X., De Smedt, I., Richter, A., Begoin, M., Errera, Q., Johnston, P. V., Kreher, K., & De Mazière, M. 2011. Global observations of tropospheric BrO columns using GOME-2 satellite data. *Atmos. Chem. Phys.*, **11**(4), 1791–1811.

Tjernström, M., Žagar, M., & Svensson, G. 2004. Model Simulations of the Arctic Atmospheric Boundary Layer from the SHEBA Year. *Ambio*, **4–5**, 221–227.

Toyota, K., McConnell, J. C., Lupu, A., Neary, L., McLinden, C. A., Richter, A., Kwok, R., Semeniuk, K., Kaminski, J. W., Gong, S.-L., Jarosz, J., Chipperfield, M. P., & Sioris, C. E. 2011. Analysis of reactive bromine production and ozone depletion in the Arctic boundary layer using 3-D simulations with GEM-AQ: inference from synoptic-scale patterns. *Atmos. Chem. Phys.*, **11**(8), 3949–3979.

Tuckermann, M., Ackermann, R., Golz, C., Lorenzen-Schmidt, H., Senne, T., Stutz, J., Trost, B., Unold, W., & Platt, U. 1997. DOAS-observation of halogen radical-catalysed arctic boundary layer ozone destruction during the ARCTOC-campaigns 1995 and 1996 in Ny-Alesund, Spitsbergen. *Tellus B*, **49**(5), 533–555.

Van Roozendael, M., Wagner, T., Richter, A., Pundt, I, Arlander, D W, Burrows, J P, Chipperfield, M, Fayt, C, Johnston, P V, Lambert, J C, Kreher, K, Pfeilsticker, K, Platt, U, Pommereau, J P, Sinnhuber, B M, Tornkvist, K K, & Wittrock, F. 2002. Intercomparison of BrO measurements from ERS-2 GOME, ground-based and balloon platforms. *Adv. Space Res.*, **29**(11), 1661–1666.

Vandaele, A., Hermans, C., Simon, P., Carleer, M., Colin, R., & Fally, S. 1998. Measurements of the NO2 absorption cross-section from 42 000 cm(-1) to 10 000 cm(-1) (238-1000 nm) at 220 K and 294 K. *J. Quant Spectrosc. Radiat. Transfer*, **59**(3-5), 171–184.

Vandal, G. M., Fitzgerald, W. F., Boutron, C. F., & Candelone, J. P. 1993. Variations in mercury deposition to Antarctica over the past 34 000 years. *Nature*, **362**, 621–623.

Vasilkov, A. P., Joiner, J., Haffner, D., & Bhartia, P. K. 2010. What do satellite backscatter ultraviolet and visible spectrometers see over snow and ice? A study of clouds and ozone using the A-train. *Atmos. Meas. Tech.*, **3**(3), 619–629.

Volkamer, R., Spietz, P., Burrows, J., & Platt, U. 2005. High-resolution absorption cross-section of glyoxal in the UV-vis and IR spectral ranges. *J. Photochem. Photobiol. A*, **172**(1), 35–46.

Wagner, T. 1999. *Satellite Observations of Atmospheric Halogen Oxides*. PhD thesis, University of Heidelberg.

Wagner, T., & Platt, U. 1998. Satellite mapping of enhanced BrO concentrations in the troposphere. *Nature*, **395**(6701), 486–490.

Wagner, T., Leue, C., Wenig, M., Pfeilsticker, K., & Platt, U. 2001. Spatial and temporal distribution of enhanced boundary layer BrO concentrations measured by the GOME instrument aboard ERS-2. *J. Geophys. Res.*, **106**(D20), 24,225–24,235.

Wagner, T., von Friedeburg, C., Wenig, M., Otten, C., & Platt, U. 2002. UV-visible observations of atmospheric O4 absorptions using direct moonlight and zenithscattered sunlight for clear-sky and cloudy sky conditions. *J. Geophys. Res.*, **107**, 4424.

Wagner, T., Ibrahim, O., Sinreich, R., Frieß, U., von Glasow, R., & Platt, U. 2007. Enhanced tropospheric BrO over Antarctic sea ice in mid winter observed by MAX-DOAS on board the research vessel Polarstern. *Atm. Chem. Phys.*, **7**, 3129–3142.

Wagner, T, Beirle, S, & Deutschmann, T. 2009. Three-dimensional simulation of the Ring effect in observations of scattered sun light using Monte Carlo radiative transfer models. *Atmos. Meas. Tech.*, **2**(1), 113–124.

Wagner, T., Deutschmann, T., & Platt, U. 2009b. Determination of aerosol properties from MAX-DOAS observations of the Ring effect. *Atmos. Meas. Tech.*, **2**(2), 495–512.

Walker, N., Partington, K., & Van Woert, M. 2006. Arctic sea ice type and concentration mapping using passive and active microwave sensors. *IEEE T. Geosci. Remote*, **44**(12), 3574–3584.

Wang, P., Stammes, P., van der A, R., Pinardi, G., & van Roozendael, M. 2008. FRESCO+: an improved O_2 A-band cloud retrieval algorithm for tropospheric trace gas retrievals. *Atmos. Chem. Phys.*, **8**, 6565–6576.

Weisstein, E. W. 2000. *Albers equal-area conic projection.* MathWorld – A Wolfram web resource. Available online at `http://mathworld.wolfram.com/AlbersEqual-AreaConicProjection.html`.

Wennberg, P. 1999. Bromine explosion. *Nature*, **397**, 299–301.

Wernli, H., & Davies, H. C. 1997. A lagrangian-based analysis of extratropical cyclones. I: The method and some applications. *Q. J. Roy. Meteor. Soc.*, **123**(538), 467–489.

Wessel, S., Aoki, S., Winkler, P., Weller, R., Herber, A., H.Gernandt, & Schrems, O. 1998. Tropospheric ozone depletion in polar regions – A comparison of observations in the Arctic and Antarctic. *Tellus B*, **50**(1), 34–50.

Wilmouth, D., Hanisco, T., Donahue, N., & Anderson, J. 1999. Fourier transform ultraviolet spectroscopy of the A (2)Pi(3/2) <– X (II3/2)-I-2 transition of BrO. *J. Phys. Chem. A*, **103**(45), 8935–8945.

Winker, D M, Hunt, W H, & McGill, M J. 2007. Initial performance assessment of CALIOP. *Geophys. Res. Let.*, **34**, L19803.

Xie, S., Klein, S. A., Yio, J. J., Beljaars, A. C. M., Long, C. N., & Zhang, M. 2006. An assessment of ECMWF analyses and model forecasts over the NorthSlope of Alaska using observations from the ARM Mixed-Phase ArcticCloud Experiment. *J. Geophys. Res.*, **111**(D5), D05107.

Yang, X., Pyle, J. A., & Cox, R. A. 2008. Sea salt aerosol production and bromine release: Role of snow on sea ice. *Geophys. Res. Let.*, **35**, L16815.

Yilmaz, S. 2012. *Retrieval of Atmospheric Aerosol and Trace Gas Vertical Profiles using Multi-Axis Differential Optical Absorption Spectroscopy.* PhD thesis, University of Heidelberg.

Zeng, T., Wang, Y., Ridley, K. Chance E. V. Browell B. A., & Atlas, E. L. 2003. Widespread persistent near-surface ozone depletion at northern high latitudes in spring. *Geophys. Res. Let.*, **30**(24), 2298.

Zeng, T., Wang, Y., Chance, K., Blake, N., Blake, D., & Ridley, B. 2006. Halogen-driven low-altitude O_3 and hydrocarbon losses in spring at northern high latitudes. *J. Geophys. Res.*, **111**, D17313.

Acknowledgements – Danksagung

Die vorliegende Doktorarbeit habe ich zu gleichen Teilen in zwei verschiedenen Arbeitsgruppen, an zwei Instituten und zwei verschiedenen Orten angefertigt. Trotz der räumlichen Entfernung zwischen Heidelberg und Mainz und der dabei nötigen Flexibilität, haben mir die Kollegen hier wie dort die Integration in ihre Arbeitsgruppe ermöglicht – habt vielen Dank für das jederzeit herzliche Willkommen und die schöne Zeit an beiden Enden der Rheintalstrecke! Darüber hinaus möchte ich den folgenden Einzelpersonen für ihren Betrag zu dieser Arbeit danken.

⋆ Zunächst möchte ich meinem Doktorvater Prof. Ulrich Platt danken, dass er diese Arbeit "zwischen den Welten" der boden- und satellitengestützten atmosphärischen Fernerkundung ermöglicht hat. Nicht weniger danken möchte ich Prof. Thomas Wagner vom MPI in Mainz für die gründliche Betreuung über die gesamte Zeit hinweg und seine unerschütterliche Motivationskraft. Beide Betreuer gestatteten mir großzügige Freiheiten und ermöglichten mir die regelmäßige Teilnahme an internationalen Konferenzen und Workshops. Zahllose Diskussionen und Anregungen, nicht nur während der PAC-Meetings, waren von unschätzbarem Wert für diese Arbeit und haben mir geholfen, das Ziel nicht aus den Augen zu verlieren.

⋆ Ebenfalls nicht vermisst haben möchte ich die Diskussionen und die Zusammenarbeit mit den beiden weiteren Mitgliedern meines PACs, Dr. Udo Frieß und Dr. Rolf Sander. Nicht nur in Barrow sondern auch in Heidelberg und Mainz hatten beide immer ein offenes Ohr für meine Anliegen.

⋆ Vielen Dank an PD Dr. Christoph Garbe für die spontane Übernahme des Zweitgutachtens.

⋆ Tineke Lelieveld und Elmar Uherek danke ich für ihre Unterstützung seitens der MPI Research School in Mainz.

⋆ I would like to thank the following individuals for inspiring discussions both professional and personal: Hans-Werner Jacobi, Lars Kaleschke, Frode Stordal, Florent Dominé, Kim Holmén, Nicolas Theys, Andreas Richter, Augusto Mangini, John Orlando, Steve Sjösted, Lee Mouldin, and Johan Ström.

⋆ Thanks to the whole OASIS team at Barrow. Despite the trouble in the beginning I sure learned a lot from you guys. From BASC, I would like to thank Lewis Brower, Nook Acker for their spirit and support. Roy Ahmoagak for inspiring chats while killing time on the tundra.

⋆ In Heidelberg konnte ich immer auf die seelisch-moralische als auch fachliche Unterstützung im Dickicht der Halogenchemie von Joëlle Buxmann zählen. Dafür

lieben Dank. Außerdem war ihr Büro die Quelle pechschwarzer Heißgetränke, welche mich gepaart mit einem guten Plausch immer wieder durch schwierige Zeiten gebracht haben.

⋆ Bedanken für stets fruchtbaren Gedankenaustausch möchte ich mich bei Christoph Hörmann, der ebenfalls den Spagat zwischen Heidelberg und Mainz praktiziert. Und sollte der jeweils andere einmal in Gegenphase gependelt sein, so gibt es ja immer noch das Telefon.

⋆ Marloes Penning de Vries, Johannes Lampel, Steffen Beirle, Denis Pöhler und Selami Yilmaz danke ich für eifriges Korrekturlesen und viele konstruktive Anmerkungen.

⋆ Ein spezieller Dank auch an Steffen Dörner, der mir im Laufe meiner Doktorarbeit die Meteorologie Stück für Stück näher brachte. Außerdem danke ich Linda Smoydzin und Daniel Kunkel vom meteorologischen Notdienst am MPI für ihren Einsatz in letzter Minute.

⋆ Ohne die Hilfe von Hella Riede, Heini Wernli, Michael Sprenger, Gregor Gläser und natürlich Rüdiger Sörensen wäre mir die Inbetriebnahme von LAGRANTO auf unseren Servern in Mainz nicht gelungen. Vielen Dank für die Hilfe bei dieser verzwickten Aufgabe. Außerdem möchte ich Conny Mies für ihre tatkräftige Unterstützung in allen Satellitendatenbelangen danken. Chalkidiki war doch gar nicht so schlecht, oder?

⋆ Meinen Zimmerkollegen in Heidelberg und Mainz für Konzentration, Kontemplation und Ablenkung: Jörg Lippold, Katja Seitz, Kira Rehfeld, Sebastian Rau, Benny Antz, Eva Kröner, Andreas Dagenbach, Sebastian Jäcker, Michael Grzegorski, Ellen Eigemeier und Beke Kremmling.

⋆ Holly Reay, James France, Josh McGrath and Patrick Boylan for brightening up the gray routine at Barrow. It was hilarious.

⋆ Vielen Dank für die Zeitvertreib im IC an Thierry Marbach, Frank Keppler, Daniela Polag, Klaus-Peter Heue und Alke Jugold.

⋆ Der IUP Fußballmannschaft, die mich bei Sturm, Eis und sengender Hitze jeden Mittwoch auf den Platz, ob drinnen oder draußen, lockt. Dabei konnte ich Fußball doch noch nie leiden...

⋆ Meinen Freunden Joris Verschaeve und Gabriel Ziegler für ihren Beitrag zu dieser Arbeit. Beide haben mich beständig auf die jeweilig der Numerik und Statistik eigenen Fallstricke aufmerksam gemacht.

⋆ Meinen Eltern vielen Dank für die Unterstützung und das Vertrauen, dass sie mir jederzeit entgegen bringen.

⋆ Last but not least möchte ich Angela danke sagen, dafür dass sie da ist und mir gerade in der Endphase mit Kraft und Tat zur Seite stand.